Photophysics of TADF Emitters and their application in OLEDs

ROBERTO SHIGUERU NOBUYASU-JUNIOR

Photophysics of TADF Emitters and their application in OLEDs

Roberto S. Nobuyasu Jr.

Organic Electroactive Materials Research Group

Department of Physics

University of Durham

A Thesis submitted to the Faculty of Science, Durham University, for the Degree of Doctor of Philosophy

April 2018

Photophysics of TADF Emitters and their application in OLEDs

Roberto S. Nobuyasu Jr.

Abstract

This thesis presents the photophysical characterization and device performance of a series of small molecules and copolymers showing thermally activated delayed fluorescence (TADF). This triplet harvesting mechanism allows triplet states to contribute to the light generation process, thus increasing the efficiency of organic light emitting diodes (OLEDs). TADF based OLEDs with internal quantum efficiency (IQE) close to 100% have already been demonstrated. However, many aspects of the mechanism still remain unclear and need to be tackled in order to design novel and more efficient TADF molecules, with emission in different regions of the spectrum. In order to maximize the TADF mechanism in different organic systems, the interplay between the charge transfer state and local triplet excited states are studied in detail and it was found that the mixing of CT and local triplet states is essential to achieve efficient reverse intersystem crossing (RISC). The consequence of introducing bulky side groups on the D unit was also studied and the luminescence from these molecules varies from efficient TADF to strong phosphorescence at room temperature. Remarkably, in clear contrast with the donor substituted molecules, their acceptor substituted analogues are strong TADF emitters. Furthermore, the fine-tuning of TADF efficiency in copolymers was explored by using spacer groups in a range of polymeric structures, overcoming the theoretical IQE limit for pure fluorescent compounds in solution-processed OLEDs. Moreover, the contribution of TADF emission in Cu-complexes showing aggregated induced emission was studied to probe the effects of vibrations on the luminescence quenching in these complexes.

Organic Electroactive Materials Research Group, Department of Physics

University of Durham

Declaration

All material contained in this thesis is original and is the result of my own work except where explicit reference is made to the work of others.

This thesis has not been submitted in whole or part for the award of a degree at this or any other university.

Photophysics of TADF Emitters and their application in OLEDs

Roberto S. Nobuyasu Jr.

Acknowledgments

I am grateful for the unconditional efforts of my supervisor, Dr. Fernando Dias, for the continuous support during my study and related research, for his patience, motivation, and immense knowledge.

A very special gratitude goes to all the OEM group, with a special mention to my co-supervisor Prof. Andy Monkman and my colleagues Paloma, Daniel, Dr. Christopher, Rongjuan and Dr. Data.

Thanks for all collaborators, Prof M. Bryce's (Chemistry department, Durham University) and Dr T. Penfold's (Chemistry department, Newcastle University) research group.

Thanks for all assistance provided by the university staff, I greatly appreciated all their help.

Thanks for the financial support from the CAPES Foundation, Ministry of Education-Brazil through the mobility programme Science Without Borders.

Also thanks to the good friends that I made during these years in Durham, specially, Erhan and Arunas.

Thanks for all your encouragement!

Primeiramente agradeço a minha família, meus pais, Celia e Roberto e meu irmão Akira, pelo apoio. Minha namorada Roberta, pelo carinho e atenção que dedicou a mim e pelo apoio incondicional durante todos esses anos.

Agradeço a todos os meus amigos que me ajudaram nessa jornada, que mesmo estando distantes sempre me apoiaram em todas as etapas: Daniel, Tiago, Gustavo, Guilherme, Tony, entre tantos outros.

Dedicated to my family:

My parents, Roberto and Celia,

My brother, Rafael

And my beloved girlfriend, Roberta

Content

Abbreviations list

CBP - 4,4′-Bis(N-carbazolyl)-1,1′-biphenyl

CT - Charge transfer

DCM – Dichloromethane

ETL – Electron transport layer

EQE - External quantum efficiency

HOMO - Highest occupied molecular orbital

HTL – Hole transport layer

iCCD - Intensified charged coupled device

IC - Internal conversion

ICT - Intramolecular charge transfer

ISC - intersystem crossing

LUMO - Lowest unoccupied molecular orbital,

LE - Locally excited state

MCH - Methyl cyclohexane

mCP - 1,3-Bis(N-carbazolyl)benzene

Nd:YAG - Neodymium doped yttrium aluminium garnet

NPB - N,N′-Bis(naphthalen-1-yl)-N,N′-bis(phenyl)benzidine

(P)OLED - (Polymer) organic light emitting diode

PF - Prompt fluorescence

DF - Delayed fluorescence

PH - Phosphorescence

PL - Photoluminescence

PLQY - Photoluminescence quantum yield,

PVA – Poly(vinylalcohol)

rISC - Reverse intersystem crossing

RT - Room temperature

TADF - Thermally activated delayed fluorescence

TAPC - 4,4′-Cyclohexylidenebis[N,N-bis(4-methylphenyl)benzenamine]

TCTA - Tris(4-carbazoyl-9-ylphenyl)amine

TPBi - 2,2′,2"-(1,3,5-Benzinetriyl)-tris(1-phenyl-1-H-benzimidazole)

TTA - Triplet-triplet annihilation

2-MeTHF - 2-Methyltetrahydrofuran

1. INTRODUCTION

1.1 Motivation

Artificial light has changed the human behaviour and activities throughout history. Leaving behind light sources such as oil, gas and firewood, the first electric arc lamp was conceived in 1876 by Pavel Yablochkov. [1] A few years later the incandescent light bulb was developed independently by Thomas Edison and Joseph Swan.[2] Since then the development and applications in lighting related technologies has continued, and in the 1970s, the first commercial compact fluorescent lamps were developed by E. Hammer, showing 75% less energy consumption than incandescent light bulbs. [3] Research in solid state lighting started in the 1920s,[3] however, the first Light-Emiting Diode (LED) used for lighting appeared only in the 60s, when N. Holonyak Jr. established the first LED with emission in the visible region.[4] Then, in the 90s, Isamu Akasakic, Hiroshi Amano and Shuji Nakamura established the first blue LED. For which they were awarded the Nobel prize in 2014.[5]

Nowadays, there are about 30 billion light bulbs in operation around the globe, resulting in an energy consumption around 18% of the total electricity produced worldwide just for lighting.[6] From these, only a small percentage consists a low power consumption lighting, LEDs or high efficient fluorescent bulbs. Moreover, and according with the United Nations Environmental Programme, in 2010 the energy consumption due to lighting in Europe was around 15% of the total energy produced, and the trend was increasing. Figure 1 shows a sequence of two pictures of Europe at night with 18 years difference between them. The ratio of illuminated-to-dark area has increased significantly.

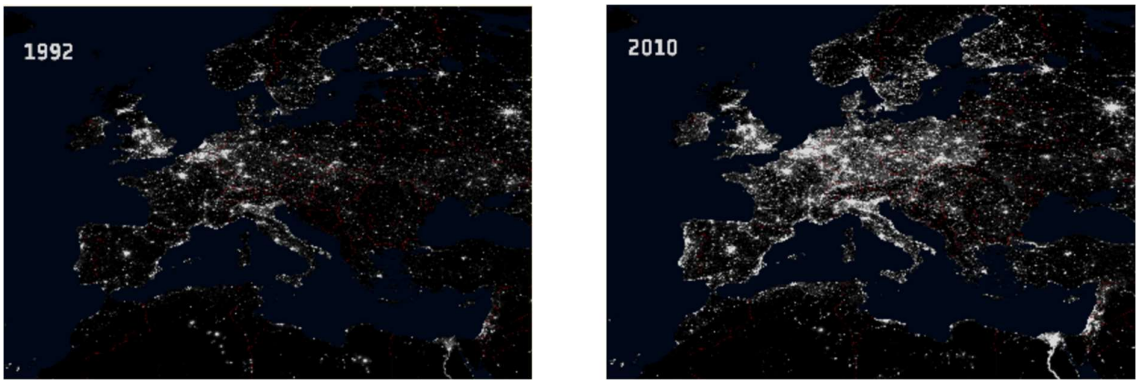

Figure 1 – Set of images showing the Europe at night in 1992 and 2012.
https://www.nasa.gov/sites/default/files/styles/full_width_feature/public/images. ***NASA/NOAA. Accessed 19/03/2018***

The search for more economical and environmental friendly light sources is therefore entirely justified. Studies in the electroluminescence of organic compounds were motivated by this long ambition, and it was firstly reported in carbazole in 1954 by A. Bernanose.[7] Followed by reports of electroluminescence in anthracene crystals, reported in 1963 by Pope's group,[8] and in 1967, in tetracene crystals by R. Signerski.[9] The first organic based LED (OLED) was reported in 1986, by C. W. Tang, and Van Slyke,[10] and the electroluminescence of poly-(phenylenevinylene), (PPV), reported in the 1990s, pioneered the design of light-emitting diodes based on polymeric materials, which could be fabricated by solution methods.[11] The era of optoelectronic inks was initiated.

The organic LEDs have already demonstrated their potential for commercial applicability in TVs and in screens of mobile phones, in which good size pixel control is required. These devices have shown significant development in the last decade, offering nowadays excellent image resolution, contrast and operational lifetimes capable of challenging inorganic LEDs. OLEDs have thus attracted great interest from several multinational companies, including Merck, Novaled, Kyulux, Mitsubishi Chemical Corporation, Nissan Chemical Industries, Sumitomo Chemicals, Dow Chemical, LG Chem, and DuPont, that have been working in close collaboration with academia on the optimization of devices and materials. Examples of commercial organic LED products are given in Figure 2. The potential for academic and social impact in this field is therefore enormous.

Figure 2 – Flexible white OLED panel and 65" OLED TV.
http://www.lgoledlight.com/portfolio_page/400x50mm (accessed 19/03/2018) and TV model LG Signature OLED65W7V 65"

A variety of organic materials have been developed to use in OLEDs, including small molecules, oligomers and polymers. They are cheaper to produce, relatively abundant, and have limited negative environmental impact, and importantly their properties can be tuned through molecular structural design. However, despite the great progresses that have been

made in the last decade, the performance of OLEDs still need improvement in multiple fronts to increase device efficiencies and operational lifetime, so their commercial potential is maximized. The broad motivation for this thesis is to participate and contribute to this challenge. Improving the stability materials and luminescence efficiencies, including maximizing the fraction of light that is extracted from these devices are the main fronts were research efforts are concentrated.

The research work in this thesis is focused on a longstanding question that is intrinsically related with the way OLEDs work. In organic materials the device driving electrical current creates excited state species called excitons with different spin multiplicity, singlet excitons (spin 0) and triplet excitons (spin 1). Unfortunately, the luminescence efficiency of singlet and triplet excitons is dramatically different. Singlets are often highly emissive and directly contribute to light emission in the device, whereas, triplets are mostly non-emissive excitons, therefore, unable to contribute to the light emission in a device. To make things worse, singlet and triplet excitons in OLEDs are formed in a ratio of 1:3. Therefore, 75 % of the charge recombination events do not contribute to the light generation. The internal efficiency of an OLED is thus limited to 25%. Recently, a major breakthrough was proposed by C. Adachi's group to solve this problem. Adachi proposed an old photophysical mechanism known as E-type delayed fluorescence, and now identified as thermally activated delayed fluorescence (TADF), to harvest triplet states in OLED emitters without using heavy metals. The TADF mechanism is based on triplet states being up-converted to the singlet manifold using the thermal energy bath. The mechanism is thus purely intramolecular and strongly dependent on the energy difference between singlet and triplet excitons. In the first reported TADF materials the efficiency was very low. Major progress has been made since then and nowadays TADF-based OLEDs have reached internal efficiencies close to 100%, as a result of strong developments in the material's design and understanding of the TADF mechanism, but despite this very significant progress many challenges still lie ahead. Efficient TADF emitters in the green region are now frequently reported in the OLED literature, but TADFs with emission in the blue and in the red are rarer, particularly in the blue region, and the first NIR-TADF emitters just started to appear. For solution-processed devices, TADF polymers are an ambitious goal, but not yet fully realized. The triplet harvesting mechanism in TADF materials is still not fully understood and this limits their molecular design of TADF emitters. The material's stability also needs improvement, and improving the luminescence efficiency and decreasing the lifetime of TADFs a major ambition.

This thesis starts with the investigation of the TADF mechanism in a small molecule formed by electron-donor (D) and electron-acceptor (A) units linked in near orthogonal orientation. The effects of molecular geometry, and the energy alignment between the different singlet and triplet states in a green TADF emitter is investigated, showing profound implications in the mechanism efficiency. This work has been published in *Adv. Optical Mater. 2016, 4, 597–607*. The work then investigates the effect of restricting molecular vibrations in D-A and D-A-D derivatives of the same TADF emitter. The dynamic nature of the TADF mechanism is demonstrated. By restricting vibrations around the D-A axis, in which imposing the adoption of different conformations, resulting in TADF being quenched, and instead room-temperature phosphorescence is observed. A first paper on this topic was published *Chem. Commun., 2016, 52, 2612*, and a second paper is in preparation to be submitted soon. The study of these molecular restricted structures was also a first step towards the realization of TADF polymers, which is the focus of the next two chapters. The first part of the work in TADF polymers is included in the paper mentioned above, published in the *Advanced Optical Materials*. The other chapter also published in *Macromolecules 2016, 49, 5452−5460*. Finally, the observation of TADF is used as a tool to probe the role of internal conversion in luminescence quenching in copper complexes, and is published in *Chem. Eur. J. 10.1002/chem.201701862*.

1.2 Bibliography

1 History of the Public Lighting of Paris. *Nature* **1933**, *132*, 888.

2 Hargadon, A. B.; Douglas, Y. *Adm. Sci. Q.* **2001**, *46* (3), 476.

3 Bowers, B. Oxford University Press, **1998**.

4 Vojak, B. A.; Laidig, W. D.; Holonyak, N.; Camras, M. D.; Coleman, J. J.; Dapkus, P. D. *J. Appl. Phys.* **1981**, *52* (2), 621–626.

5 Riechert, H. Lighting the 21st Century: Isamu Akasaki, Hiroshi Amano, and Shuji Nakamura Received the 2014 Nobel Prize in Physics for the Development of the Blue Light-Emitting Diode. *Phys. Status Solidi Appl. Mater. Sci.* **2015**, *212* (5), 893–896.

6 Powell, L.; Zissis, G.; Ikeda, H. *IEEE Industry Applications Magazine*. 2008.

7 Bernanose, A.; Marquet, G. *J. Chim. Phys.* **1954**, *51*, 255.

8 Pope, M.; Swenberg, C. E. **1999**, second edition.

9 Kalinowski, J.; Godlewski, J.; Signerski, R. *Mol. Cryst. Liq. Cryst.* **1976**, *33* (3–4), 247–259.

10 Tang, C. W.; Vanslyke, S. A.; Tang, W. *Appl. Phys. Lett.* **1987**, *51* (12), 913.

11 Burroughes, J. H.; Bradley, D. D. C.; Brown, A. R.; Marks, R. N.; Mackay, K.; Friend, R. H.; Burns, P. L.; Holmes, A. B. *Nature* **1990**, *347* (6293), 539–541.

2. Triplet Harvesting mechanisms in Organic Light Emitting Diodes (OLEDs)

This chapter introduces the basic aspects of using heavy-metal complexes, triplet-triplet annihilation and thermally activated reverse intersystem crossing as mechanisms that have been applied in harvesting triplet excitons in organic emitters, with the aim to improve the efficiency of OLEDs.

2.1 Limitations to the Efficiency in Organic Light Emitting Diodes (OLEDs)

An universal way to measure the efficiency of an OLED is using the External Quantum Efficiency (EQE). This is an absolute value that directly measures the number of photons that are produced in the device divided by the number of electrons that are injected. This ratio can be broken down into four basic steps. 1) the charge balance, i.e. the efficiency of excitons being formed when charge carriers are injected, 2) the luminescence efficiency of the chromophore singlet excited state, 3) the fraction of singlet to triplet excitons that are produced, as triplet states are usually non-emissive, and the fraction of light that is extracted from the device (due to differences in refraction index a large percentage of the light that is produced in the device suffers total internal reflection and is trapped in the device). The scheme in Figure 1 represents the breakdown of the EQE in these fundamental steps.

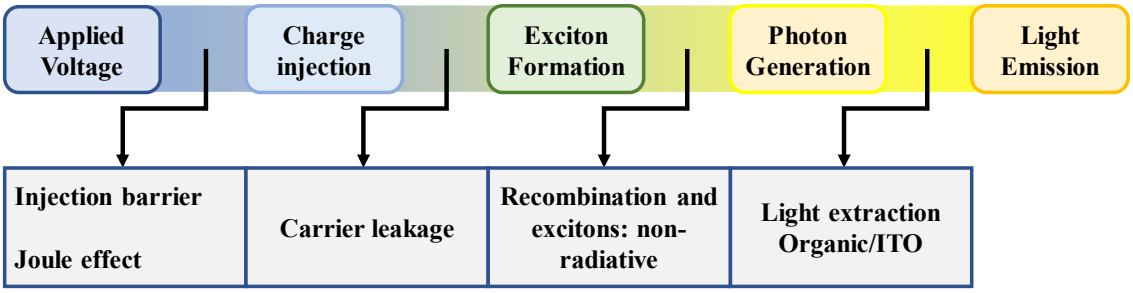

Figure 1 – Parameters which concern the external quantum efficiency.

The first OLEDs were produced with pure fluorescent compounds. In this case even if molecules exhibiting PLQY close to 100% are used, the maximum EQE possible is below 5%. This is because of the limitation imposed by the spin statistics in organic emitters, i.e. in pure fluorescent emitters the fraction of emissive singlet excitons that are created from charge recombination in an OLED is below 25%, and as the light extraction efficiency is often around 20%, the maximum EQE possible is around 5%. Therefore, mechanisms to harvest

triplet excitons in organic emitters and convert them to emissive singlet excitons are paramount to improve device efficiency.

Firstly, it was proposed to use heavy-metal complexes containing Ir(III) and Pt(II) as a way to promote the radiative decay directly from the triplet state.[1–3] This mechanism has been very successful, and several heavy-metal based emitters were developed for emission in the green and red regions with triplet harvesting efficiencies close to 100%. However, developing stable blue emissive complexes has been challenging. The use of triplet-triplet annihilation (TTA) was also introduced as way to convert triplet states in emissive singlets, but in this case the efficiency is limited to 40%,[4] and this option has never materialised as a viable strategy to improve device efficiencies. Finally, the use of emitters showing thermally activated delayed fluorescence (TADF) was introduced by Adachi's group in 2011,[5] as a way of harvesting triplet excitons using molecules where the energy difference between the singlet and triplet excited states is of just a few meV. In this case, the thermal energy bath triplets is used to up-convert triplet states to the emissive singlet manifold, using reverse intersystem crossing. These up-converted triplets then emit in the form of delayed fluorescence. TADFs are already very successful in the green emissive region, reaching triplet harvesting efficiencies close to 100%, and major progress has been achieved recently in the development of TADF emitters in the blue and red regions. The strong interest around the TADF mechanism is observed in the trend of the number of publications in this topic shown in Figure 2.

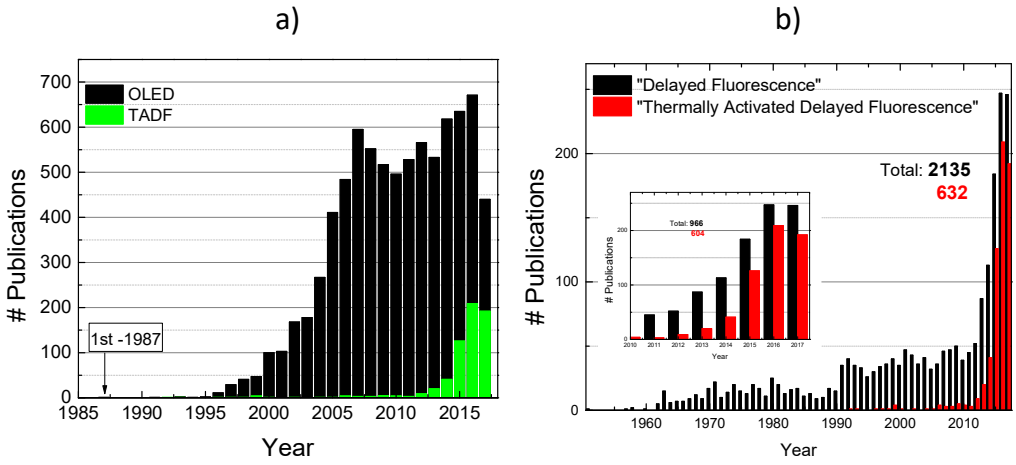

Figure 2 – a) Number of publications by topic: OLED (black) and TADF (green). b) Number of publications with only "Delayed Fluorescence" (black) compared with the topic "Thermally Activated Delayed Fluorescence" (red).

In parallel with the study of the mechanisms created to improve triplet harvesting, research has been also carried out in order to develop methods to increase the fraction of light that can be extracted from devices. Among others, this objective has been pursued by creating ways of aligning the emitting chromophores in the device, in ways that minimize total internal reflection of the emitted light. Light extraction efficiencies have thus increased to values around 40%, when perfectly aligned films are used, boosting device's EQE t0 values around 30%. The investigation of triplet harvesting mechanisms in OLED emitters, and in particular TADF, are the focus of this work and are therefore discussed in more detail in the rest of this chapter.

2.2. Mechanisms for triplet harvesting in organic semiconductors.

Excited states in organic molecules are formed with distinct spin arrangement, and involving large exchange interactions, due to the localized nature of these excitations, which give origin to electronic states with spin 0, the singlet state, and spin 1, the triplet state. This difference in the electron spin arrangement of molecular excited states gives origin to vastly different properties. The singlet state is usually short-lived – just a few nanoseconds – and can be strongly emissive, giving origin to the emission of fluorescence. In contrast the triplet state is mostly non-emissive, as the transition of triplet states to the singlet ground state is forbidden by spin. The decay of triplet states, therefore, occurs mostly via non-radiative processes, and with a lifetime in the order of microsecond to seconds. Triplets are thus often referred as dark states, because of its non-emissive character.

The differences between singlet and triplet states are of paramount importance in organic light emitting diodes (OLEDs). The 25% statistical limit in the formation of singlet excitons imposes a serious limitation to the electroluminescent efficiency in OLEDs. As three times more triplets than singlets are formed from charge carrier recombination, a simple calculation shows that for each electron-hole recombination event, only one quarter are likely to become a singlet excitation state and thus contribute to the generation of electroluminescence. The three main mechanisms that have been proposed to harvest triplet states in organic molecules are discussed below.

2.3 Organo-Metallic complexes.

Phosphorescent complexes that are formed between organic ligands and heavy atoms such as Ir(III) and Pt(II), create large spin-orbit coupling interactions, which induce mixing of singlet and triplet states to overcome the spin-forbidden nature of the triplet transition to the singlet

ground state. Strong phosphorescence can thus be observed in these complexes, leading to internal device efficiencies close to 100%. The spin-orbit coupling in these materials is strongly influenced by the high atomic number of the metal,[2,3,6] and iridium and platinum are usually used. However, in order to avoid the effects of concentration quenching and triplet-triplet annihilation, which rapidly would quench the triplet population, the phosphorescent emitters are dispersed in hosts with high charge mobility when used in OLEDs. The use of hosts creates additional difficulties, as the hosts are required to have triplet energy higher than the triplet level of the emitter to avoid quenching due to triplet-triplet energy transfer from the emitter to the host molecules. The mechanism is represented in Figure 3 and works very well in the green and red regions of the spectrum.

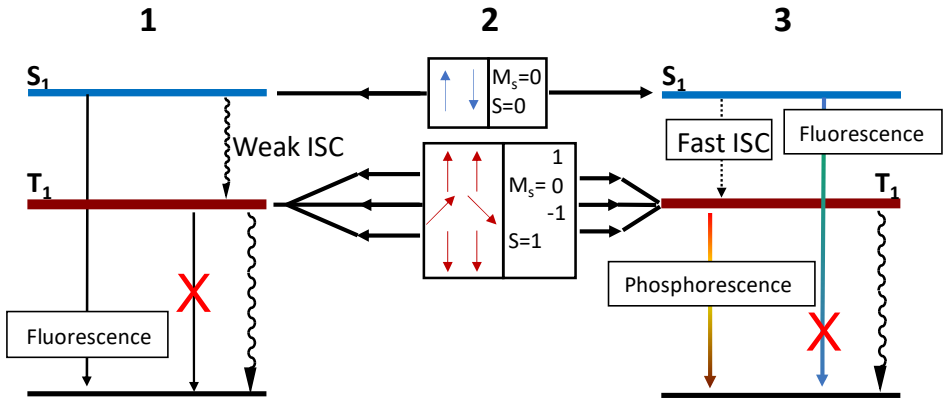

Figure 3 - Scheme of the Triplet and Singlet harvesting in an organic-metal complex: 1- standard fluorescent emitter, 2- Spin statistics ^1S and ^1T and in 3- Organo-metallic complex.

However, in the blue region it is difficult to find suitable hosts where the complexes can be dispersed, due to the high energy of the triplet state that is required, and also the complexes tend to become unstable and prone to degradation. Figure 4, shows a few examples of organic complexes that exhibits the heavy atom effect.

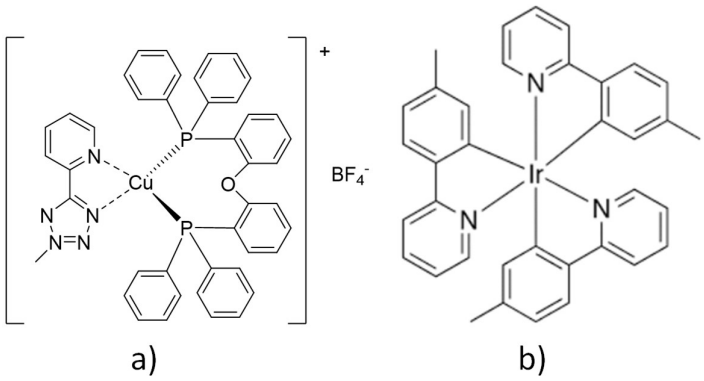

Figure 4 – Molecular structure of a) Copper complex (GF1), and b) $Ir(mPPY)_3$, as examples of molecules containing heavy atoms.

2.4 Triplet-triplet annihilation (P-type delayed fluorescence).

When a high density of triplets is created either using charge recombination or high excitation doses in molecules with strong triplet formation yield, as in the case of heavy metal complexes, these triplets have high probability to collide and interact with each other. In this process the annihilation of one of the colliding triplets may occur with the generation of an emissive singlet state. This is in general known as the Triplet-Triplet Annihilation mechanism, and it has been proposed to be used in OLEDs because the singlet state that is generated as a result of the TTA event gives origin delayed fluorescence. This fluorescence is called "delayed" because the emissive singlets are appearing from the triplet and this emission will decay with a half of the triplet lifetime. The TTA process happens through the bimolecular exciton-exciton interaction, and thus has higher probability in materials where the excitons have greater mobility or are confined in a narrow region, such as in oligomers and polymers. When colliding, two triplets have three different possible ways to combine their spins: one of the possible ways to combine the spins creates one singlet state, a second way creates three triplet states, and a third possibility gives origin to five states of multiplicity 2 (quintet). In this way two triplets may collide to give 9 different states, one singlet, with probability 1/9, three triplets with probability 1/3, and five quintets with probability of 5/9.[7] OLEDs using pure fluorescent emitters, such as anthracene, have been reported with EQEs above the 5% theoretical limit due to the occurrence of TTA.[8]

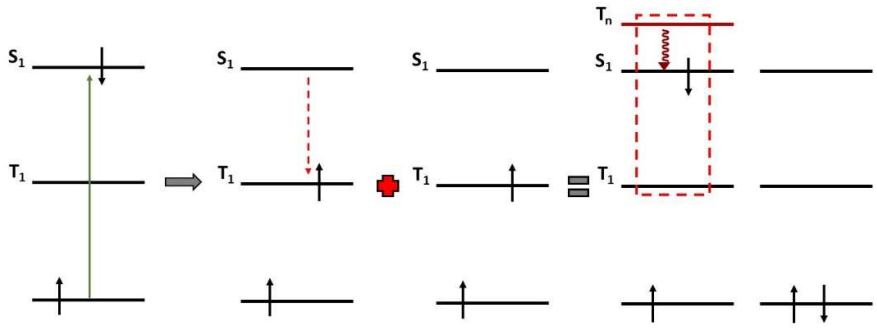

Figure 5 - Triplet annihilation mechanism in the event that $2E_{T1} > E_{S1}$. DF is due to the triplet-triplet annihilation process.

The relative position of the singlet and triplet energy levels has a strong influence on the contribution of the TTA mechanism to the electroluminescence. For example, in the case where the energy of two triplets ($2E_{T1}$) is larger than the energy of the singlet state (S_1), but smaller than the energy of an excited triplet (Tn), only singlet states can be formed, and assuming the high energy quintuplets are not formed, since this require the excitation of two

electrons simultaneously, the fraction of singlet states formed by TTA is of 50%, and the singlet yield in a device is 25% +0.5x75%=62.5%, arising the device EQE_{max} to 12.5%, shown in Figure 5. When delayed fluorescence is observed it is important to assign the mechanism to TTA or TADF. The main difference is that while TADF is an intramolecular mechanism, TTA is bimolecular. Therefore, the dependence of the delayed fluorescence with excitation dose gives dependence one (TADF) or two (TTA), and the measurement of the power dependence of the delayed fluorescence is an important tool to distinguish the two mechanisms that is often used in the next chapters.

2.5 Thermally Activated Delayed Fluorescence (E-type delayed fluorescence).

Thermally activated delayed fluorescence (TADF) is operative in molecules having very small energy splitting between their lowest triplet (T_1) and singlet (S_1) states, e.g. less than 0.2 eV. In this situation the thermal energy is enough for triplets to be up-converted back to singlet states by reverse intersystem crossing (RISC). This mechanism allows 100% triplet harvesting in OLEDs, without the need of using rare heavy metals.

$$J = \int \varphi_1 \varphi_2^* \frac{1}{r_{12}} \varphi_2 \varphi_1^* dr \qquad 1$$

The efficiency of TADF is mainly controlled by the magnitude of the energy difference between the singlet and triplet states, ΔE_{ST}, which is defined by the magnitude of the exchange energy, and is directly proportional to the overlap integral given in equation 1. Minimization of ΔE_{ST} implies the minimization of the exchange integral, J, and thus the minimization of the overlap between the HOMO and LUMO orbitals. This is achieved in molecules that have excited states with strong charge transfer character, promoted by the presence of electron-donor (D) and electron-acceptor(A) units, as those represented in Figure 6, where the HOMO-LUMO overlap is minimum.

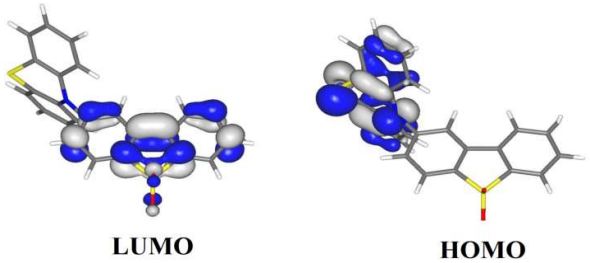

Figure 6 – Chemical structure of Ren5 with the HOMO and LUMO orbitals localized respectively, in the phenothiazine (electron donor) and dibenzothiophene-S,S-dioxide (electron acceptor) units.

The TADF mechanism is described schematically in Figure 7. The electronic states formed directly on S_1 can decay directly to the ground state (S_0) ($k_F = k_f + k_{IC}$) giving origin to fluorescence, often referred by prompt fluorescence (PF), or suffer intersystem crossing (k_{isc}) to the triplet state (T_1). The excited triplet states (k_{PH}) can then decay to the ground state via phosphorescence (k_{ph}) or internal conversion (k_{IC}), ($k_{PH} = k_{ph} + k_{IC}$) or undergo reverse intersystem crossing (k_{rISC}) back to the singlet state, where they can then decay radiatively to the ground state, and give origin to delayed fluorescence (TADF). The effective singlet-triplet energy gap ΔE_{ST} is often between the charge transfer singlet state (^{1}CT) and the lowest triplet state in the system, frequently triplet state localized on one of the units, D or A (^{3}LE).

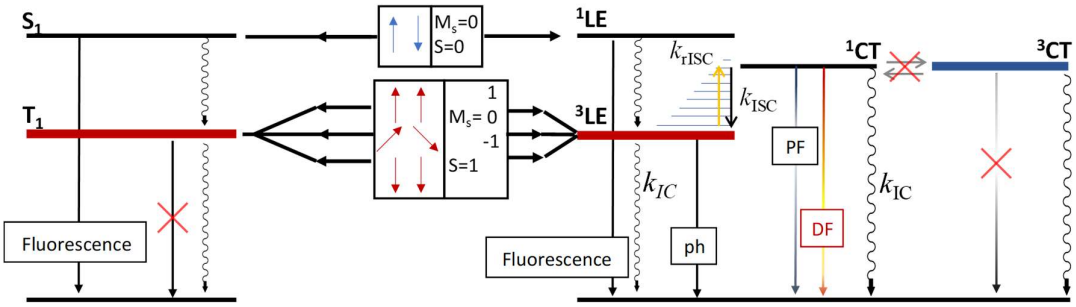

Figure 7 - Schematic representation of the TADF mechanism. In the TADF chromophore (right) the triplet states are harvested back from the lowest triplet, ^{3}LE, to the charge transfer singlet 1CT due to reverse intersystem crossing.

The reverse intersystem crossing mechanism involves a fast equilibrium (10^{12} s^{-1}) between ^{3}LE (T_1) and upper T_1 states (T_1*), followed by a slower intersystem crossing step from T_1* back to ^{1}CT (S_1). The entire reverse intersystem crossing step is strongly affected by the energy gap between S_1 and T_1, and by temperature and is described by an Arrhenius type law (Equation 2).[7,9–11]

$$k_{rISC} = k_{rISC}^0 e^{-\frac{\Delta E_{ST}}{k_B T}} \quad (2)$$

In the long time regime, i.e. longer that the lifetime of the prompt-fluorescence, the singlet lifetime decays with the triplet lifetime, according with equations 3-6.

$$\frac{dS_1}{dt} = -k_f S_1 + k_{rISC} T_1 \quad (3)$$

$$\frac{dT_1}{dt} = -(k_{ph} + k_{rISC}) T_1 \quad (4)$$

$$S_1(t) = \frac{k_{rISC}}{k_f - k_{rISC} - k_{ph}} T_0 e^{-(k_{rISC} + k_{ph}).t} \quad (5)$$

$$T_1(t) = T_0 e^{-(k_{rISC} + k_{ph}).t} \quad (6)$$

The yield of singlet states created by reverse intersystem crossing is given in equation 28, and can be close to 100%, when the RISC rate is faster that the deactivation pathways of the triplet state, $k_{rISC} >> k_{IC} + k_{ph}$

$$\phi_{rISC} = \frac{k_{rISC}}{k_{rISC}+k_{IC}+k_{ph}} \backsimeq 1 \qquad 7$$

The energy alignment between the charge transfer singlet (^{1}CT), the localized triplet state (^{3}LE) and the charge transfer triplet state (^{3}CT) has profound influence on the efficiency of the RISC mechanism. This is summarized on Figure 8, showing the case where the ^{3}CT is below ^{3}LE and below ^{1}CT (I). In this case, as RISC is inefficient between 1CT and ^{3}CT, reverse internal conversion or state mixing, between ^{3}LE and ^{3}CT has to be involved for efficient RISC to be possible. In case II, ^{1}CT and 3CT are both above the local triplet, RISC will occur directly from ^{3}LE to ^{1}CT, depending on the energy difference between these two states. In III, the energy difference between ^{3}LE, ^{1}CT and ^{3}CT is negligible. This is the ideal situation for maximum TADF efficiency. Finally, in IV, ^{1}CT and ^{3}CT are the lowest states in the system. Once more, as RISC directly between ^{1}CT and ^{3}CT is inefficient, the effective singlet-triplet gap is between ^{1}CT and ^{3}LE, and reverse internal conversion and state mixing might be involved.

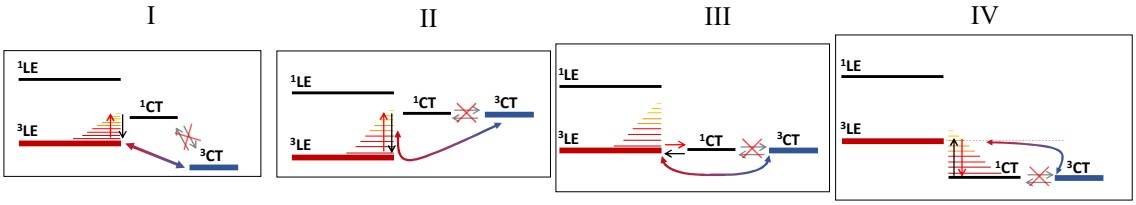

Figure 8 – Schematic representation of the possible arrangement between the singlet and triplet charge transfer states (^{1}CT and ^{3}CT), and the local triplet state (^{3}LE).

Recently the spin-vibronic mechanism has been proposed by T. Penfold to describe the TADF mechanism in the molecule represented in Figure 6.[12] Penfold and co-authors propose that RISC involves a strong correlation between the three states, ^{3}LE, ^{1}CT and ^{3}CT, comprising a fast equilibrium between ^{3}LE and ^{3}CT, as function of the vibronic coupling and the energy gap, with the ^{3}LE state acting as an intermediary state that couples the ^{1}CT and ^{3}CT states, due to the vibrational overlap of the quasi-degenerated CT states.

2.6 Bibliography

1 Baldo, M. A, Forrest, S. R., Nature **1998**, *395*, 151–154.

2 Adachi, C, Baldo, M. A, Thompson, M. E, Forrest, S. R. *J. Appl. Phys.* **2001**, *90* (10),

5048–5051.

3 Xiao, L, Chen, Z, Qu, B, Luo, J, Kong, S, Gong, Q, Kido, J. *Adv. Mater.* **2011**, *23* (8), 926–952.

4 Baldo, M. A, Adachi, C, Forrest, S. R. *Phys. Rev. B - Condens. Matter Mater. Phys.* **2000**, *62* (16), 10967–10977.

5 Sandanayaka, A. S. D, Matsushima, T, Adachi, C. *J. Phys. Chem. C* **2015**, *119* (42), 23845–23851.

6 Forrest, S. R, Baldo, M. A, O'Brien, D. F, You, Y, Shoustikov, A, Sibley, S, Thompson, M. E. *Nature* **1998**, *395* (6698), 151–154.

7 Turro, N. J, Ramamurthy, V, Scaiano, J. C. Principles of Molecular Photochemistry: An Introduction. *Book* **2009**, 495.

8 Kondakov, D. Y. *J. Appl. Phys.* **2007**, *102* (11).

9 Baleizão, C, Berberan-santos, M. N, Baleizão, C, Berberan-santos, M. N. **2007**, *204510*.

10 Dias, F. B. *Philos. Trans. R. Soc. A Math. Phys. Eng. Sci.* **2015**, *373* (2044), 20140447–20140447.

11 Ogiwara, T, Wakikawa, Y, Ikoma, T. *J. Phys. Chem. A* **2015**, *119* (14), 3415–3418.

12 Gibson, J, Monkman, A, Penfold, T. Chem. Phys. Chem., **2016**, 2956-2961

3. Experimental Methods

The main experimental apparatus and techniques used in this work are described here in detail. The mastery of experiment techniques is an important aspect that allows recording data of excellent quality, felicitating interpretation and data analysis. The purpose of this chapter is to collect and record important details that are essential for those working daily in the laboratory to obtain valuable data.

3.1 Sample preparation: Spin-casting

The spin-casting technique, also known as spin-coating, allows the even deposition of thin films of organic molecules from solution. The films are deposited covering the entire surface of the substrate, achieving thicknesses in the range of ten-to-hundred nanometers.

Films of polymers are fabricated by first dissolving the materials in an appropriate organic solvent, usually in a concentration of 10 mg/ml. This is followed by covering the substrate with a few drops of the solution. The substrate is then made to spin at 1200 rpm. In this process the solvent rapidly evaporates, leaving a solid film deposited evenly on the substrate surface. Firstly, the substrate (1) is fixed in the spinner using vacuum suction (2), using a pipette, a few drops of the solution are deposited covering the whole surface of the substrate. (3) Spinning the substrate ejects the excess of solution and forms a solid film on the surface of the substrate, (4) the thin film is left drying for 24 hours, in order to remove any excess solvent. Figure 1 represents a scheme of the spin-casting process.

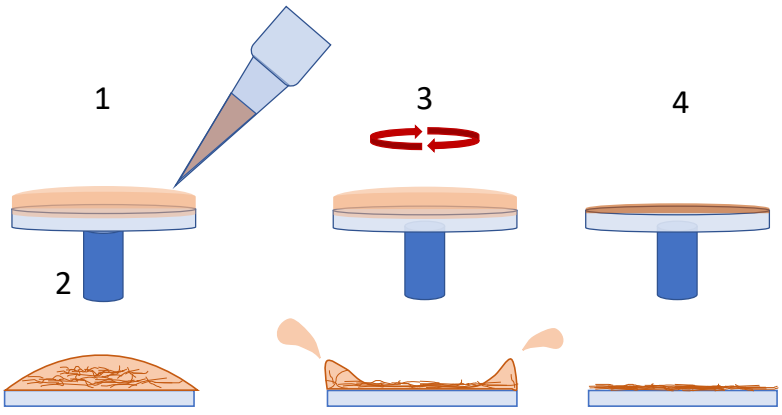

Figure 1 – Spin-casting technique illustration.

Solutions are prepared initially weighing the pure polymer, and then adding solvent. The solution concentration is decisive for the control of the film thickness. The polymer solution is brought into a magnetic stirrer for 24 hours, and the thin films are then manufactured as described above, allowing precise control of the film thickness. Polymeric thin films for optical and electrical measurements can be fabricated on several types of substrate, including quartz,

sapphire, Si/SiO_2, glass, depending on the type of study that will be performed. For devices, or when electric fields need to be applied the material is deposited on a glass substrate covered by a transparent electrode Indium Tin Oxide (ITO) is the most common choice.

Unfortunately, small molecules usually do not form good thin films, due to their low molecular weight, which makes the solution less viscous. An inert polymer (Zeonex) is then used as host, mixing the solutions of small molecules ([c] from 2.5 to 10 mg/ml) and polymer host ([c] = 170 mg/ml) in a ratio of 1:1.

3.2 UV-Vis Absorption Spectroscopy

UV-VIS absorption spectroscopy is performed on a UV-3600double beam spectrophotometer (Shimadzu) - experimental scheme shown in Figure 2. The light sources used in this apparatus are an Halogen lamp for the visible and infrared (IR) regions and a Deuterium lamp for the UV region (λ<400 nm) (1). The wavelength is selected with a double-grating monochromator (2), the selected wavelength is then divided in the beam-splitter (3), in order to create two independent beams that pass alternatively through the sample (solution or film) and the reference (4), and finally detected by a photodiode (5).

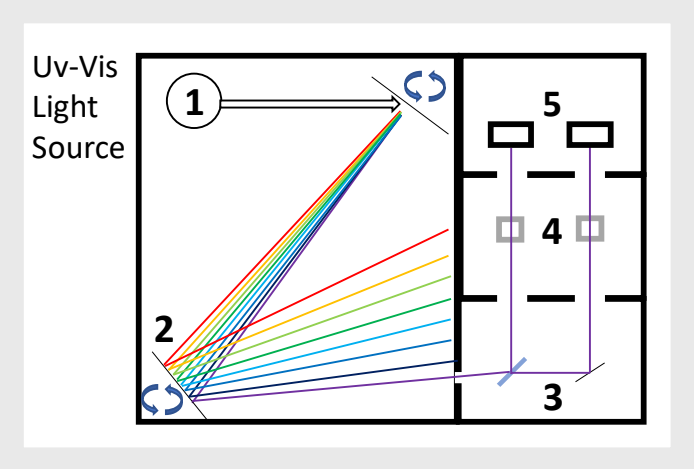

Figure 2 – Scheme of UV-3600 double beam spectrophotometer experimental scheme.

3.3 Steady state Photoluminescence

Steady-state fluorescence spectra are collected using a fluorometer (Fluorolog - Horiba Jobin Yvon), schematically represented in Figure 3. The excitation is achieved using a Xe lamp (1), that is directed through a double monochromator (2) for wavelength selection, and is incident in the sample (4), solution or film. Fluorescence is then collected at right angle geometry, through another double monochromator (5) and collected by a photomultiplier tube (7).

Emission spectra are obtained using fixed excitation wavelength, and scanning the entire region of interest, performing the integration of the light signal at each wavelength. It is also possible to collect excitation spectra. In this case, the emission wavelength is kept constant, while scanning the excitation wavelength through the entire absorption region of the sample. Emission and excitation spectra can also be collected as a function of temperature using cryostats. Spectra are corrected for detector response and for the lamp profile and intensity fluctuations. The size of the slits aperture, for excitation (3) and emission (5), and integration time can also be adjusted.

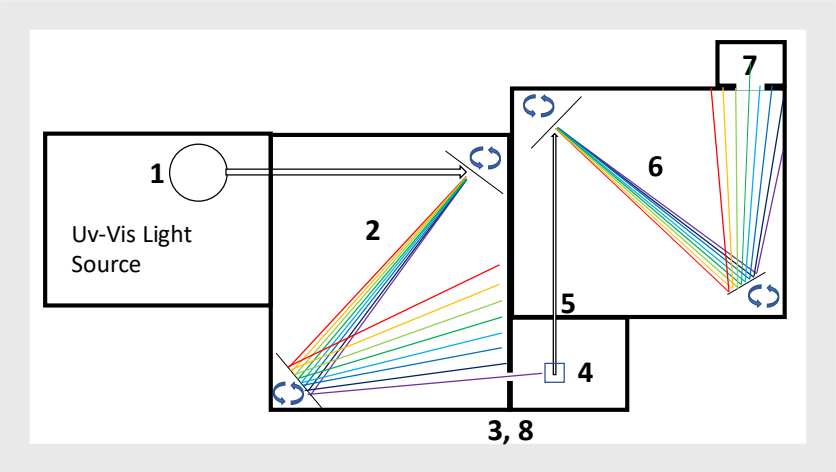

Figure 3 – Fluorometer experimental scheme.

3.4 Time-Resolved Gated Luminescence

Sample excitation is performed with a Nd:YAG pulsed laser (1), working at 10 Hz repetition rate, with 150ps pulse width. Three excitation wavelengths are available, 266nm, 355 nm, and 532 nm. Excitation can also be achieved by a nitrogen laser (2), MNL 100, working from 1 to 30 Hz repetition rate, with 3 ns pulse width. A series of mirrors (3), a flipping mirror (4) and the beam splitter (5) form the beam optical path to the sample holder (4). Two convergent lenses are used to collimate and focus the photoluminescence beam, which is then collected through a JY-190 spectrograph (7) and detected with an intensified iCCD camera (Stanford Computer Optics 4 Picos), with 200 ps time resolution (8). This setup allows the collection of both fluorescence (short lived) and phosphorescence (long lived) spectra and decays using a gated-acquisition method. The experimental setup scheme is given in Figure 4.

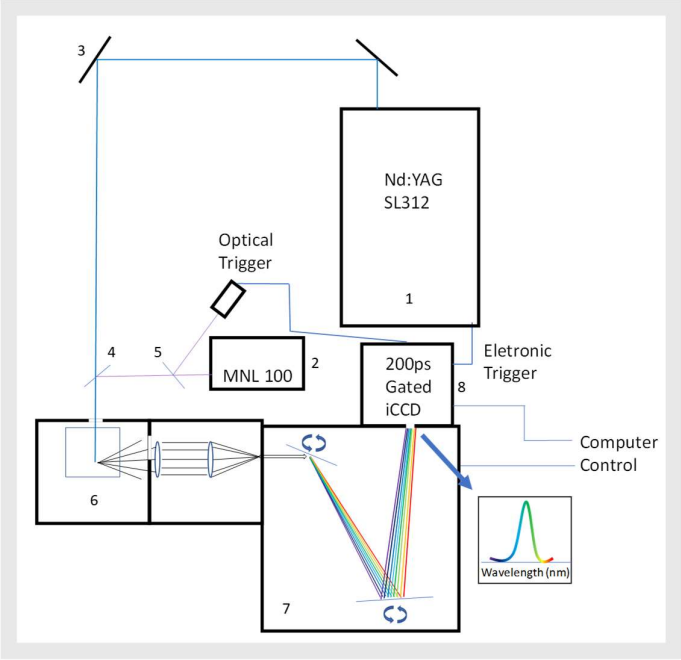

Figure 4 - Time resolved gated luminescence apparatus scheme.

The luminescence intensity is collected over a specified integration time, but just after a delay time, also specified by the user. Changing the delay time, but keeping the integration time constant, i.e. analogous to taking instant photo shots at different consecutive times, allows the luminescence decay profile to be registered. Photoluminescence lifetimes follow an exponential function, for long emission lifetime there are less photons being emitted, therefore, in order to allow measuring signals at extremely long delay times, and keeping a good signal to noise ratio, the integration times are varied following a logarithmic law (see Figure 5). This factor is then corrected by dividing the integrated signal by the integration time corresponding to each delay time. This results in recording the real number of photons per unit of time, which enables recording the emission decay.

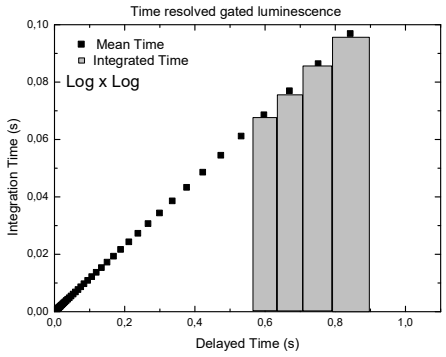

Figure 5 - Time delay and integration time plotted in a logarithmic scale.

3.5 Photoluminescence Quantum Yield (PLQY)

The determination of fluorescence quantum yields is of paramount importance on the characterization of organic molecules for applications involving photoluminescence and electroluminescence. The determination of PLQY in solution is made using a standard method based on the comparison of the photoluminescence efficiency in the sample under investigation against the efficiency of a suitable reference compound. The determination of PLQY in solid samples is more complex than in solution and requires using an integrating sphere for the measurement of absolute photoluminescence quantum efficiencies. The procedure used in this work is based on the method proposed by Greenham et al.[1]

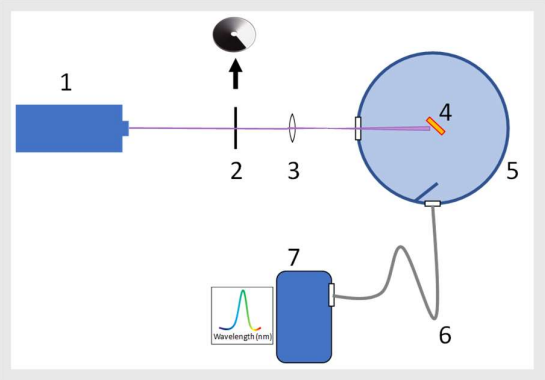

Figure 6 – PLQY experimental scheme

The laser beam (1), used as the excitation, passes through a neutral density filter (2), a convex lens (3), and reaches the sample (4), located inside the integrating sphere (5). The interior surface of the integrated sphere is coated by Spectraflect[1] which is a white and highly reflective material, model 4P-GPS-040-SF LABSPHERE, which scatters both the excitation beam and the sample's luminescence, making it evenly distributed on the inside surface of the sphere.
The total luminescence power emitted by the sample, as well as the total excitation light power absorbed by the sample, can thus be measured free of any inaccuracies caused by the highly directional nature of the sample's luminescence in solid state. The scattered luminescence and excitation beam are then collected through the optical fibre (6) and recorded using an Ocean-Optics spectrophotometer (7). A scheme of the experimental setup is given in Figure 6.

[1] https://www.labsphere.com/site/assets/files/1831/pb-13026_rev01.pdf

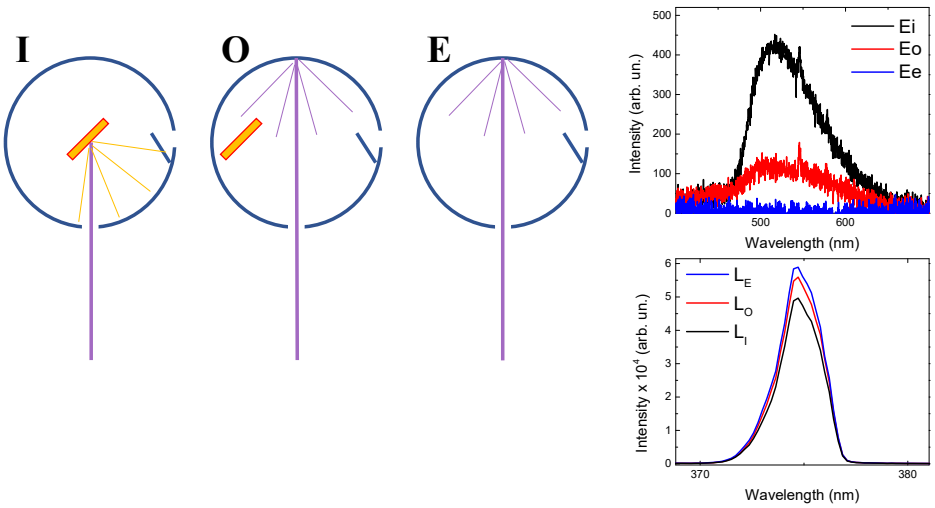

Figure 7 - Laser and sample position for PLQY measurement with the respective spectra

The experimental PLQY measurement consists of three steps: (1) Using a constant excitation laser power for all measurements, collecting the excitation laser profile and the photoluminescence spectra, when the sample is directly excited. These are identified as L_i and E_i, respectively; (2) repeat the measurement with the sample placed out of the laser beam. These signals are identified as L_o and E_o, respectively, and account for the contribution of secondary excitations. (3) Repeat the experiment for the empty sphere. In this situation there is no emission and the laser profile is identified by L_e. The geometry used in steps 1-3 and the spectra obtained in each step are shown in Figure 7.

The photoluminescence quantum yield (η) is then determined using eq. (1):

$$\eta = \frac{E_I(1-A)E_O}{A.L_E} \qquad 1$$

Where A is:

$$A = \frac{L_O - L_I}{L_O} \qquad 2$$

3.6 Freeze-pump-thaw. Oxygen degassing of liquid samples

Oxygen is an important quencher of the triplet excited states in organic molecules, and also of long-lived singlet states. The ground state of the molecular oxygen is a triplet state, and so energy transfer from the triplet excited state of the chromophore to the oxygen molecule's ground state is usually very efficient. Therefore, the evaluation of spectroscopic signals involving triplet states requires previous degassing of the samples under study. For measurements in solution, a special cuvette, in Figure 8, is employed to allow removing the

oxygen dissolved in the solution using a method known as Freeze-Pump-thaw. This consists of freezing the solution located in the container (3), using a liquid nitrogen bath, and simultaneously removing the gas via the secondary input (2) with a vacuum pump. After removing all the gas for a few minutes the tap (1) is closed and the solution is let to warm up at room temperature. The previous steps are repeated in a sequential manner for five times. Finally, the solution is transferred to the quartz cuvette (4).

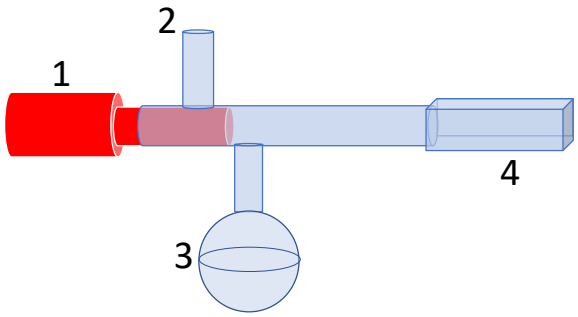

Figure 8 – Schematic representation of the degassing cuvette.

3.7 Temperature Dependent Measurements.

Measurements taken as a function of temperature are essential in the work performed in this thesis. A Janis VNF100 cryostat was used, shown schematically in Figure 9 to perform these measurements This cryostat consists on : (1) the sample chamber with ~~a~~ double quartz windows, inside which the sample holder is located. The height and angle of the film are controlled using a manual knob at the top of the cryostat (2). Nitrogen filling aperture (3), external vacuum chamber (4) to isolate the sample chamber, temperature controller plug is connected in (5) and (6) valve to control the sample chamber vacuum level.

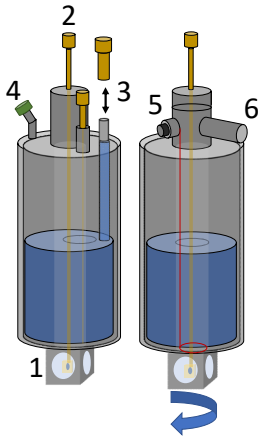

Figure 9 – Schematic representation of the Nitrogen cryostat.

For liquid samples a special cuvette is used, with a longer tube than the cuvette present in Figure 8, to fit inside the cryostat. After the inside and external chambers are under vacuum (4). The nitrogen reservoir is filled with liquid nitrogen. This reservoir is connected to the sample chamber by a capillary tube, which allows nitrogen vapour to go inside the sample chamber. This is the low-temperature source. Electrical heating is powered by the temperature controller, Lake Shore-Model 331, to allow controlling the sample temperature in the interval from 77 K to 320 K.

3.8 Cyclic Voltammetry

The first step on the fabrication of OLEDs is to select the appropriate compounds for the secondary layers used to transport and confine charge carriers in the active emissive layer, Figure 10-1. The determination of the ionization (Ep) and reduction (En) potentials, which are related with the energy of the compound's frontier orbitals HOMO and LUMO, and are indispensable physical properties to be determined priory to device fabrication is usually performed using cyclic voltammetry.

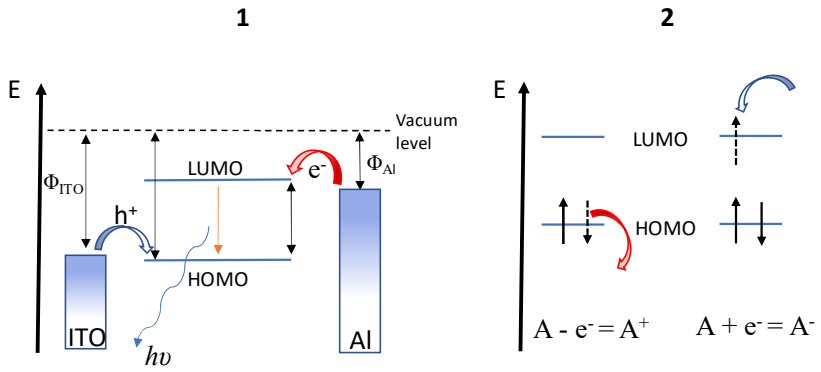

Figure 10 – 1: the energy level scheme of an hypothetic device; 2: the oxidation and reduction experimental scheme.

The cyclic voltammetry (CV) experiment is conducted using an electrochemical cell and three electrodes, the reference and the working electrodes, and the auxiliary electrode. The compound under study is dissolved in an organic solvent - typically dichloromethane (DCM) or tetrahydrofuran (THF) - together with a non-reactive electrolyte, typically tetrabutylammonium hexafluorophosphate (TBA *PF6)*, see Figure 11 for a schematic representation of the experimental apparatus.

A cyclic voltammogram is obtained by measuring the voltage between the reference and the working electrodes during the potential scan, and measuring the current between the working

electrode and the auxiliary electrode as a function of the voltage that is applied between the working electrode and the reference electrode.

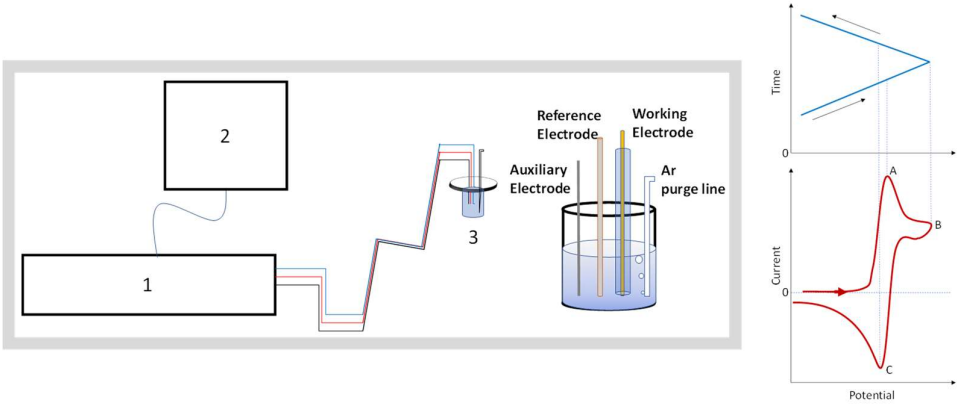

Figure 11 - Cyclic voltammetry apparatus scheme and cyclic voltammogram.

In this work, it has been used DCM has been used as the solvent for the determination of the oxidation potential and THF to determine the reduction potential, which is more stable under reduction conditions. The electrolyte (TBA *PF6*), is used in both situations with a concentration of 0.1 M. Ferrocene is used as a standard in the determination of oxidation and reduction potentials, usually in a concentration smaller than 10 mM, to avoid any secondary reaction due to the high concentration of ferrocene.

Firstly, a background current is obtained just with the electrolyte solution, to check if any contamination may be present in the system, which would generate a current signal. This gives us the background signal that is expected if everything is in appropriate conditions for the measurement to proceed. Following this initial step, the electrolyte solution with ferrocene is measured. This gives the oxidation/reduction potentials of the standard. Then start measuring the oxidation potential of the electrolyte solution with the compound. In this, the voltage is scanned from 0 to 1 V, increasing as long as it is necessary to include the whole signal for the oxidation. Following this determination, the ferrocene standard is added and the measurement repeated. This is a double check on the system to ensure that everything is correct. For the determination of the reduction potential, the electrolyte solution is previously purged with argon gas for thirty minutes, before running the experiment. This is to remove oxygen dissolved in the solution, since the reduction potential of oxygen is within the range of the potential scan used in this determination and it will interfere with the electroanalytical signal. Finally, after each measurement with ferrocene, the electrochemical cell and the electrodes are cleaned.

The analysis of the CV data gives the electron affinity (EA) and the ionization potential (IP) directly from equations 3 and 4, respectively.

$$IP = -(Ep + 5.1)\ [eV] \quad (3)$$

$$EA = -(En + 5.1)\ [eV] \quad (4)$$

where En and Ep are the onset of the reduction and oxidation waves, against the Fc/Fc+ (5.1 eV). The electrochemical band-gap is determined as the difference between the electron affinity and ionization potential energy levels (Equation 5):[2–4]

$$E_G^{CV} = EA - IP\ [eV] \quad (5)$$

3.9 Ellipsometry

Another important parameter on the optimization of OLEDs is the thickness of the different layers in the device. When the device is fabricated, thickness of the different layers is essentially controlled by the rate of deposition. This is determined by the change on the oscillation frequency of a quartz crystal, piezoelectric effect based sensor, as the vapor coats the crystal surface. However, as the crystal and the substrate are in different locations, it is in general inaccurate to assume that the sensor and the substrate have exactly the same deposition rates. Therefore, a calibration is necessary. This is called the tooling factor of the material. Basically it is a process to link the deposition rate in the quartz crystal with the real film thickness, determined by an independent process. Ellipsometry has been used as a independent way to measure film thickness.[5]

Start by producing a sample thin film with 100 nm thickness, estimated directly from the crystal reading. Than using the ellipsometry to determine the real thickness of this film, and thus correcting the previous value of the tooling factor. Obviously, the tooling factor is unique for each material, and as so needs to be measured for each new material that is investigated.

The ellipsometry method consists of evaluating the changes in polarization of an incident beam caused by reflection on the film surface. The polarization of the incident beam is analyzed in two components, one parallel to the plane of incidence and another perpendicular to this plane. The plane of incidence contains the normal to the film surface and the propagation vector of the incoming radiation. Scheme of the ellipsometer shown in Figure 12.

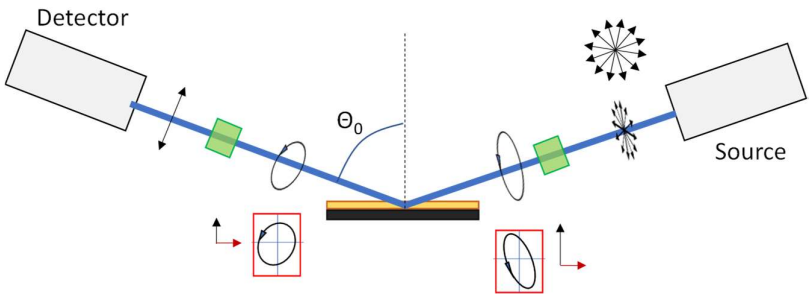

Figure 12 – Ellipsometry apparatus.

The film thickness is determined due to the interference between the beam that is directly reflected at the film surface, and the beam travelling through the film and being reflected at the substrate. This interference can be constructive or destructive, depending on the relative phase of the two beams, and is very sensitive to the film thickness. The experimental parameters p_s, p_p, ρ and Δ, are also related to the changes in polarization that the light beam undergoes when changing medium. Obviously, for an accurate determination of the film thickness using this method it is necessary to know very well the optical properties of the substrate. In this work, silicon dioxide as the substrate, for which the optical properties have been very well characterized by other laboratories.

In order to have a good signal for the ellipsometry experiments the film thicknesses should be around 150 nm, and the wavelength of the incident light beam should be outside the absorption region of the material under study.

However, theses measured parameters are still not directly correlated with the thickness of the film. In order to associate it with the film parameters, numerical simulation fittings have to be used in order to fit the dependence of the variables with the incident angle, from where the film thickness is determined as one of the fitting parameters. The diagram in Figure 13 summarize the experiment and the fitting used to determine the sample thickness.

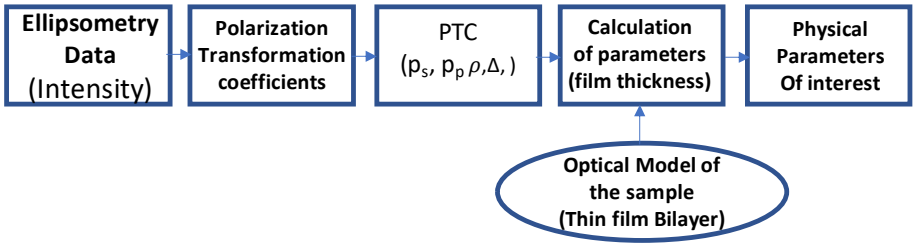

Figure 13 – Graphic scheme for thickness determination.

3.10 Fabrication of Organic Light Emitting Diodes.

Organic light emitting diodes (OLEDs) can be fabricated directly from solution or using vacuum deposition methods. In brief, OLEDs are multi-layered structures containing an emitting layer, usually formed by an organic host doped with the emitter, which is sandwiched between two other organic layers. The role of these additional layers is to facilitate the transport and injection of electrons and holes from the two opposite electrodes, one of which is transparent. The emitter can be a conjugated polymer, usually used in solution processed devices, or a small molecule. The host is usually a small molecule with good ambipolar transport. For the transporting/injection layers small molecules are also usually used. Finally the electrodes are a combination of lithium-fluoride and aluminium for electron injection and indium tin oxide (ITO) as the transparent electrode, used for hole injection, see schematic representation of an OLED in Figure 14.

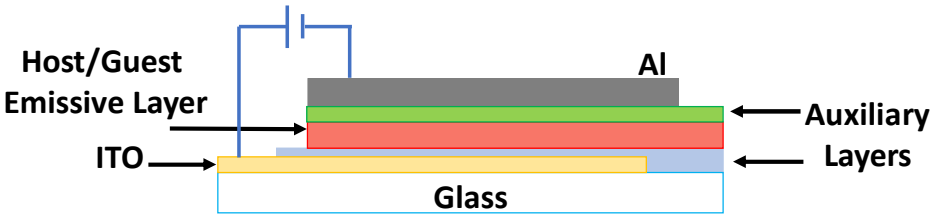

Figure 14 – OLED structure scheme.

Applying a voltage between the two electrodes, with the ITO electrode at positive potential relatively to the Al electrode, injects electrons and holes in the active layer, passing through the transporting layers, which are mainly responsible for the conductivity and charge balance in the bulk film. These transport layers are also used to block charges to reach the opposite electrode, therefore, forcing their recombination in the emitting layer.

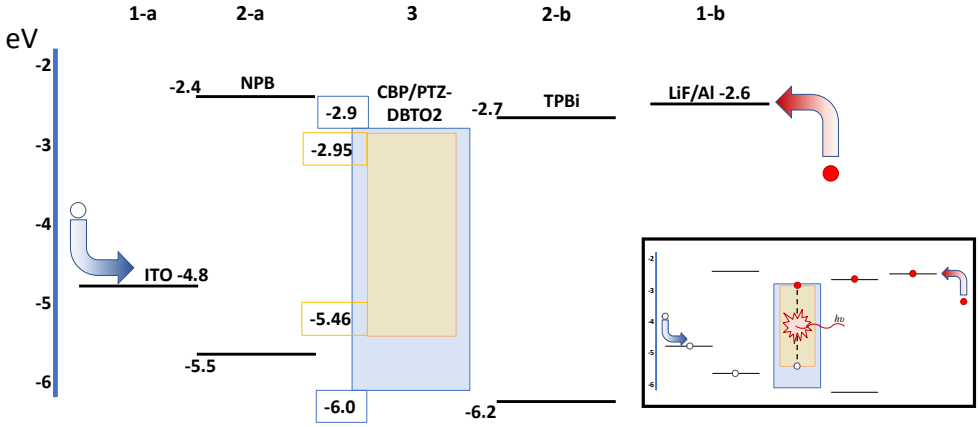

Figure 15 – OLED energy diagram with NPB and TPBi as charge transport layers.

Opposite charge carriers are thus forced to recombine in a same molecule due to Coulomb interactions and lead to the formation of highly localized excitons, which when recombine radiatively, provide the electroluminescence that is observed in these devices. See Figure 15 for a schematic representation of the electroluminescence mechanism in OLEDs.

3.11 Charge Transport Materials for OLEDs

In order to improve the injection and transport of charge carriers, charge transport layers are used to minimize the injection barriers, effectively decreasing the drive voltage required to drive the device. Then, localizing the charge carriers in the active layer will increase the probability for them to recombine. For this effect, additional layers are used as electron or hole blocking layers, creating energy barriers, to prevent the flow of electrons and holes, respectively. Finally, these layers also allow a better adhesion to the anode and serve to smooth the anode surface in the device structure. Sublimated materials with purification higher than 99.9% are usually used.

Compounds that were used to produce the OLED in this thesis as hole transport layers were **TAPC** 4,4′-cyclohexylidenebis[N,N-bis(4-methylphenyl)benzenamine], **NPB**, N,N′-bis(naphthalen-1-yl)-N,N′-bis(phenyl)benzidine, **mCP,** 1,3-bis(N-carbazolyl)benzene and **TCTA**, tris(4-carbazoyl-9-ylphenyl)amine. As Electron transport layer CBP, 4,4′-bis(N-carbazolyl)-1,1′-biphenyl and **TPBi**, 2,2′,2"-(1,3,5-benzinetriyl)-tris(1-phenyl-1-H-benzimidazole) were used, whose structures are shown in Figure 16 and the energy levels, HOMO/LUMO are shown in Figure 17.

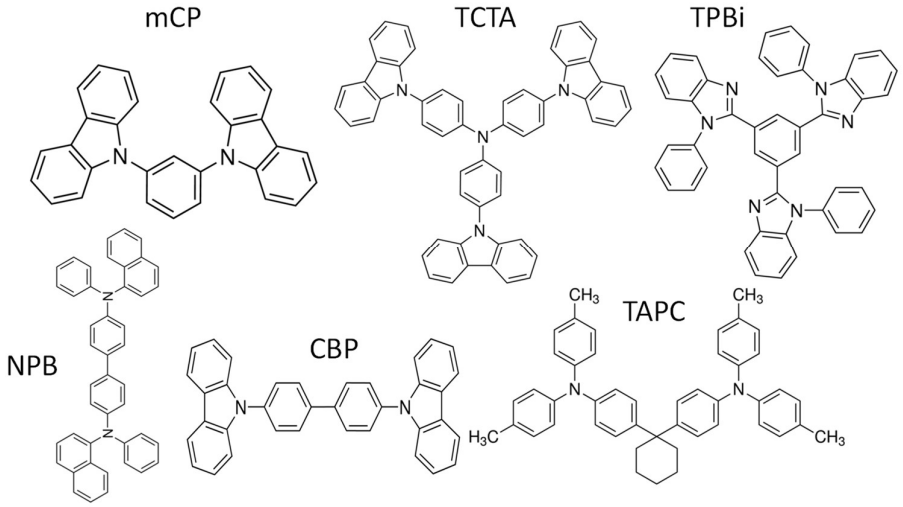

Figure 16 – Materials employed as transport layer used in the OLED structure for this thesis.[2]

[2] Commercial compounds

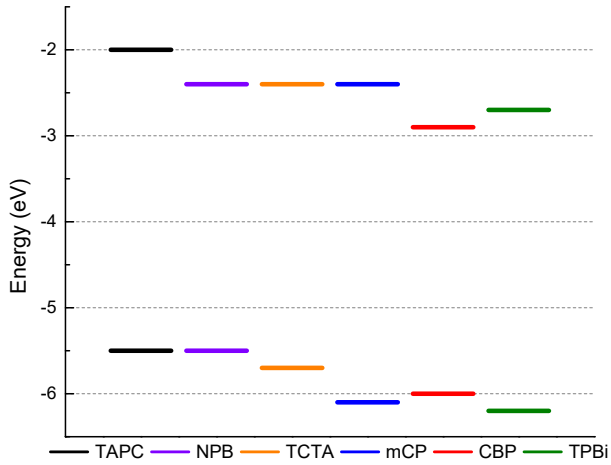

Figure 17 – HOMO/LUMO energy levels of TAPC (black), NPB (purple), TCTA (orange), mCP (blue), CBP (red) and TPBi (green).

3.12 Substrate Cleaning

OLED devices were fabricated using precleaned ITO (Indium-Tin Oxide) coated glass substrates (Ossila) with a sheet resistance of 20 Ω/cm^{-2} and an ITO thickness of 100 nm.

Prior to layer deposition, all the substrates go through a cleaning process, consisting of sequentially cleaning substrates with acetone, followed by isopropanol, for ten minutes, using ultra-sonic immersion (Ultrawave U50). Then, after carefully drying the substrates with nitrogen. Plasma cleaning process (Electronic Diener Femto) is applied for four minutes.

3.13 Fabrication of OLEDs by Solution Processed Methods.

Solution processed OLEDs are fabricated directly from solution, using spin-coating as the film deposition method. After the cleaning stage, the hole-injection material PEDOT:PSS is spin-coated directly on to the clean ITO substrate as the hole-injection layer. The emissive layer, usually formed by a conjugated polymer, or a small molecule dispersed in a polymeric host, is then deposited from a chlorobenzene solution (10 mg/mL) directly on the PEDOT:PSS layer by spin-coating at 1500 rpm, usually to form a 40 nm thick emissive layer. Other combinations are possible to use as emissive layers. For example in host/guest emissive layers, a blend solution of 10% polymer and 90% single host (mCP, CBP) or combined host (25% TAPC and 65% TCTA) in chlorobenzene are usually used. The emissive layer is then usually annealed at 80 °C for 30 min, in order to remove the residual solvent. Finally, Lithium fluoride and aluminium are deposited by thermal evaporation.

In the solution process method it is very hard to perform multi-layer deposition. However, orthogonal solvents may be used to try avoiding dissolution from previous layers, when attempting fabrication of multi-layer devices.

3.14 Fabrication of OLEDs, using Vacuum Sublimation Methods.

In contrast with solution process methods, vacuum sublimation allows for the deposition of multilayers, therefore, giving the opportunity to fabricate more complex structures and significantly increasing the performance of these devices.

The device manufacture consists of a sequential process in which organic compounds are heated under high vacuum, and the vapour condenses on the surface of a substrate. All the elements necessary for the vapour deposition are contained inside the vacuum chamber (1), a high vacuum is then used, to avoid the presence of oxygen, which would easily oxidize the compounds. The organic compounds, and the materials for the electrodes, are located in specific crucibles (2-a), which can be heated up using electrical resistances (2-b), see Figure 18. Masks, see Figure 19, are used to control the region of deposition for each layer. The samples' holder and respective masks are located on the top of the chamber (3).

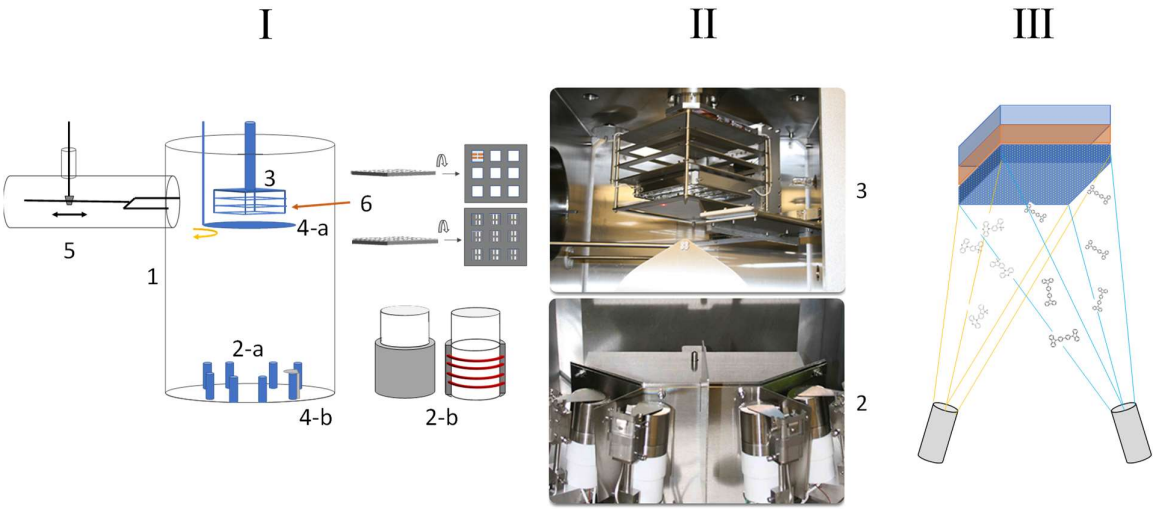

Figure 18 – I: Illustration of deposition system, II picture of the crucible set and the sample holder and III the co-deposition illustration of PTZ-DBTO2 and CBP.[II]

This holder is made to spin to achieve homogenous deposition of the film. Shutters are used for the sample (4-a) and crucibles (4-b) to control the flux of vapour to be deposited on the substrate surface. A piezoelectric device is used to control the thickness of the thin films. Finally, the fork (5) provides a way to change the mask (6) and the samples holder (6) when this is necessary without having to open the vacuum chamber. Figure 18, represents

schematically the deposition process in a Kurt J. Lesker Spectros II, system. With the schematic device fabrication in Figure 19.

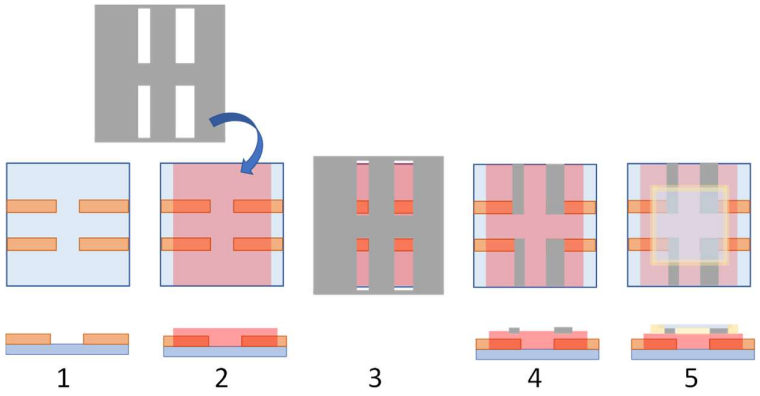

Figure 19 – Schematic illustration of top and side view of device fabrication.

3.15 OLED characterization.

The performance characterization of OLED devices involves measuring the typical I-V-L (current-voltage-luminance) curves. This consists of recording the I(V) and the electroluminescence spectra for each step in voltage. The objective is to fully characterize the electroluminescence process and determine other parameters, such as the device external quantum efficiency (E.Q.E), luminance efficiency and brightness.[6]

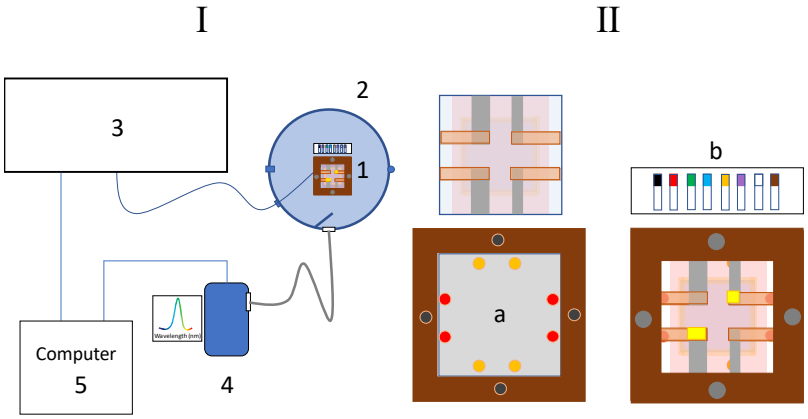

Figure 20 – OLED's optical and electrical characterization scheme.

A schematic representation of the experimental apparatus is given in Figure 20-I and II, showing schematically the device's layout in 2x2 arrangement. Figure 21, shows a photograph of our device characterization system. The sample holder (1) is located inside an integrating sphere (2), wire connections are provided for electrically driving the device (3). An optical fibre spectrometer (Ocean Optics) (4) is used to collect the device luminescence, which is

finally recorded in a computer (5). Figure 20-II is an highlight of the sample holder (a), in which it is possible to select the OLED (b).

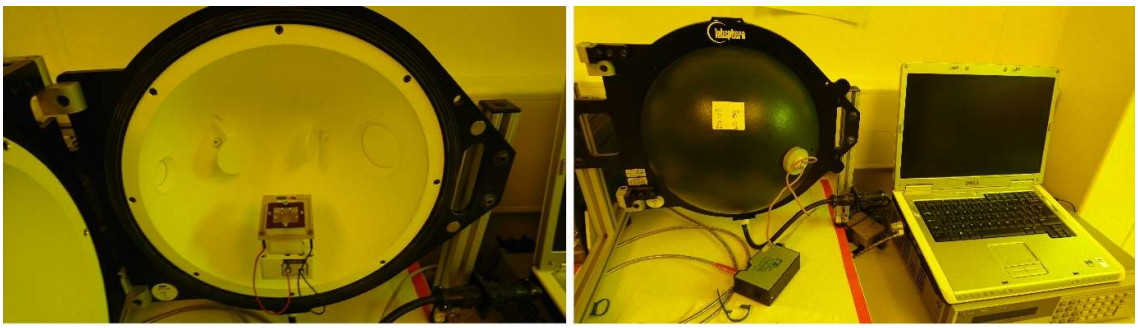

Figure 21 – Photograph of OLED's characterization

3.16 Device Efficiency

The efficiency of an OLED device is controlled by four main factors summarized in Figure 22, (1) the electron-hole capture efficiency (χ), which affects the probability of an exciton being formed. This factor can be optimized to 100%, using hole and electron blocking layers and thereby forcing the formation of the exciton in the emissive layer. (2) The quantum yield of fluorescence (Φ_f), this is an intrinsic material property which can also be optimized to be close to 100% and measures the efficiency of the radiative recombination process. (3) The yield of singlet excitons (β) formed by electron-hole recombination. Excited states in organic molecules are formed with distinct spin arrangement, and involve large exchange interactions, due to the localized nature of these excitations. These differentiate the singlet state, with zero spin multiplicity, and the triplet state, with spin multiplicity one. This difference in the electron spin arrangement of molecular excited states, gives origin to vastly different properties. The singlet state is usually short-lived – a few nanoseconds – and strongly emissive, giving origin to fluorescence emission when decaying to the ground-state because the transition between two singlet states is spin allowed, whereas the decay of the excited triplet state is forbidden by spin. The decay of triplet states, therefore, occurs mostly via non-radiative processes and with a lifetime in the order of microsecond to seconds. Triplets are thus often referred as dark states, because of its non-emissive character.

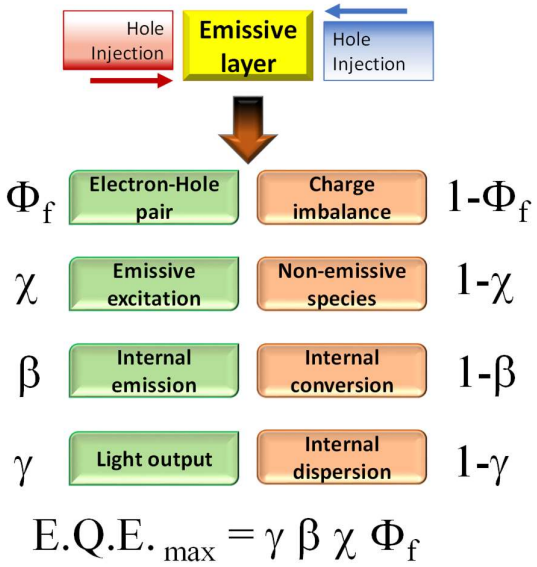

Figure 22 – Parameters related with the external quantum efficiency.

The differences between singlet and triplet states are of paramount importance in the efficiency of OLEDs. In the way these devices work, and assuming that simple statistics govern the charge recombination process, singlet and triplet states are formed in a ratio of 1:3, i.e. there are three 'dark' triplet excited states for each singlet emissive state. The yield of formation of singlet states is thus at most 25%. The device internal efficiency of pure fluorescent OLEDs is thus limited to 25%. Finally, (4) the light-extraction ratio (γ) is at most 30%, and so the maximum external device efficiency is limited at 5%. Other mechanisms are therefore necessary to take EQE values above the 5% limit, and the research of these mechanisms is one of the main objectives of this thesis.

3.17 Luminous Efficiency

Light produced from a given area of a device is expressed in candela (Cd), a standard unit of luminous intensity, defined as the radiant intensity of a monochromatic light at 555 nm with 1/683 watt per steradian, as the spectral luminous efficacy for monochromatic radiation in this particular wavelength is 683 lumens per watt. The ratio integrated luminous intensity/electrical current is the current efficiency (η_L) and is given in equation 10:[6,7]

$$\eta_L = \frac{L}{J} = \frac{\frac{Cd}{m^2}}{\frac{A}{m^2}} = \frac{Cd}{A} \qquad 6$$

The luminous energy efficiency is defined in equation 11, given in lumens (lm) per watt (η_p):

$$\eta_p = \frac{L.\pi}{J.V} = \eta_L.\frac{\pi}{V} = \frac{Cd.rad}{A.V} = \frac{Lm}{W} \qquad 7$$

3.18 External Quantum Efficiency[6]

Device brightness is a visual perception; output optical power (OP), the intensity of a radiating source, can also be represented in terms of lumens where the corresponding OP to 1 lumen in function of wavelength is given by:

$$OP(\lambda) = \frac{1}{683.V(\lambda)} \quad 8$$

The number of photons within 1 lumen of flux, where E = ($h.c$)/ λ:

$$P(\lambda) = \frac{\lambda}{683.V(\lambda).\mathrm{h.c}} \quad 9$$

V(λ) is a standard function established by the Commission Internationale de l'Éclairage (CIE). and may be used to convert radiant energy into luminous efficiency, also colour matching function.

The total luminescence (I_t) of the device can be given by integrating the whole electroluminescence spectrum.

$$\int_a^b I(\lambda)d\lambda \quad 10$$

The total extracted luminescence (P_{ext}) of the device can be given by integrating the whole electroluminescence spectrum, where α(λ) is the correction curve for a given experimental system.

$$P_{ext} = \int_a^b \frac{\alpha(\lambda).I(\lambda)}{683.V(\lambda)}d\lambda \quad 11$$

For each electron injected, it is expected to have one photon, in order to estimate the efficiency is necessary to have the number of electrons injected into the device:

$$n_e = \frac{J.A}{q} \quad 12$$

The experimental determination of the External Quantum Efficiency (EQE) is given by the number of photons emitted externally per second (P_{ext}) from the device per injected electrons per second (n_e) and it is usually expressed as a percentage:

$$EQE = \frac{P_{ext}}{n_e} \quad 13$$

In others words, the external quantum efficiency of an OLED can be calculate by recording the EL spectrum and the electroluminescence versus current density.

The software used in this experiment requires the following input: pixel area, integration and delay time for the spectrum recording, and also its possible average, integrating sphere response (calibration); increment, initial and final voltage and maximum current. Finally, it does the computation of the secondary results generating the files for each one, via software interface.

3.19 Bibliography

1 Greenham, N. C.; Samuel, I. D. W.; Hayes, G. R.; Phillips, R. T.; Holmes, A. B.; Friend, R. H.; Chemical Physics Letters, **1995**, 241, 89-96.

2 Data, P.; Pander, P.; Lapkowski, M.; Swist, A.; Soloducho, J.; Reghu, R. R.; Grazulevicius, J. V. *Electrochim. Acta* **2014**, *128*, 430–438.

3 Cardona, C. M.; Li, W.; Kaifer, A. E.; Stockdale, D.; Bazan, G. C. *Adv. Mater.* **2011**, *23* (20), 2367–2371.

4 Bredas, J.-L. Mind the Gap! *Mater. Horiz.* **2014**, *1* (1), 17–19.

5 Ellipsometry, by; McCrackin, F. L.; Passaglia, E.; Stromberg, R. R.; Steinberg, H. L. *J. Res. Natl. Bur. Stand. Phys. Chem.* **1963**, *67* (4), 366-377.

6 De, D.; Pereira, S.; Data, P.; Monkman, A. P. *Disp. Imaging, **2016** 2*, 323–337.

7 Sliney, D. H. *Photochem. Photobiol.* **2007**, *83* (2), 425–432.

4. Photophysics of TADF in the Asymmetric Donor-Acceptor PTZ-DBTO2.

This chapter describes the investigation of the photophysical properties of an asymmetrical TADF emitter, including device fabrication. Phenothiazine-dibenzothiophene-S,S-dioxide (PTZ-DBTO2), formed by a phenothiazine electron donor unit (D) and a dibenzo-S,S-dioxide acceptor (A) ,is one of the first asymmetrical molecules reported that show strong TADF emission. Herein, it is demonstrated that the interplay between the charge transfer state and local triplet states of the D or A units, as well as molecular conformation have crucial importance on the efficiency of the TADF mechanism.

This chapter is published in: Nobuyasu, R. S. et al., Rational Design of TADF Polymers Using a Donor–Acceptor Monomer with Enhanced TADF Efficiency Induced by the Energy Alignment of Charge Transfer and Local Triplet Excited States. Adv. Optical Mater. 2016, 4, 597–607.

4.1 Introduction

Thermally activated delayed fluorescence, (TADF),[1] also known as E-type delayed fluorescence,[2] has very rapidly gained interest as a mechanism to improve OLED efficiencies. The possibility of harvesting 100% of the excitons formed by direct charge recombination, without requiring the use of expensive and scarce metals, such as iridium or platinum,[3] and avoiding the degradation issues affecting organic phosphors in the blue spectral region give these molecules a prime role in the field of OLEDs.[4] TADF is also finding application in fluorescence imaging due to the extended fluorescence lifetime and large Stokes shift observed in most TADF emitters. This allows filtering out the sample auto fluorescence and avoids scattering effects.[5] TADF is thus of general interest for any area where extending the excited state lifetime would bring significant advantages.

The observation of efficient TADF requires the non-emissive triplet excited states to be able to cross back to the emissive singlet manifold, from where they can then contribute to the overall emission. This reverse intersystem crossing (RISC) mechanism uses the thermal energy to promote the up-conversion of lower-energy triplet states into the emissive singlet manifold.

The efficiency of the TADF mechanism is essentially controlled by the energy splitting between the singlet and triplet states (ΔE_{ST}), which needs to be minimized, and the nonradiative pathways available for the excited singlet and triplet states to decay, which need to be suppressed in order to obtain high fluorescence quantum yields and long triplet excited state lifetimes.[6]

To achieve a small energy splitting between the singlet and triplet excited states, molecules are designed with excited states of strong charge transfer character. This creates a small overlap between the highest occupied and lowest unoccupied molecular orbitals, HOMO and LUMO, respectively. Further minimization of the singlet-triplet gap is achieved by using electron-donor (D) and electron-acceptor (A) units linked in nearly perpendicular relative orientation, which results in extremely small exchange energy and therefore negligible ΔE_{ST} values, contributing to the maximisation of the efficiency of the RISC process.

One aspect that remains unclear in the reverse intersystem crossing mechanism is the role of spin orbit coupling (SOC) and the possible role of hyperfine coupling (HFC). Previous work has shown that in the one-electron approximation, intersystem crossing due to spin orbit coupling between the singlet charge transfer state (^{1}CT) and a locally triplet excited state (^{3}LE) is of fundamental importance to harvest triplet states, since the interconversion between the ^{1} CT and ^{3}CT states is often not efficient.[7,8] Therefore, the presence of a local triplet energetically close to the CT manifold should strongly influence the efficiency of the TADF mechanism. Here, the photophysics of an asymmetrical D-A molecule with strong TADF emission is investigated in detail, focusing on particular on the effects promoted by the energy alignment between the CT manifold and local triplet excited states of the D and A units, and the effects of molecular conformation. The proximity of local triplet excited states (^{3}LE), e.g., ^{3}D or ^{3}A, above or below the DA charge transfer states (CT) is shown to enhance significantly the efficiency of the TADF mechanism in PTZ-DBTO2. Moreover, the presence of axial and equatorial conformers of PTZ-DBTO2 is confirmed, showing pronounced differences in their TADF responses.

4.2 Molecular Structure and cyclic voltammetry

The TADF emitter investigated in this work is identified as PTZ-DBTO2.[a] It is based on phenothiazine as the electron donor unit (D) and dibenzothiophene-*S,S*–dioxide as the electron acceptor (A) unit. The PTZ-DBTO2 molecular structure is represented on Figure 1a, with the D and A units highlighted in blue and red, respectively. Computational simulations[b] reveal the presence of equatorial and axial conformers in PTZ-DBTO2, see Figure 1b, with the equatorial form being the most stable. Importantly in both conformers the D-A units are arranged in near perpendicular orientation. However, in contrast with the computational

[a] PTZ-DBTO2 was synthesized in Prof. Martin Brice's group, Chemistry Department, Durham University.
[b] Computational simulations performed in the group of Dr. Penfold, School of Chemistry, Newcastle University.

studies, the form identified by single-crystal X-ray analysis, Figure 1c, is the axial form. This is probably due to the influence of intermolecular interactions present in the crystal.

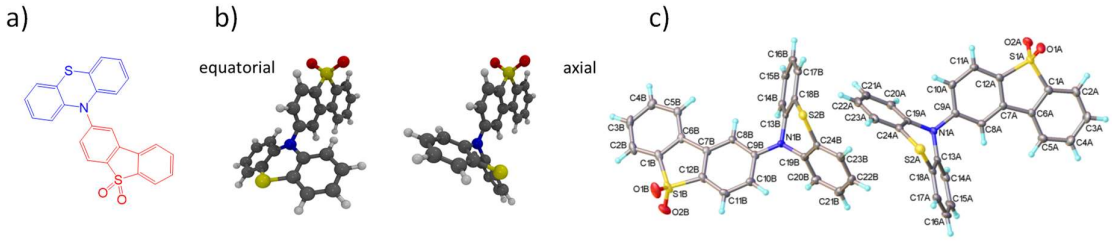

Figure 1 – a) PTZ-DBTO2 molecular structure, D and A units highlighted in blue and red, respectively. b) PTZ-DBTO2 conformers identified in computational simulations D-A arrangement in PTZ-DBTO2, confirmed in near orthogonal geometry by computational simulations. c) X-ray crystal structure of PTZ-DBTO2.[c]

The HOMO-LUMO energy levels of PTZ-DBTO2, −5.4 eV and −2.95 eV, respectively, were determined by cyclic voltammetry data analysis, taking into consideration that the redox potentials, electron affinity (EA) and ionization potential (IP), directly correspond to the LUMO and HOMO energies, respectively. The HOMO and LUMO roughly correspond to the HOMO of the donor phenothiazine, and the LUMO of the acceptor dibenzothiophene-*S,S*–dioxide.

4.3 Photophysics: Absorption and Steady-State Fluorescence

Figure 2 shows a) the absorption and b) emission spectra of the individual D and A fragments and of PTZ-DBTO2, all in dilute methylcyclohexane (MCH) solution.

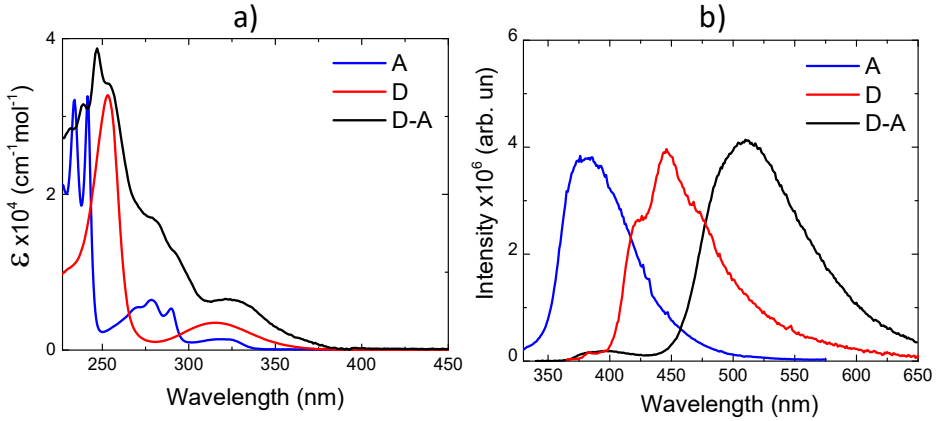

Figure 2 – a) Absorption spectra of the D, A fragments and of PTZ-DBTO2 in MCH solution. b) Fluorescence of D, A and PTZ-DBTO2 in MCH solution.

[c] X-Ray crystal structure performed by Dr. Andrei S. Batsanov, Chemistry Department, Durham University.

The absorption spectrum of PTZ-DBTO2 is almost entirely formed by the superposition of the D and A absorptions (Figure 2a). This is consistent with the limited conjugation between the D and A units that is imposed by the nearly perpendicular orientation of the D-A units.

The fluorescence from PTZ–DBTO2 appears broad and featureless, however strongly affected by the polarity of the medium in which the PTZ-DBTO2 molecule is dissolved, and appears clearly red-shifted from the D and A emissions, with maxima at 356 nm (A) and 445 nm (D) in MCH, see Figure 2b. This gives strong indication for the charge transfer character of the PTZ-DBTO2 excited state. The Stokes shift in PTZ-DBTO2 is also large, with the emission maximum shifting between 540 and 630 nm depending on the solvent polarity (Figure 3). The emissive singlet state in PTZ-DBTO2 is thereafter identified as ^{1}CT. This emission band has been assigned to the equatorial conformer in PTZ-DBTO2.[9]

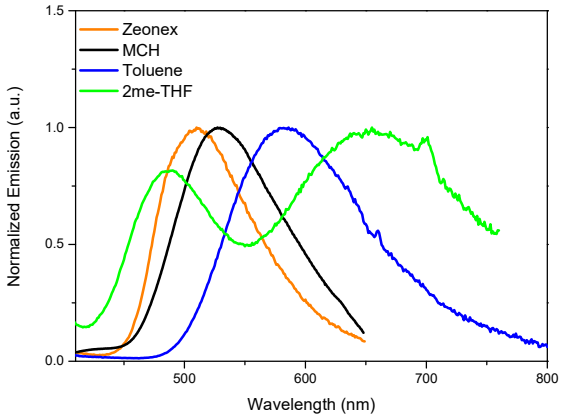

Figure 3 – Emission spectra of PTZ-DBTO2 in solution and dispersed in zeonex host. A strong solvatochromic effect is observed with increasing solvent polarity. The spectrum obtained in 2Me-THF clearly reveals the presence of two conformers.

Remarkably, the emission spectrum of PTZ-DBTO2 in 2Me-THF shows a clear second band at higher energies, peaking around 480 nm, which has been assigned to the presence of the axial conformer in PTZ-DBTO2, see Figure 1b.[9] In strong polar media, such as in 2Me-THF and other polar solvents, the emission of the low energy ^{1}CT state is strongly quenched, and the emission from the high-energy axial conformer becomes more evident. Similar observation is made, when the emission in MCH is collected in the presence of oxygen. As oxygen quenches the delayed emission from the ^{1}CT state, fluorescence from this axial conformer at higher energies is more easily observed.

Direct population of the ^{1}CT state is obtained by excitation at the edge of the PTZ-DBTO2 absorption, where a weak $S_0 \rightarrow {}^1$CT absorption band ($\varepsilon \backsimeq 10^2$ mol^{-1}cm^{-1}) is observed at high concentrations, extending up to 440 nm, see Figure 4.

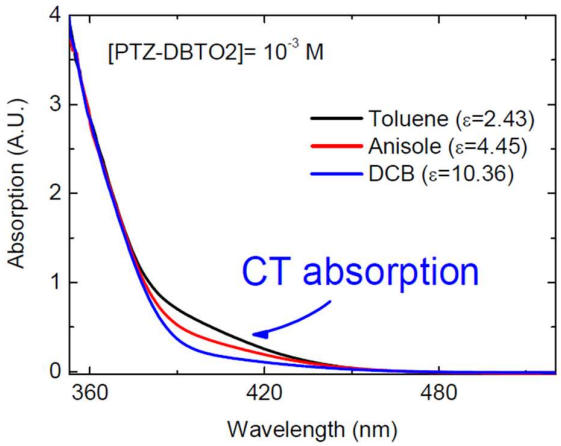

Figure 4 – Absorption of PTZ-DBTO2 obtained at high concentration (10^{-3} M) in solvents of increasing polarity (DCB = 1,2-dichlorobenzene). A weak CT absorption is identified at the onset of the main absorption band.

4.4 Time-Resolved Studies

As already mentioned, the nearly perpendicular D–A orientation and strong CT character of the excited state gives rise to an extremely small overlap integral between the HOMO and LUMO orbitals, see Figure 5. This results in very small singlet–triplet energy splitting between the lowest singlet and triplet charge transfer excited states, ^{1}CT and ^{3}CT, respectively. However, the presence of a ^{3}CT state could not be inferred from our spectroscopy data, probably because the extremely small overlap between the HOMO and LUMO orbitals in PTZ-DBTO2, result in the singlet and triplet CT states, being practically degenerate.

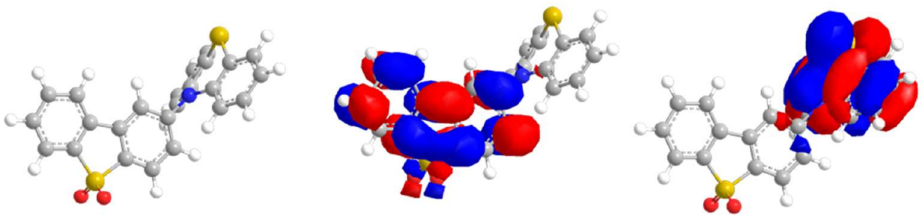

LUMO -2.368 eV HOMO -5.482eV

^{1}CT = 1.6130 eV ^{3}CT= 1.6065 Δ_{ST} = 7.4 meV

Figure 5 - Optimized PTZ-DBTO2 HOMO and LUMO orbitals. S_1 and T_1 energies are also calculated showing a small singlet-triplet energy splitting.[d]

[d] Simulation performed by Martin Bryce's research group.

The energy of the singlet ^{1}CT in Zeonex is determined at RT from the onset of the DF time resolved spectrum at 2.66 eV, see Figure 6a. At low temperatures, however, the onset of the ^{1}CT emission spectrum slightly contracts and the ^{1}CT energy is determined at 2.61 eV, see Figure 6b. The ^{1}CT energy is therefore determined between 2.61 and 2.66 eV.

At early times, emission from a local excited state ^{1}LE, carrying contributions from ^{1}D and ^{1}A emission, is also observed with intensity maximum around 420 nm, see Figure 6a. The near perpendicular arrangement between the D and A molecular units causes very low electronic coupling between them and greatly slows down the D–A electron transfer step. Direct recombination from the ^{1}LE singlet state, e.g. ^{1}D or ^{1}A, is thus able to compete with the population of the ^{1}CT state.

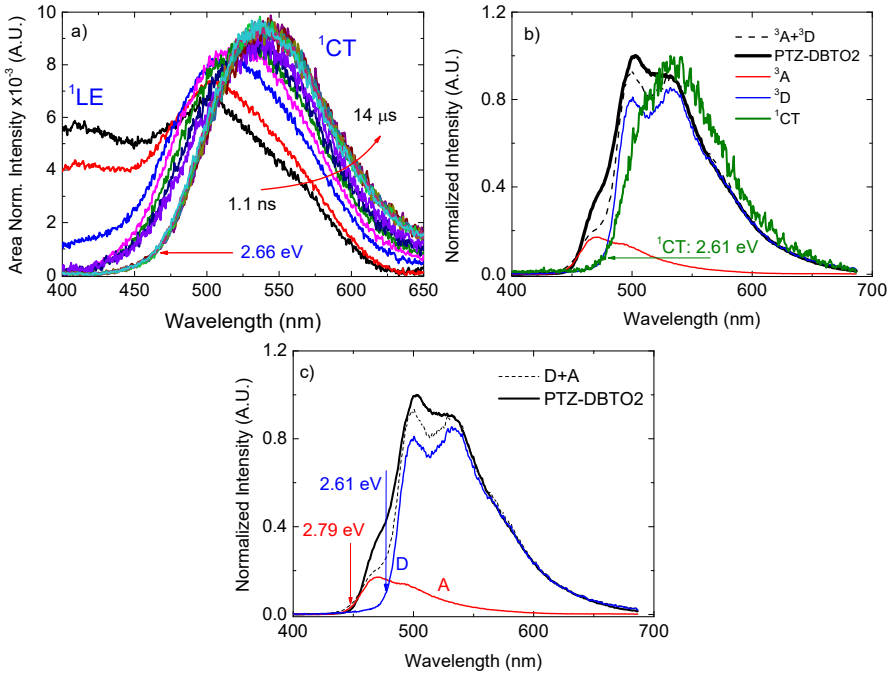

Figure 6 - a) Time-resolved emission spectra of PTZ-DBTO2 at room temperature. b) Phosphorescence of PTZ-DBTO2, compared with the phosphorescence of the isolated D and A fragments, and with the ^{1}CT emission at 77 K. c) Phosphorescence of PTZ-DBTO2, compared with the phosphorescence of the isolated D and A fragments, with determination of the ^{3}A and ^{3}D energies. All spectra obtained in zeonex.

The phosphorescence spectra of the individual D and A fragments and of PTZ-DBTO2 are compared in Zeonex matrix at 77 K in Figure 6c. At this low temperature, the DF is sufficiently weak and phosphorescence from PTZ-DBTO2 is easily observed. Interestingly, the PTZ-DBTO2 phosphorescence occurs from a local triplet state (^{3}LE) carrying clear signatures from the D and A units, ^{3}D and ^{3}A, respectively. It is however, unclear whether

these are two triplet states emitting separately or in fast equilibrium, or just one triplet state that carries contributions from both ^{3}A and ^{3}D. The higher energy triplet (^{3}A) is measured by the onset of the phosphorescent spectra in the acceptor unit (^{3}A), at 2.79 eV, and the low energy triplet state localized in the D phenothiazine (^{3}D) emits at 2.61 eV, see Figure 6c. The singlet-triplet energy difference between ^{1}CT and ^{3}A is, therefore, of 0.13 eV, and between ^{1}CT and ^{3}D of less than 0.05 eV. Both energy differences represent very small ST energy gaps, which explain the strong TADF in PTZ-DBTO2.

If just one triplet state is assumed, then using the onset of the phosphorescence to determine the energy of this local triplet state (^{3}LE) in PTZ-DBTO2 - without separating the contributions of the ^{3}A and ^{3}D - the triplet energy is determined at 2.79 eV, giving a Δ_{ST} gap of 0.13 eV at room temperature. The experimental singlet-triplet gap is, therefore, one order of magnitude higher than the gap between ^{1}CT-^{3}CT, calculated as 7.4 meV, shown in Figure 5.[e] Note that at low temperature, the energy difference between the ^{1}CT state and the ^{3}LE increases by 0.05 eV, to 0.18 eV. However, with increasing temperature the onset of the ^{1}CT slightly expands, which reflects the change in the Boltzmann distribution of the ^{1}CT state, and the energy gap between ^{3}LE and ^{1}CT decreases.

Figure 7 shows the steady-state fluorescence from the individual D (peak at 448 nm), and A (peak at 381 nm) fragments and of PTZ-DBTO2 are compared with the PTZ-DBTO2 delayed fluorescence (DF) obtained in rigid Zeonex matrix at room temperature.

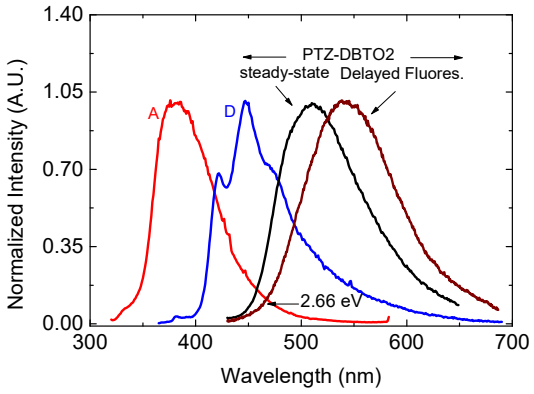

Figure 7 - Steady-state emission spectra of the single D, A fragments and of PTZ-DBTO2, compared with the PTZ-DBTO2 delayed fluorescence. The delayed fluorescence spectrum is collected at 1 μs delay time, and integrated over 20 μs.

The steady state emission of PTZ-DBTO2 appears blue-shifted relatively to the delayed fluorescence (DF). This is due to the pronounced spectral relaxation of the ^{1}CT state that is

[e] Calculated using the B3LYP/6-31G(d) level by S. Batsanov.

observed in Figure 6a. In the steady-state, the emission of non-relaxed CT states and of ^{1}LE is included, shifting the spectrum to slight higher energies. However, the energy of the ^{1}CT state determined from the integrated time resolved DF spectrum, agrees well with the previous determination, giving the ^{1}CT energy at 2.66 eV.

4.5 Steady-State Emission as a Function of Temperature

The steady-state fluorescence of PTZ-DBTO2 in Zeonex as a function of temperature is shown in Figure 8. Between 320 K and 180 K, the PTZ-DBTO2 fluorescence is dominated by ^{1}LE and ^{1}CT emissions, peaking at 396 and 510 nm, respectively (Figure 8-a). A clear isoemissive point is observed between the ^{1}LE and ^{1}CT emissions, with the intensity of the ^{1}CT emission decreasing when the temperature decreases, and the ^{1}LE emission showing the opposite trend (Figure 8-b). This confirms that the ^{1}LE and ^{1}CT states are kinetically linked species. Finally, below 180 K, ^{3}LE phosphorescence emerges and starts to dominate the emission spectra, show in Figure 8-c.

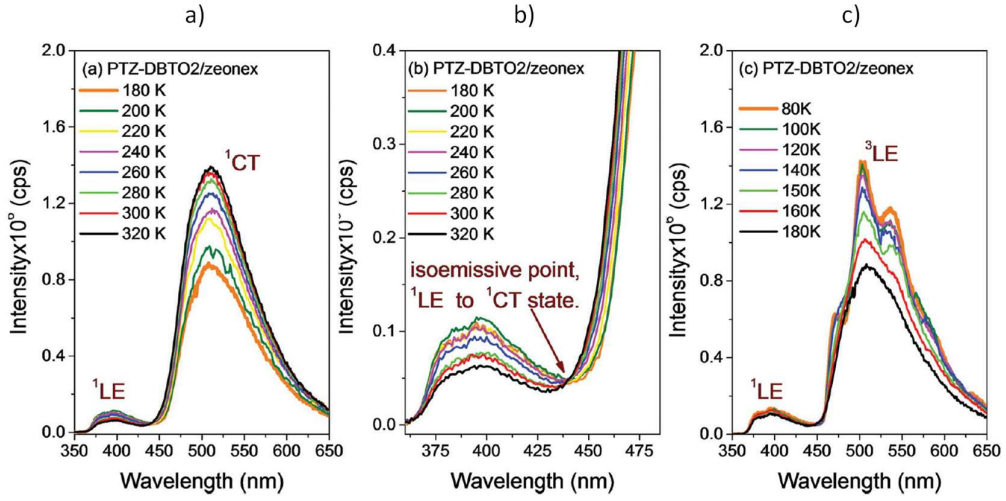

Figure 8 - PTZ-DBTO2 steady-state fluorescence in Zeonex, from 320 to 180 K. ^{1}LE and ^{1}CT emissions are observed. b) A clear isoemissive point is observed between the ^{1}LE and ^{1}CT emissions. c) PTZ-DBTO2 steady-state luminescence in Zeonex, from 180 to 80 K. ^{1}LE fluorescence and ^{3}LE phosphorescence are observed.

4.6 Time-Resolved Fluorescence as a Function of Temperature

The PTZ-DBTO2 fluorescence decay in Zeonex obtained at room temperature is followed over a time interval covering six decades, see Figure 9-a. Prompt (PF) and delayed fluorescence (DF) components are clearly observed, and both PF and DF components can only be fitted with the sums of two exponentials; a single exponential fitting of the PF decay region is also shown in red. This multi-exponential decay process is probably due to a wide

range of D-A dihedral angles in PTZ-DBTO2 molecules, due to conformational heterogeneity appearing as a result of host-guest interactions, which creates a distribution of ST energy gaps, directly affecting the intersystem crossing (ISC) and RISC rate constants, k_{ISC} and k_{RISC}, respectively.

Figure 9b shows the excitation power dependence of the delayed fluorescence in PTZ-DBTO2, dispersed in Zeonex at room temperature. The integral of the delayed fluorescence, collected with 1 μs delay time, and integrated over 100 μs, shows a perfect linear dependence with excitation power (gradient 1), showing that the origin of the DF in PTZDBTO2 is entirely due to a monomolecular process.[10]

Finally in Figure 9-c, the fluorescence decay of PTZ-DBTO2 in Zeonex is followed as a function of temperature. The PF shows almost no variation with temperature, consistent with negligible internal conversion (IC). However, the DF component shows clear temperature dependence, decreasing in intensity at low temperatures, in agreement with an Arrhenius type process. The DF emission is thus unambiguously assigned to a TADF mechanism. At low temperatures and long delay times the slower decay of phosphorescence is also observed.

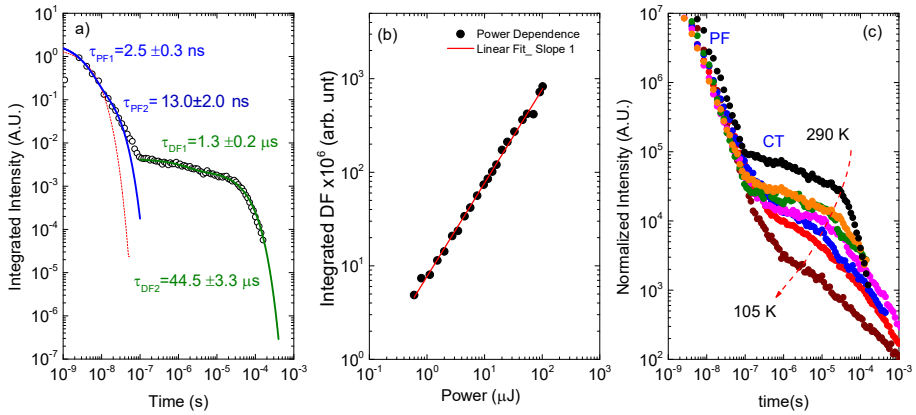

Figure 9 - a) PTZ-DBTO2 fluorescence decay, collected in Zeonex at room temperature. b) DF linear dependence with excitation power. c)Temperature dependence of PTZ-DBTO2 fluorescence decays.

4.7 The influence of local triplet excited states on TADF.

Previously, it was assumed that the TADF harvesting step involved RISC and ISC between the singlet and triplet CT states.[1] However, this process is formally forbidden for perpendicular HOMO and LUMO orbitals, which is the case in PTZ-DBTO2, due to unfavorable spin–orbit coupling (SOC) and Franck–Condon factors.[10–12] However, crossing between the ^{1}CT state and an energetically close local triplet state may be efficient, as was shown by Dance et al.[13]

Hyperfine coupling (HFC) can also, in principle, interconvert ^{1}CT to ^{3}CT and back.[14,15] However, the exchange energy, i.e., approximately the energy difference between ^{1}CT and ^{3}CT states, would need to be smaller than the typical hyperfine energy of a large organic system, typically 20 μeV, which makes HFC rather inefficient in most TADF systems. Therefore, in PTZ-DBTO2, the near degeneracy of the CT manifold and the local triplet state is crucial to promote enhanced ISC due to spin–orbit coupling, and given the very small energy gap between ^{3}LE, i.e. ^{3}A and ^{3}D, and ^{1}CT, this is also ideal for thermally activated RISC.

The importance of the energy alignment between the CT manifold and the ^{3}A or ^{3}D triplet states can be tested by looking at the TADF efficiency in solvents of increasing polarity. This shifts the ^{1}CT state to lower energies without significantly affecting the ^{3}LE, since this state has negligible dipole moment. These studies are discussed in this section and summarized in Figure 10.

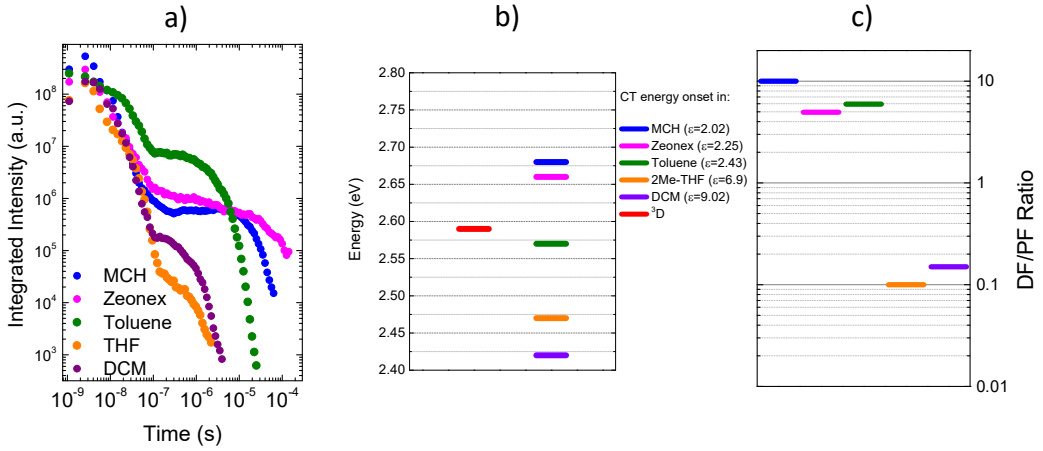

Figure 10 - Influence of solvent polarity on the contribution of TADF to the PTZ-DBTO2 fluorescence at room temperature. a) time resolved fluorescence decays obtained in solvents of increasing polarity; b) Energy of the ^{1}CT state, in solvents of increasing polarity, compared with the energies of the ^{3}A and ^{3}D triplet states; c) emission ratio between the delayed and prompt fluorescence components, determined from steady-state spectra obtained in degassed and aerated conditions.

The TADF efficiency, measured from time-resolved data (Figure 10a), and DF/PF ratio by steady-state photoluminescence (Figure 10c), is stronger in media with low polarity, such as MCH, zeonex and toluene, shown in Figure 10b , where the energy gap between ^{1}CT and ^{3}D or ^{3}A is relatively small. In the more polar DCM and 2Me-THF, the ^{1}CT is well below the two local triplets, making RISC unfavorable. However, as the ^{1}CT emission in PTZ-DBTO2

is also strongly quenched in more polar solvents, this effect is better analyzed by comparing the rates of ISC and RISC in MCH and toluene.

Figure 11a, shows the time resolved fluorescence decays of PTZ-DBTO2 in toluene and MCH. The delayed fluorescence lifetime is markedly shorter in toluene, 2.2 µs, than in MCH, 17.8 µs. This indicates a faster RISC rate in toluene than in MCH, which is consistent with the smaller energy gap between the ^{1}CT and the ^{3}D state in this solvent.

Surprisingly, when the TADF efficiency is measured in steady-state conditions, comparing the emission in aerated and degassed samples, the DF/PF ratio in MCH is double that in toluene, see Figure 11b and 10c. This seems in clear conflict with the faster DF decay, and stronger emission in toluene, considering the PF and DF contributions (Figure 11a). This discrepancy is however, just apparent and is resolved when considering that the prompt-fluorescence (PF) decay is longer in toluene than in MCH, see Figure 11a.

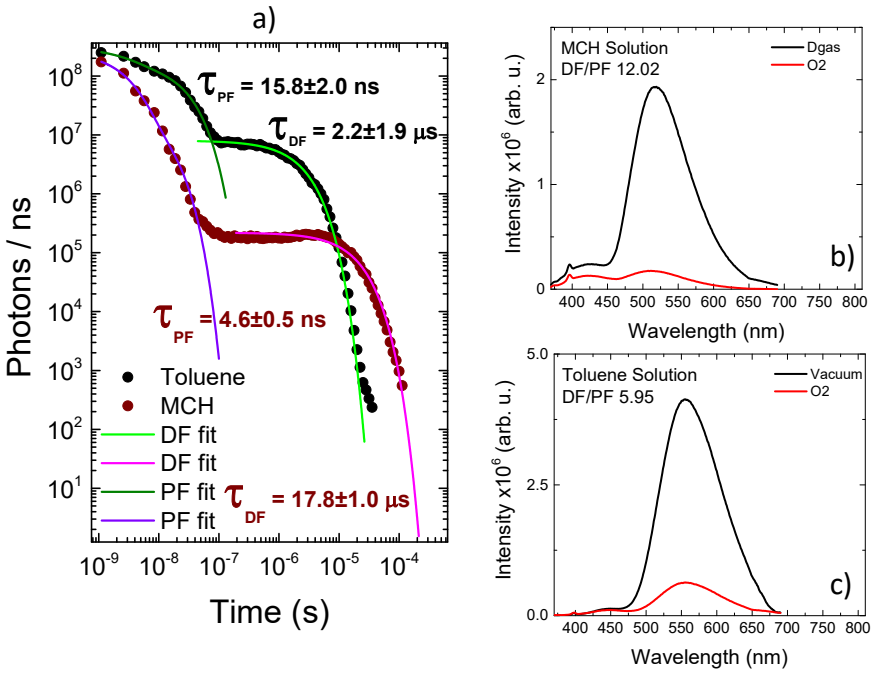

Figure 11 – a) Time-resolved fluorescence decays of PTZ-DBTO2 in MCH and toluene. Steady-state emission spectra of PTZ-DBTO2 in b) MCH and c) toluene in aerated and degassed solutions at room-temperature.

The average lifetime of the prompt emission $\bar{\tau}_{PF}$ for PTZ-DBTO2 in MCH is 4.6 ns and in toluene 15.8 ns. This indicates that part of the luminescence in toluene that is assigned to PF, already contains contribution from DF, due to a more rapid RISC process in toluene. As this contribution occurs in the ns time range and it is less affected by the presence of oxygen, it will result in a smaller DF/PF ratio in steady-state measurements. In other words, some

triplets in PTZ-DBTO2 are able to cross back to the singlet manifold before being quenched by oxygen. This explains the stronger emission of PTZ-DBTO2 in aerated toluene solutions, when compared with their counterpart in MCH.

4.8 Kinetics of TADF

In general terms, the fluorescence yield of TADF emitters contains contributions from prompt (PF) and delayed fluorescence (DF), as given in equation 1, where the relative PF and DF contributions, represented by Φ_{PF} and Φ_{DF}, are governed by the ISC and RISC rate constants.

$$\Phi_F = \Phi_{PF} + \Phi_{DF} \qquad 1$$

Strong TADF is observed in molecules with relatively high triplet formation yield, Φ_{ISC}, and where the yield of singlet states formed by reverse intersystem crossing is also strong, $\Phi_{RISC} \approx 1$. These are conditions that occur in compounds where the pathways for non-radiative decay (IC) affecting the triplet excited state are strongly suppressed, and the energy gap between the singlet and triplet states is small, usually less than 0.15 eV. In these conditions, the fluorescence yield of a TADF emitter involves recycling of triplet excited states through consecutive steps of radiative decay (fluorescence), and ISC/rISC, i.e. in a first step, the initial singlet population may decay to the ground state or suffer ISC to the triplet state. A second step then follows, which will involve the up-conversion of the triplet states back to the singlet manifold, from where they can again decay to the ground-state (2nd generation of fluorescence) or suffer ISC (2nd generation of ISC), and so on. This process is schematized in Figure 12.

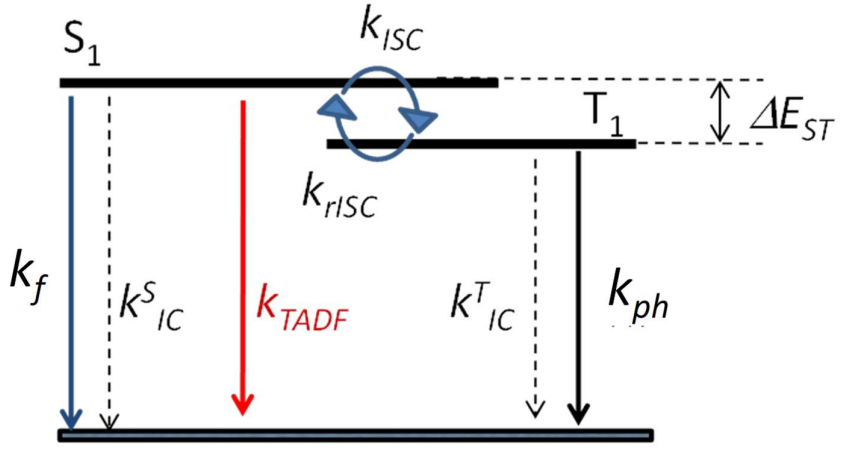

Figure 12 – Photophysical rates constants involved in TADF.

$$\Phi_F = \Phi_{PF} + \Phi_{DF} = \sum_{i=0}^{n} \Phi_{PF}(\Phi_{ISC}\Phi_{rISC})^i = \Phi_{PF}\frac{1}{1-\Phi_{ISC}\Phi_{rISC}} \quad 2$$

The total luminescence yield of a TADF compound is then given by Eq. 2. This eq. is of fundamental importance because it shows that the reverse intersystem crossing yield, Φ_{RISC}, is close to 100%, when the ratio between the delayed and prompt fluorescence, Φ_{DF}/Φ_{PF}, is above four. In this situation, the product $\Phi_{ISC}\Phi_{RISC}$ in equation 2 is larger than 0.8, see equation 3, and as the triplet yield is limited by the fluorescence yield, $\Phi_{ISC} \leq 1-\Phi_{PF}$, the yield of reverse intersystem crossing, Φ_{RISC}, will be close to 1. [16]

$$\Phi_{ISC}\Phi_{RISC} = \frac{\Phi_{DF}/\Phi_{PF}}{1+\Phi_{DF}/\Phi_{PF}} \quad 3$$

The photophysical characterization of TADF systems with $\Phi_{DF}/\Phi_{PF} \geq 4$ is significantly simplified, and, in such cases, the triplet yield is determined directly from Eq. 4.

$$\Phi_{ISC} = \frac{\Phi_{DF}/\Phi_{PF}}{1+\Phi_{DF}/\Phi_{PF}} \quad 4$$

Once the ISC yield is determined, the ISC rate is also obtained using equation 5.

$$k_{ISC} = \Phi_{ISC}\tau_{PF} \quad 5$$

Finally, the RISC rate is obtained from equation 6.

$$k_{RISC} = \frac{\Phi_{RISC}}{\tau_{DF}}\left(1+\frac{\Phi_{DF}}{\Phi_{PF}}\right) \quad 6$$

For PTZ-DBTO2 in MCH solution k_{RISC} is determined as 6.8×10^5 s^{-1}, and in toluene as $k_{RISC} = 2.7 \times 10^6$ s^{-1}. The ISC yield of PTZ-DBTO2, Φ_T, is 91.6 % in MCH and 85.7%, in toluene.[7,2,3] As the average lifetime of the prompt emission, $\bar{\tau}_{PF}$, of PTZ-DBTO2 in MCH is 4.6 ns and in Toluene 15.8 ns, the k_{ISC} rate is determined as 1.9×10^8 s^{-1} for MCH and 5.4×10^7 s^{-1} in toluene solution. Standard values for k_{ISC} for pure organic molecules vary from 10^6 s^{-1} to 10^8 s^{-1} and for molecules containing heavy atoms can achieve values around 10^{10} s^{-1} – 10^{11} s^{-1}. As predicted the better energy alignment between the ^{1}CT and ^{3}LE in toluene, compared with MCH, renders faster RISC rate in this solvent.

4.9 The effect of molecular conformation on the PTZ-DBTO2 emission

It was mentioned earlier that the formation of the axial conformer in PTZ-DBTO2 was particularly evident in 2Me-THF. Therefore, it is also important to discuss the photophysics

of PTZ-DBTO2 in this solvent, to evaluate the effects of molecular conformation on the TADF mechanism.

The steady-state emission of PTZ-DBTO2 in 2Me-THF solution is shown in Figure 13 as a function of temperature. Three emissive bands are clearly observed at room-temperature, see Figure 13a. The emission peaking around 420 nm matches the region where the ^{1}D and ^{1}A units emit. This emission band is, therefore, assigned to the local excited singlet state, ^{1}LE. The intermediate emission band with maximum around 490 nm is assigned to the axial conformer, and finally the more red-shifted band is assigned to the equatorial conformer. The contribution of the ^{1}LE emission is residual above 220 K, but starts to increase below this temperature, to finally dominate the emission spectrum at 120 K (see Figure 13b). This shows that the formation of the ^{1}CT state is suppressed at low temperatures. Remarkably, the red-shifted emission band, peaking at 650 nm, and assigned to the equatorial conformer, is completely quenched below 260 K. Surprisingly the intensity of the middle emission band peaking around 490 nm, and assigned to the axial conformer continues to increase with decreasing temperature up to 160 K, see Figure 13a. Finally, below this temperature, the ^{1}LE fluorescence and phosphorescence from ^{3}LE start to dominate the entire spectrum.

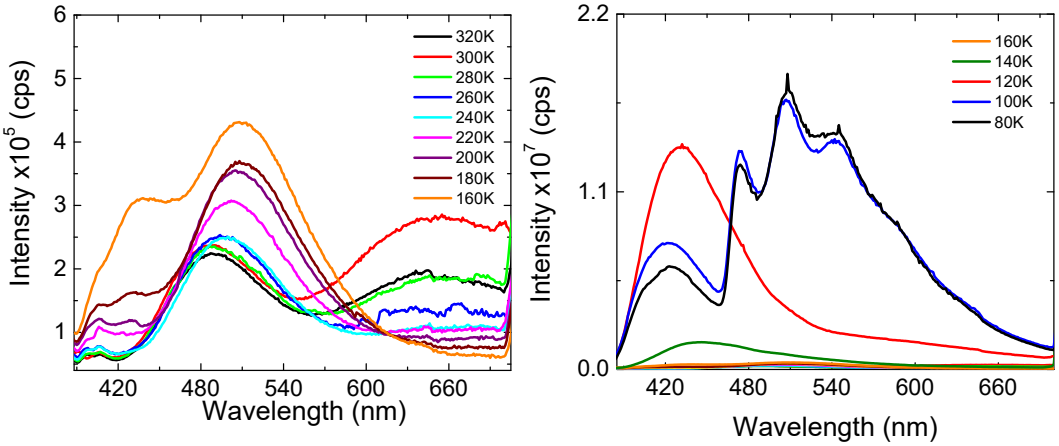

Figure 13 - Steady-state photoluminescence of PTZ-DBTO2 in 2Me-THF solution, as a function of temperature. Note the marked difference in intensity for the emission above and below 160 K.

Time-resolved emission spectra of PTZ-DBTO2 in 2Me-THF are shown in Figure 14 at 290 K (a) and 100 K (b, c). The spectra at 290 K is dominated by the two emission bands corresponding to the axial and equatorial forms of PTZ-DBTO2 – the ^{1}LE emission is not observed, probably because the fast decay of this emission at RT is below the temporal resolution of our system. The emission band around 650 nm, corresponding to the ^{1}CT equatorial form of PTZ-DBTO2 dominates the time-resolved spectrum between 1 ns and 150

ns, see the inset of Figure 14a. However, area normalized emission spectra, (Figure 14a), promptly reveal that there are two emissive species in PTZ-DBTO2, and that the lifetime of the equatorial form is shorter than the axial form. Remarkably, after 150 ns the equatorial form is no longer observed, and the axial form dominates the emission.

In contrast, the time-resolved emission of PTZ-DBTO2 at 100 K, shows two clear bands. An emission band peaking at 440 nm, which entirely dominates the spectrum at 1.1 ns, and progressively decays, while the intensity of the ^{1}CT band rises, peaking at 580 nm, to finally be the only emission present at 234 ns, Figure 14b. Then, from 300 ns onward, and up to 70 ms, the ^{1}CT emission band progressively shifts to shorter wavelengths, and the phosphorescence from the ^{3}LE state starts to emerge, and entirely dominates the emission at later times.

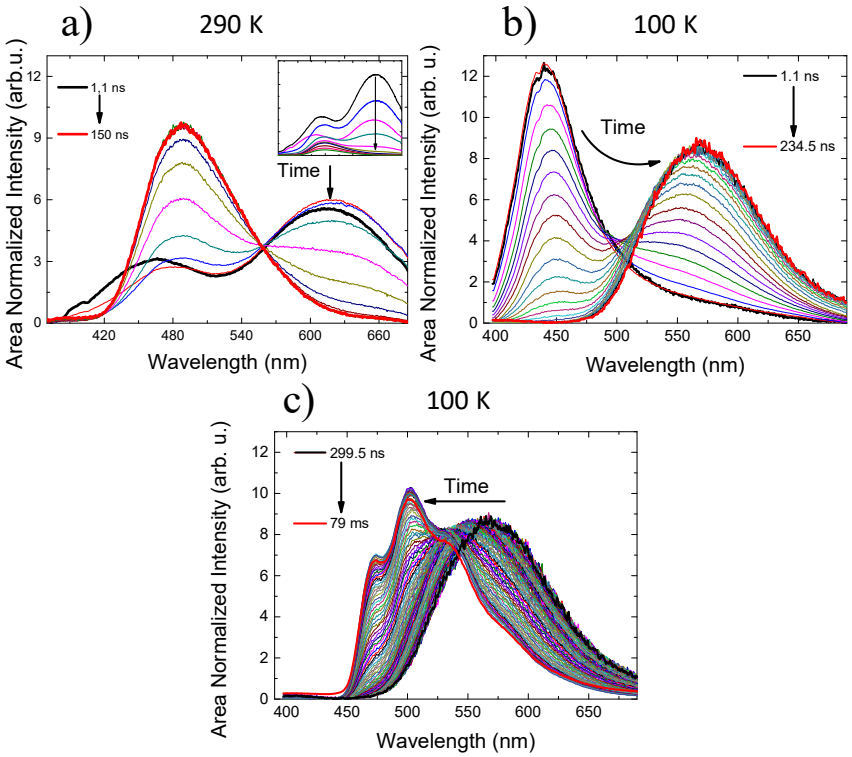

Figure 14 –Area normalized time resolved emission spectra of PTZ-DBTO2 in 2Me-THF at a) 290 K and b,c) 100 K.

The emission behaviour observed in Figure 14a shows that that the lifetime of the axial form in PTZ-DBTO2 is longer that the equatorial form. However, at 100 K, in the first 230 ns a slow decay of the ^{1}LE fluorescence is observed and long-lived ^{1}CT fluorescence from the equatorial form. At longer times, i.e. in the microsecond and ms regime, the emission is originally still dominated by fluorescence from the equatorial form and later by ^{3}LE

phosphorescence. No emission from the axial form is detected, however, the ^{1}LE fluorescence and ^{3}LE phosphorescence are so intense that it may be that fluorescence from the axial form cannot be observed.

The steady-state emission spectra of PTZ-DBTO2 in the presence of oxygen also reveals the presence of the equatorial and axial forms. The emission spectra in Figure 15 are normalized on the emission peak of the axial form. The relative intensities of the axial and equatorial emissions reveal that in toluene, where the energy gap between the ^{1}CT and ^{3}LE states is minimized, fluorescence from the equatorial form dominates, whereas in the other solvents the axial and equatorial forms show almost equal contributions. Note that in the presence of oxygen, the TADF contribution is negligible in MCH and 2Me-THF, but there is strong indication that this is not the case in toluene.

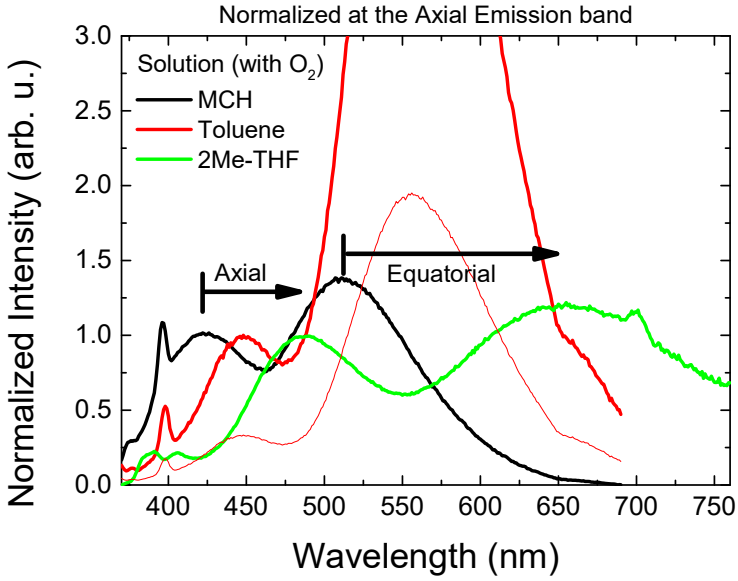

Figure 15 – Solvatochromism of the two distinct conformers in oxygen saturated solution, in MCH (black), toluene (red) and 2Me-THF (green). The emission spectra are normalized at the maximum of the axial emission band. The thin red line spectra in toluene were adjusted in order to compare the equatorial emission band shape.

Moreover, the steady-state emission of PTZ-DBTO2 in MCH and toluene, in aerated and degassed solutions, shown figures 11b and c, also show that the axial form is less affected by the presence of oxygen. This indicates a smaller contribution of DF in the emission of the axial conformer, possibly due to a larger singlet-triplet gap in this conformer.

Finally, to investigate whether the axial and equatorial forms exist in the ground state, or are formed just upon excitation occurs, the excitation spectra of PTZ-DBTO2 in 2Me-THF with emission collected at the two emission bands are compared in Figure 16.

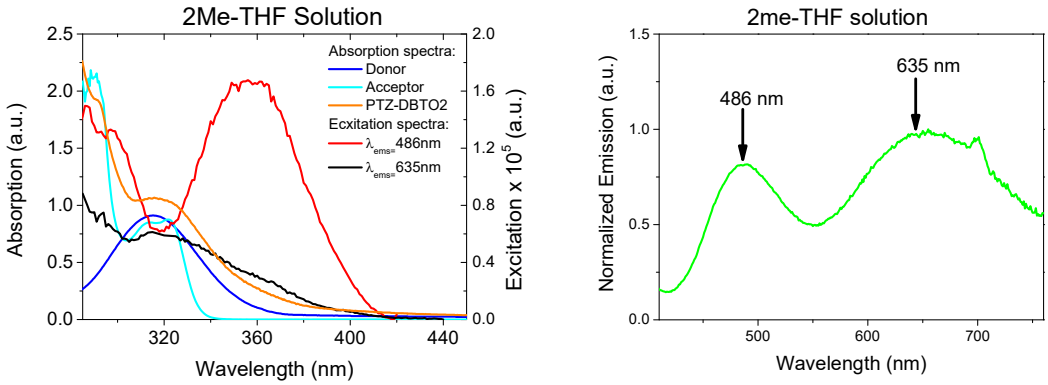

Figure 16 – Absorption spectra of the donor (dark blue) and the acceptor (cyan) and of PTZ-DBTO2 (orange) in 2Me-THF. Excitation spectra of PTZ-DBTO2 in 2Me-THF with emission collected at the emission maxima of the two conformer emission, 486 nm for the axial form, and 635 nm for the equatorial. Emission spectra of PTZ-DBTO2 in 2Me-THF excited at 355 nm.

The excitation spectra collected at λ_{EMS} = 637 nm (equatorial form) follows the absorption spectra of PTZ-DBTO2, showing contributions of both D and A absorptions. On the other hand, the excitation spectra collected at λ_{EMS} = 486 nm (axial form), shows a strongly red-shifted feature at the edge of the PTZ-DBTO2 absorption. This absorption band is, therefore, assigned to the direct absorption of the axial form in PTZ-DBTO2, showing that both axial and equatorial forms of PTZ-DBTO2 exist prior to excitation.

4.10 PTZ-DBTO2 OLEDs: Fabrication and characterization

The performance of prototype devices is shown in Figure 17**.** Devices containing PTZ-DBTO2 as the emitter in CBP host (DEV1), (architecture: ITO/NPB(40 nm)/10% PTZ-DBTO2:CBP(20 nm)/TPBi (50 nm)/LiF(1 nm)/Al(100 nm), give excellent performance with EQE of ≃22%, at low luminance (<100 cd/m^2). For 100 cd/m^2 the EQE drops slightly to 19.4%. In contrast with the device made of PTZ-DBTO2 dispersed in CBP, the device with a pure PTZ-DBTO2 layer (DEV2) has much lower efficiency (≃3%). Here, the lower efficiency is mainly due to the low charge mobility in the emissive layer and possibly to the effect of TTA due to less triplet confinement in the pure PTZDBTO film. Devices made of PTZ-DBTO2 show excellent performance with EQE higher than 20%, Figure 17d.

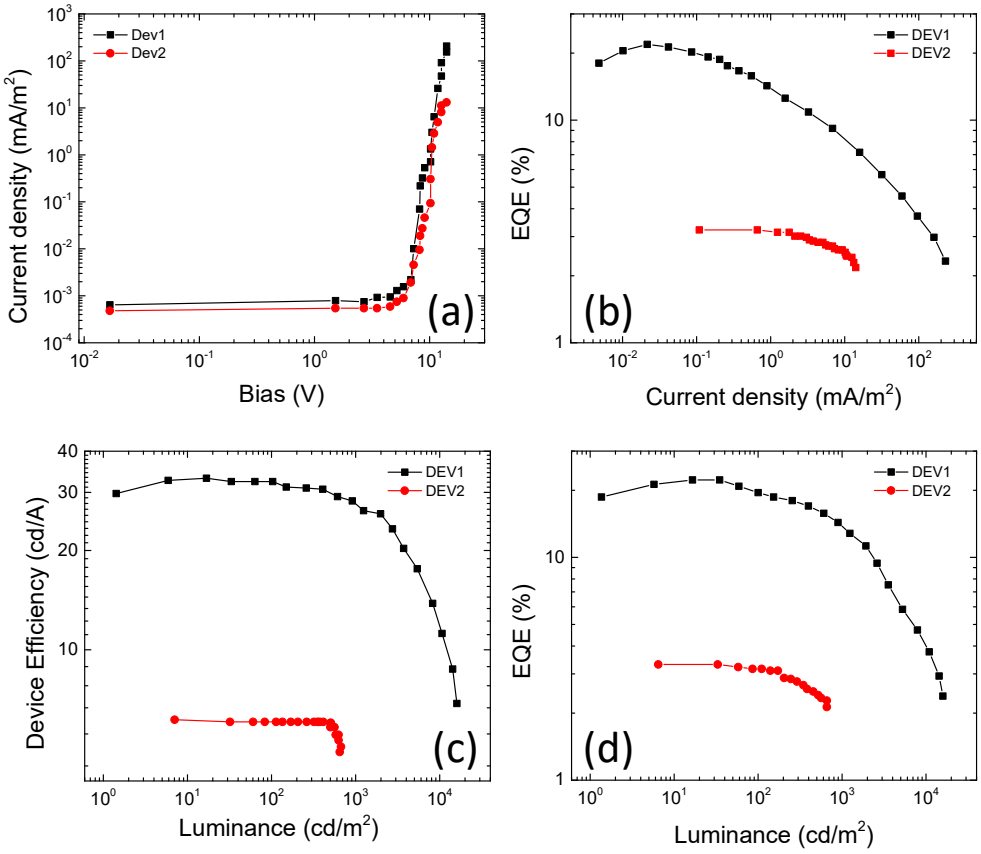

Figure 17 - Characteristics of working OLED devices. a) Current density versus bias, b) EQE versus current density, c) device efficiency versus luminance, and d) EQE versus luminance.

4.11 Conclusions

In conclusion, the photophysics of TADF in PTZ-DBTO2 was investigated in detail. PTZ-DBTO2 shows very pronounced TADF. The nearly perpendicular arrangement between the D and A units, and the energy alignment of the CT manifold with the local triplet excited states in PTZ-DBTO2 result in very small singlet-triplet splitting and enhanced charge transfer spin orbit coupling, which enhances TADF. Axial and equatorial forms of PTZ-DBTO2 are clearly identified in the emission of this compound, with distinct TADF contributions, strongly suggesting that the equatorial form with the PTZ unit oriented perpendicularly to the DBTO2 moiety favours faster RISC due to better coupling with the triplet state. These observations motivate the investigation of the effect of different molecular forms and restricted geometry on the efficiency of TADF in PTZ-DBTO2 derivatives. This is the subject of the next two chapters.

4.12 Bibliography

1 Uoyama, H.; Goushi, K.; Shizu, K.; Nomura, H.; Adachi, C. Nature **2012**, 492 (7428), 234–238.

2 Hatchard, C. G. R., Soc. Chem. **1961**, 1894–1904.

3 Baldo, M. A.; Forrest, S. R. **1998**, 395,, 151–154.

4 Schmidbauer, S.; Hohenleutner, A.; König, B. Adv. Mater. **2013**, 25 (15), 2114–2129.

5 Xiong, X.; Song, F.; Wang, J.; Zhang, Y.; Xue, Y.; Sun, L.; Jiang, N.; Gao, P.; Tian, L.; Peng, X. J. Am. Chem. Soc. **2014**, 136 (27), 9590–9597.

6 Baleizão, C.; Berberan-santos, M. N.; Baleizão, C.; Berberan-santos, M. N. 2007, 204510.

7 Dias, Fernando B., Santos J., Graves D., Data P., Nobuyasu R. S., Fox M. A., Batsanov A. S., Palmeira T., Berberan-Santos M. N., Bryce M. N., A. P. Monkman, Adv. Sci. **2016,** 3, 1600080

8 Lim, B. T.; Okajima, S.; Chandra, A. K.; Lim, E. C. Chem. Phys. Lett. **1981**, 79 (1), 22–27.

9 Etherington, M. K.; Franchello, F.; Gibson, J.; Northey, T.; Santos, J.; Ward, J. S.; Higginbotham, H. F.; Data, P.; Kurowska, A.; Lays, P.; Santos, D.; Graves, D. R.; Batsanov, A. S.; Dias, F. B.; Bryce, M. R.; Penfold, T. J.; Monkman, A. P. Nat. Commun. **2017**, 8, 1–11.

10 Dias, F. B. Philos. Trans. R. Soc. A Math. Phys. Eng. Sci. **2015**, 373 (2044), 20140447–20140447.

11 Lim, T.-B.; Cho, K. H.; Kim, Y.-H.; Jeong, Y.-C. Opt. Express **2016**, 24 (16), 17950.

12 Forrest, S. R. The Path to Ubiquitous and Low-Cost Organic Electronic Appliances on Plastic. *Nature*. **2004**, pp 911–918.

13 Dance, Z. E. X.; Mickley, S. M.; Wilson, T. M.; Ricks, A. B.; Scott, A. M.; Ratner, M. A.; Wasielewski, M. R. *J. Phys. Chem. A* **2008**, *112* (18), 4194–4201.

14 Scott, A. M.; Wasielewski, M. R. *J. Am. Chem. Soc.* **2011**, *133* (9), 3005–3013.

15 Ogiwara, T.; Wakikawa, Y.; Ikoma, T. *J. Phys. Chem. A* **2015**, *119* (14), 3415–3418.

16 Jankus, V.; Data, P.; Graves, D.; McGuinness, C.; Santos, J.; Bryce, M. R.; Dias, F. B.; Monkman, A. P. *Adv. Funct. Mater.* **2014**, *24* (39), 6178–6186.

5. The interplay of thermally activated delayed fluorescence (TADF) and room-temperature phosphorescence in organic sterically-constrained charge-transfer molecules.

A series of phenothiazine–dibenzothiophene-S,S-dioxide charge-transfer molecules have been synthesized with increasing steric restriction for the donor unit to rotate around the donor–acceptor axis. This steric effect significantly alters the relative contributions of TADF and phosphorescence. Bulky substituents on the 1-(and 9) position(s) of the phenothiazine result in no TADF in the solid state, and instead strong phosphorescence is observed at ambient temperature. These results highlight the importance of vibronic coupling to the efficiency of reverse intersystem crossing and outcome of the TADF mechanism

This work is published in: Jonathan S. Ward, Roberto S. Nobuyasu, Andrei S. Batsanov, Przemyslaw Data, Andrew P. Monkman, Fernando B. Dias and Martin R. Bryce, The interplay of thermally activated delayed fluorescence (TADF) and room temperature organic phosphorescence in sterically-constrained donor–acceptor charge-transfer molecules, Chem. Comm., 2016, 52, 2612-2615

5.1 Introduction

The study of new fluorescent and phosphorescent emitters is central to the development of a wide range of optoelectronic technologies, including organic light-emitting diodes (OLEDs), electrochromic devices, sensors and fluorescence imaging.[1] Spin statistics dictate that the internal efficiency of OLEDs using traditional fluorescent emitters, which utilise only singlet excited states for light emission, is limited to 25%.[2] Phosphorescent emitters based on transition metal complexes, especially third row ions such as Ir(III) and Pt(II), are popular because the heavy metal facilitates spin-orbit coupling and harvesting of both singlet and triplet excitons by enhanced intersystem crossing (ISC). Internal quantum efficiencies (IQEs) approaching 100% can be achieved by this mechanism.[3] However, these phosphors suffer from limited stability in practical applications, especially for blue and white emission, and the scarcity and expense of precious metals restricts their commercial applications.

Triplet fusion is an alternative way to convert triplets into emissive singlet states although the IQE in this process is limited to a theoretical maximum of 62.5%.[4,5] Currently, a leading strategy is to exploit thermally activated delayed fluorescence (TADF) to convert triplets to singlet states with a potential IQE of up to 100% using all-organic (metal-free) materials.[6-10]

The mechanism of TADF is fundamentally different from traditional fluorescence. TADF uses thermal energy to assist reverse intersystem crossing (RISC) of lower-energy triplet states into emissive singlets. Two main parameters control this mechanism: (i) the energy splitting between the lowest singlet (S_1) and triplet (T_1) states should be minimised, and (ii) the non-radiative pathways by which the excited singlet and triplet states can decay need to be suppressed in order to achieve high fluorescence quantum yields and long triplet excited state lifetimes.[11,12]

Based on the TADF properties of a wide range of donor-acceptor (D-A) molecules,[13-21] it is clear that a prerequisite for efficient TADF is the spatial separation of the highest occupied molecular orbital (HOMO) on the electron donor and the lowest unoccupied molecular orbital (LUMO) on the electron acceptor moieties of the emitter molecule. This can be achieved by enforcing a twist between the planes of the D and A moieties to restrict the conjugation leading to an intramolecular charge transfer (ICT) state with a small (ΔE_{S1T1}) energy gap.[13] For example, tuning of TADF in the green – orange region has been achieved by stabilisation of the ICT state between a phenoxazine donor unit and 2,4,6-triphenyl-1,3,5-triazine acceptor unit separated by a large twist angle.[14] A 9,9'-spirobifluorene unit has been used to enforce orthogonality between D and A units in a TADF emitter.[15] Systematically engineering the twist angles within a series of D–A structures is, therefore, an important strategy for understanding the parameters which control the overall emission, including TADF, in these types of molecules.

5.2 Molecular structure and Characterization

Here it is reported a series of D–A–D and D–A molecules based on phenothiazine donor and dibenzothiophene-*S,S*-dioxide acceptor units in which the steric bulk of alkyl groups on the donor restricts rotation around the C–N bond linking the D and A units. Remarkable effects of this functionalization on the structural and photophysical properties of the molecules are observed. Compounds **1**[22] and **6**[23] exhibit efficient TADF in zeonex films whereas the more sterically hindered analogues **3** and **4**, which have less conformational flexibility, show strong contributions from phosphorescence, even at RT.

Functionalization of the phenothiazine unit(s) with alkyl substituents at the 1 (and 9) position(s) affords the new compounds **2-5**, **7**, **8**, Figure 1.

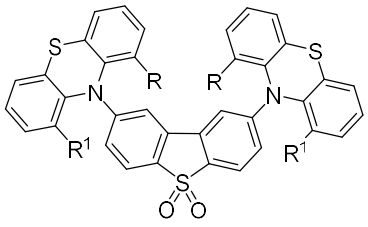

	R	R^1
1	H	H
2	Me	H
3	*i*-Pr	H
4	*t*-Bu	H
5	Me	Me

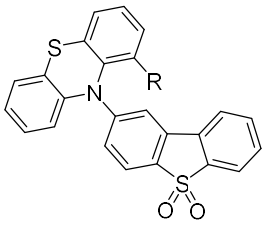

	R
6	H
7	Me
8	*i*-Pr

Figure 1 - Structures of D–A–D and D–A molecules.[1]

The structures of molecule **2** ·THF, molecules **3** and **5** ·$2CH_2Cl_2$ and **7** were determined by single-crystal X-ray diffraction and are shown in Figure 2.

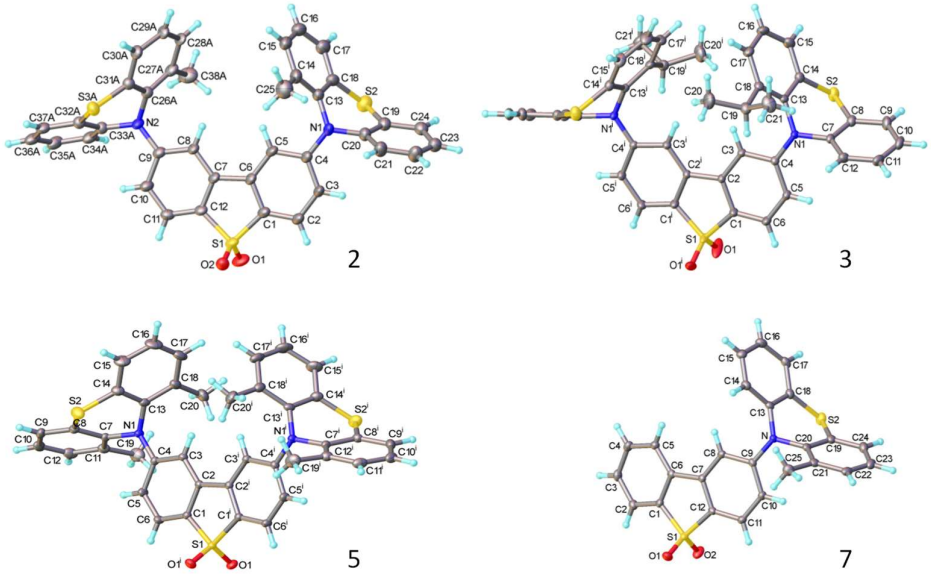

Figure 2 – X-ray structure of compounds 2, 3, 5 and 7.[2]

The dibenzothiophene moiety in **2** and **5** is practically planar; in **3** it is slightly twisted and in **7** folded, with the two arene rings forming a dihedral angle of 6.9° and 12.5°, respectively. The molecules of **3** and **5** possess a crystallographic two-fold axis, hence the phenothiazine substituents have transoid orientation with respect to the dibenzothiophene plane, i.e. their S atoms lie on opposite sides of this plane. **2** has a similar conformation, although the molecule has no crystallographic symmetry. Interestingly, one of the phenothiazine moieties [at C(9)]

[1] Molecules were synthesized by Martin R. Bryce's research group.
[2] X-Ray structure were determine by Andrei Batsanov.

is disordered in a 0.6:0.4 ratio between two conformations, with the methyl substituent on opposite sides of N(2) and the tricyclic system liberating around the N(2) as the pivot, to provide room for the methyl group. The phenothiazine moiety is always folded along the N…S vector, forming a dihedral angle of 128.7° (**3**), 135.5° (**5**) and 135.3° (**7**). In **2**, the ordered phenothiazine moiety is folded by 131.1° and the disordered one by 133.6° or 135.0°. In every case, the N atom is substantially pyramidalised; its lone pair is oriented favourably for conjugation with the dibenzothiophene π-system rather than with the arene rings of phenothiazine itself. Therefore, the N-C(dibenzothiophene) bond is shorter than N-C(phenothiazine), on average by 0.035 Å in **3** and **5** and 0.039 Å in **7** (s.u. 0.001-0.002 Å); the similar difference (0.038 Å) in **2** is not statistically significant due to disorder and high s.u. The packing of **2** and **5** is characterised by stacking (π-π) interactions between phenothiazine arene rings (related via inversion centres and therefore parallel) with interplanar separations of 3.50 and 3.60 Å (intermittently) in **2**, or 3.66 Å (uniformly) in **5**. These interactions link molecules into infinite chains (SI S8). No stacking is evident in the structures of **3** and **7**.

The ^{1}H NMR spectra of **1**,[22] **2**, **5–8** at 298 K display sharp peaks showing that there is one species in solution at this temperature on the NMR timescale. In contrast, compounds **3** and **4** which have a bulkier ^{i}Pr or ^{t}Bu substituent on each phenothiazine ring exhibit restricted rotation. The spectrum of compound **3** at 298 K clearly shows two species in solution: upon heating, the peaks coalescence to reveal only one species at 373 K, shown in Figure 3.

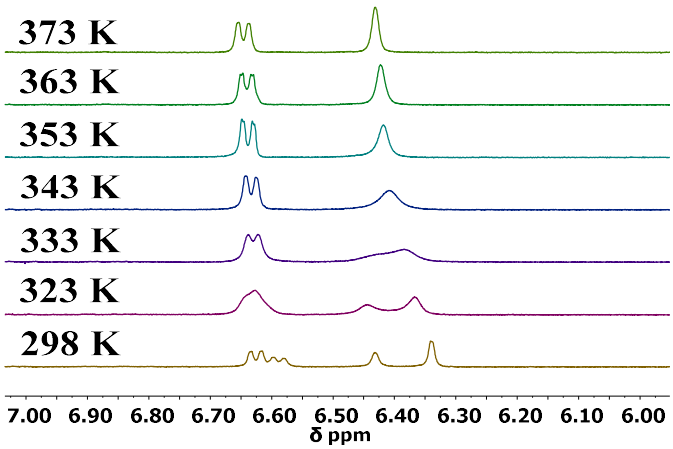

Figure 3 - 500 MHz Variable temperature ^{1}H NMR experiments for **3** from 298 – 373 K in DMSO-d_6.[3]

[3] NMR measurements were performed by Martin R. Bryce's research group..

^{1}H NOESY and ROESY NMR experiments strongly suggest that the two species are interconverting with each other (Figure 4 a and b, respectively).

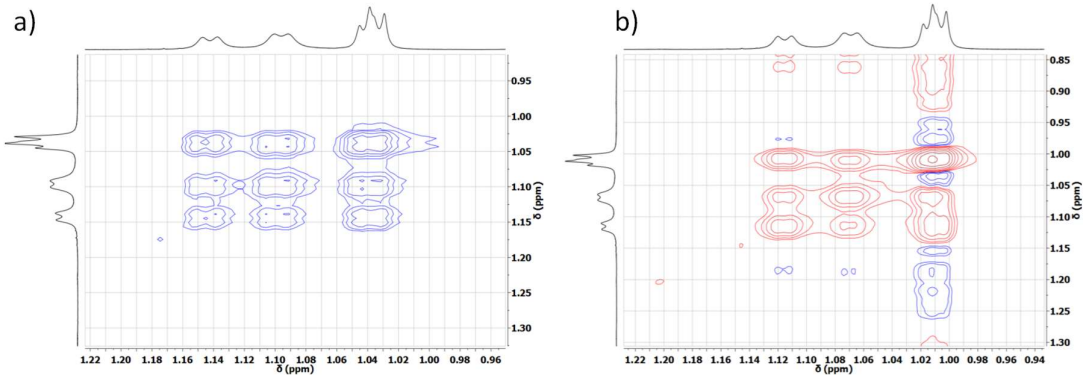

Figure 4 -a) ^{1}H NOESY of compound 3 at 298 K. b) ^{1}H ROESY of compound **3** at 298 K.

The presence of these two species is likely to be due to up-up and up-down configurations of the ^{i}Pr or ^{t}Bu groups with respect to the acceptor.

For the *t*-butyl analogue **4**, at 298 K selected peaks are extremely broad and the spectra at 348 K and 373 K are comparable to **3** at 298 K. Rotation in compound **4** is still partially restricted even at 373 K, shown in Figure 5.

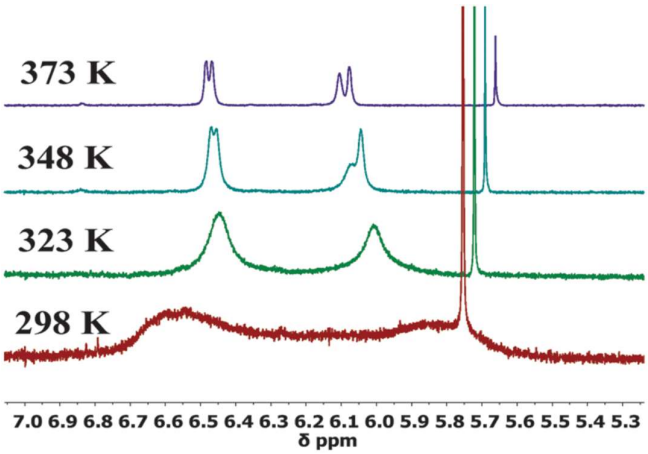

Figure 5 - 500 MHz variable temperature 1H NMR experiments for **4** from 298–373 K in DMSO-d6.

^{1}H NOESY NMR experiments with **4** also demonstrate there is some exchange occurring between the two very broad peaks at 298 K (Figure 6).

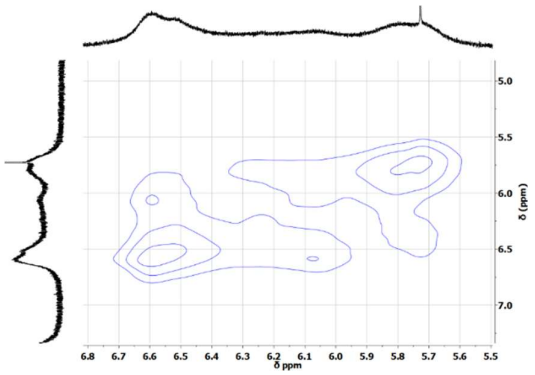

Figure 6 -^{1}H NOESY of **4** at 298 K.

5.3 Cyclic Voltammetry

All the investigated compounds show both oxidation and reduction processes. The D–A derivatives of dibenzothiophene-*S,S*-dioxides (**7**, **8**) had slightly lower HOMO levels (ca. 0.03 eV) and much lower LUMO levels (ca. 0.1 eV) than their corresponding D–A–D analogues (**2**, **3**). With increasing of the size of alkyl side group a significant decrease in the HOMO was observed as a result of increased steric hindrance within the molecules. There is almost no difference in the energy of the HOMO-LUMO levels between *t*-butyl mono-substitution (compound **4**) and dimethyl substitution (compound **5**) suggesting that in both compounds there is an extensive twist between the planes of the D and A units, shown in Table 1.

Table 1 - HOMO-LUMO levels for all compounds.

Molecules	HOMO (eV)	LUMO (eV)
1 (R=H)	-5.4	-3.1
2 (R = Me)	-5.78	-2.70
3 (R = ^{i}Pr)	-5.92	-2.71
4 (R = ^{t}Bu)	-6.11	-2.68
5 (R/R' = Me)	-6.11	-2.67
6 (R=H)	-5.4	-2.95
7 (R= Me)	-5.81	-2.80
8 (R = ^{i}Pr)	-5.90	-2.79

5.4 Photophysical characterization: Steady-State Fluorescence.

Photophysical measurements on **2**–**8** reveal how the increasingly bulky phenothiazine donors affect their optical properties, primarily by restricting rotation around the N-C bond that links

the D and A units. Consistent with previous work,[16] it has been shown that **1** and **6** emit strongly *via* a TADF mechanism.[22,23] Figure 7 and Figure 8 show the absorption and emission spectra of compounds 1-8 in toluene solution and in zeonex, respectively.

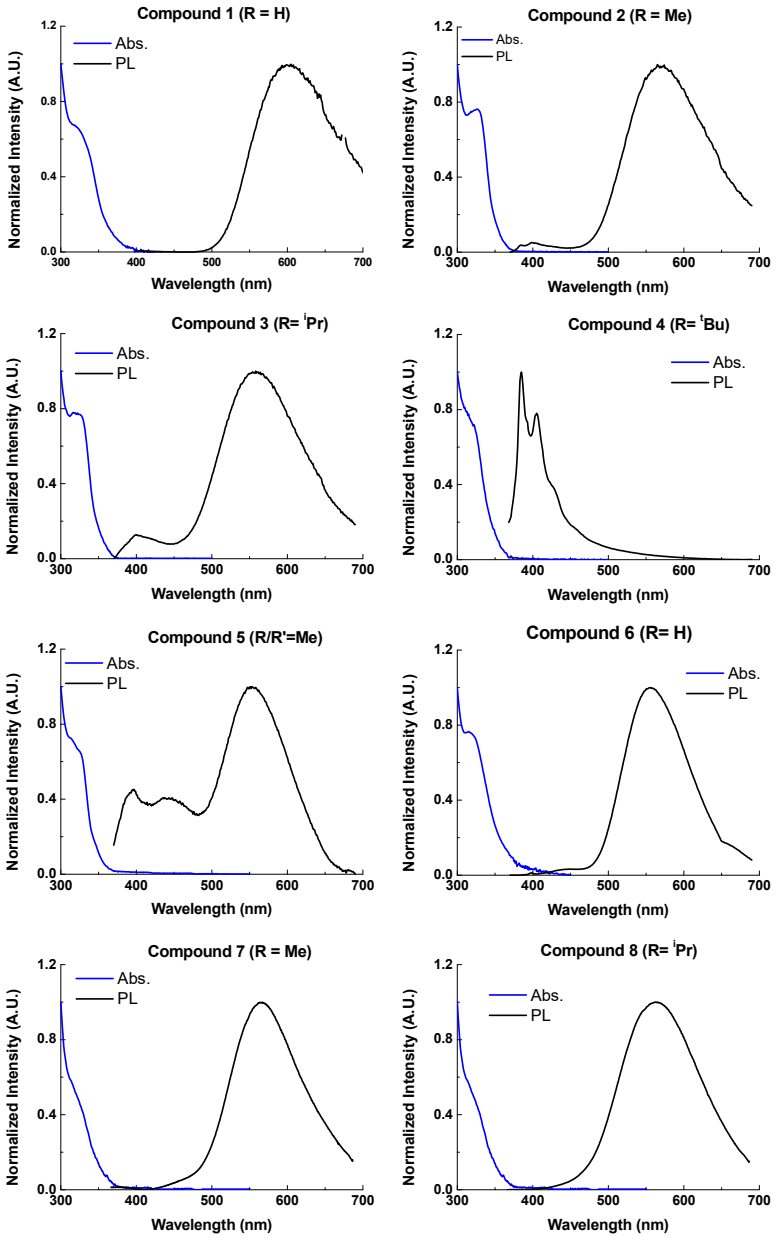

Figure 7 - Steady State Emission/Absorption in toluene for **1–8**, excited at 355 nm, without oxygen at 290 K.

In toluene solution all compounds show charge transfer like emission, with exception of compound **4**, where the rotation around the C-N axis is strongly restricted by the presence of two bulkier tBu groups. Remarkably in solid film (zeonex), the emission of all substituted compounds shows well-structured luminescence. This is in clear contrast with the emission of

the unsubstituted compounds (**1** and **6**), which keep their CT-like emission even in solid state. The presence of the side groups has thus clear influence on the spectroscopic properties of compounds **1-8**.

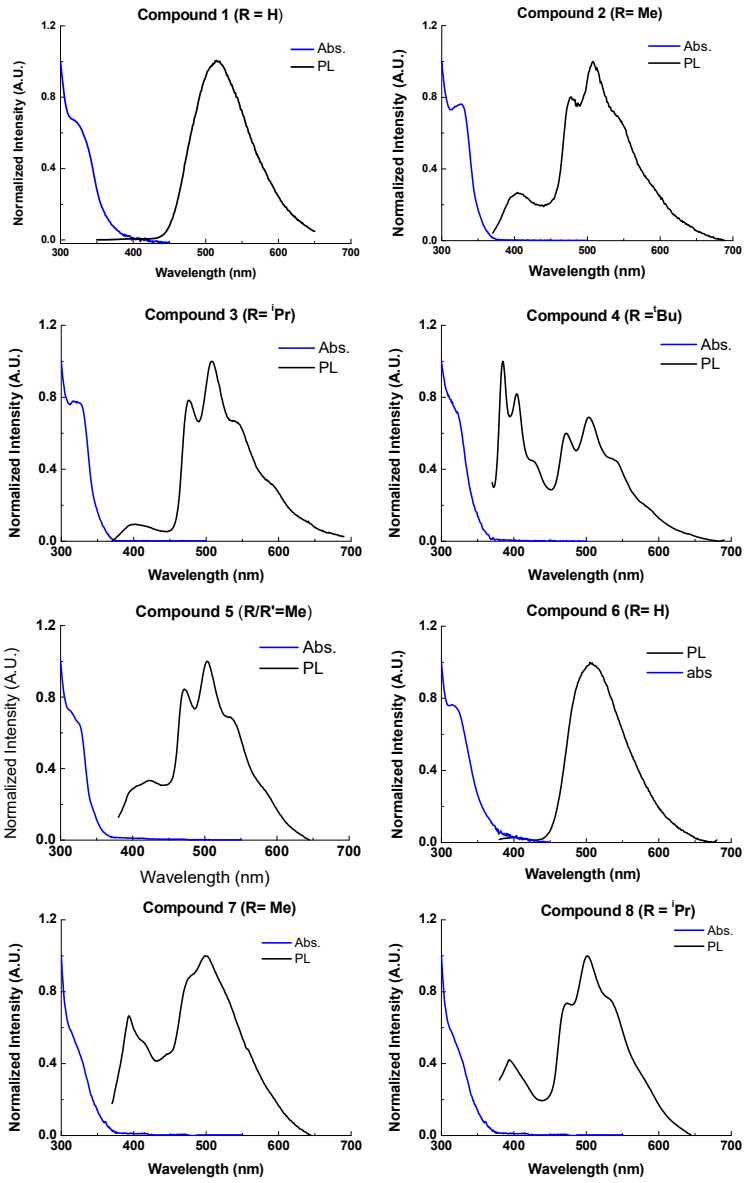

Figure 8 - Steady State Emission in zeonex thin film. Absorption in toluene for **1–8**, excited at 355 nm at 298 K.

5.5 Time-Resolved Luminescence

The D–A compound **7** has a methyl group in the 1-position on phenothiazine compared to **6**, and this has a dramatic effect on the emission of this molecule. The same difference is also observed in the D–A–D molecule **2**.

Introduction of the methyl group into molecules **2** and **7** (Figure 9) increases the lifetime of the DF emission in toluene solution (when compared with molecules **1** and **6**). Similar observations are made for compounds **3**, **4** and **5**, when compared with compound **1**, and for compound **8**, when compared with **6** (Figure 10). In general, the introduction of the side substituents results in less intense and longer-lived TADF decay. This is particularly evident for the decay of molecule **4**, where even in toluene solution no ^{1}CT emission is observed.

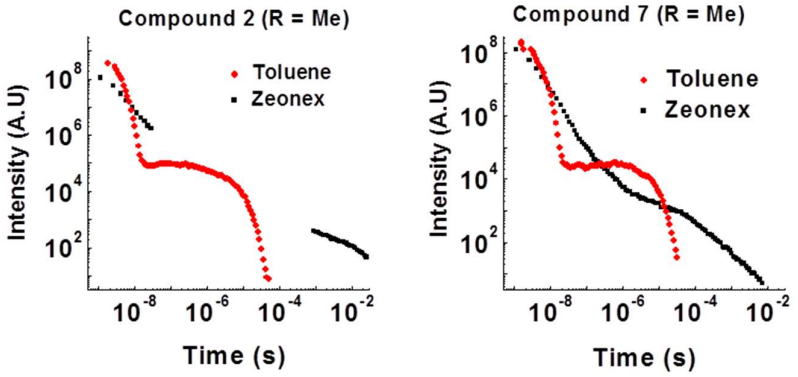

Figure 9 - Time-resolved emission decay for **2** and **7** at 290 K (355 nm excitation).

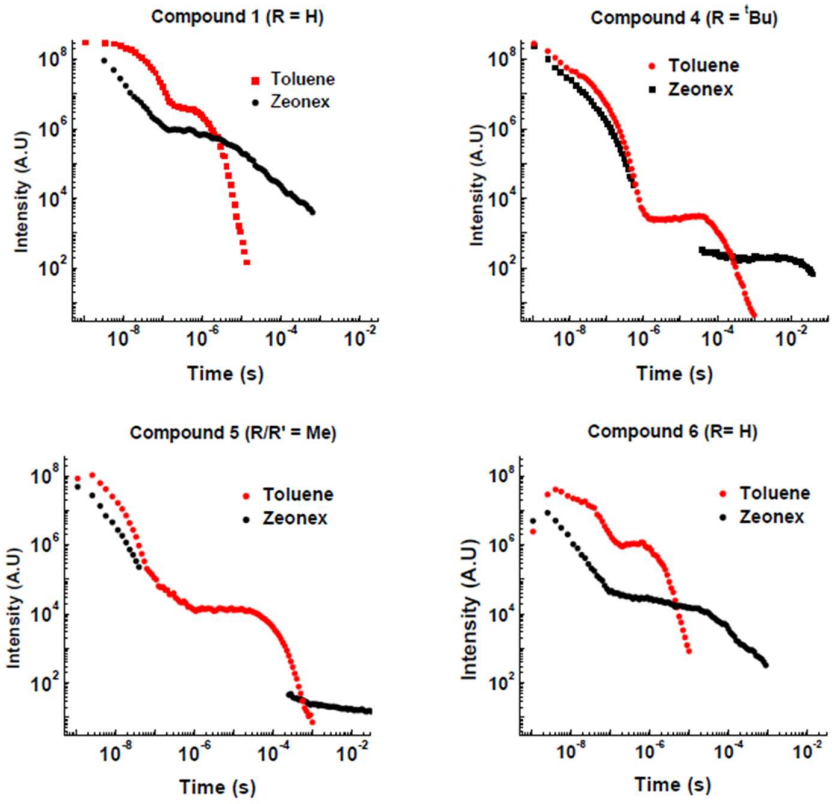

Figure 10 - Time resolved emission decay for compounds **1**, **4**, **5** and **6** in toluene and zeonex at 290 K.

The emission decays of the substituted compounds also show clear differences with the luminescence decays of compounds **1** and **6** in zeonex film. While the unsubstituted compounds show continuous luminescence decays with relatively shorter lifetimes, the luminescence decays from the substituted compounds appear interrupted during some time intervals, as shown by the small period of no emission at 10^{-7} s, and are in general longer-lived than in solution. The interruption on the luminescence decay is caused by the marked reduction on the radiative rate, which causes significant luminescence signal harder to be collected in the delay-integration times. This clearly indicates that the character of a well resolved emission is different from the CT-like fluorescence that is observed for the unsubstituted compounds.

5.6 TADF vs Phosphorescence

Temperature and power dependence data confirm that the delayed emission in compound **2** in toluene still occurs *via* a TADF mechanism (Figure 11). However, a reduction in intensity of the delayed fluorescence on introduction of the methyl group into **2** is observed when compared with the unsubstituted molecule.

It can be proposed that the methyl group slows molecular reorganization processes resulting in a slower initial electron transfer step as well as increasing the ^{1}CT state lifetime. These effects increase the efficiency of the non-radiative decay, and promote direct decay from ^{1}D-^{1}A states, as well as reducing the number of CT states initially created. This is evidenced by the increasing contribution of emission around 400 nm in the steady-state data (Figure 7).

The pronounced influence of the side groups in the TADF emission is clearly seen in the case of compound **4**, where even in toluene solution no ^{1}CT emission is observed.

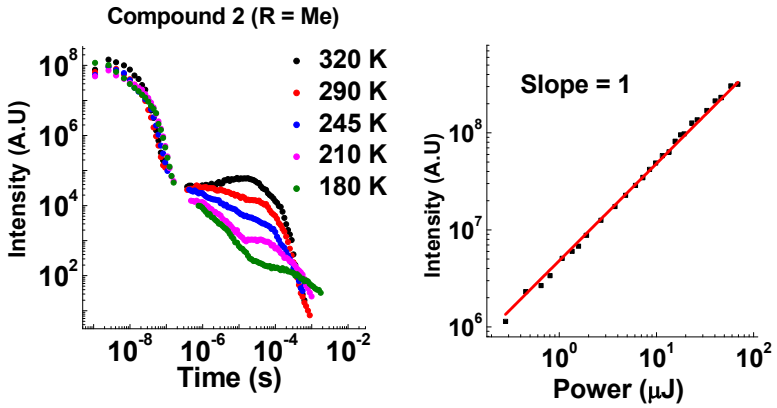

Figure 11 - Left: Temperature dependence of emission decay in toluene for **2**. Right: Power dependence of DF emission in toluene for **2** (400 ns delay and 50 μs integration time).

The most noticeable difference between unsubstituted **1** and methyl substituted **2** is that in the solid state in a zeonex film, the TADF emission is no longer present. A large time gap with no emission is observed in **2** after the fast donor fluorescence decays. It is suggested that the methyl group's ability to restrict reorganization is enhanced in the solid state, resulting in such slow electron transfer that the donor states may have all decayed before appreciable electron transfer occurs. The unusual feature in the solid state is that **2** emits significantly more *via* phosphorescence compared with **1**. Quenching experiments of the emission with oxygen show also that **2** and **7** have increasing phosphorescent character in solid state (Figure 12). This is consistent with the efficient ISC to the donor triplet state instead of CT formation.

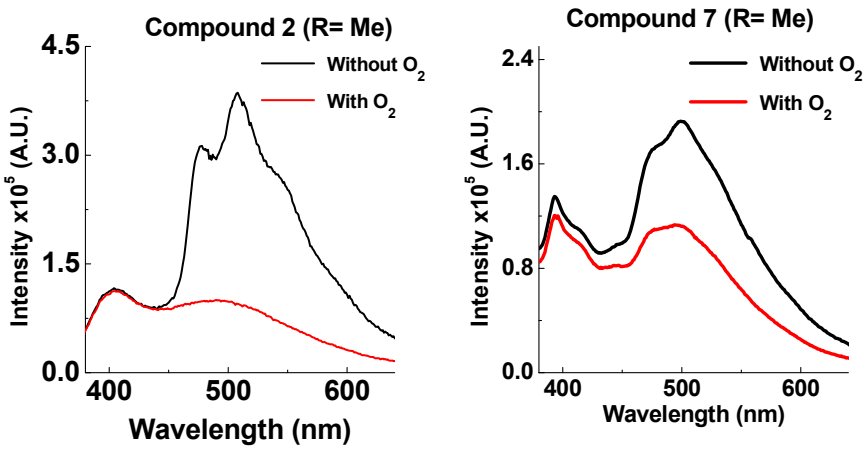

Figure 12 - Emission of **2** and **7** at 290 K in zeonex (excited at 355 nm).

The D–A–D structure 2 shows more phosphorescence emission than its D–A analogue **7**. More fine structure is observed with **2** and significantly more quenching is observed in the presence of oxygen. This room temperature phosphorescence is unusually strong for an organic molecule,[24–27] and the methyl group plays a key role. With increasing steric hindrance, compounds **3** and **8**, the phosphorescence increases even further (Figure 13).

With a bulkier ^{i}Pr group in the D-A system **8**, TADF is still observed in solution as it is apparent from the decays in Figure 13, and measured in function of temperature in Figure 14. In zeonex no TADF is observed, but strong phosphorescence is observed at RT. For the D-A-D system **3**, the amount of TADF is lowered significantly, even in toluene solution. This correlates with the solution NMR studies, showing restricted rotation.

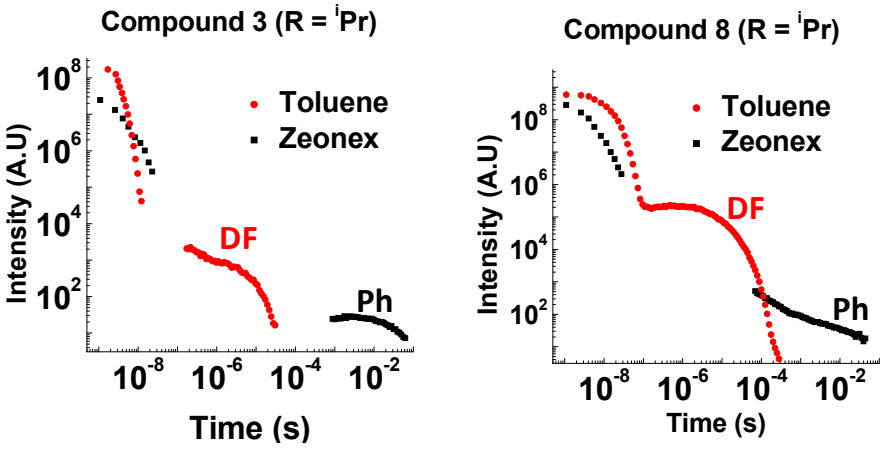

Figure 13 - Time-resolved emission decay for **3** and **8** at 290 K (355 nm excitation).

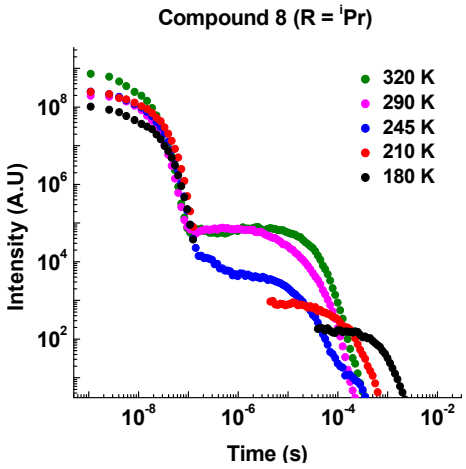

Figure 14 - Time resolved emission for **8** in toluene, varying temperature.

With the two iPr systems 3 when compared with **8**, the extent of phosphorescence increases significantly, shown in Figure 15.

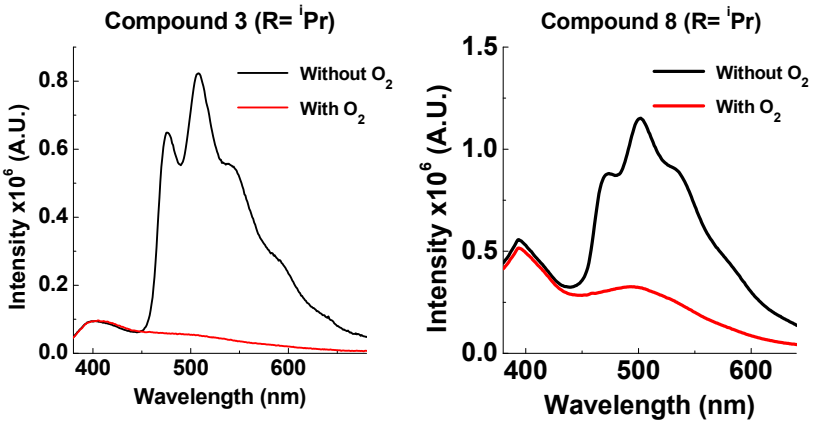

Figure 15 - Emission of **3** and **8** at 290 K in zeonex (excited at 355 nm).

The emission of **3** and **8** in zeonex shows even more fine structure compared with **2** and **7** due to the increased ratio of phosphorescence to ^{1}CT fluorescence. D–A–D **3** with two ^{i}Pr groups, prevents molecular movement more than in the D–A analogue **8** (Figure 2). The emission from **3** in the solid state consists almost entirely of phosphorescence as shown by the large decrease in emission on introduction of oxygen. It is unusual for an organic molecule to decay almost completely by phosphorescent pathways. However, temperature dependence studies in solid state show that **8** does not emit *via* a TADF mechanism, which will be discussed below (Figure 17). The introduction of these bulkier groups acts like a switch, turning off electron transfer and turning on phosphorescence.

Having observed the drastic change caused by an ^{i}Pr group, ^{t}Bu groups were introduced into **4**, and two methyl groups were attached onto each phenothiazine in **5.** A large contribution from phosphorescence is observed in the solid state of **4** (Figure 16), and there is also a large contribution of fast fluorescence from the excited S_1 state. It is proposed that the motion in **4** in the solid state is so restricted that electron transfer from the ^{1}D-^{1}A states to the ^{1}CT state is prevented. This results in fast fluorescence decay from S_1 (^{1}A and ^{1}D) and long lived phosphorescence (^{3}A and ^{3}D) as the main radiative pathways for the excited state to decay. Supporting evidence for extended ^{1}D emission in **4** is seen in time-resolved studies (Figure 10). Compound **5** also shows strong phosphorescence at RT, but less ^{1}A and ^{1}D fluorescence than **4**, which correlates with the less bulky substituents.

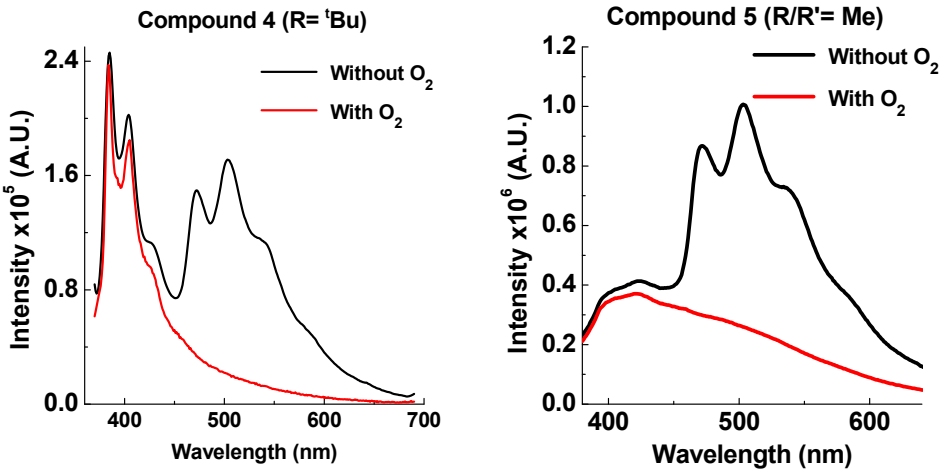

Figure 16 - Emission of **4** and **5** at 290 K in zeonex (excited at 355 nm).

5.7 Distinction between TADF and Phosphorescence Emissions

As both TADF and phosphorescence involve triplet harvesting, it is important to be able to differentiate them. Several standard ways can be used to distinguish these two emissions and are highlighted below:

1 - TADF originates from a singlet state with charge transfer character and appears as a broad, structureless Gaussian band and is strongly affected by the polarity of the solvent showing a shift to lower energies when the solvent polarity increases, concomitant with a large permanent dipole moment of the CT state. In contrast with TADF, the phosphorescence is due to direct emission from a triplet excited state, normally a local triplet state, and appears with a well-resolved spectrum, as is the case here, and without showing significant shifts with the solvent polarity concomitant with a local exciton having near zero dipole moment. This can be easily seen by comparing the emissions of compound **1** and **5** in zeonex (shown in Figure 7). The restriction effect due to the presence of the two Me groups in **5**, enhances emission from ^{1}LE at 400 nm, suppresses the CT state and activates ^{3}LE phosphorescence.

2 - TADF involves harvesting from a triplet state to a singlet state with CT character, and this process is thermally activated, i.e., by decreasing the temperature less TADF emission is observed. In contrast, the phosphorescence involves direct emission from the triplet state and so by decreasing the temperature the quenching effect of vibrations is reduced and the phosphorescence intensity increases, as observed in the present work (Figure 17).

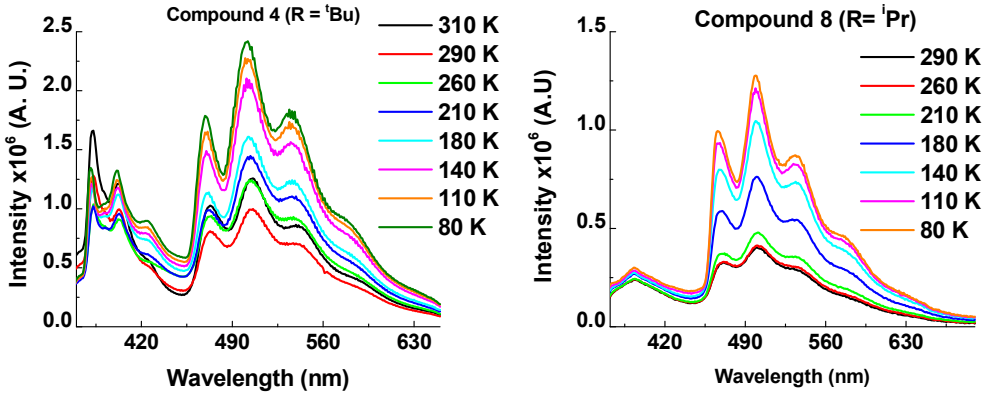

Figure 17 - Temperature dependence of emission of compounds **4** and **8** in zeonex.

3 - The lifetime of both TADF and phosphorescence follows the triplet state. However, TADF results from the interconversion of triplet states into singlet states by reverse intersystem crossing, and direct phosphorescence involves only the decay of the triplet state to the ground state. In the case of TADF the triplet lifetime is affected by an additional

deactivation process and so TADF lifetimes are shorter than phosphorescence lifetimes. This effect can be observed by comparing the luminescence decays of compounds **6** (no phosphorescence) and **4** (phosphorescence) in zeonex, as shown in Figure 10.

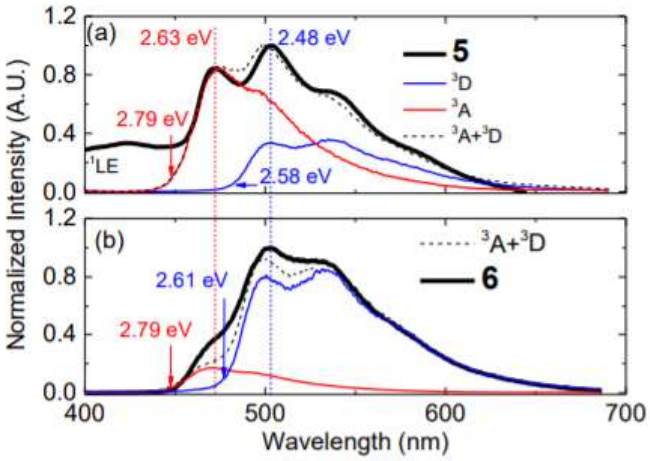

Figure 18 – Phosphorescence spectra of molecule **5** and **6**.

4 - Finally in Figure 18, phosphorescence in these compounds is the emission from a local triplet excited state and carries the clear signature of the phosphorescence emission of the phenothiazine donor (^{3}D) and dibenzothiophene-*S,S*-dioxide acceptor (^{3}A). This is seen in the figure above, where the phosphorescence of compound **6** at low temperature is compared with the phosphorescence of compound **5** at RT, and both are compared with the phosphorescence of the donor and acceptor isolated fragments. Clearly the phosphorescence of **5** and **6** are similar to the superposition of the phosphorescence of D and A which strongly indicates that the phosphorescence is from a local triplet state and not from a CT state.

5.8 Conclusion

In conclusion, suppressing vibrational quenching in a series of D–A–D and D–A molecules strongly activates phenothiazine phosphorescence. By sterically engineering near-orthogonal orientation and restricting rotation between the D and A fragments, in the solid state the main non-radiative deactivation pathway that affects the lowest triplet excited state is thus supressed and so phosphorescence from phenothiazine is not quenched. This provides valuable mechanistic information on TADF and has led to strongly phosphorescent molecules at room temperature.

5.9Bibliography

1 Yam V. W. W., Wong K. M.-C., *Chem. Commun*., **2011**, 47, 11579-11592

2 Aldo M. A., O'Brien D. F., Thompson M. E., Forrest S. R., *Phys. Rev. B,* **1999**, 60, 14422–14428.

3 Baldo M. A., O'Brien D. F., You Y., Shoustikov A., Sibley S., Thompson M. E., Forrest S. R., *Nature* **1998**, 395, 151-154.

4 Kondakov D. Y., Pawlik T. D., Hatwar T. K., Spindler J. P., *J. Appl. Phys.,* **2009**, 106, 124510.

5 King S. M., Cass M., Pintani M., Coward C., Dias F. B., Monkman A. P., Roberts M., *J. Appl. Phys.,* **2011**, 109, 074502.

6 Uoyama H., Goushi K., Shizu K., Nomura H., Adachi C., *Nature* **2012**, 492, 234.

7 Tao Y., Yuan K., Chen T., Xu P., Li H., Chen R., Zheng C., Zhang L., Huang W., *Adv. Mater.,* **2014**, 26, 7931.

8 Goushi K., Yoshida K., Sato K., Adachi C., *Nature Photon.* **2012**, 6, 253.

9 Zhang Q., Li J., Shizu K., Huang S., Hirata S., Miyazaki H., Adachi C., J. Am. Chem. Soc., **2012**, 134, 14706.

10 Adachi C., *Japanese J. Appl. Phys*., **2014**, 53, 060101.

11 Berberan-Santos M. N., Garcia J. M. M., *J. Am. Chem. Soc.,* **1996**, 118, 9391.

12 Baleizão C., Berberan-Santos M. N., *J. Chem. Phys*., **2007**, 126, 204510.

13 Zhang Q., Kuwabara H., Potscavage W. J., Huang S., Hatae Y., Shibata T., Adachi C., *J. Am. Chem. Soc*., **2014**, 136, 18070−18081.

14 Tanaka H., Shizu K., Nakanotani H., Adachi C., *Chem. Mater*., **2013**, 25, 3766−3771.

15 Nakagawa T., Ku S-Y., Wong K-T., Adachi C., *Chem. Commun.,* **2012**, 48, 9580–9582.

16 Dias F. B., Bourdakos K. N, Jankus V., Moss K. C., Kamtekar K. T., Bhalla V., Santos J., Bryce M. R., Monkman A. P., *Adv. Mater*., **2013**, 25, 3707-3714.

17 Chen P., Wang L-P., Tan W-Y., Peng Q-M., Zhang S-T., Zhu X-H., Li F., *ACS Appl. Mater. Interfaces,* **2015**, 7, 2972−2978.

18 Wang H., Xie L., Peng Q., Meng L., Wang Y., Yi Y, Wang P, *Adv. Mater*., **2014**, 26, 5198–5204.

19 Mei L., Hu J., Cao X., Wang F., Zheng C., Tao Y., Zhang X., Huang W., *Chem. Commun.,* **2015**, 51, 13024-13027.

20 Xu S., Liu T., Mu Y., Wang Y. F., Chi Z., Lo C. C., Liu S., Zhang Y., Lien A., Xu J., *Angew. Chem. Int. Ed.,* **2015**, 54, 874–878.

21 Leitl M. J., Krylova V. A., Djurovich P. I., Thompson M. E., Yersin H., *J. Am. Chem. Soc*., **2014**, 136, 16032-16038

22 Dias, Fernando B., Santos J., Graves D., Data P., Nobuyasu R. S., Fox M. A., Batsanov A. S., Palmeira T., Berberan-Santos M. N., Bryce M. N., A. P. Monkman, Adv. Sci. **2016**, 3, 1600080

23 Nobuyasu, R. S.; Ren, Z.; Griffiths, G. C.; Batsanov, A. S.; Data, P.; Yan, S.; Monkman, A. P.; Bryce, M. R.; Dias, F. B. Adv. Opt. Mater. **2016**, 4 (4).

24 Gong Y., Chen G., Peng Q., Yuan W. Z., Xie Y., Li S., Zhang Y., Tang B. Z., *Adv. Mater*., **2015**, 27, 6195-6201.

25 Reineke S., Seidler N., Yost S. R., Prins F., Tisdale W. A., Baldo M. A., *Appl. Phys. Lett.*, **2013**, 103, 093302–093302-5.

26 Xu J. J., Takai A., Kobayashi Y., Takeuchi M., *Chem. Commun.*, **2013**, 49, 8447-8449.

27 Koch M., Perumal K., Blacque O., Garg J. A., Saiganesh R., Kabilan S., Balasubramanian K. K., Venkatesan K., *Angew. Chem. Int. Ed.*, **2014**, 53, 6378-6382.

6. The influence of Molecular Geometry on the Properties of D-A and D-A-D, TADF Emitters, Induced by Steric Hindrance

Molecules containing electron-donor (D) and electron-acceptor (A) units create excited states of charge transfer character and promote the separation of the HOMO-LUMO orbitals. This effect is even more pronounced when the D and A units are orthogonal to each other. Here, it is demonstrated that while the introduction of bulky substituents as side groups are an effective form of restricting rotation around the D-A axis, it also has profound effect on the efficiency of the reverse intersystem crossing (RISC) mechanism. A series of D-A and D-A-D molecules based on phenothiazine (D) and dibenzothiophene-S,S-dioxide (A), substituted with different bulky groups is studied to understand the influence of these substituents on the molecular geometry and energy alignment between the charge transfer state and local triplet states, expanding the work discussed in chapter six. The luminescence from these molecules varies from efficient TADF to strong phosphorescence at room temperature, just as a consequence of introducing bulky side groups on the D unit. Remarkably, in clear contrast with the donor substituted molecules, their acceptor substituted analogues are strong TADF emitters.

To be submitted.

6.1 Introduction

The electrical current used to drive organic light emitting diodes (OLEDs) creates a large proportion of non-emissive triplet states due to the localized nature of the excitons in organic materials. This effect creates large exchange interactions and leads to the formation of excited states with spin 0 (singlet) and spin 1 (triplet).[1] Moreover, a fraction of the singlet states (S_1) created upon charge recombination may be converted to triplet states (T_1), due to intersystem crossing (ISC) caused by local hyperfine interactions, which affect the initially created charge transfer state,[2] and due to spin-orbit coupling causing ISC from S_1 to T_1.[3]

Singlet and triplet states have significant different properties. Whereas the singlet state lives for just a few nanoseconds and is often highly emissive, the decay of the triplet state occurs in the microsecond and even millisecond time range, and is frequently non-emissive.[3] Since singlet and triplet states are formed in a ratio of 1:3 in OLEDs, the formation of triplet states is a major loss mechanism in the efficiency of these devices. This problem has been driving the research in OLEDs since they were discovered in the nineties,[4,5] and ultimately led to the application of organic heavy-metal complexes, which have since then been the benchmarking materials for phosphorescent OLEDs.[6,7] OLEDs with IQEs of nearly 100% have been

fabricated with metal complexes, owning to the fast intersystem crossing (ISC) and room temperature phosphorescent properties of these materials, which are promoted by the presence of heavy-metals, such as iridium(III) and platinum(II). However, while the heavy metal complexes have many advantages, they also show significant problems when applied in light emitting diodes. They are scarce, expensive, may present environmental challenges, and are affected by degradation in the blue spectral region.[8,9] These issues may create difficulties for the utilization of these materials in applications that require high volume manufacturing, such as in lighting and display technologies. Therefore, alternative materials free of heavy metals are needed.

Molecules showing thermally activated delayed fluorescence (TADF) have been introduced in recent years and are a viable alternative to heavy-metal complexes.[10,11] TADFs are designed with electron donor (D) and electron acceptor (A) units covalently linked in ways that produce a very small energy gap between the singlet and triplet states, (ΔE_{ST}), just a few hundred meV is often observed. In these conditions, a significant population of the triplet state occupies upper vibrational levels and are able to cross back to the singlet manifold due to reverse intersystem crossing (RISC), giving origin to delayed fluorescence.[12]

OLEDs made of TADFs have shown impressive performances, often with external efficiencies (EQE) above 25%, but mainly in the green region of the visible spectrum. For emission in the blue and red regions, the performance of TADFs is usually weaker.[13] Moreover, a pronounced device efficiency roll-off is frequently observed at high current densities. The reasons for this dramatic drop in performance of OLEDs is not entirely clear, but triplet-triplet annihilation and triplet-polaron quenching processes have been indicated as the most probable causes, due to the long luminescence lifetime of TADFs.[14] TADFs with short luminescence decay lifetime are required to solve the device efficiency roll-off, which is nowadays one of the highest priorities in the OLEDs field. Deeper understanding of the TADF mechanism is thus necessary to resolve these drawbacks and optimize device performances.[15]

Small singlet-triplet energy gaps have been achieved in molecules with electron donor (D) and electron acceptor (A) units covalently linked in D-A and D-A-D structures. The formation in these molecules of excited states with strong charge transfer character (CT), leads to a vanishing overlap between the frontier molecular orbitals, HOMO and LUMO respectively. This effect strongly minimizes the exchange energy and leads to small singlet-triplet energy splitting. However, ΔE_{ST} can be further diminished by tuning the relative

orientation of the D and A units in near orthogonality.[16,17] The dihedral angle between the D and A units and the molecular geometry assume, therefore, key importance on tuning ΔE_{ST}, and maximizing TADF.

The observation of significantly different TADF performances in regio-isomers of a TADF emitter,[18] and the observation of luminescence decays that strongly deviate from the exponential regime and approach a power-law decay, when the emitter is dispersed in solid hosts, due to the presence of conformational heterogeneity induced by solvation effects,[19,20] gives additional evidence for the key role of the D-A dihedral angle and molecular geometry on the determination of ΔE_{ST} in TADF emitters.

However, the up-conversion of triplet states through the RISC mechanism is not only controlled by the magnitude of the singlet-triplet gap. Obviously, a small ΔE_{ST} gives better chance for triplets to cross back to the singlet manifold, but this is not sufficient condition for efficient TADF to be observed. Evidence has been gathered to support the importance of electron-phonon coupling, and mixing of charge transfer and localized electronic states to promote RISC. [12,19,21,22]

Previous studies in a series of phenothiazine (D) and dibenzothiophene-S,S-dioxide (A) TADF molecules, using D-A and D-A-D structures, with the donor phenothiazine substituted with side bulky groups, to force the D-A in near orthogonal geometry, have shown that while in the unsubstituted D-A and D-A-D molecules very strong TADF is observed, even in solid thin films, in the substituted emitters the TADF emission is strongly supressed, and in some of the cases almost entirely replaced by room temperature phosphorescence.[23] These observations clearly indicate the importance of molecular conformation on the TADF mechanism, and show that restricting the dynamic rocking of the D groups around the DA axis strongly limits the TADF efficiency, which beautifully demonstrates the vibronic-coupling mechanism in TADF.[21,22]

Here, the study of D-A and D-A-D molecules with restricted molecular geometry is expanded. Molecules functionalised with bulky side substituents in different positions of the D and A units are investigated to unravel the influence of different substituents on the energy of the singlet and triplet excited states and molecular geometry. It was found that the energy of the ^{1}CT state is increasingly shifted to higher energies with increasing bulkiness of the substituent in the D unit, i.e. bulky side groups increasingly restrict the dynamic rotation around the DA axis, destabilize the ^{1}CT state, and quench TADF emission. Remarkably, when the substitution occurs in the acceptor unit, while the destabilization of the ^{1}CT still

occurs, the effect is much weaker, and instead of decreasing the intensity of TADF is enhanced.

6.2 Chemical structures

The chemical structures of the molecules studied in this work are shown in Figure 1. Molecules **1** and **9** are the unsubstituted D-A-D and D-A versions, which are used in this study as reference. The remaining molecules are substituted with side groups in different positions. Molecules **2** to **5**, are D-A-D, and are all substituted on the phenothiazine donor. Molecules **6** and **7**, are also D-A-D, but substituted on the dibenzothiophene-*S,S*-dioxide acceptor, molecule **8** is also D-A-D, but substituted in both D and A units. Finally, molecules **10** to **12** are the asymmetric D-A versions substituted on the donor unit, with the difference that molecule **12** is substituted at the external position, thus not being affected by the steric hindrance.

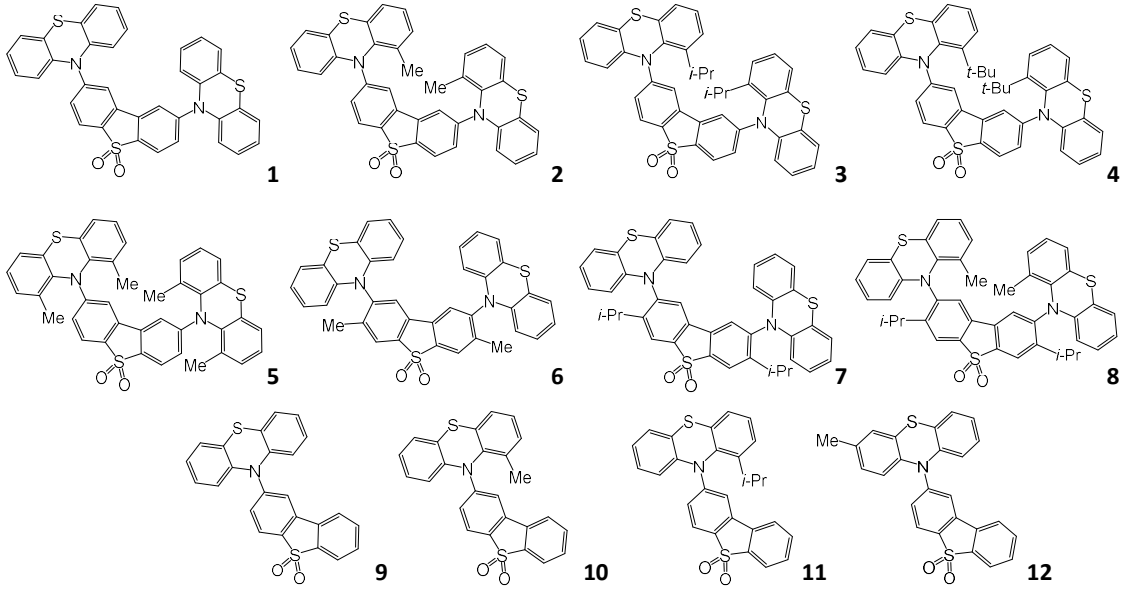

Figure 1 - Molecular structures of the emitters investigated in this work.[1]

With this comprehensive mapping of structural substitutions it is able to fully address the influence of the side groups on the TADF efficiency, covering the steric effects that influence both the molecular geometry and the energy of electronic excited states. This allows studying the intricate role of both contributions on the photophysics of TADF emitters.

[1] Molecules were synthesized by Martin Bryce's research group.

6.3 Cyclic Voltammetry

All compounds show oxidation and reduction processes in cyclic voltammetry (CV) studies, (Figure 2). The redox potentials, electron affinity (EA) and ionization potential (IP), were determined from the onset of oxidation and reduction processes. For compounds **1** to **4**, top row in Figure 1, the IP potential increases with increasing the size of the alkyl groups, varying from -5.4 eV in **1**, to -6.1 eV, in **4** (see Figure 2). The effect on the EA energy is the opposite, but less pronounced.

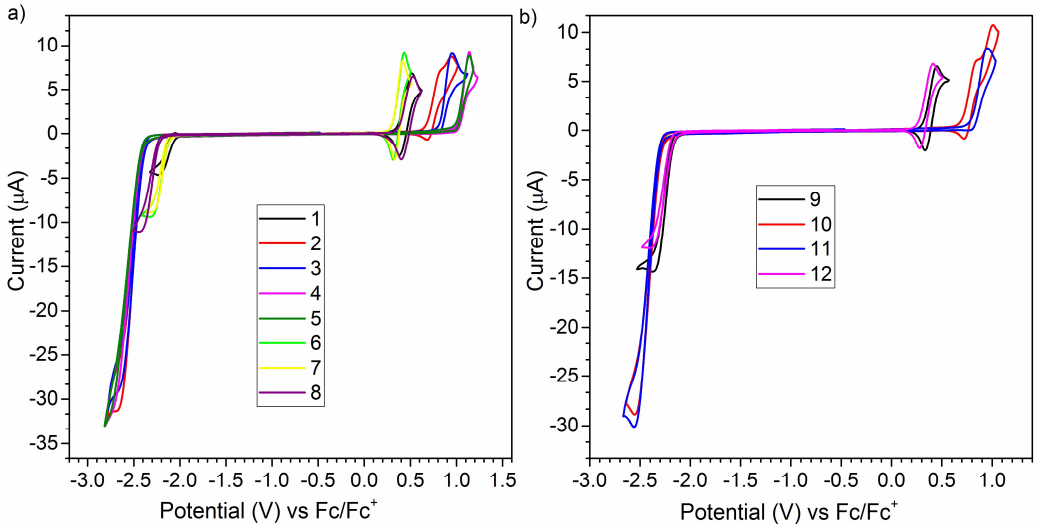

Figure 2 - Cyclic voltammetry of 2mM concentration of investigated compounds in 0.1M Bu_4NBF_4/DCM. Measurement conditions: scan rate 50 mV/s, Ag/AgCl – quasi-reference electrode, calibrated against a ferrocene/ferrocenium redox couple.

With increasing bulkiness of the side groups the EA energy varies from -3.09 eV in **1**, to -2.68 eV in **4**, see Figure 3. These are probably the consequences of larger steric hindrance and increasing tension in the phenothiazine group, introduced by the steric effect in the D-A and D-A-D molecules. Interestingly, there is almost no difference in the IP and EA energy levels of the *t*-butyl mono-substituted, **4**, and the methyl bi-substituted **5,** showing that the stress caused by the presence of the two methyl groups in the phenothiazine donor is similar to the effect caused by the bulkiest t-Bu group.

Similar behaviour is observed for the DA derivatives, compounds **9**-**11**, see Figure 2. With increasing bulkiness of the alkyl side group the IP energy is stabilized, while the EA is destabilized. The bulkier side groups force the angle between donor and acceptor to increase, making oxidation more difficult. However, when the phenothiazine donor is substituted with a methyl group in the external position (compound **12)** no significant effect is observed, i.e.

compounds **9** and **12** have similar IP and EA energies. This indicates that there is no influence on the dihedral angle between the donor and acceptor groups, when the substitution occurs in the external positions of the phenothiazine, as expected. Figure 3 shows a schematic of the evolution of the IP and EA energies for the molecules **1-12**.

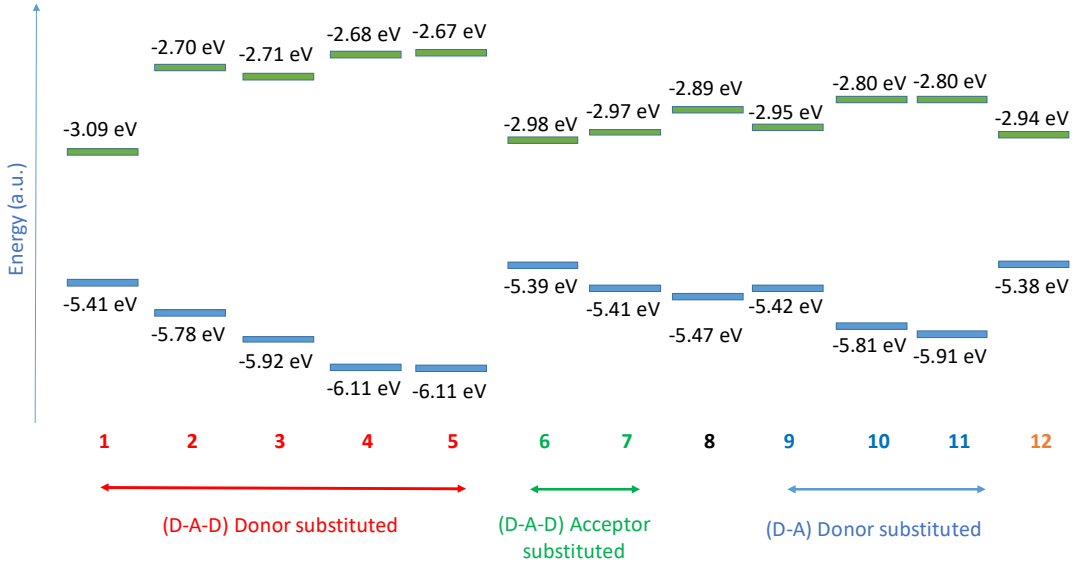

Figure 3 - Evolution of the IP and EA potentials with substitution on the donor and acceptor units. Compounds **1-5** are D-A-D, substituted in the D unit. Compounds **6** and **7** are also D-A-D but substituted on the acceptor unit, and **8** is a D-A-D compound substituted in both donor and acceptor. Compounds **9-12** are D-A, substituted in the donor unit.

When the substitution occurs in the acceptor unit, the IP remains almost unaffected, i.e. compounds **1**, **6** and **7**, show similar IP energies, shown in Figure 3. There is however, a very small change in the EA energy, but this is not correlated with the size of the alkyl side group. Interestingly, when the *i-propyl* group is substituted in the already methyl substituted phenothiazine, see compound **8**, the influence of the methyl group on the phenothiazine donor is less pronounced, see the relative changes observed between compounds **1** and **2**, with methyl substitution on the phenothiazine donor, and compounds **7**, **8**, where the methyl substitution on the donor unit occurs in presence of the *i-propyl* substituted acceptor.

6.4 Computational Results[2]

Molecules **1**, **9** and their substituted D-A-D and D-A forms can exhibit more than one stable conformer, with both the H-intra and H-extra folded conformers of the phenothiazine being possible. This allows formation of parallel quasi-axial (ax) and perpendicular quasi-equatorial

[2] All the simulations were performed by Thomas Penfold's research group.

(eq) conformers, as shown in Figure 4 for compound **9**. For the D-A-D molecules there is also the possibility for mixed conformers to exist. In which, one donor is in quasi-axial and the other is in quasi-equatorial orientation. The nomenclature of axial and equatorial conformers is taken from Stockmann et al.,[24] and is in reference to the N–S axis and plane of the phenyl rings.

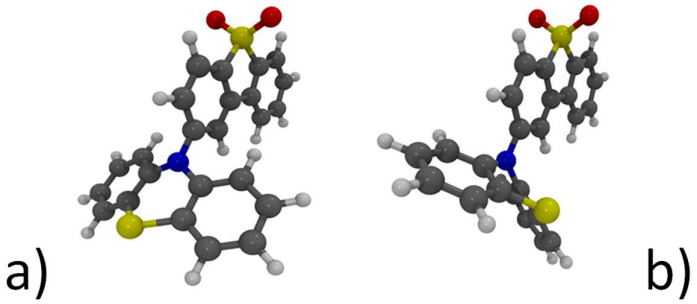

Figure 4 - a) Quasi-equatorial and b) Quasi-axial conformers of molecule **9.**

Table 1 -Set of tables showing the HOMO/LUMO, Dipole and Boltzmann distribution weights for all the molecular conformers: Axial (Ax.), Equatorial (Eq.) and Mixed (M.) t

	1			**5**			**8**		
Conformer	Ax.	Eq.	M.	Ax.	Eq.	M.	Ax.	Eq.	M.
Rel. Energy (eV)	0.00	0.15	0.07	0.00	0.64	0.33	0.20	0.16	0.00
Dipole (D)	10.86	4.04	9.07	10.70	8.4	10.43	11.05	4.97	9.75
E_{HOMO} (eV)	-7.11	-6.65	-6.64	-7.18	-7.09	-7.09	-6.99	-6.78	-6.80
E_{LUMO} (eV)	-1.02	-1.49	-1.24	-0.99	-1.39	-1.17	-0.86	-1.38	-1.06
Boltzmann Weighting	0.94	0.00	0.06	1.00	0.00	0.00	0.11	0.61	0.28

	2			**3**			**4**		
Conformer	Ax.	Eq.	M.	Ax.	Eq.	M.	Ax.	Eq.	M.
Rel. Energy (eV)	0.00	X	X	0.00	X	X	0.00	X	X
Dipole (D)	10.86	X	X	10.83	X	X	10.82	X	X
E_{HOMO} (eV)	-7.17	X	X	-7.17	X	X	-7.31	X	X
E_{LUMO} (eV)	-1.00	X	X	-0.99	X	X	-0.98	X	X
Boltzmann Weighting	1.00	X	X	1.00	X	X	1.00	X	X

	6			**7**		
Conformer	Ax.	Eq.	M.	Ax.	Eq.	M.
Rel. Energy (eV)	X	0.00	X	X	0.00	X
Dipole (D)	X	4.94	X	X	4.72	X
E_{HOMO} (eV)	X	-6.66	X	X	-6.77	X
E_{LUMO} (eV)	X	-1.36	X	X	-1.36	X
Boltzmann Weighting	X	1.00	X	X	1.00	X

	9			10			11			12		
Conformer	Ax.	Eq.	M	Ax.	Eq.	M.	Ax.	Eq.	M.	Ax.	Eq.	M.
Rel. Energy (eV)	0	0.06	X	0.00	X	X	0.00	X	X	0.00	0.08	X
Dipole (D)	9.33	6.22	X	9.18	X	X	9.38	X	X	9.89	6.41	X
E_{HOMO} (eV)	-7.18	-6.64	X	-7.26	X	X	-7.30	X	X	-7.16	-6.56	X
E_{LUMO} (eV)	-1.09	-1.34	X	-1.09	X	X	-1.08	X	X	-1.08	-1.33	X
Boltzmann Weighting	0.91	0.09	X	1.00	X	X	1.00	X	X	0.95	0.05	X

Table1 shows the relative energies for all of the major conformers of the 12 molecules studied herein. The D-A-D molecules, **1**, **5** and **8** exhibit minima for the two pure conformers and mixed conformations. However, bulky substituents tend to force the molecule towards a particular conformation. When the substitution occurs in the internal positions of the phenothiazine donor the axial conformation is favoured, whereas substitution on the acceptor moiety favours the equatorial conformation. For the D-A molecules, the same trend is observed, with bulky substituents in the internal position of the phenothiazine favouring the formation of the axial conformer.

As it was recently demonstrated the different conformers have profound influence on the electronic structure.[18] The axial conformers exhibit the largest energy gap between the HOMO and LUMO due to the stabilization of the HOMO in this form. Whilst one should be careful about direct interpretation of excited state energies from Kohn-Sham HOMO-LUMO energy gaps, this is consistent with the high CT energy observed for the axial conformers.[18] The stabilization of the HOMO is due to its ability to delocalize over both the donor and acceptor groups, as shown in Figure 5 for molecules **1** and **9**.

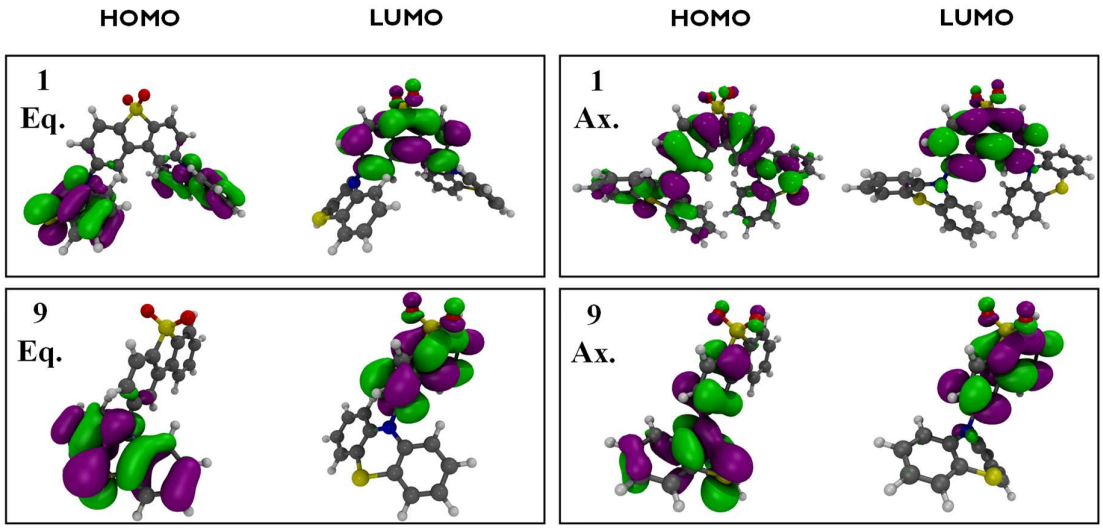

Figure 5 – HOMO/LUMO for molecules **1** and **9** in the axial and equatorial conformations.

The absorption spectra were calculated for all the 12 molecules and are shown in Figure 6. The calculations broadly reproduce the general trends observed experimentally, but the electronic transitions are slightly shifted to shorter wavelengths by ~50 nm.

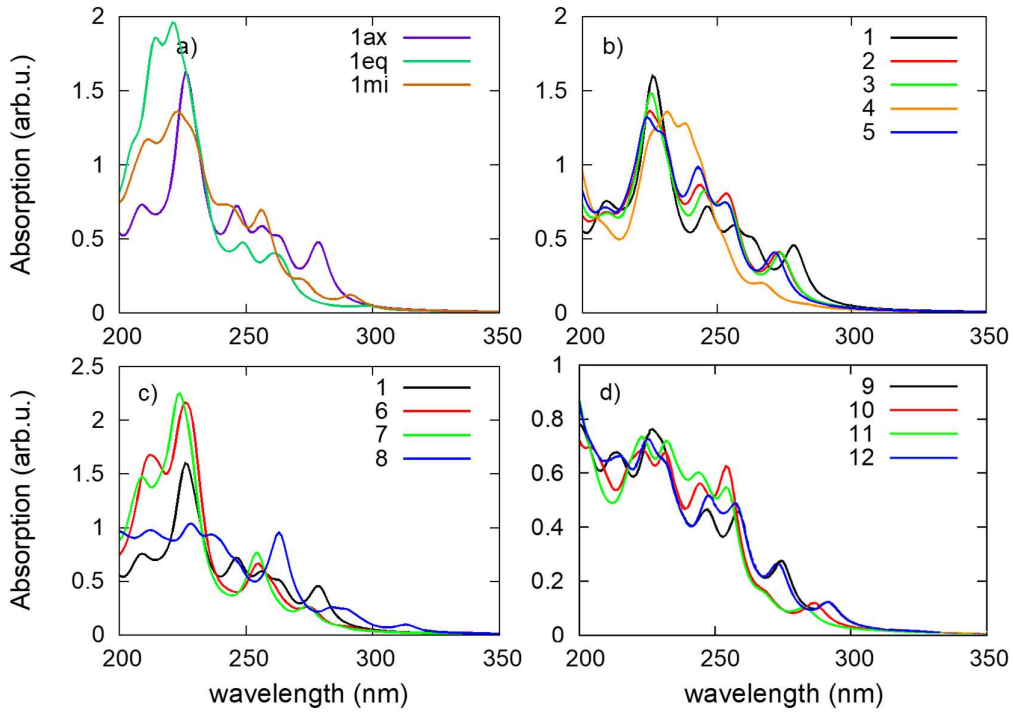

Figure 6 – Simulated absorption spectra of molecules **1**-**12**.

Figure 6a, shows the signatures for the axial and equatorial conformers, and the mixed conformations. The calculated absorption spectra for molecules **1** to **5**, Figure 6b, indicate that the axial conformer is dominant in these molecules. In contrast, molecules **6** and **7**, Figure 6c, clearly indicate that the equatorial conformer is predominant. Finally, molecules **9**-**12**, Figure 6d, exhibit relatively broad featureless absorption spectra due to the increased mixing of the donor and acceptor electronic structures, and no clear predominance of the axial or equatorial conformers is observed. The absorption spectra corresponding to the individual conformers, i.e. without Boltzmann weighting are shown in Figure 6.

Figure 7 shows the calculated emission energies (red filled circles) plotted against the peak of the experimental emission spectra (black open circles). The calculated values again reproduce the trends observed experimentally.

Most compounds show emission in the region of 550-650 nm. This corresponds to emission that is dominated by the equatorial conformer. However, the presence of the axial conformer is revealed by an emission band occurring around 450 nm.[18]

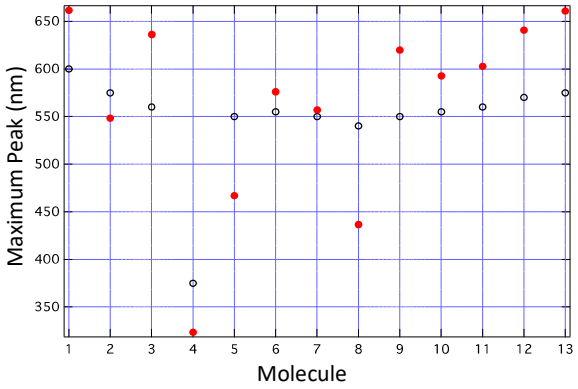

Figure 7 - Calculated emission energies (red filled circles) plotted against the peak of the experimental emission spectra (black open circles).

As the axial conformer predominates in molecules where the phenothiazine donor is substituted with bulkier side groups, emission in this region is more evident for compounds **2**, **3**, **4** and **5**. Molecule **4** in particular, represents an extreme case where the steric hindrance caused by the bulkier *t*-Bu groups causes complete quenching of the equatorial emission. However, it is especially interesting to note that the emission from the equatorial form still dominates, even for the molecules where the equatorial conformer is not favoured (**9**, **12**) or was unable to be formed (**2**-**4**, **10**, and **11**) in the ground state. Therefore, and very importantly, the observation of strong equatorial emission in most molecules indicates the presence of conformational switching once the excited state is populated. This can be explained by the observation that for molecules **1** and **9** and their substituted D-A-D and D-A counterparts, excitation of the S_1 charge transfer state is accompanied by an elongation of the D-A distance. This separation reduces the steric hindrance, making the equatorial form more stable and allowing the transition axial to equatorial to occur in the excited state.

6.5 UV-VIS Absorption in solution

Figure 8a shows the absorption spectra of the unsubstituted molecules, **1** and **9**, in dichloromethane (DCM) dilute solution, compared with the absorption of the D and A single fragments in the same solvent. DCM was selected for these studies due to the high cut-off (220 nm) of this solvent, which allows following the signatures of both D and A units in the deep UV region. The absorption of the D phenothiazine unit is clearly identified by two well-defined bands, one peaking at 250 nm and the other around 325 nm. The absorption of the acceptor, dibenzothiophene-*S,S*-dioxide, is also clearly identified, showing a band that peaks around 280 nm. In general terms, the absorption of compounds **1** and **9** are well reproduced

by the superposition of the absorption of the single fragments, with the exception of a weak tail (low oscillator strength) that is observed up to 450 nm, which is attributed to the direct absorption of the charge transfer state (CT).[19,23,25] However, when the D unit is substituted with bulky side groups, as for example in molecules **2** to **5**, marked differences are observed in the absorption spectra, when compared with the absorption of their unsubstituted analogue (Figure 8b). With increasing bulkiness of the side group the absorption band appearing at 250 nm becomes increasingly broadened, and the molar absorption coefficient in this region decreases, suggesting a decrease on the oscillator strength of the electronic transitions associated with the D unit. Moreover, the absorption tail that extends up to 450 nm in **1** and **9**, due to the presence of the CT absorption band, is also increasingly suppressed. This indicates that the direct absorption of the CT state is restricted in the D-substituted compounds. In contrast, the absorption spectra of molecules **6** and **7**, also D-A-D, but substituted in the acceptor with groups methyl and *i*-propyl, respectively, show enhanced molar absorption coefficient around 250 nm (Figure 8c). This is a clear signature of the phenothiazine donor unit, and showing no broadening effect in the D region, as these two molecules are substituted just in the acceptor unit. Notably, the signature of the acceptor unit is also more clearly observed in compounds **6** and **7** than in compounds **1**-**5**, suggesting that the substitution of the acceptor units uncouples more effectively the electronic linkage between the D and A units.

Finally, in molecule **8**, substituted with a methyl group in the D unit at position 1, and *i*-propyl groups in the A unit, the vibrational structure in the acceptor unit is lost once more, and the peak around 250 nm is again broader, showing weaker oscillator strength, and confirming the effects due to the substitution on the D unit.

In the asymmetrical D-A set of molecules the substitution occurs only on the donor unit (Figure 8d). Molecule **10** is substituted at position 1, with one methyl group, and molecule **11** is substituted in the same position with one *i*-propyl group. As expected, the absorption peak around 250 nm, which is assigned to the D unit, is strongly suppressed, and the spectra are dominated by the absorption of the A unit. In the case of molecule **12**, which is substituted in the D unit, but at position 3, with a methyl group, the behaviour is clearly different. As the substitution occurs in the "external" region of the D unit, the absorption spectrum almost replicates the absorption spectrum of the unsubstituted D-A molecule **9**.

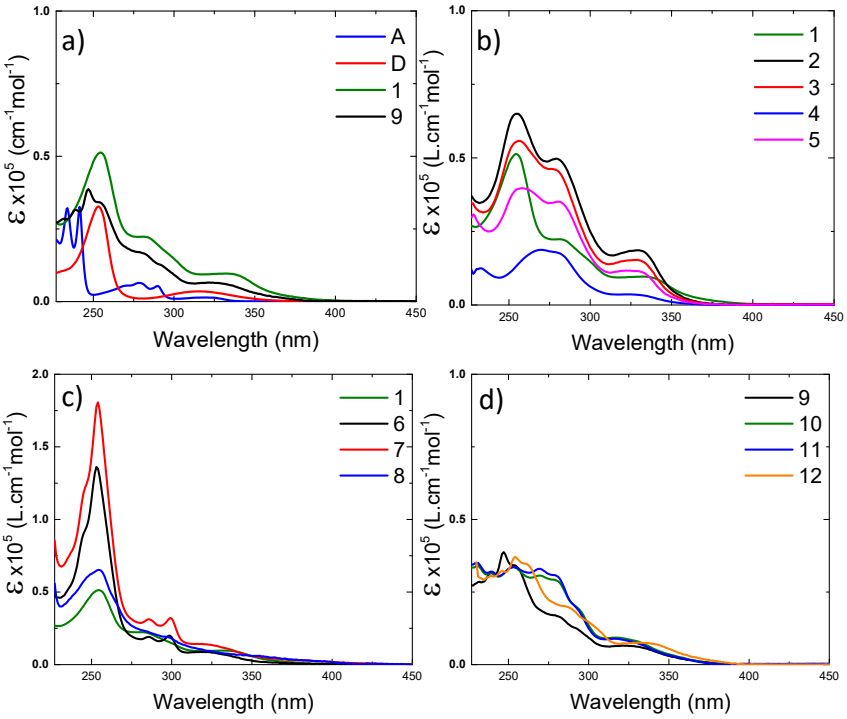

Figure 8 - Absorption spectra in dichloromethane. a) Donor, Acceptor and the unsubstituted D-A-D and D-A molecules, **1** and **9**; b) D-A-D molecules with the substituents in the donor, **1** to **5**; c) D-A-D molecules with the substituents in the acceptor **6** and **7**, and for molecule **8** in both D and A units; d) D-A molecules with substituents in the donor, **10** and **12**.

The UV-Vis absorption data is, therefore, entirely consistent with the CV data, showing the influence of substitution position on the electronic properties of the donor or acceptor regions due to the steric-hindrance effect introduced by the side groups. This affects the D-A relative orientation and molecular geometry and strongly restricts rotation around the DA axis, but also affects the conformation of the donor phenothiazine itself.

6.6 Steady-state emission in toluene solution and in zeonex film

Photoluminescence experiments were performed in toluene solution and zeonex film, under inert atmosphere or in vacuum. Figure 9a, shows the emission spectra of molecules **1** to **5**. The unsubstituted molecule **1** shows red-shifted broad emission, consistent with the CT character of the emissive singlet excited state, peaking around 600 nm. However, for molecules **2-5,** the substituted versions of **1,** the ^{1}CT emission band shifts to higher energies with increasing steric-hindrance caused by the substituent in the donor. This effect is also consistent with the CV data, as it indicates that the energy gap between the HOMO of the donor and the LUMO of the acceptor increases with the bulkiness of the side group, shown in

Figure 3. The emission spectra of these molecules is also narrower, and the ^{1}CT emission is accompanied by an emission band around 400 nm, which is assigned to the radiative decay of the local excited state, identified by ^{1}LE, and possibly the emission from the axial conformer emitting around 450 nm. The intensity of this emission increases with the bulkiness of the substituent group. This effect is particularly pronounced in molecule **4**, substituted with a t-butyl group. In **4** the ^{1}CT emission is practically completely quenched, and the ^{1}LE emission dominates the entire spectrum, showing that the steric-effect imposed by the side group also affects the formation and stabilization of the CT state.

Figure 9b shows the emission of the molecules substituted in the acceptor, also in toluene solution, compared with the emission of the unsubstituted molecule **1**. The ^{1}CT emission in **6** and **7**, which are substituted in the acceptor unit with methyl and *i*-propyl groups, respectively, appears blue-shifted, but no other significant effects are observed. However, the emission in molecule **8**, substituted with methyl and i-propyl groups in the donor and acceptor, respectively, shows a slightly further blue shift, compared with **6** and **7**.

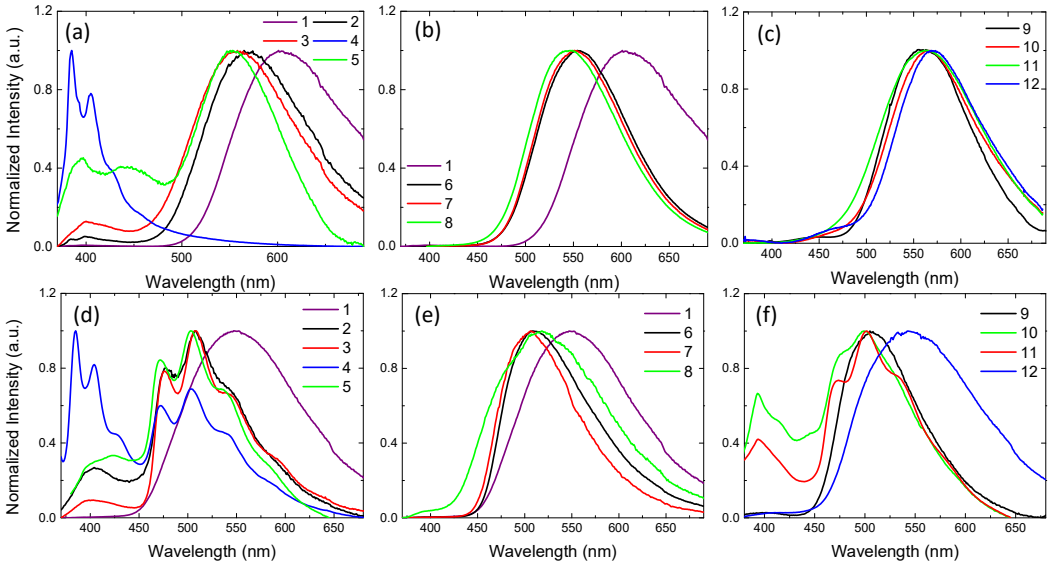

Figure 9 - Steady state emission in degassed toluene solution and in zeonex obtained at room temperature for molecules: (a, d)**1**-**5**, (b, e)**1**, **6**-**8**, and c, f) **9**-**13**.

Figure 9c shows the emission spectra in toluene solution of the asymmetrical D-A molecules with substituents in the D unit, molecules **10**, **11** and **12**. The spectral shifts induced by the substitution at the D unit are significantly smaller, when compared with the shifts observed in the D-A-D counterparts. The emission of molecule **10** is slightly red shifted relative to the emission of the unsubstituted molecule **9**. A similar effect is observed for molecule **12**. However, the emission of molecule **11**, substituted with a bulkier i-propyl group, appears

broader than all the others, but peaking at a similar wavelength than the unsubstituted molecule. So, generally speaking, the effect of the side groups on the emission of the asymmetrical D-A molecules is weaker than in their D-A-D counterparts. Note also that the emission of **9**, appears significantly blue-shifted when compared with the emission of **1**, showing that ^{1}CT state is more stabilized in the D-A-D structure than in the asymmetrical D-A.

In contrast with the emission in solution, the steady-state emission spectra of compounds **2**-**5** in zeonex solid film show dual luminescence, composed of ^{1}LE fluorescence and phosphorescence (Figures 9d to 9f). Interestingly, the phosphorescence in the D-A-D and D-A molecules matches the phosphorescence of the donor or acceptor units, and is reproduced by adding the phosphorescence spectra of the D and A units in different weights, as it is exemplified in figure 10, for molecules **3**, **7** and **9**.

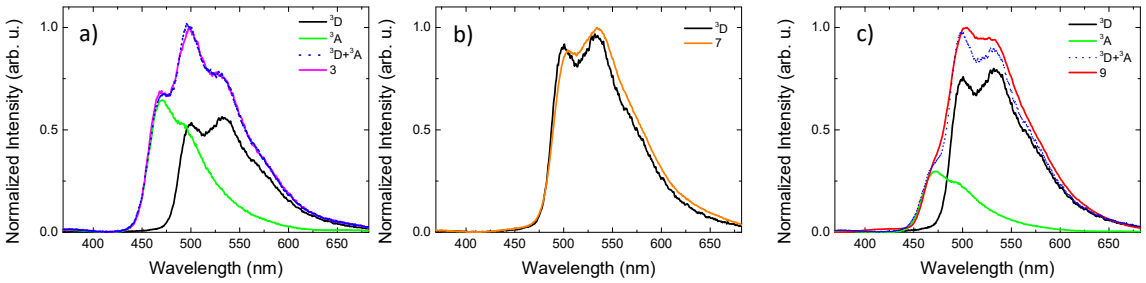

Figure 10 – Phosphorescence spectra of the Donor (black) and Acceptor (green) with the respective intensity weights in the sum (blue dots): a) molecule **3** (pink); b) molecule **7** (orange) and c) molecule **9** (red).

Noticeably, and in clear contrast with the donor substituted molecules **3** and **9**, which show contributions of the D and A units in their phosphorescence spectra, the acceptor substituted molecule **7**, shows phosphorescence from the D phenothiazine only. The high energy shoulder due to the phosphorescence from the acceptor unit is completely absent. This indicates that for molecules with the axial conformation, the phosphorescent spectra exhibit contributions from both D and A triplet states, but in the acceptor substituted molecules, **6** and **7**, which adopt the equatorial conformation, only phosphorescence from the triplet of lower energy, localized in the D unit, is observed (Figure 11). The only exception to this pattern is molecule **8**, showing broader phosphorescence, probably due to the presence of mixed, axial and equatorial, conformers in this compound (in red, Figure 11c), however **8** is also substituted in the D unit.

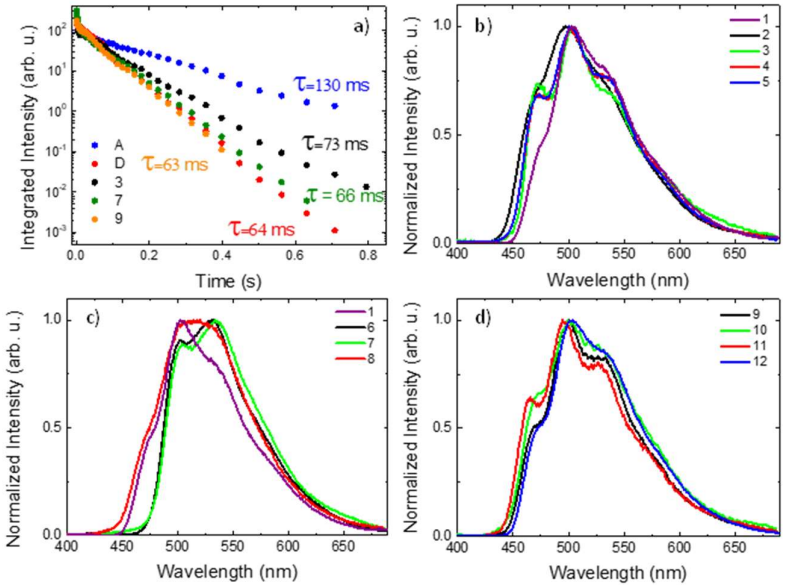

Figure 11 – a) Phosphorescence lifetime of compounds D, A, **3**, **7** and **9** recorded in Zeonex matrix at 80 K. Phosphorescence spectra of compounds **1-12** obtained in zeonex at 80 K. b) D-A-D donor substituted **1-5**; c) D-A-D acceptor substituted **6-8** and d) D-A, donor substituted **9-12**.

Figure 12 shows the area normalized time resolved phosphorescence spectra of molecules **3**, **7** and **9**. Molecules **3** and **9**, with the predominant axial conformer, show pronounced spectral variation over time, giving indication for the presence of more than one emitting species, as the phosphorescence of the D and A units have different lifetimes (Figure 11a). In contrast, the phosphorescence in compound **7**, with the dominant equatorial conformer, shows limited spectral variation, giving indication of a single triplet emitting species.

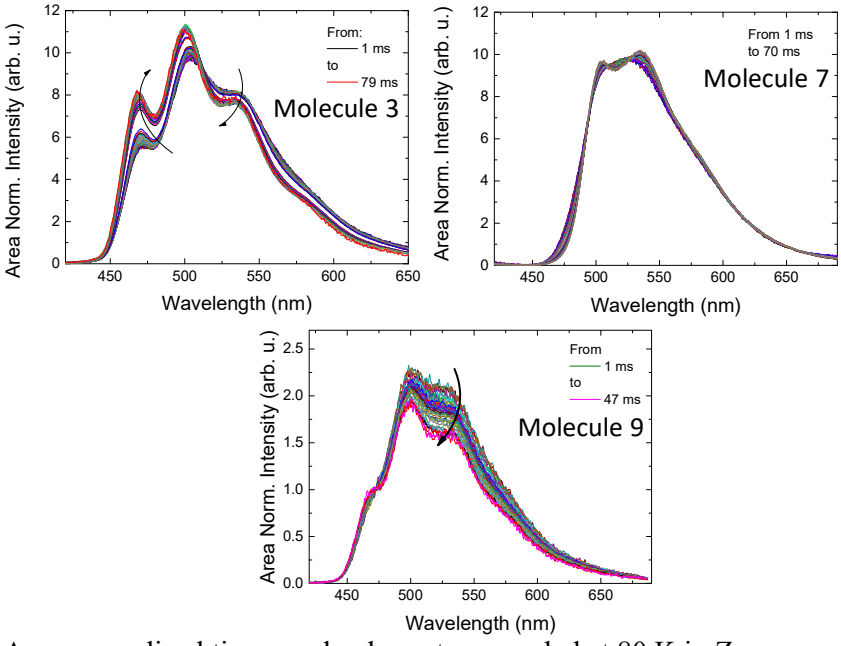

Figure 12 – Area normalized time resolved spectra recorded at 80 K in Zeonex matrix.

Table 2 shows the photoluminescence quantum yield of molecules **1**-**12**, measured in zeonex film at room temperature, under normal atmosphere, but corrected for the quenching effect of oxygen. The molecules that exhibit a strong TADF contribution to the overall luminescence, **1**, **6**, **7**, **9** and **12**, also present stronger PLQY than the other emitters. This is consistent with the decrease on the molar absorption coefficient of the D substituted compounds, **2**-**5** and **10**-**11**, which indicates that the radiative rate constant of the singlet emissive state is also affected by the D substitution. This decrease on the radiative rate constant of the singlet state favours the competition with the ISC rate, which explains why the D substituted molecules are good phosphorescent emitters in solid state.

Table 2 - The photoluminescence quantum yield in solid state, Zeonex matrix at RT.[3a]

Molecules	PLQY	Molecules	PLQY
1	0.32	7	0.38
2	0.07	8	0.18
3	0.08	9	0.42
4	0.09	10	0.13
5	0.07	11	0.11
6	0.32	12	0.21

6.7 The Influence of substituent groups on the ^{1}CT energy

Figure 13 represents the variation of the ^{1}CT energy along all the molecules used in this study. In Figure 13a the energy of the singlet ^{1}CT is determined in toluene and in Figure 13b determined in zeonex. The energies of the triplet states, ^{3}D, ^{3}A and the ^{3}LE are determined in zeonex in both figures. The ^{1}CT energy is determined from the onset of the emission spectra, using time resolved spectra, so the energy of the relaxed charge transfer state is obtained without being affected by the emission of the short lived ^{1}LE state. Four different groups can be identified in Figure 13a. In the first one, (blue line-squares), the energy of the ^{1}CT state in D-A-D molecules (D substituted), molecules **1-5**, shows a clear progression towards higher energies, with increasing bulkiness of the substituent. This is consistent with the CV data in Figure 3. The unsubstituted molecule **1** shows the most stabilized ^{1}CT energy (2.43 eV) in this group, whilst molecule **4**, substituted with the bulkier t-butyl group, shows almost no ^{1}CT emission, and the spectrum is dominated by ^{1}LE type emission. Molecules **2** and **5** can be also directly compared, because they are substituted with the same methyl group and exactly

[3a] Experiments performed in a Hamamatsu equipment: C11347-11Quantaurus-QY Absolute PL quantum yield spectrometer. With an estimated error of 15%.

in the same position, however, whilst **2** is substituted with just one methyl group, **5** is substituted with two methyl groups in the D unit. Therefore, the effect in **5** is more pronounced, as for example the restriction imposed to the rotation around the D-A axis is stronger in **5** than in **2**. Therefore the ^{1}CT state is less stabilized in **5** than in **2**, and the ^{1}CT energy in **5** is shifted to higher energies.

In the second group (pink line, circles) are molecules **6**-**8**. Molecules **6** and **7** are substituted in the acceptor unit with methyl and *i-propyl* groups, respectively. Once more, the ^{1}CT energy shifts to higher energies with increasing bulkiness of the substituent group. However, the variation is now much less pronounced, showing that the effect of the acceptor substitution on the ^{1}CT energy is smaller than when the substitution occurs in the D unit. This observation is entirely consistent with the CV data, and strongly suggests that the substituents in the D units may be clashing with each other, imposing a strong restriction to the rotation around the DA axis, and forcing the molecules to adopt a different geometry. Molecule **8**, substituted in the acceptor unit with *i-propyl*, as **7**, but with an additional methyl group in the donor unit, shows the ^{1}CT energy shifting to slightly higher energies, when compared with **7**. Again, this is consistent with stronger restriction to the rotation around the D-A axis.

In the third group, (red line, triangles), are molecules **9** to **11.** These show a similar trend to the molecules in group 1, as expected. However, since these are now asymmetrical D-A molecules the restriction effect is not so pronounced and the variation is smaller than in group 1. However, there is a clear trend with the ^{1}CT energy shifting to higher energies with the bulkiness of the substituted group.

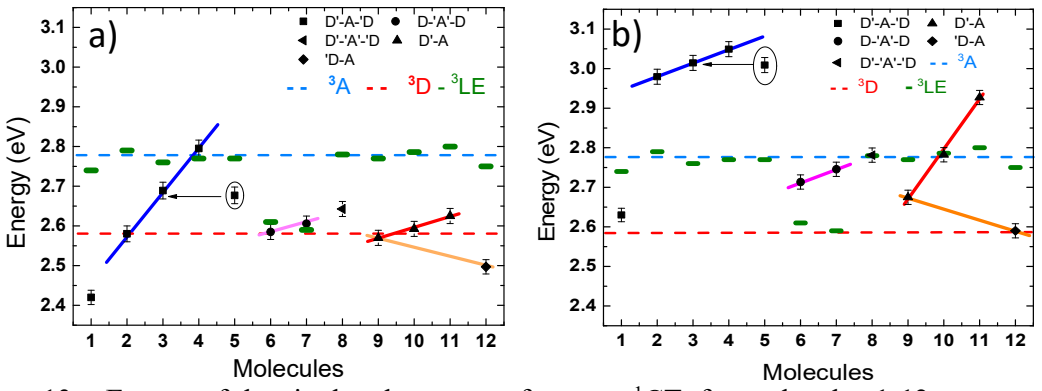

Figure 13 – Energy of the singlet charge transfer state, ^{1}CT, for molecules **1-12** measured in a) toluene solution and b) zeonex (black symbols). Triplet energy of the acceptor (dash green line) and of the donor (dash red line) fragments. Triplet energy of compounds **1-12** determined from their phosphorescence onset (light blue trace).

Finally, molecule **12**, with the substitution occurring in the D unit, but in the outer position, so imposing no restriction to the rotation around the DA axis, shows the ^{1}CT energy that is directly compared with the unsubstituted molecule **9.** In this case instead of a blue shift, the ^{1}CT energy is more stabilized than in the unsubstituted molecule. This effect is also consistent with the CV data, as the HOMO-LUMO energy difference in **9** is 2.47 eV, and in **12** is 2.44 eV. Therefore, the methyl substitution in the outer position of the phenothiazine ring, in the absence of geometric restrictions, slightly stabilizes the CT state.

The trend in the ^{1}CT energies in zeonex follows a similar variation to that observed in toluene. However, compounds **2-5** and **11**, have ^{1}CT energies well above their triplet states. Whereas, compounds **1**, **6**, **7**, **8**, **9**, **10** and **12** show ^{1}CT energies close to the energy of the triplet states, ^{3}D, ^{3}A or ^{3}LE. Compounds **8** and **10** in particular show ^{1}CT states isoenergetic with the ^{3}LE.

6.8 The influence of substituent groups on the TADF contribution

The TADF mechanism involves the recycling of singlet and triplet states, mediated by the intersystem crossing, k_{ISC}, and reverse intersystem crossing, k_{RISC}, rates, occurring between the singlet (S_1) and triplet (T_1) states, according to the scheme in Figure 14. The excited states, S_1 and T_1, are also affected by internal conversion, represented by k^S_{IC} and k^T_{IC}, and by their radiative decay rates, k_f, and k_{Ph}, accounting for the fluorescence and phosphorescence emissions.

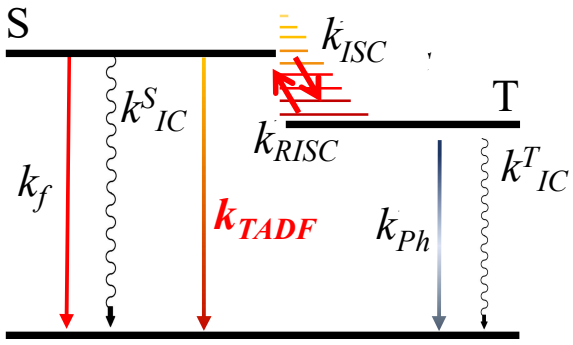

Figure 14 - Schematic representation of the TADF mechanism.

The total emission in a TADF emitter,Φ_f, is therefore formed by prompt, Φ_{PF}, and delayed fluorescence, Φ_{DF}, components due to the triplet harvesting, as described in the scheme given in Figure 14. Strong TADF is observed in molecules with relatively strong triplet yield, Φ_T, and where the yield of singlet states formed by reverse intersystem crossing, Φ_{RISC}, is also

very high. Equation 1, gives the product between the yield of triplet formation, Φ_T, and the yield of singlet states formed by reverse intersystem crossing, Φ_{RISC}, as a function of the ratio between DF and PF.

$$\Phi_T \Phi_{RISC} = \frac{\Phi_{DF}/\Phi_{PF}}{1+\Phi_{DF}/\Phi_{PF}} \qquad 1$$

Eq. 1 shows that triplet states are harvested with efficiency close to 100%, when the ratio between the delayed and prompt fluorescence components Φ_{DF}/Φ_{PF} is above four. This situation is usually obtained in TADF emitters with a singlet-triplet energy splitting less than 150 meV, or even slightly above this. Providing the RISC rate dominates over the non-radiative IC affecting the triplet state. However, showing that a small singlet-triplet energy splitting is not sufficient condition to obtain efficient triplet harvesting and strong TADF contribution.

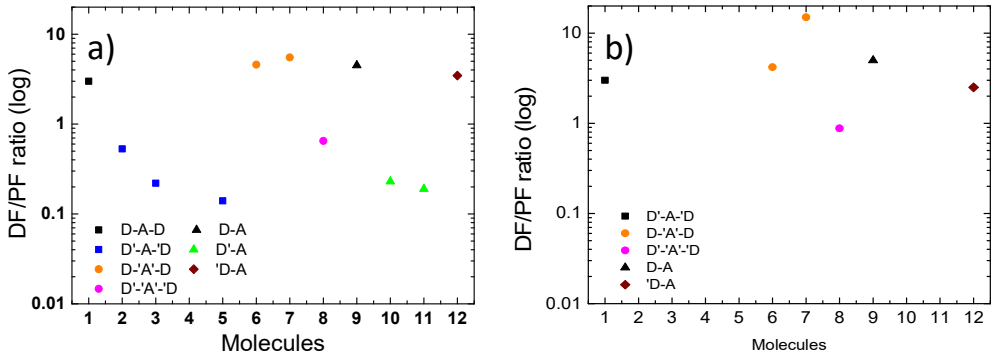

Figure 15 - Ratio of delayed and prompt fluorescence (DF/PF) determined in: a) toluene solution, b) zeonex matrix.

Figure 15a and 15b, show the Φ_{DF}/Φ_{PF} ratio for all molecules in this study, measured in toluene solution (15a) and in zeonex (15b), by comparing degassed and aerated samples in steady-state conditions. As oxygen quenches the triplet states very efficiently, the fluorescence intensity in aerated conditions gives the PF component, but under nitrogen atmosphere or in vacuum the triplet states are able to contribute to the overall emission through delayed fluorescence. Therefore, the emission in degassed conditions contains contributions from both prompt and delayed fluorescence. In zeonex, TADF is only observed for molecules **1**, **6**, **7**, **9** and **12**.

In toluene solution, see Figure 15a, strong TADF is observed in the unsubstituted molecules, **1** and **9**, in molecules **6** and **7**, which are substituted in the acceptor unit, and suffer less hindrance in the DA rotation, and also in molecule **12**, which is substituted in the D unit, but in its external position. In all the other molecules, the TADF contribution is weaker,

particularly in **4**, where the TADF is entirely quenched. This confirms that by restricting the rotation around the DA axis the efficiency of the RISC mechanism is significantly diminished.

Clearly, the efficiency of the TADF mechanism in stronger on compounds where the DA rotation is not restricted and good energy alignment between the ^{1}CT state and the ^{3}D exists, not the ^{3}LE. It is the lowest energy triplet in the system that influences the RISC mechanism. Therefore, the triplet energy determined from the onset of the phosphorescence spectra, without deconvolution in its ^{3}D and ^{3}A components gives the incorrect ST energy gap and no correlation at all with the TADF efficiency.

The DF/PF ratio in molecules **1**, **6**, **7**, **9** and **12** is in the range 3 to 5. For **1** the energy gap between ^{1}CT and the ^{3}D is 110 meV, but a larger gap exists between ^{1}CT and ^{3}LE, due to contribution of ^{3}A to the overall phosphorescence. For **6** and **7**, the ^{1}CT state is isoenergetic with the ^{3}D state and ^{3}LE, as ^{3}A phosphorescence is not observed in these two molecules. Compounds **6** and **7** are the two strongest TADF emitters in the series. Molecules **9** and **12** are also strong TADF emitters, both with a small energy gap between ^{1}CT and ^{3}D, but far apart from the ^{3}LE state (again due to contribution of the ^{3}A phosphorescence).

Worthy of note, in molecules **2**, **8**, **10** and **11**, the singlet-triplet energy splitting between ^{1}CT and ^{3}D is small (Figure13Figure 12a). However, despite this small energy gap, no strong TADF is observed. This is because in these molecules the DA rotation is strongly restricted by the side groups. It can be addressed that the weak TADF in these compounds is caused by the large energy gap between ^{1}CT and ^{3}LE. However, this is clearly not the reason why TADF is weak in these compounds. Molecules **1** and **12** have an even larger gap between ^{1}CT and ^{3}LE and are good TADF emitters. Moreover, in the donor substituted molecules, **2-5**, (blue squares in Figure 15a) the rotation around the D-A axis is strongly restricted, as reported recently.[23] In all these compounds the TADF is very weak. This occurs despite a small energy gap between the ^{1}CT and the ^{3}D states, as in **2**, for example. Therefore, these results give strong evidence that the TADF mechanism requires the presence of vibrational modes to assist triplet harvesting.

These results also explain the observation of the blue-shifted ^{1}CT emission in the substituted compounds, and the more intense ^{1}LE emission that is observed in these molecules. Furthermore, the observation of room-temperature phosphorescence in molecules **2-5** and **11**, when dispersed in zeonex, clearly show that it is the suppression of the RISC rate, and not the effect of enhanced internal conversion that is responsible for the weaker TADF efficiency in these compounds.

The trend on the ^{1}CT energies in zeonex is similar to the one observed in toluene. With no surprise molecules **1**, **6**, **7**, **9** and **12** are strong TADF emitters. In all these molecules the energy gap between ^{1}CT and the ^{3}D is small. Surprisingly, molecule **7** is an excellent TADF emitter, showing a DF/PF ratio in zeonex of 16, despite the gap between ^{1}CT and ^{3}D being larger than in molecules **1**, **9** and **12**. This occurs probably because the substitution with the bulkier *i-propyl* groups in the acceptor force this molecule in the more favourable equatorial form, whereas molecules **1**, **9** and **12** have more mixed conformers.

Finally, molecules where TADF is very weak in zeonex have ^{1}CT energies further apart the ^{3}D state, have restricted DA rotation, and adopt the axial conformer.

6.9 Time Resolved Fluorescence

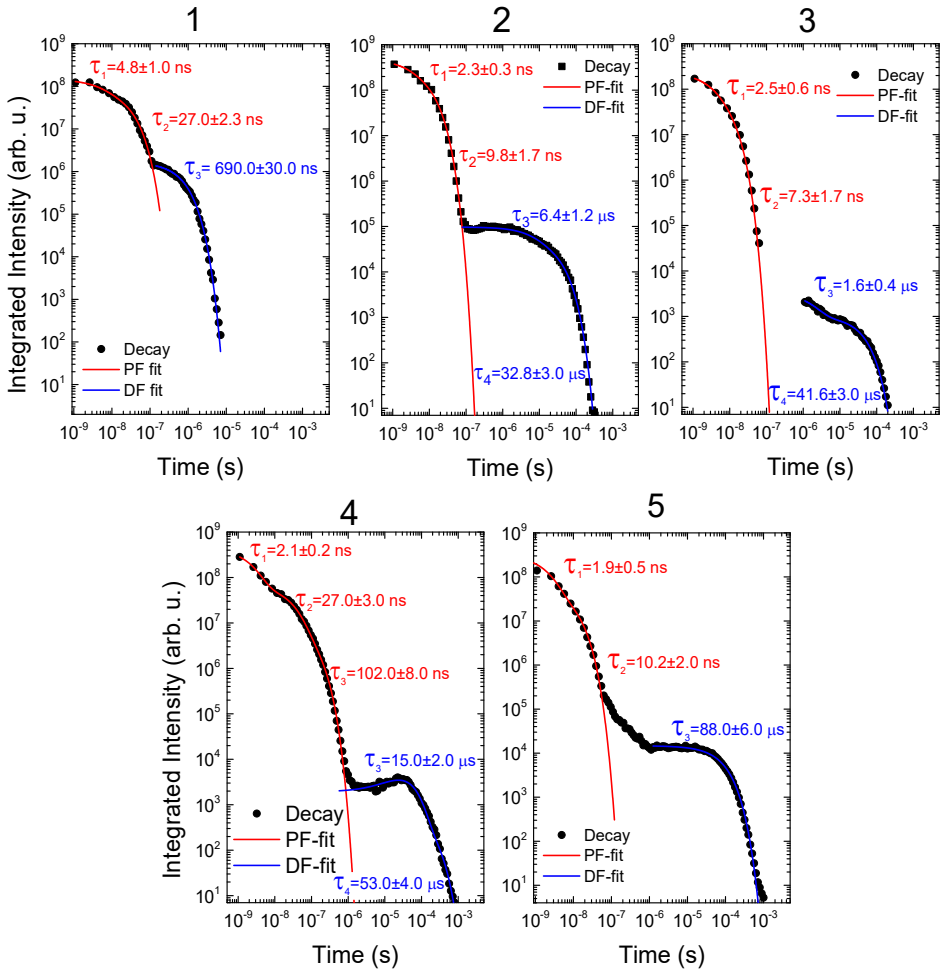

Figure 16 – Time-resolved luminescence decays for molecules **1-5** in toluene at room temperature.

In order to further confirm our observations, time resolved fluorescence decays were collected to evaluate the influence of the substituent groups on the triplet lifetime. Since the TADF emission is the result of triplet harvesting, the lifetime of the triplet state and the lifetime of TADF should be the same.[12] Therefore, molecules where the triplet harvesting is more efficient, those where strong TADF is observed, should have shorter TADF lifetimes. Figure 16-18 shows the time-resolved fluorescence decays for all the molecules in this study, collected in degassed toluene solution at room temperature.

Unsubstituted molecule **1**, in the top row, shows mono-exponential TADF decay with a lifetime of 0.69 µs. However, the substituted counterparts of **1**, molecules **2-5**, show increasingly longer and complex TADF decays, and smaller TADF contribution. Molecules **2-4**, substituted in the donor unit with increasingly bulky groups, show TADF decays that are bi-exponential, with a faster component in the 1µs to 15 µs range, followed by a longer decay component that varies from 32 µs to 53 µs. Note that the long decay component in **4**, is not due to TADF, but to TTA. Molecule **5**, which is substituted in both D and A units with methyl groups, shows even slower decay, with 88µs.

In the middle row, molecules **6** and **7**, which are substituted in the acceptor unit with methyl and *i-propyl* groups, and adopt the equatorial geometry, show remarkably mono-exponential TADF decays, with lifetimes of 4.8 µs, and 14.6 µs. Molecule **8**, which is substituted in the A unit with *i-propyl* groups and with methyl groups in each D unit, shows a TADF lifetime of 77.9 µs (Figure 17).

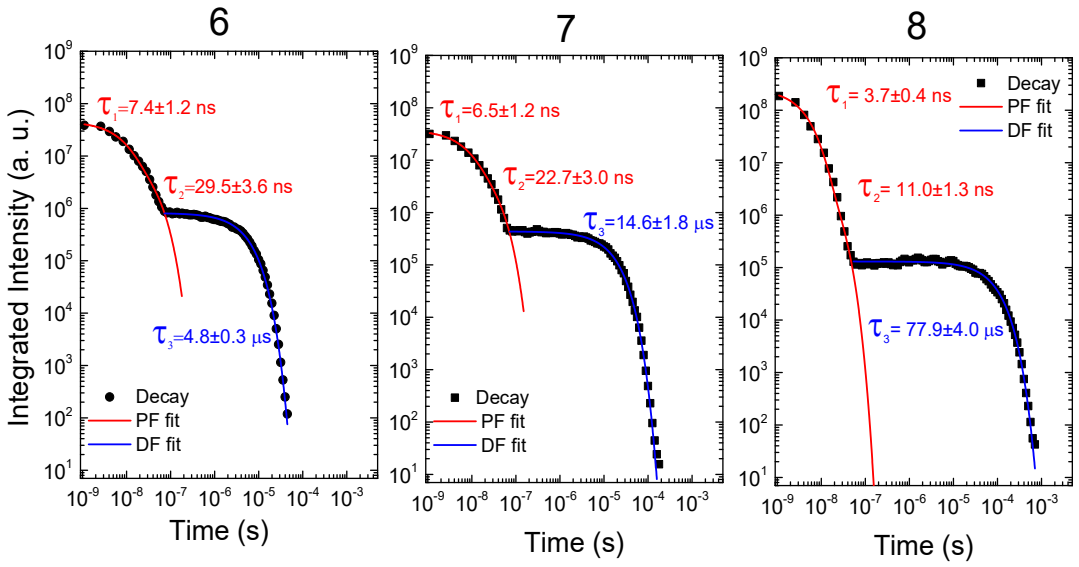

Figure 17 - Time-resolved luminescence decays for molecules **6-8** in toluene at room temperature.

In the lower row of Figure18, molecules **9** to **12**, the asymmetrical D-A molecules are all substituted in the D unit and weaker restrictions to the rotation around the DA axis are expected in this group, when compared with their D-A-D counterparts, as the effect of the side groups on the donor bashing in to each other is not present. However, still some hindrance is present when the D unit is substituted in the internal position. In the unsubstituted molecule **9,** a very strong TADF emitter, with ^{1}CT state practically degenerate with the local triplet ^{3}LE state, and with no restrictions to the DA rotation, the reverse intersystem crossing is strong, therefore, the triplet state should decay quickly. Accordingly, the TADF decay in **9** is mono-exponential with a lifetime of 2.5 µs. This is in clear contrast with molecules **10** and **11**, with TADF lifetimes of 34.8 µs and 25.9 µs, respectively. These molecules are both substituted in the D internal positions and thus the rotation around the DA axis is affected by the steric-effect caused by the substituents. Finally, molecule **12**, which is substituted in the external position of the donor unit, thus with no hindrance effect, shows strong TADF with a mono-exponential decay of just 1.5 µs.

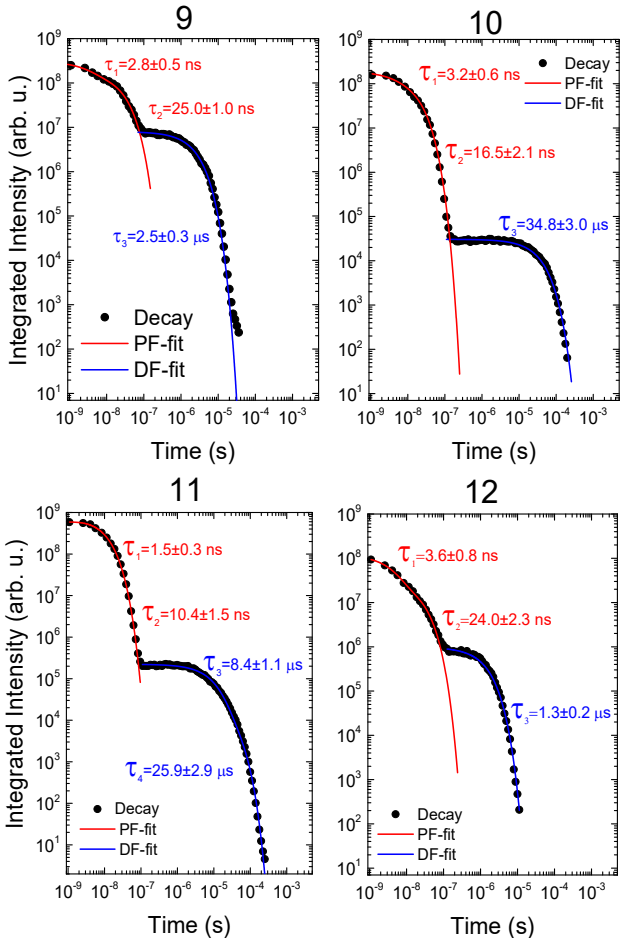

Figure 18 - Time-resolved luminescence decays for molecules **9-12** in toluene at room temperature.

The time resolved fluorescence decays agree with previous data showing once more that the substitution in the phenothiazine D unit strongly affects the efficiency of the RISC mechanism. This effect is observed independently of a good energy alignment between the ^{1}CT singlet state and the local triplet (^{3}LE), confirming the importance of tuning the molecular conformation and keeping active specific vibrational modes to enhance the RISC mechanism.

6.10 Conclusions

In summary, molecular structures with bulky substituents in the D unit, which restrict dynamic rocking around the DA axis and force the adoption of the axial conformer, show low TADF efficiency. In contrast, the molecules **6** and **7**, which are substituted in the acceptor unit, and where the equatorial form is predominant, show strong TADF. The effect is more pronounced in the D-A-D than in the D-A molecules, which shows that the dominant hindrance effect arises from the side groups on the donor sterically hindering each other, rather than acceptor-donor clashes. The experimental evidence indicates that a small energy gap is not sufficient to guarantee strong TADF, and that the mechanism requires the presence of vibrational modes, i.e. the dynamic rocking of the D or A units around the DA axis, and specific molecular conformation to assist triplet harvesting. This scenario fully confirms recent theoretical results, and will guide the design of new TADF emitters.

6.11 Bibliography

1 Reineke, S.; Seidler, N.; Yost, S. R.; Prins, F.; Tisdale, W. A.; Baldo, M. A. *Appl. Phys. Lett.* **2013**, *103* (9), 93302.

2 Kraus, H.; Bange, S.; Frunder, F.; Scherf, U.; Boehme, C.; Lupton, J. M. *Phys. Rev. B* **2017**, *95* (24), 1–5.

3 Köhler, A.; Bässler, H. *Mater. Sci. Eng. R Reports* **2009**, *66* (4–6), 71–109.

4 Burroughes, J. H.; Bradley, D. D. C.; Brown, A. R.; Marks, R. N.; Mackay, K.; Friend, R. H.; Burns, P. L.; Holmes, A. B. *Nature* **1990**, *347* (6293), 539–541.

5 Tang, C. W.; Vanslyke, S. A. *Appl. Phys. Lett.* **1987**, *51* (12), 913–915.

6 Forrest, S. R.; Baldo, M. A.; O'Brien, D. F.; You, Y.; Shoustikov, A.; Sibley, S.; Thompson, M. E. H *Nature* **1998**, *395* (6698), 151–154.

7 Adachi, C.; Baldo, M. A.; Thompson, M. E.; Forrest, S. R. *J. Appl. Phys.* **2001**, *90* (10), 5048–5051.

8 Sivasubramaniam, V.; Brodkorb, F.; Hanning, S.; Peter, H.; Elsbergen, V. Van;

Boerner, H.; Scherf, U.; Kreyenschmidt, M. **2009**, *130*, 640–649.

9 Schmidbauer, S.; Hohenleutner, A.; König, B. *Adv. Mater.* **2013**, *25* (15), 2114–2129.

10 Uoyama, H.; Goushi, K.; Shizu, K.; Nomura, H.; Adachi, C. *Nature* **2012**, *492* (7428), 234–238.

11 Dias, F. B.; Bourdakos, K. N.; Jankus, V.; Moss, K. C.; Kamtekar, K. T.; Bhalla, V.; Santos, J.; Bryce, M. R.; Monkman, A. P. *Adv. Mater.* **2013**, *25* (27), 3707–3714.

12 Dias, F. B.; Penfold, T. J.; Monkman, A. P. *Methods Appl. Fluoresc.* **2017**, *5* (1), 12001.

13 Tao, Y.; Yuan, K.; Chen, T.; Xu, P.; Li, H.; Chen, R.; Zheng, C.; Zhang, L.; Huang, W. *Adv. Mater.* **2014**, *26* (47), 7931–7958.

14 Sandanayaka, A. S. D.; Yoshida, K.; Matsushima, T.; Adachi, C. *J. Phys. Chem. C* **2015**, *119* (14), 7631–7636.

15 Sandanayaka, A. S. D.; Matsushima, T.; Adachi, C. *J. Phys. Chem. C,* **2015**, *119* (42), 23845–23851.

16 Zhang, Q.; Kuwabara, H.; Potscavage, W. J.; Huang, S.; Hatae, Y.; Shibata, T.; Adachi, C. *J. Am. Chem. Soc.* **2014**, *136* (52), 18070–18081.

17 Wong, M. Y.; Zysman-Colman, E. *Adv. Mater.* **2017**, *29* (22).

18 Etherington, M. K.; Franchello, F.; Gibson, J.; Northey, T.; Santos, J.; Ward, J. S.; Higginbotham, H. F.; Data, P.; Kurowska, A.; Dos Santos, P. L.; Graves, D. R.; Batsanov, A. S.; Dias, F. B.; Bryce, M. R.; Penfold, T. J.; Monkman, A. P. *Nat. Commun.* **2017**, *8*, 14987.

19 Dias, Fernando B., Santos J., Graves D., Data P., Nobuyasu R. S., Fox M. A., Batsanov A. S., Palmeira T., Berberan-Santos M. N., Bryce M. N., A. P. Monkman, Adv. Sci. **2016**, 3, 1600080.

20 Northey, T.; Stacey, J.; Penfold, T. J. T*J. Mater. Chem. C* **2017**, *5* (42), 11001–11009.

21 Gibson, J.; Monkman, A. P.; Penfold, T. J. *ChemPhysChem* **2016**, No. 1, 2956–2961.

22 Gibson, J.; Penfold, T. J. *Phys. Chem. Chem. Phys.* **2017**, *19* (12), 8428–8434.

23 Ward, J. S.; Nobuyasu, R. S.; Batsanov, A. S.; Data, P.; Monkman, A. P.; Dias, F. B.; Bryce, M. R. *Chem. Commun.* **2016**, *52*, 3–6.

24 Stockmann, A.; Kurzawa, J.; Fritz, N.; Acar, N.; Schneider, S.; Daub, J.; Engl, R.; Clark, T. *J. Phys. Chem. A* **2002**, *106* (34), 7958–7970.

25 Nobuyasu, R. S.; Ren, Z.; Griffiths, G. C.; Batsanov, A. S.; Data, P.; Yan, S.; Monkman, A. P.; Bryce, M. R.; Dias, F. B. *Adv. Opt. Mater.* **2016**, *4* (4), 597–607.

7. TADF in Copolymers: Towards Solution Processed TADF Devices.

The photophysics of TADF in two PTZ-DBTO2 copolymers, COPO1 and COPO2, is discussed in this chapter. In both copolymers the PTZ-DBTO2 is used as the monomer unit. However in COPO1, PTZ-DBTO2 is used as pendant, whereas in COPO2 it is part of the copolymer backbone, separated by dibenzothiophene (DBT) units, which are used as spacers. Obtaining TADF in large molecules is difficult due to the strong competition between the reverse intersystem crossing and excited state quenching mechanisms that are facilitated in polymers, such as internal conversion and triplet-triplet annihilation. COPO1 and COPO2 are two of the first reported copolymers showing efficient TADF.

This work is published in: Roberto S. Nobuyasu, Zhongjie Ren, Gareth C. Griffiths, Andrei S. Batsanov, Przemyslaw Data, Shouke Yan, Andrew P. Monkman, Martin R. Bryce, and Fernando B. *Dias. Rational Design of TADF Polymers Using a Donor–Acceptor Monomer with Enhanced TADF Efficiency Induced by the Energy Alignment of Charge Transfer and Local Triplet Excited States.* Adv. Optical Mater. **2016**, 4, 597–607.

7.1 Introduction

Despite the great progress that has been made in the field of thermally activated delayed fluorescence emitters, (TADF), in recent years, particularly for emitters in the green spectral region, still major research is necessary to fully understand the TADF mechanism, and to facilitate the design of new molecular structures, showing efficient TADF emission in different regions of the visible spectrum. Nowadays, most TADF OLED devices are fabricated by vacuum deposition. However, solution-processing methods continue being very attractive for OLEDs due to their simplicity and lower cost, when compared to vacuum deposition. The possibilities offered by processing film deposition directly from solution are very attractive, and in particular in the case of polymers can be used to achieve better alignment of the chains in order to increase charge mobility and potentially enhancing device efficiencies due to better light extraction.[1] However, while TADF OLEDs fabricated from solution have been reported recently with a small-molecule emitter dispersed in diphenyldi(4-(9-carbazolyl)phenyl)silane host,[2] to date TADF has been very rarely observed in conjugated oligomers and polymers. Mainly because films of small molecules deposited from solution usually suffer from poor quality. Therefore, the advantages offered by solution processing methods, such as spin-coating, spray-on, and ink-jet printing, which allow rapid deposition over large areas at room temperature, and using large flexible substrates,[1] are still largely unavailable for TADF devices. Further work is thus necessary to investigate ways to promote efficient TADF in large molecules that are more suitable for solution processed devices.

Two factors explain why the observation of TADF is challenging in oligomers and polymers. First, simultaneously achieving small ΔE_{ST} and suppressing internal conversion is very difficult in molecules containing many atoms. Second, intramolecular and intermolecular triplet–triplet annihilation (TTA) is often operative and efficiently quenches the triplet population in polymers and oligomers.[3] Indeed, it is mainly to avoid TTA that small TADF molecules are dispersed in hosts with high triplet energy levels. Unfortunately, host molecules often adversely influence the photoluminescence (PL) and electroluminescence (EL) properties of TADF emitters, causing large variations in the emission yield and lifetime, due to host–guest exciplex formation,[4] and heterogeneities in the host–guest molecular geometries.[5] Host–guest systems are also susceptible to phase separation due to the differences between the molecular structures of the constituent molecules, which may result in unstable luminescence. Therefore, achieving efficient TADF in pristine materials, i.e., without using host–guest systems, is of major interest and has only very recently been reported.[6]

Here, we report the synthesis, photophysics and device fabrication of two copolymers showing efficient TADF emission. During the developments of this research, Albrecht et al.[7] reported TADF in films of a solution-processable, nondoped, dendrimer. However, the dendritic structure is clearly distinct from the polymers described here. More recently, and in parallel with this work, Nikolaenko et al.[8] reported TADF in a linear polymer, but structurally different from our polymers. The EQE reported in Nikolaenko's work is around 10%, but this is only at a current density of 0.01 mA/cm^2 and giving ≃2 cd m^2. At higher current densities, 10 mA/cm^2, the EQE is around 3%.

7.2 Polymer Structure and Electrochemistry

The two copolymers studied in this work are based on the asymmetric D-A unit, PTZ-DBTO2, previously discussed in Chapter 04. PTZ-DBTO2 was functionalized and incorporated into copolymers, COPO1 and COPO2, which show efficient TADF in their pristine films. Figure 1 shows the absorption and steady-state emission spectra of COPO1 and COPO2 in their pristine films. Highlighted in Figure 1a are the electron donor, in blue, and the electron acceptor, in red, used in PTZ-DBTO2. The phenyl group in COPO1 and the dibenzothiophene, (DBT), used in COPO2 are used as spacer groups, highlighted in green, to better confine the excitation in the TADF moiety. Thus suppressing TTA.

The absorption of COPO1 and COPO2 in their pristine films is shown in Figure 1b, and is in excellent agreement with the absorption of the monomer unit. However, both polymers show their absorption slightly red-shifted relative to the absorption of the PTZ-DBTO2 unit. This is

particularly evident in COPO2, which is more conjugated. The emission spectra in both copolymers overlap with each other and also match with the emission of PTZ-DBTO2, both peaking at 565 nm.

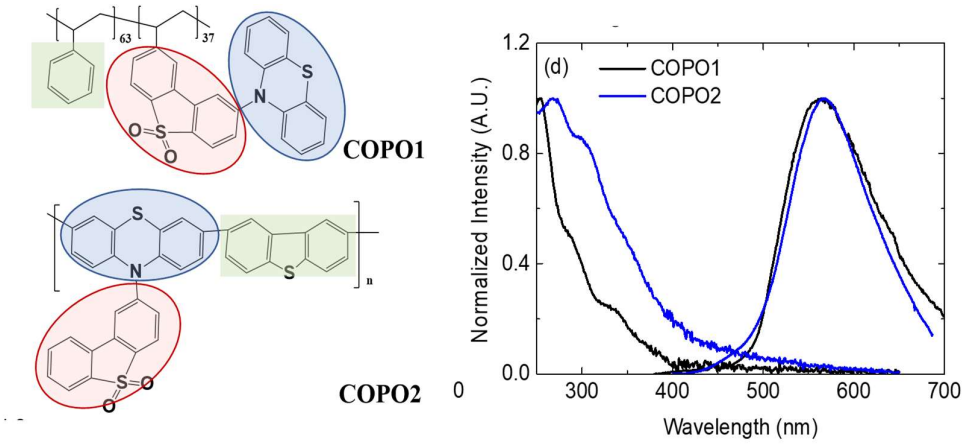

Figure 1 - Chemical structures of copolymers COPO1 and COPO2. Normalized absorption and steady-state emission spectra of COPO1 and COPO2 in their pristine films.[1]

The ionization potential (IP) and electron affinity (EA) were measured using cyclic-voltammetry, giving HOMO and LUMO energy levels for PTZ-DBTO2, at -5.4 eV and -2.95 eV, respectively, and for the two copolymers, COPO1, -5.35 and –2.9 eV, and COPO2, –5.3 and –3.0 eV.

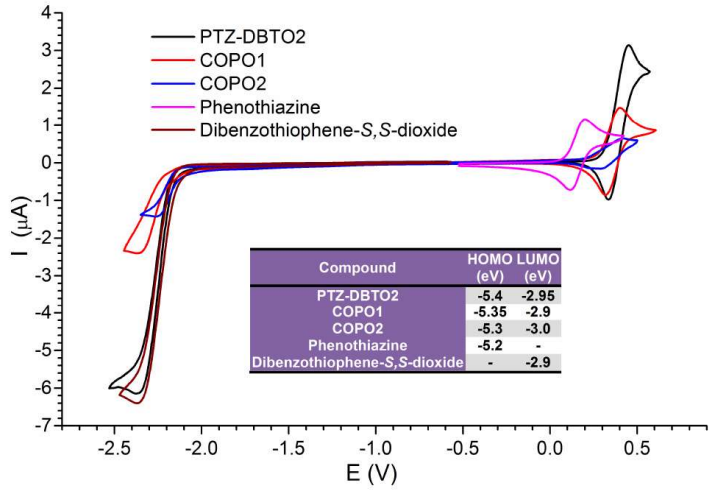

Compound	HOMO (eV)	LUMO (eV)
PTZ-DBTO2	-5.4	-2.95
COPO1	-5.35	-2.9
COPO2	-5.3	-3.0
Phenothiazine	-5.2	-
Dibenzothiophene-*S*,*S*-dioxide	-	-2.9

Figure 2 - CV characteristics of PTZ-DBTO2, COPO1, COPO2 and the individual D and A molecules.

[1] Polymers were synthesized by Martin Bryce's research group.

These electrochemistry data were obtained from the CV data analysis performed by Dr. P. Data. Taking into consideration that the EA and IP directly correspond to the LUMO and HOMO energies respectively, see Figure 2.

The data established that the amphoteric redox behavior of the DA unit, PTZ-DBTO2, is retained in the two copolymers, and in general the copolymers and PTZ-DBTO2 have a very similar oxidation potential, with COPO2 showing slightly lower oxidation onset potential, which is consistent with the increased conjugation length, when compared to COPO1. A larger difference is observed in the reduction part of the CV: COPO1 is slightly more difficult to reduce than both COPO2 and PTZ-DBTO2. This is possibly due to steric effects which make it more difficult during the doping process, as the D-A units are a side group in the COPO1.

7.3 Photophysical properties

The rational design of the two copolymers, COPO1, containing PTZ-DBTO2 as a pendant group, and COPO2 with the donor phenothiazine inserted in the polymer backbone, but separated with dibenzothiophene spacers with larger energy gap, had the objective of confining the excitons in the PTZ-DBTO2 TADF unit, while still taking advantage of the polymer properties. Notably, both polymers show TADF in pristine film, i.e., with no need of using high triplet host materials to confine the triplet states in the TADF emitter. This clearly demonstrates that reverse intersystem crossing is able to compete with TTA and internal conversion processes in tailored polymers, even without using high triplet hosts to disperse the TADF emitter.

The fluorescence quantum yields (PLQY) were measured in pristine thin films using an integrating sphere, giving ϕ_F=17.3±2.5 % for COPO1 and ϕ_F =14.2±2.3 % for COPO2.

The fluorescence decay of COPO1 in pristine thin film is shown in Figure 3a. As for the monomer PTZ-DBTO2, two decay regimes are clearly identified. A fast decay region, which can be fitted with two exponentials of 3.85 ns and 23.5 ns, which are assigned to the prompt fluorescence component (PF). This relatively fast emission decay is followed by a much slower decay, assigned to the delayed fluorescence (DF), which shows also a complex decay characteristic, showing three differentiated time constants, 0.11 μs, 0.9 μs, and 2.1 μs. The DF contribution to the overall emission in COPO1 is calculated as 45%.

The dependence of the delayed emission with excitation dose in COPO1 at room temperature, is shown in Figure 3b. The integrated delayed fluorescence is collected with 1 μs delay time, and integrated over 100 μs, showing a perfect linear dependence with excitation dose (gradient 1). The DF is thus originated from a monomolecular process.[9,10]

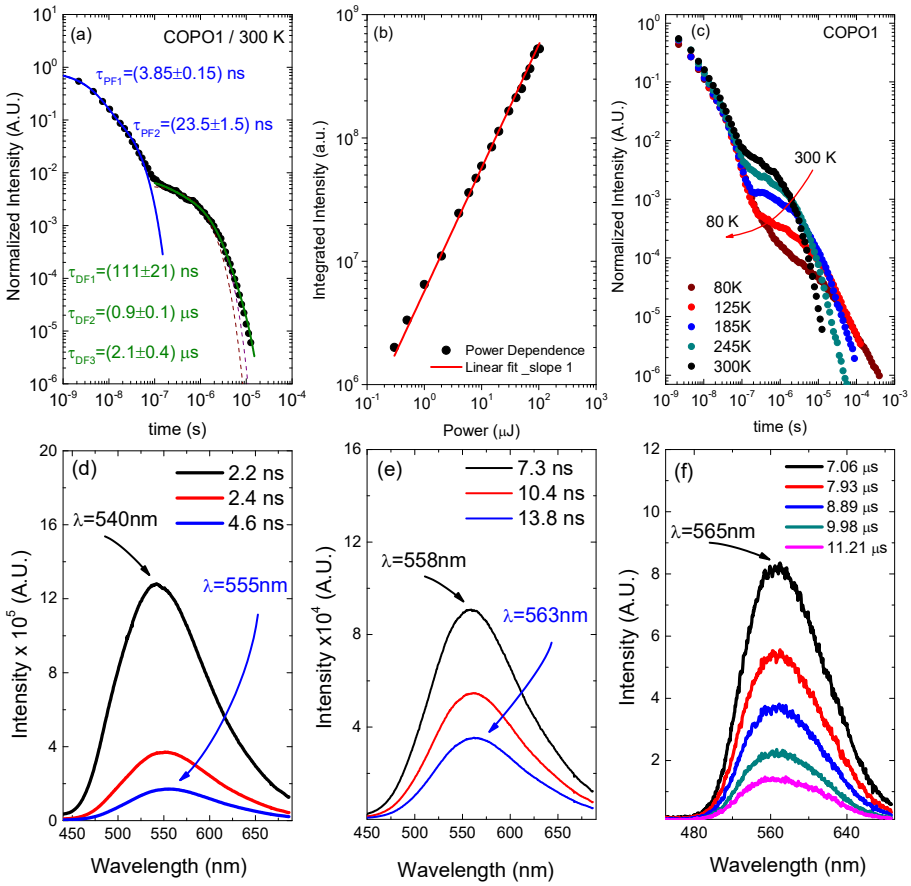

Figure 3 - (a) COPO1 fluorescence decay, collected in pristine thin film at room temperature. Prompt (PF) and delayed (DF) fluorescence components are clearly observed. Single and double exponential fits to the TADF component are shown in dark red. A perfect fit is only obtained with three exponentials. (b) TADF linear dependence with excitation power. (c) Temperature dependence of COPO1 fluorescence decays. (d-f) Time resolved fluorescence spectra of COPO1 pristine films at room temperature.

The temperature dependence of the COPO1 fluorescence decay is shown in Figure 3c. The PF component shows no variation with temperature, suggesting negligible internal conversion (IC), as in the case of PTZ-DBTO2. However, the DF component clearly decreases with temperature. The threshold delay time at which TADF significantly deviates from the PF decay also increases with decreasing temperature, and we also see the TADF lifetime increasing with decreasing temperature; both observations are consistent with a longer triplet lifetime due to a slower reverse intersystem crossing rate at lower temperatures. The DF in COPO1 is thus assigned to a TADF mechanism.

The excited state dynamics observed in PTZ-DBTO2 at early times is much less pronounced in COPO1 films. In this copolymer only a small redshift is observed at very early times in the

emission band, but no other spectral relaxation is observed after 15 ns, i.e., no deviation from the normal charge transfer (^{1}CT) emission, other than its intensity decay is observed in the time resolved spectra. However, the ^{1}CT emission observed at later times shows pronounced spectral narrowing, with the emission onset shifting from 475 nm at shorter times to 502 nm in the μs time range, see Figure 3d–f. The ^{1}CT energy is thus determined from the time resolved spectra obtained in the μs time domain, where pure ^{1}CT emission is observed. In COPO1 the relaxed ^{1}CT is thus determined at 2.47 eV.

The excited state dynamics observed in PTZ-DBTO2 at shorter times is much less pronounced in COPO1 films. In this copolymer only a small red-shift is observed at very early times in the emission band, but no other spectral relaxation is observed after 15 ns, i.e., no deviation from the normal charge transfer (^{1}CT) emission, other than its intensity decay is observed in the time resolved spectra. However, the ^{1}CT emission observed at later times shows pronounced spectral narrowing, with the emission onset shifting from 475 nm at shorter times to 502 nm in the μs time range, see Figure 3d–f. The ^{1}CT energy is thus determined from the time resolved spectra obtained in the μs time domain, where pure ^{1}CT emission is observed. In COPO1 the relaxed ^{1}CT is thus determined to be 2.47 eV.

With decreasing temperature the fluorescence decays in the TADF region of COPO1 become increasingly more complex and the three exponential fit observed at room temperature is inadequate to fit the entire decay (Figure 3c). This is probably due to the wide distribution of D-A bonding angles and random distribution of monomer units in the copolymer, which directly affect conjugation. There are also a number of other reasons that can cause the decay to become more complex at low temperatures, including an increasing contribution from long-lived ^{3}LE phosphorescence, increasing TTA, and film heterogeneity.

The excited state dynamics in COPO2 is even more pronounced than in COPO1, see Figure 4. At early times, the fluorescence emission of COPO2 peaks at 535 nm, but rapidly shifts to lower energies, peaking at 555 nm at 8.4 ns, 565 nm at 11.5 ns, and 575 nm from 100 ns to 2.8 μs. It then shifts back to shorter wavelengths, peaking at 557 nm at 31 μs. This behavior is due to a stronger energetic relaxation in the ^{1}CT emission and probably due to underlying phosphorescence, which becomes increasingly important when the DF becomes weaker.

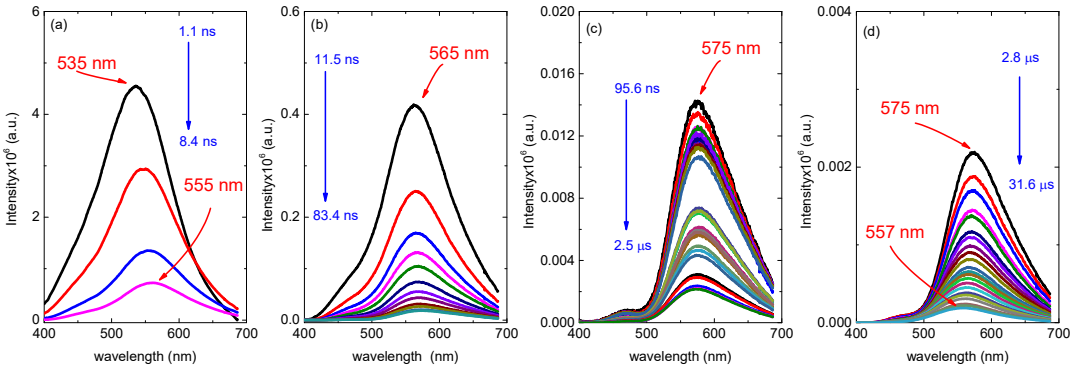

Figure 4 - Time resolved spectra of COPO2 pristine films at room temperature.

The energy of the ^{1}CT state was determined in COPO2 to be 2.43 eV, using the time resolved spectra around 2 µs, in order to avoid the influence of spectral relaxation and underlying phosphorescence. Consistent with more pronounced spectral dynamics in COPO2, the fluorescence decay obtained at room temperature showed very complex behavior (Figure 5) and even a three-exponential fit is not appropriate to fit the decays in the DF region.

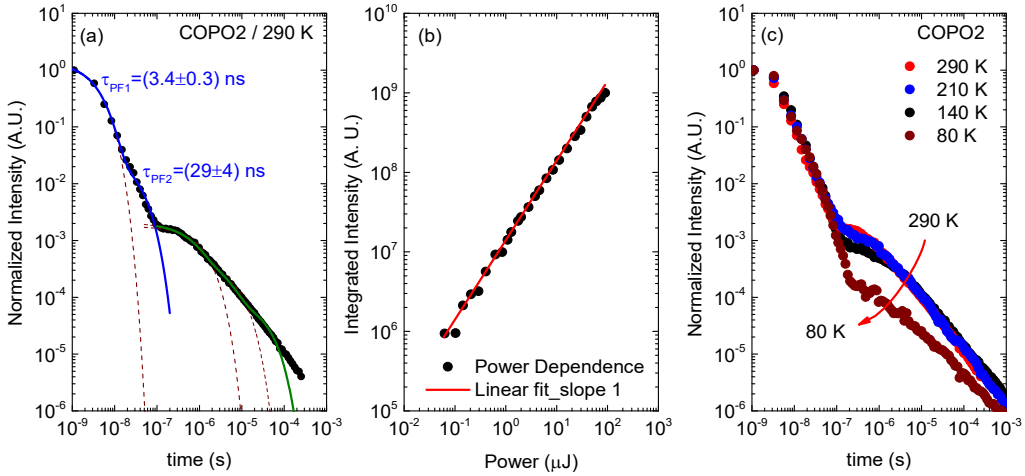

Figure 5 – (a) COPO2 fluorescence decay, collected in pristine thin film at room temperature. Prompt (PF) and delayed (DF) fluorescence components are clearly observed. A perfect fit for the PF component is obtained with two exponentials. Exponential fits with one (PF), and two (DF) exponentials are also shown in dark red. (b) DF linear dependence with excitation power. (c) Temperature dependence of COPO2 fluorescence decays.

However, the PF still decays with a biexponential profile with time constants similar to those observed in COPO1, 3.4 ns and 29 ns. In the DF region, the decay appears more complex, showing a long lived component that extends into the ms time range, and cannot be entirely fitted even by a sum of three exponential functions.

As for COPO1, the integrated delayed fluorescence in the COPO2 pristine film, collected with 1 μs delay time and integrated over 100 μs, shows a perfect linear dependence with excitation power (gradient 1 in figure 5b). This clearly identifies the origin of DF in COPO2 to a monomolecular process.

The fluorescence decay in COPO2 films, obtained as a function of temperature is shown in Figure 5c . As in previous cases, the PF component shows no variation with temperature, while the DF component decreases as expected at low temperatures, showing that the DF in COPO2 is also due to TADF.

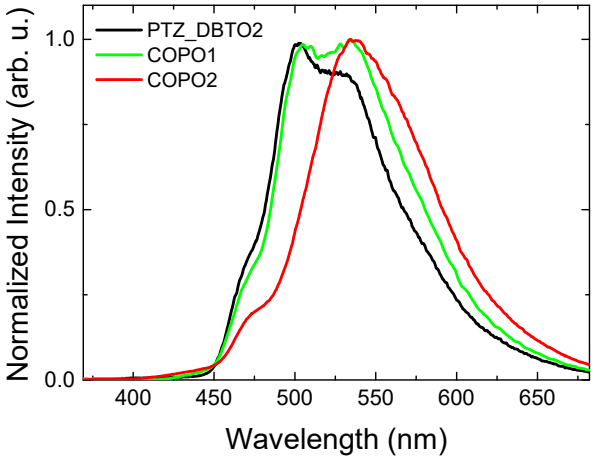

Figure 6 – Phosphorescence spectra of PTZ-DBTO2 (black), COPO1 (green) and COPO2 (red) in Zeonex matrix at 77 K

The phosphorescence spectra of PTZ-DBTO2 in Zeonex, COPO1, and COPO2 obtained at 80 K are compared in Figure 6. Both COPO1 and COPO2 show clear phosphorescence from a local triplet excited state, ^{3}LE, as it occurs in PTZ-DBTO2. However, while for COPO1 the phosphorescence is very similar to that observed in PTZ-DBTO2, in COPO2 the phosphorescence appears poorly resolved. This is probably due to the conjugation effect between the donor and the spacer. However, the contribution of the ^{3}LE phosphorescence is still observed as a shoulder at 474 nm. This is not surprising since in COPO1 the emitter is used as a pendant group, while in COPO2 is part of the main chain, and so is more affected by conjugation.

The time evolution of the phosphorescence spectra in COPO1 and COPO2 are shown in Figures 7a and 7b, respectively, in the form of area normalized spectra in the ms range. In both cases the emission at longer times shows a more pronounced band between 450 and 500 nm, which is assigned to ^{3}LE phosphorescence. In COPO1 the effect is more easily identified, as the spectra at 39 ms perfectly matches the ^{3}LE phosphorescence. In COPO2 the

phosphorescence is blurred by a strong overlap with the CT delayed fluorescence. Moreover, in COPO2, an isoemissive point is observed in the time-resolved, area-normalized, emission spectra, showing that there are two species still emitting in the system. Clearly, the ^{3}LE phosphorescence and the ^{1}CT delayed fluorescence. This indicates that at low temperature the triplet states in COPO2 are still able to be up-converted to the singlet manifold. Whereas in COPO1 reverse intersystem crossing is no more active at low temperatures. Most probably, the fact that in COPO2 the TADF unit is part of the polymer backbone facilitates triplet harvesting at low temperature. However, this might occur by a TTA process, instead of TADF. The strong overlap and similar lifetimes of the ^{3}LE and ^{1}CT luminescence, makes the two mechanisms impossible to be distinguished.

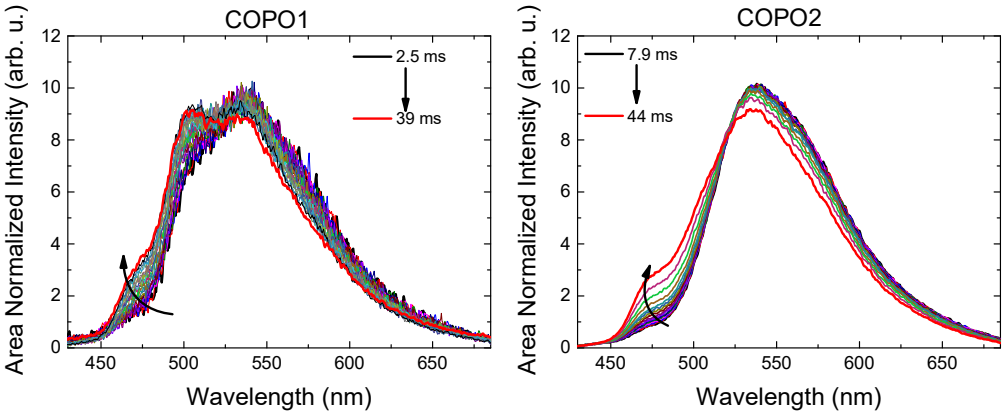

Figure 7 - Area normalized time resolved spectra of pristine thin film: COPO1 and COPO2, at 80 K

7.4 OLED fabrication and characterization

OLED devices were fabricated using ITO (Indium-Tin Oxide) coated glass substrates purchased from Ossila, with a sheet resistance of 20 $\Omega.cm^{-2}$ and an ITO thickness of 100 nm. The diodes had a pixel size of 2 mm by 1.5 mm. Active layers were prepared from DCM solutions with COPO at 10 $mg.mL^{-1}$ blended with 4,4′-bis(N-carbazolyl)-1,1′-biphenyl (CBP), with the ratio 10%COPO:90%CBP (w/w). The active polymer layers were produced by spin-coating deposition at 1500 rpm. The small molecule and cathode layers were thermally evaporated using the Kurt J. Lesker Spectros II deposition apparatus at 10^{-6} mbar. All organic materials and aluminum were deposited at a rate of 1 Å s^{-1} and between 0.1 and 2 $A.s^{-1}$ for coevaporated layers. The LiF layer was deposited at 0.2 Å s^{-1}. The device structure was ITO/PEDOT:PSS (40 nm)/10% COPO1 in CBP (25 nm)/TPBi (50 nm)/LiF(1 nm)/Al (100 nm)

as DEV1 and ITO/PEDOT:PSS (40 nm)/10% COPO2, 40% PBD in PVK(25 nm)/TPBi (50 nm)/LiF(1 nm)/Al (100 nm) as DEV2. Prototype device performances are shown in Figure 8.

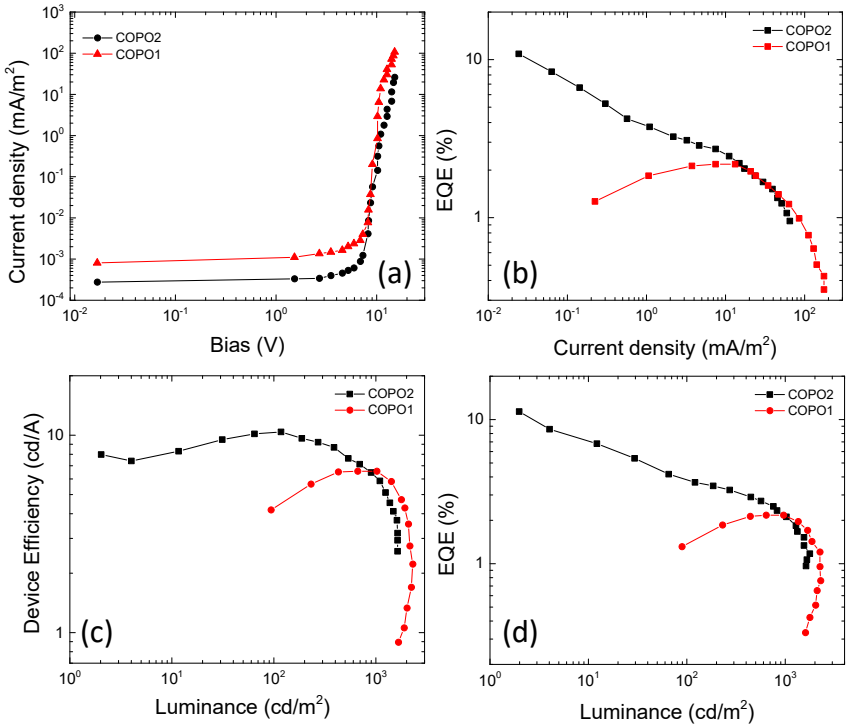

Figure 8 - Characteristics of working OLED devices with: COPO1 (red) COPO2 (black). a) current density versus bias, b) EQE versus current density, c) device efficiency versus luminance, and d) EQE versus luminance.

The polymer-based devices were less stable than the PTZ-DBTO2 TADF device, showing larger efficiency roll-off at higher brightness. The highest efficiency was obtained for COPO1 (DEV1) derivative 2.3% at 7 V. The COPO2 based device (DEV2) demonstrated 11.05% at 5.5 V. Reference values measured at 100 and at 1000 cd/m^2 are displayed in Table 1. Further device optimization is necessary to decrease the turning on voltage, and suppress the efficiency roll-off, as well as achieving better device efficiency.

Table 1 – Device prototypes characteristics

Device	Luminance (cd.m^{-2})	Voltage (V)	EQE (%)	Luminous Power Efficiency (lm.W^{-1})	Current Efficiency (cd.A^{-1})
COPO1	100	5.5	1.4 ± 0.29	1.9	4.5
COPO1	1000	7.5	2.1 ± 0.26	2.9	6.3
COPO2	100	7.8	3,5 ± 0.22	3.9	10
COPO2	1000	11.5	2.1 ± 0.24	1.5	5.7

7.5 Conclusions

Two copolymers showing efficient TADF were synthesized and characterized. It was shown that the reverse intersystem crossing mechanism is able to compete with internal conversion and triplet-triplet annihilation, even in large molecules such as COPO1 and COP2. This work gives clear guidelines for the design of TADF polymers and opens the door for the TADF mechanism in solution-processed OLEDs. Despite the prototype solution processed devices based on COPO1 and COPO2 showing lower efficiency than the vacuum deposited PTZ-DBTO2 device, this work shows that optimized polymer structures, and better device fabrication methods will be able to improve device performances. We believe that there is now new potential for exploring TADF in solution-processed polymer LEDs, using less costly and more flexible deposition methods, such as spin-coating and inkjet printing, for large area deposition.

7.6 Bibliography

1 Forrest, S. R. *Nature*. **2004**, 911–918.

2 Cho, Y. J.; Yook, K. S.; Lee, J. Y. *Adv. Mater.* **2014**, 6642–6646.

3 Rothe, C.; Monkman, A. *J. Chem. Phys.* **2005**, *123* (24).

4 Jankus, V.; Data, P.; Graves, D.; McGuinness, C.; Santos, J.; Bryce, M. R.; Dias, F. B.; Monkman, A. P. *Adv. Funct. Mater.* **2014**, *24* (39), 6178–6186.

5 Méhes, G.; Goushi, K.; Potscavage, W. J.; Adachi, C. *Org. Electron. physics, Mater. Appl.* **2014**, *15* (9), 2027–2037.

6 Zhang, Q.; Tsang, D.; Kuwabara, H.; Hatae, Y.; Li, B.; Takahashi, T.; Lee, S. Y.; Yasuda, T.; Adachi, C. *Adv. Mater.* **2015**, *27* (12), 2096–2100.

7 Albrecht, K.; Matsuoka, K.; Fujita, K.; Yamamoto, K. *Angew. Chemie - Int. Ed.* **2015**, *54* (19), 5677–5682.

8 Nikolaenko, A. E.; Cass, M.; Bourcet, F.; Mohamad, D.; Roberts, M. *Adv. Mater.* **2015**, *27* (44), 7236–7240.

9 Dias, F. B.; Bourdakos, K. N.; Jankus, V.; Moss, K. C.; Kamtekar, K. T.; Bhalla, V.; Santos, J.; Bryce, M. R.; Monkman, A. P. *Adv. Mater.* **2013**, *25* (27), 3707–3714.

10 Dias, F. B. *Philos. Trans. R. Soc. A Math. Phys. Eng. Sci.* **2015**, *373* (2044), 20140447–20140447.

8. TADF in Copolymers: Spacer effect

In t*his study is reported a series of TADF copolymers, using the TADF monomer PTZ-DBTO2 as a pendant unit, separated by* styrene spacer *groups, with varying ratios between spacer and the TADF chromophore to evaluate the effect of the polymer architecture on the efficiency of the TADF mechanism. The copolymer's photophysics is characterized and prototype solution-processed devices fabricated.*

The work in this chapter is published in: Zhongjie Ren, Roberto S. Nobuyasu, Fernando B. Dias, Andrew P. Monkman, Shouke Yan, Martin R. Bryce. Pendant homopolymer and copolymers as solution-processable thermally activated delayed fluorescence materials for organic light-emitting diodes. Macromolecules ***2016****, 49, 5452−5460.*

8.1 Introduction

Organic light-emitting diodes (OLEDs) have been in continuous development since the early 1960s.[1,2,3] To improve the external quantum efficiency (EQE) of OLEDs, extensive studies have focused on synthesizing new emissive materials.[4–7] One of the most important challenges in this field stems from the fact that fluorescent materials harvest emission only from singlet excitons and thus have the limitation of reaching a maximum internal quantum efficiency (IQE) of 25%, whereas statistically 75% triplet excitons are wasted.[8] Harvesting triplet excitons is therefore crucial to achieve OLED devices with 100% IQE.

In contrast to pure fluorescent emitters, phosphorescent materials produce light by utilizing both triplet and singlet excitons resulting in almost 100% IQE.[9–11] However, phosphorescent materials incorporate expensive and scarce metals such as iridium or platinum and display significant degradation in the blue spectral region.[12,13]

Metal free, thermally activated delayed fluorescence (TADF) materials are considered to be the third-generation emitters for OLEDs.[14–18] The basic requirement for efficient TADF is that the highest occupied and lowest unoccupied molecular orbital, HOMO and LUMO, respectively, are spatially separated to achieve a small energy gap between the lowest lying singlet and triplet states. In this way, both triplet and singlet excitons are utilized via thermal up conversion of the lowest excited triplet state (T_1) to the singlet state (S_1), together with fluorescence emission from the S_1 state, leading to a potential IQE of up to 100%.

Small molecules have been extensively investigated in this context, and for some very high efficiency TADF OLEDs have been reported. For example, 10,10-(sulfonylbis(4,1-phenylene))bis(9,9-dimethyl-9,10-dihydroacridine) (DMACDPS) emits in the blue region with 19.5% EQE.[19] A maximum EQE of 28.6% was obtained in the green region by Lee's group.[20]

However, complicated vacuum deposition techniques and precise processing controls are required for many small molecule based devices to ensure high reproducibility.

Solution processing techniques, such as spin-coating or inkjet printing, offer the advantages of lower cost, simpler process, and large area device fabrication.[21,22] Solution processing has been applied successfully to a few small-molecule TADF OLEDs based on 2,4,5,6-tetra(3,6-di-tert-butylcarbazol-9-yl)-1,3-dicyanobenzene (t4CzIPN) and close analogues.[23,24] However, polymer TADF emitters are particularly suitable for solution processing technologies. The design and synthesis of TADF oligomers and polymers is challenging, and there are no clear guidelines for their optimal molecular structures. First, simultaneously achieving a small energy splitting between the singlet and triplet states (ΔE_{ST}) and suppressing internal conversion is very difficult in molecules containing numerous atoms. Second, the triplet population in polymers is easily quenched by intramolecular and intermolecular triplet−triplet annihilation.[25] Nonetheless, significant progress has been made recently, and the following examples place the present work in context. Albrecht et al.[26] reported TADF in films of solution processable, nondoped carbazole-based dendrimers with a triazine core: OLED devices with a G3 dendrimer (21 carbazole units) as the active emitting layer gave green electroluminescence with EQE_{max} of 3.4% and a maximum luminance of >1000 cd m^{-2}. Nikolaenko et al.[27] reported a linear TADF polymer obtained by a block polymerization approach of three monomers with triazene−amine−triazene emitter units of various lengths spaced with nonconjugate segments. No information was given on the molecular weight or polydispersity of the material. The polymer showed EQE_{max} of 10% at very low current densities and green emission with EQE > 4.5% at 100 cd m^{-2}. Yang et al.[28] synthesized copolymers from three monomer components, with a backbone of polycarbazole and 10-(4-(5-phenyl-1,3,4-oxadiazol-2-yl)-phenyl)-10h-phenoxazine as pendant TADF units. The most efficient copolymer in the series had a low molecular weight of 3280 with polydispersity index (PDI) 1.77; EQE_{max} of 4.3% and EQE 2.4% at 100 cd m^{-2} and maximum power efficiency 11.2 $lm.W^{-1}$ were obtained for bluish-green emission. Very recently, Lee et al.[29] reported two polymers with a backbone consisting of alternating electron donating units (carbazole in pCzBP or acridine in pAcBP) and accepting benzophenone (BP) units.

The molecular weights were in the range $(8.7–9.2) \times 10^4$ (PDI 1.2−1.5). A green pCzBP OLED had EQE_{max} of 8.1 ± 0.7%, maximum current efficiency of 24.9 ± 1.7 cd A^{-1}, and maximum power efficiency of 9.0 ± 0.7 $lm.W^{-1}$ at low luminance. A yellow pAcBP device had higher performance with EQE_{max} of 9.3 ± 0.9% and 8% at 1000 cd m^{-2}, maximum current efficiency

of 31.8 ± 1.1 cd.A^{-1}, and maximum power efficiency of 20.3 ± 1.8 lm.W^{-1}. Zhu et al. reported a TADF polymer with donor (carbazole) and acceptor (9,10-dihydroacridine) as backbone and pendant units, respectively.

In the present work, it is reported in detail the properties and OLED performance of three copolymers: pCopo1, pCopo2, and pCopo3. The copolymers comprise different ratios of PTZ-DBTO2 and styrene units and were designed to study the effect of PTZ-DBTO2 content on the TADF properties. Styrene was chosen as a cheap and readily available monomer to provide spacer units between the pendant TADF groups in the copolymers, thereby reducing the intramolecular and inter-molecular triplet−triplet annihilation of adjacent TADF units.

The PTZ-DBTO2 homopolymer (Homopo) is also studied for comparison. Steady-state and time-resolved fluorescence spectroscopic data confirm the TADF properties of the polymers. The OLED device data demonstrate that the copolymers give dramatically better performance than the homopolymer, establishing the benefit of minimizing interactions of the TADF units. Green-emitting devices of pCopo1 achieve EQE_{max} as high as 20.1%, with EQE 5.3% at 100 cdm^{-2}.

8.2 Polymer structure and Electrochemistry

In order to explorer the spacer's effect in the pendant copolymer a series of polymers were synthesized with varying spacer/monomer ratio, see Figure 1, and based on our previous COPO1 polymer. As previously mentioned, the presence of the spacer aims to "linearly" confine the TADF unit, to favor reverse intersystem crossing and minimizing triplet-triplet annihilation. Figure 1 shows the molecular structure of polymers pCopo1−3 and the homopolymer. All polymers were prepared by the radical polymerization of styrene and 2-(10H-phenothiazin-10-yl)-8-vinyldibenzothiophene-S,S-dioxide[31] with molar feed ratios of 80:20, 70:30, 50:50, and 0:100, respectively. The ratios of the styrene and TADF units in the copolymers were estimated from elemental analysis data to be 63:37, 54:46, and 33:67 for pCopo1−3, respectively, indicating the higher reactivity of the TADF monomer compared to the styrene group in the copolymerization reaction.

The four polymers are all readily soluble in common organic solvents, such as dichloromethane, THF, and chlorobenzene. They are therefore suitable for thin film formation using spin-coating, dipping, and casting techniques.

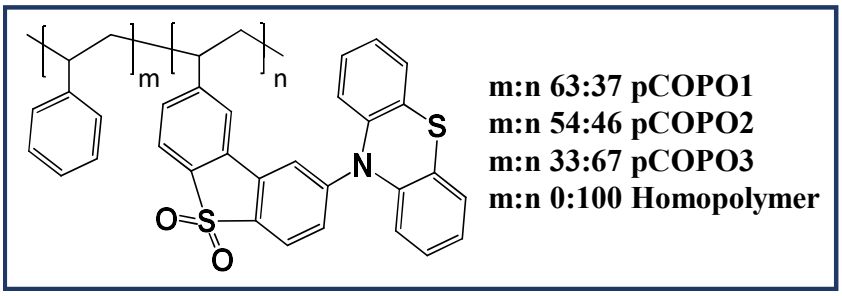

Figure 1 – Molecular structure of the pendant copolymers studied in this chapter. Styrene$_m$-PTZ-DBTO2$_n$ with different ratios.[1]

The thermal properties of the polymers were investigated by differential scanning calorimetry (DSC) and thermogravimetric analysis (TGA) performed by our collaborator Shouke Yan's group. A distinct glass transition temperature (T_g) is observed for each polymer with values ranging from 217 °C for pCOPO1, 229 °C for pCOPO2, 252 °C for pCOPO3 and 269 °C for the homopolymer. In addition, there are no observed exothermic peaks resulting from crystallization during the scan ranges for all the polymers, indicating an excellent amorphous glass state stability.[32] Molecular weight, polydispersity (PDI) and HOMO/LUMO energy levels for all four polymers were performed in the Shouke Yan's group, and are shown in table 1.

The electrochemical behavior of the four polymers was investigated by cyclic voltammetry (CV) in degassed anhydrous acetonitrile solution. The data show quasi-reversible oxidation and reduction processes for all polymers (Table1) corresponding to electrochemical doping and "dedoping" during the potential sweeps. pCopo1 has very similar oxidation and reduction potentials to unsubstituted phenothiazine donor and dibenzothiophene-S,S-dioxide acceptor units, respectively.[30] All the polymers display similar oxidation and reduction behaviour as the process is centered on the PTZ-DBTO2 TADF units.[31] A slight increase in oxidation potential is observed when the content of styrene decreases; i.e., the homopolymer is harder to oxidize than the copolymers, which may be attributed to the relatively higher conjugation of present in the homopolymer.[32] This is also consistent with the absorption spectra. The homopolymer is also more difficult to reduce than the copolymers. Possibly due to the enhanced steric congestion that could make it more difficult to flatten the structure of the polymer chains during the electron transfer process. The HOMO and LUMO energy levels of all the polymers were calculated according to the internal reference ferrocene redox couple in acetonitrile by using equations (1) and (2), and are given in table 1:[33,34]

[1] Synthesized by Shouke Yan's research group.

$$E_{HOMO} = -(E_{(onset,ox\ vs\ Fc+/Fc)} + 5.1) \quad (1)$$

$$E_{LUMO} = -(E_{(onset,red\ vs\ Fc+/Fc)} + 5.1) \quad (2)$$

Two clear trends are observed as the content of styrene units is reduced (i) the HOMO level decreases and the LUMO level increases; (ii) the electrochemical band gap increases incrementally, from 2.21 eV for pCopo1 to 2.39 eV for the homopolymer.

Table 1 - Characterization Data for the Polymers

Polymers	Mw/PDI	HOMO (eV)	LUMO (eV)	Eg (eV)	DF/PF ratio (%)
pCOPO1	11500/1.6	-5.31	-3.1	2.21	44.4
pCOPO2	12700/1.7	-5.33	3.06	2.27	35.6
pCOPO3	15600/1.9	-5.42	-3.06	2.36	34.5
Homopolymer	41000/2.5	-5.43	-3.05	2.39	33.2

8.3 Absorption and Photoluminescence properties

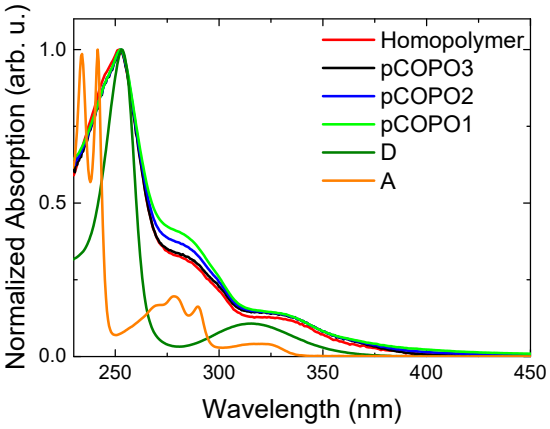

Figure 2 - Normalized absorption spectra of the homopolymer, pCOPO1-3, and the donor and acceptor individual units all in DCM solution.

The UV−vis absorption spectrum of the homopolymer (Figure 2) shows the main characteristic peaks located at ca. 285 and 330 nm, consistent with the absorption spectrum of the PTZ-DBTO2 TADF units.[31] The normalized absorption profiles for the homopolymer and pCopo1−3 are similar, with a slightly higher absorption of the acceptor unit in pCopo1 and pCopo2.

The fluorescence spectra appear broad and featureless with emission bands with λ_{max} at 572, 577, 584 and 591 nm for pCopo1, pCopo2, pCopo3 and the homopolymer, respectively. An obvious and incremental red-shift can be observed when the content of styrene decreases. In addition, the peak widths at half height of all the emissions decreased from ca. 140 nm in the homopolymer to 130 nm in pCopo1, suggesting the addition of styrene can reduce aggregation and improve the colour purity (Figure 3).

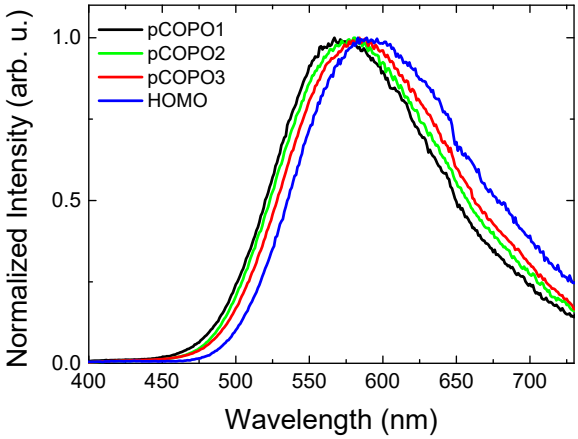

Figure 3 – Steady-state photoluminescence at room temperature in pristine thin films: pCOPO1 (black), pCOPO2 (green), pCOPO3 (red) and the homopolymer (blue)

8.4 Photophysical properties

The emissions of all polymers dispersed in zeonex matrix show higher intensity in vacuum than in oxygen. The overall luminescence of the PTZ-DBTO2 units in the polymers has a strong contribution from the triplet state (TADF). Oxygen is a well-known triplet quencher, which explains why the emission increases in vacuum. Moreover, the calculated emission ratio ($I_{Vac}/I_{O2} = (I_{PF} + I_{DF})/I_{PF} = I_{DF}/I_{PF} + 1$) decreases with a reduction in the content of styrene units, where PF and DF are prompt and delayed fluorescence, respectively. For example, the I_{DF}/I_{PF} ratio decreases from 0.35 in pCopo1 to 0.17 in the homopolymer as shown in Figure 4, which may be assigned to the styrene units dispersing the TADF units and thus preventing triplet−triplet annihilation.

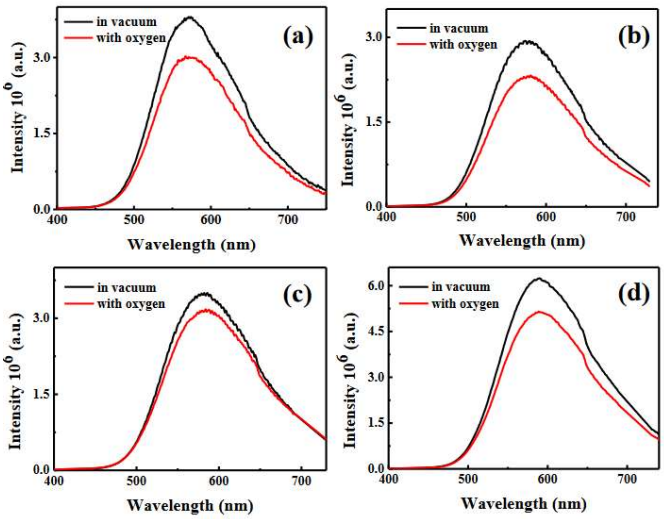

Figure 4 - Emissions of polymer film with zeonex matrix in oxygen and in vacuum . (a) pCopo1, (b) pCopo2, (c) pCopo3, (d) Homopolymer.

PLQY measurements were performed using the Hamamatsu, Quantaurus-QY Absolute PL quantum yield spectrometer (model C11347-11), as a function of the excitation wavelength, presented in Figure 5.

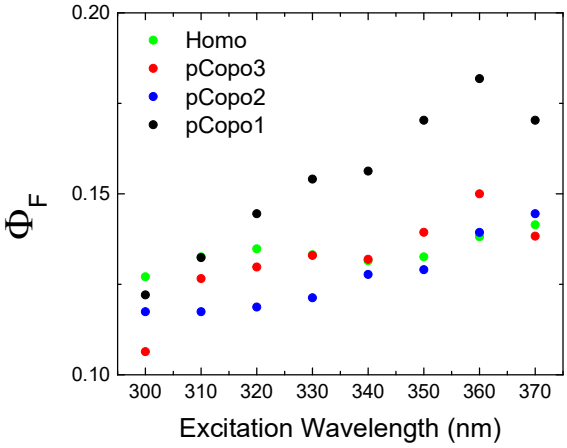

Figure 5 – Photoluminescence quantum yield of pristine thin films as a function of the excitation wavelength for the homopolymer (green), pCopo3 (red), pCopo2 (blue) and pCopo1 (black).

Remarkably the PL efficiency increases with excitation wavelength. This effect has been observed in a prototype TADF molecule and attributed to a direct excitation of the charge transfer band.[5]

8.5 Time resolved measurements

The fluorescence decays obtained in film of pCopo1–3 and the homopolymer at room temperature were monitored over a time interval of 6 decades (Figure 6). Both PF and DF components are clearly observed for all the polymers. However, PF and DF show complex decay dynamics, and the decays cannot be fitted properly by sums of exponentials. This is probably due to dispersion on the TADF barrier.

Figure 6 presents the typical temperature dependence of the fluorescence decay for all copolymers in this series. PF component shows negligible variation with temperature, as expected once the nonradiative components are not so effective in this system. However, the threshold delay time at which TADF significantly deviates from the PF decay increases with reducing temperature. Moreover, the lifetime of delayed fluorescence for all copolymers increases with decreasing temperature. These observations are consistent with a longer triplet lifetime at lower temperatures due to a slower reverse intersystem crossing rate.

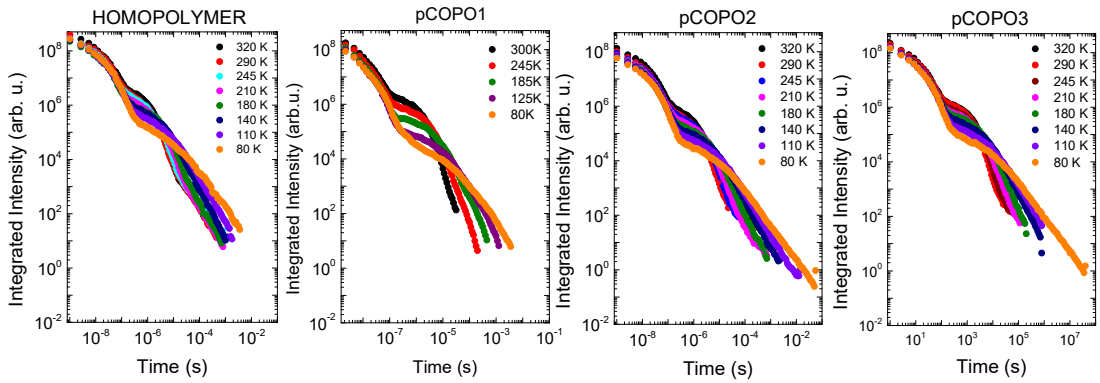

Figure 6 – Luminescence decays obtained as a function of temperature in pristine thin films of homopolymer, pCopo1, pCopo2 and pCopo3.

The excitation power dependence of the DF at room temperature is shown in Figure 7 for all the copolymers. The emission intensity increases linearly with excitation dose as predicted in a TADF mechanism. The insets show the integrated delayed fluorescence collected with 1 μs delay time and integrated over 100 μs; a clear linear dependence with excitation dose (the slope is 1) is observed. These data confirm that the DF is originated from a monomolecular process, rather than from triplet−triplet annihilation (for which the slope is 2).35 Therefore, the DF is unambiguously assigned to a TADF mechanism.

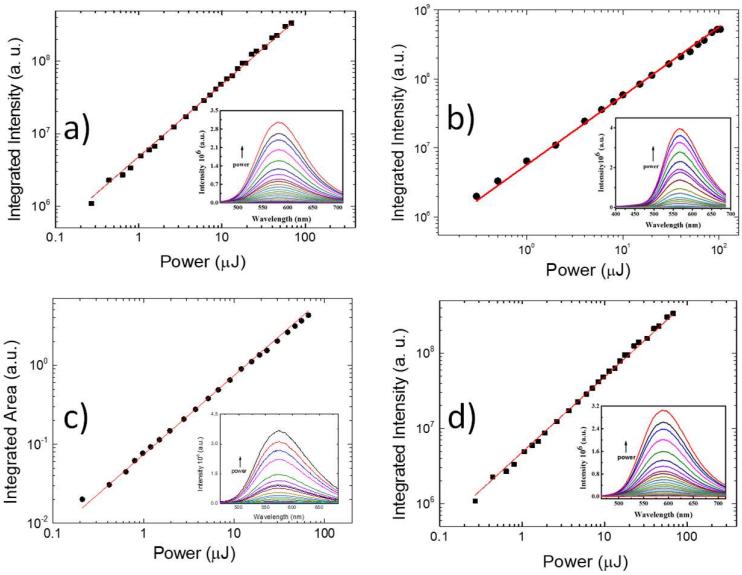

Figure 7 – Power dependence of the integrated delayed fluorescence: a) Homopolymer, b) pCopo1, c) pCopo2 and d)pCopo3.

8.6 Devices structures and Results[2]

In preliminary studies, see previous chapter, pCopo1 gave OLEDs with EQE_{max} 2.5%.[31]

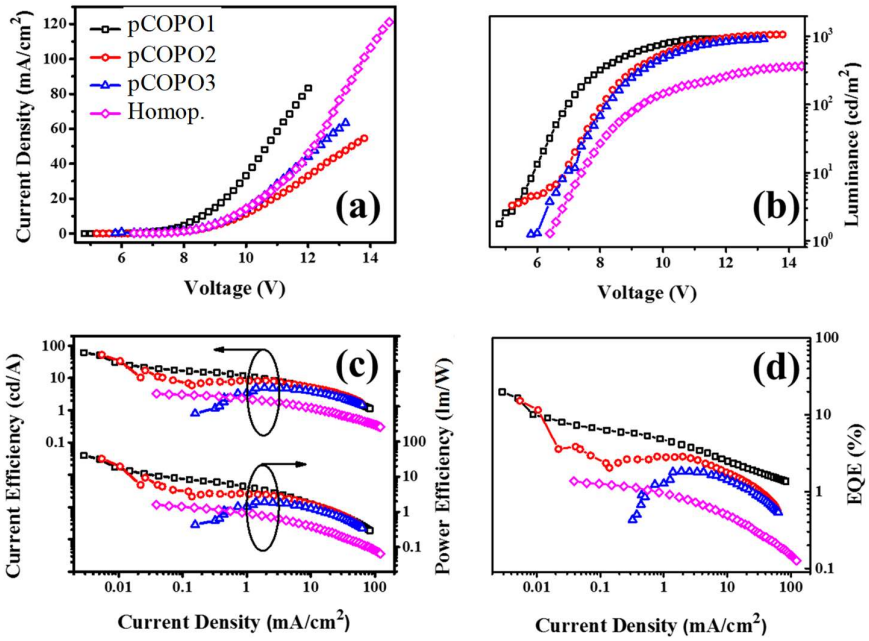

Figure 8 - **.** Characteristics of OLED devices for **pCopo1-3** and **Homopolymer** (a) current density versus voltage. (b) luminance versus voltage. c) current and power efficiency versus current density. d) EQE versus current density.

[2] Devices were performed and characterized by Shouke Yan's research group.

Herein, the structure−property relationships of pCopo1−3 and the homopolymer are explored in polymer OLEDs. Devices were fabricated with the following architecture: indium tin oxide (ITO)/PEDOT:PSS (40 nm)/10% Copo1−3 or Homopolymer and 90% 1,3-bis(carbazol-9-yl)benzene (mCP) (45 nm)/1,3,5-tris(1-phenyl-1H-benzimidazol-2-yl)benzene (TPBi) (30 nm)/LiF (1 nm)/Al (100 nm), where poly(3,4-ethylenedioxythiophene):poly(styrenesulfonic acid) (PEDOT:PSS) serves as the hole-injection layer; TPBi acts as the electron-transporting layer, and 10% pCopo1−3, Homopolymer, and 90% mCP in chlorobenzene were spin-coated to form the emitting layer. Current density−voltage and brightness−voltage curves are shown in Figure 8a,b.

Except for the homopolymer, all the copolymers reach a maximum luminance of 1000 cd/m^2. The devices exhibit driving voltages in the range of 5.8−7.4 V (recorded at a luminance of 10 cd m−2). Notably, Copo1 displays a lower turn-on voltage of 5.8 V compared with the other polymers, and the driving voltages increase with increasing the content of TADF units. This may be attributed to the relatively low LUMO of Copo1, which is beneficial to electron injection. Figure 8c, d depict current and power efficiencies and the external quantum efficiency plotted with respect to current density.

The key EL parameters are summarized in Table 2. The best EL performance is achieved for the Copo1-based device with maximum: Current Efficiency of 61.3 cd/A, Power Efficiency of 40.1 lm/W, and EQE of 20.1%. Furthermore, at the practically relevant brightness of 100 cd m^{-2} the EQE was 5.3%. Compared with previous data for pCopo1,[31] it is clear that mCP is a better host than CBP. This is most likely due to the fact that the triplet level of mCP (2.9 eV)[36] is higher than that of CBP (2.56 eV),[36] which helps to confine the triplet excited states in the TADF units. This avoids quenching due to triplet−triplet annihilation and also quenching by the host. The device performances for pCopo2, pCopo3, and homopolymer in directly comparable conditions are relatively low, indicating that the insulating spacer styrene units play an important role in the OLED properties of these polymers. The electroluminescence spectra of the polymers are shown in Figure 9.

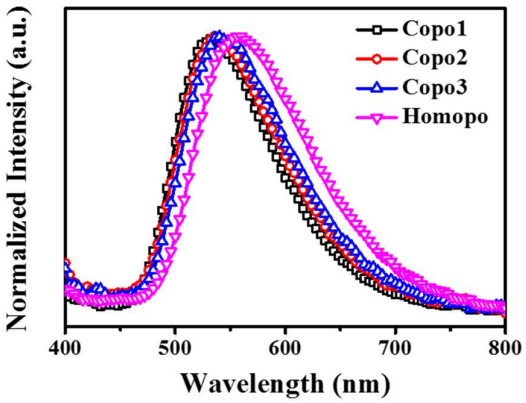

Figure 9 - Electroluminescence spectra

All of the devices exhibit emission exclusively from the TADF polymers at ca. 530−550 nm without any evidence of mCP emission at 360 nm.[37] It is notable that the peak λ_{max} value of the EL spectra shifts to longer wavelength in the sequence pCopo1 (533 nm) < pCopo2 (536 nm) < pCopo3 (539 nm) < homopolymer (556 nm). The EL spectrum of pCopo1 is very close to the TADF monomer units (PL peak at 529 nm), indicating styrene units are vital to prevent aggregation and improve color purity. Therefore, a consistent change of CIE coordinates for the devices can be seen from (0.36, 0.55) for Copo1 to (0.43, 0.51) for the homopolymer.

Table 2 - Device performance data.

	V_{10}[a] (V)	λ_{max}[b] (nm)	EQE_{100}[c] (%)	EQE_{max}[d] (%)	CE_{max}[e] (cd/A)	PE_{max}[f] (lm/W)	CIE[g] (x, y)
pCopo1	5.8	533	5.3	20.1	61.3	40.1	(0.36, 0.55)
pCopo2	6.8	536	2.8	15.2	52.5	32.6	(0.37, 0.53)
pCopo3	6.9	539	1.8	1.8	5.0	1.9	(0.39, 0.53)
Homopolymer	7.4	556	0.6	1.4	3.3	1.6	(0.43, 0.51)

[a] The driving voltage at 10 cd m^{-2}. [b]EL peak wavelength. [c] External quantum efficiency at 100 cd m^{-2}. [d] Maximum external quantum efficiency. [e] Maximum current efficiency. [f] Maximum power efficiency. [g] The Commission Internationale de L'Eclairage coordinates.

To elucidate the reason why pCopo1-based OLEDs display the best performance in this series, the triplet energies of the four polymers were determined as shown in Figure 10 according to the phosphorescent spectra for which the highest energy peak defines the triplet energy (ET).14 pCopo1 has the highest triplet energy, ET (2.46 eV), and then ET decreases with decreasing the content of styrene. In pCopo1, with the larger proportion of styrene spacers, the TADF units behave more as an isolated chromophore, and the phosphorescence is at higher energy.

This is consistent with our previous report.[31] Styrene units have low polarity; therefore, the different polymer compositions should have a minimal effect on the dielectric properties of the system.

Moreover, the triplet state is a local excited state, with negligible excited dipole moment and therefore is not significantly affected by the dielectric medium. Since the energy of the singlet state is not so affected, the singlet−triplet energy gap is smaller in pCopo1 than in the other polymers, which facilitates reverse intersystem crossing (RISC) and leads to a higher TADF contribution in pCopo1.

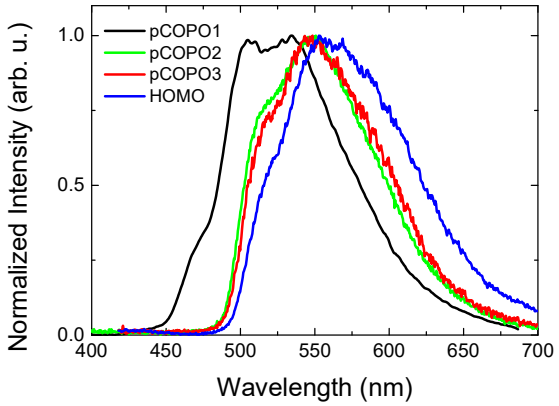

Figure 10 – Phosphorescence spectra at 80 K in pristine films, from left to right: pCOPO1 (black), pCOPO2 (green), pCOPO3 (red) and homopolymer (blue)

The singlet energy is estimated from the onset of the broad emission band, which provides a more comparable result, as demonstrated in previous studies.[38,39] The ΔE_{ST} values for pCopo1−3 and homopolymer are calculated to be 0.35, 0.46, 0.42, and 0.40 eV, respectively. It is well-known[14–18] that a small ΔE_{ST} is necessary for efficient RISC which is required for TADF, and the smaller the value of ΔE_{ST}, the faster the RISC rate. This systematic change in ΔE_{ST} in the current series of polymers correlates with their OLED performance.

The DF contribution to the overall emission is shown in Figure 11, for all the polymers. The data were obtained from the integral of the prompt and delayed fluorescence, as determined from the luminescence decay obtained in vacuum. For all the polymers, the DF is red-shifted compared with the PF, and shows an obvious spectral narrowing relative to PF (Figure 11a−d). This may be caused by the contributions of a residual local singlet excited state and the non-relaxed singlet charge transfer state in PF. As shown in Figure 11, the DF contribution is 44.4% for pCopo1, and this value decreases gradually with reducing the content of styrene to 33.2% for the homopolymer. Once more, these data are in good agreement with the determination from steady-state fluorescence and with the enhanced performance of pCopo1 in devices.

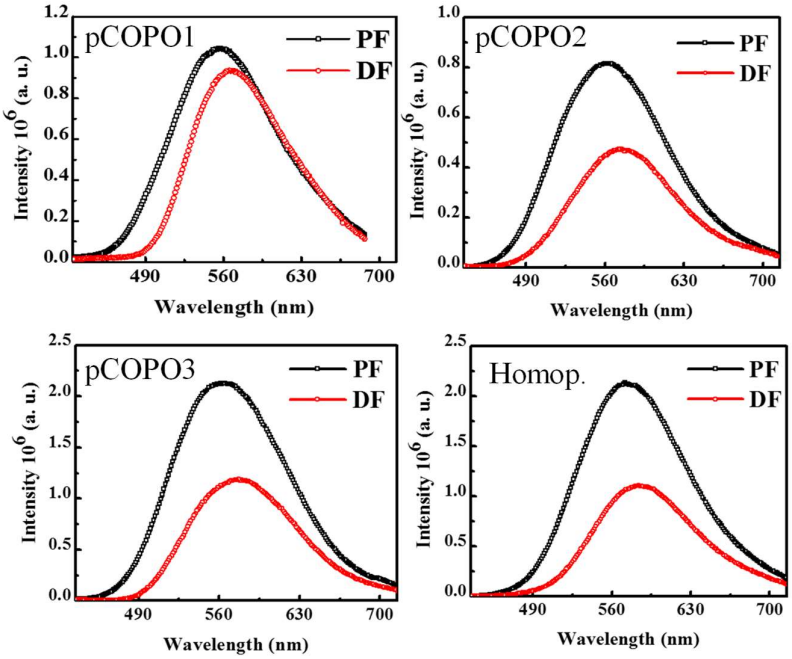

Figure 11 – Integrated prompt fluorescence (PF) and delayed fluorescence (DF) for pCOPO1, pCOPO2, pCOPO3 and homopolymer in pristine film at room temperature.

After the photophysical study presented in this set of pendant polymers, the application in devices, POLEDs, which in turn were produced and characterized by Shouke Yan's group.

8.7 Conclusions

In summary, a series of pendant polymers with PTZ-DBTO2 as TADF units and insulating styrene units as side chains have been synthesized, and their structure/property/OLED performance relationships have been established. Photophysical data confirm that for all the polymers the reverse intersystem crossing mechanism is able to compete with internal conversion and triplet−triplet annihilation. The effect of styrene content on the properties of the TADF polymers has been evaluated. The triplet energy and the delayed fluorescence contribution increases with increasing styrene content of the copolymers; meanwhile, the energy splitting between the singlet and triplet states (ΔE_{ST}) decreases with reducing styrene content of copolymers. OLED devices based in these polymers and fabricated using spin-coated emitting layers give high performance, which is enhanced for the copolymers compared to the homopolymer. The best EL performance was achieved for the pCopo1-based device with CE_{max} of 61.3 cd/A, PE max of 40.1 lm/W, and EQE_{max} of 20.1%. To our knowledge, this is the highest EQE reported to date for a TADF polymer.[26–31] Furthermore, at 100 cd m^{-2} the EQE was 5.3%. High EQE, even at very low luminance, is widely recognized as an important

figure-of-merit for OLED efficiencies.[40] The key molecular features that was developed in this work, namely, a nonconductive polymer backbone with pendant TADF units separated by non-emissive units, should be versatile for the design of new families of TADF polymers. It remains to be seen if polymers, which have the potential benefits of high thermal stability, good film forming ability, and reduced phase separation, can be widely exploited for colour tuning and enhanced TADF−OLED performance.

8.8 Bibliography

1 Pope M, Kallmann H, Magnante P, *J. Chem. Phys*. **1963**, 38, 2042−2043.

2 Helfrich W, Schneider W, *Phys. Rev. Lett*. **1965**, 14, 229.

3 Tang C. W., VanSlyke S. A, *Appl. Phys. Lett*. **1987**, 51, 913−915.

4 Chen C. H, Hsu L. C, Rajamalli, P, Chang, Y. W., Wu, F. I, Liao, C. Y, Chiu, M. J, Chou P. Y, Huang M. J, Chu L. K. *J. Mater. Chem*. C **2014**, 2, 6183−6191.

5 Su T. H, Fan C. H, Ou-Yang Y. H, Hsu L. C, Cheng C. H, *J. Mater. Chem*. C **2013**, 1, 5084−5092.

6 Li G, Zhu D, Peng T, Liu Y, Wang Y, Bryce M. R, *Adv. Funct. Mater*. **2014**, 24, 7420−7426.

7 Fukagawa, H, Shimizu, T, Hanashima, H, Osada, Y, Suzuki, M, Fujikake, H, *Adv. Mater***. 2012**, 24, 5099−5103.

8 Friend, R, Gymer, R, Holmes, A, Burroughes, J, Marks, R, Taliani, C, Bradley, D, Dos Santos, D, Brédas, J, Lögdlund, M, *Nature* **1999**, 397, 121−128.

9 Ma, Y, Zhang, H, Shen, J, Che, C, *Synth. Met*. **1998**, 94, 245−248.

10 Ikai, M, Tokito, S, Sakamoto, Y, Suzuki, T, Taga, Y, *Appl. Phys. Lett*. **2001**, 79, 156−158.

11 Tsuboyama, A, Iwawaki, H, Furugori, M, Mukaide, T, Kamatani, J, Igawa, S, Moriyama, T, Miura, S, Takiguchi, T, Okada, S, *J. Am. Chem. Soc*. **2003**, 125, 12971−12979.

12 Baldo, M. A, O'Brien, D, You, Y, Shoustikov, A, Sibley, S, Thompson, M, Forrest, S, *Nature* **1998**, 395, 151−154.

13 Schmidbauer, S, Hohenleutner, A, König, B, *Adv. Mater*. **2013**, 25, 2114−2129.

14 Zhang, Q, Li, J, Shizu, K, Huang, S, Hirata, S, Miyazaki, H, Adachi, C, *J. Am. Chem. Soc*. **2012**, 134, 14706−14709.

15 Rajamalli, P, Senthilkumar, N, Gandeepan, P, Huang, P. Y, Huang, M. J, Ren-Wu, C. C, Yang, C. Y, Chiu, M. J, Chu, L. K, Lin, H. W, *J. Am. Chem. Soc*. **2016**, 138 (2), 628−634.

16 Dias, F. B, Bourdakos, K. N, Jankus, V, Moss, K. C, Kamtekar, K. T, Bhalla, V, Santos, J, Bryce, M. R, Monkman, A. P, *Adv. Mater*. **2013**, 25, 3707−3714.

17 Tao, Y, Yuan, K, Chen, T, Xu, P, Li, H, Chen, R, Zheng, C, Zhang, L, Huang, W, *Adv. Mater*. **2014**, 26, 7931−7958.

18 Adachi, C, *Jpn. J. Appl. Phys*. **2014**, 53, 060101.

19 Zhang, Q, Li, B, Huang, S, Nomura, H, Tanaka, H, Adachi, C, *Nat. Photonics* **2014**, 8, 326−332.

20 Kim, B. S, Lee, J. Y, *Adv. Funct. Mater*. **2014**, 24, 3970− 3977.

21 Arias, A. C, MacKenzie, J. D, McCulloch, I, Rivnay, J, Salleo, A, *Chem. Rev*. **2010,** 110, 3−24.

22 Gong, S, Yang, C, Qin, J, *Chem. Soc. Rev*. **2012**, 41, 4797−4807.

23 Cho, Y. J, Yook, K. S, Lee, J. Y, *Adv. Mater*. **2014**, 26, 6642−6646.

24 Kim, Y. H, Wolf, C, Cho, H, Jeong, S. H, Lee, T. W,*Adv. Mater*. **2016**, 28, 734−741.

25 Rothe, C, Monkman, A. Regarding the Origin of the Delayed Fluorescence of Conjugated Polymers. *J. Chem. Phys*. **2005**, 123, 244904.

26 Albrecht, K, Matsuoka, K, Fujita, K, Yamamoto, K, *Angew. Chem., Int. Ed*. **2015,** 54, 5677−5682.

27 Nikolaenko, A. E, Cass, M, Bourcet, F, Mohamad, D, Roberts, M, *Adv. Mater*. **2015**, 27, 7236−7240.

28 Luo, J, Xie, G, Gong, S, Chen, T, Yang, C, *Chem. Commun*. **2016**, 52, 2292−2295.

29 Lee, S. Y, Yasuda, T, Komiyama, H, Lee, J, Adachi, C, *Adv. Mater*. **2016**, 28, 4019−4024.

30 Zhu, Y, Zhang, Y, Yao, B, Wang, Y, Zhang, Z, Zhan, H, Zhang, B, Xie, Z, Wang, Y, Cheng, Y, *Macromolecules* **2016**, 49, 4373−4377.

31 Nobuyasu, R. S, Ren, Z, Griffiths, G. C, Batsanov, A. S, Data, P, Yan, S, Monkman, A. P, Bryce, M. R, Dias, F. B, *Adv. Opt. Mater*. **2016**, 4, 597−607.

32 Koene, B. E, Loy, D. E, Thompson, M. E, *Chem. Mater*. **1998**, 10, 2235−2250.

33 Cardona, C. M, Li, W, Kaifer, A. E, Stockdale, D, Bazan, G. C, *Adv. Mater*. **2011**, 23, 2367−2371.

34 Bredas, J. L. Mind the Gap! *Mater. Horiz*. **2014**, 1, 17−19.

35 Dias, F. B, Philos. *Trans. R. Soc. A* **2015,** 373, 20140447.

36 Gong, S, He, X, Chen, Y, Jiang, Z, Zhong, C, Ma, D, Qin, J, Yang, C, *J. Mater. Chem*. **2012**, 22,2894−2899.

37 Lin, M.-S, Yang, S.-J, Chang, H.-W, Huang, Y.-H, Tsai, Y.-T, Wu, C.-C, Chou, S.-H, Mondal, E, Wong, K.-T, *J. Mater. Chem*. **2012**, 22, 16114−16120.

38 Tyson, D. S, Castellano, F. N, *J. Phys. Chem. A* **1999**,103, 10955−10960.

39 Zhang, Q, Komino, T, Huang, S, Matsunami, S, Goushi, K,Adachi, C, *Adv. Funct. Mater*. **2012**, 22, 2327−2336.

40 Jou, J.-W, Kumar, S, Agrawal, A, Li, T.-H, Sahoo, S, *J. Mater. Chem. C* **2015**, 3, 2974−3002.

9. TADF in Copolymers: White organic light-emitting diodes.

A series of pendant TADF copolymers, based on the PTZ-DBTO2 emitter, but physically separated by dibenzothiophene (DBT) spacers were synthesized with varying ratios of PTZ-DBTO2 and DBT moieties. The copolymers show dual emission with contributions from PTZ-DBTO2 and DBT emission and were used to fabricate white organic light-emitting diodes.

This work is published in: Chensen Li, Roberto S. Nobuyasu, Yukun Wang, Fernando B. Dias, Zhongjie Ren, Martin R. Bryce, and Shouke Yan. *Solution-Processable Thermally Activated Delayed Fluorescence White OLEDs Based on Dual-Emission Polymers with Tuneable Emission Colours and Aggregation-Enhanced Emission Properties*, Adv. Optical Mater. **2017**, 1700435.

9.1 Introduction

Organic light-emitting diode (OLED) devices, especially, white OLEDs (WOLEDs) are attracting great interest in display and lighting applications.[1–3] Most white luminescent materials are formed by blends of several small molecules that emit different colours spanning the entire visible spectrum.[4–7] These devices often are unstable due to significant phase segregation. In comparison, white luminescent polymers possess the advantages of enhanced control of emitter ratios, low-cost, and can be solution-processable for large-area flexible displays. [4–8] Fluorescent and phosphorescent WOLEDs have been extensively reported based on white-emitting polymers.[9,10] However, the internal quantum efficiency (IQE) of fluorescent OLEDs is only 25%,[11] and although phosphorescent OLEDs can achieve almost 100% IQE, the expensive and scarce metals used in these devices, such as iridium or platinum, create additional economic and environmental problems that restrict the application of WOLEDs in large-scale applications, such as lighting. Moreover, there is also significant degradation of emitters in the blue spectral region.[12,13]

Thermally activated delayed fluorescence (TADF) emitters are the route for the next generation OLEDs, as these materials can harvest light from both triplet and singlet excitons without noble metals.[14–17] Recently, all TADF WOLEDs and WOLEDs hybridizing TADF emitters with triplet emitters have been reported.[18–23] Adachi and co-workers demonstrated WOLEDs using red, green, and blue TADF molecules as emissive dopants, with external quantum efficiency (EQE) of >17% with Commission Internationale de l'Eclairage (CIE)

coordinates of (0.30, 0.38).[18] Hybrid WOLEDs combining fluorescent emitters and TADF emitters are desirable to improve the EQE due to their excellent stability and harvesting of both singlet and triplet excitons. Lee and co-workers developed hybrid WOLEDs with an external quantum efficiency >20% using blue or green small molecule TADF materials.[19,20] However, all the previous TADF emitters for WOLEDs are small molecules and no TADF polymer WOLEDs have been reported to date. In general, the small molecules are limited in such properties as thermal stability, mechanical robustness, and flexibility. Polymers, in contrast, can have both good thermal stability, solution processability, and facile functionality, allowing the introduction of various functional units as pendant groups.[24,25] Nowadays, polymeric materials have been proven to be ideal emissive materials for the solution-processed devices.[26–30] Therefore, some groups reported luminous polymers containing pendant TADF units, which demonstrated good performance in solution processed OLEDs. Yang and co-workers[28] synthesized copolymers from three monomer components, with a backbone of polycarbazole and 10-(4-(5-phenyl-1,3,4-oxadiazol-2-yl)-phenyl)-10*H*-phenoxazine as pendant TADF units. Those bluish-green OLEDs had EQE_{max} of 4.3% and EQE 2.4% at 100 $cd.m^{-2}$. Zhu et al.[29] reported a TADF polymer PAPTC with triazine acceptor and 9,10-dihydroacridine donor as backbone and pendant units, respectively. PAPTC had M_n 22.0 kDa and PDI 2.96. A green OLED with EQE_{max} of 12.6% at 180 $cd.m^{-2}$ was obtained. Ren et al.[30] reported a series of polymers with an insulating backbone and varying ratios of 2-(10*H*-phenothiazin-10-yl)dibenzothiophene-*S,S*-dioxide as a pendant TADF unit. Green-emitting devices with one of the polymers achieved EQE_{max} as high as 20.1%, with EQE 5.3% at 100 cdm^{-2}. However, no white-light emitting TADF polymers have been reported to date because controlling the energy transfer process and the tuning emission colours are still challenging. Emitters with delayed fluorescence often encounter severe aggregation-caused quenching (ACQ) because of the strong intermolecular interactions, which is a hindrance to improving the efficiency of OLEDs for practical applications.[31–34] In contrast, aggregation-induced emission (AIE) is a property of some molecules that have almost no fluorescence in solution, but are highly emissive in the aggregated state.[35–37] Several studies on small TADF molecules have reported noticeable emission enhancement in aggregates or in the solid state.[38, 39] Emissive materials with tunable luminescent colours are of great significance for their optical applications. Tang et al.[40, 41] found impressive colour-tunable AIE and aggregation-enhanced emission (AEE) behaviours in the solid state. Taking these into account, employing AIE or AEE to tune emission colours aiming to obtain white

emission is realistic. Therefore, the development of solution processed single white-emitting polymers with both TADF and AEE features is of importance. Nonconjugate TADF copolymers with pendant 2-(10*H*-phenothiazin-10-yl)dibenzothiophene-*S,S*-dioxide (PTZ-DBTO2) and dibenzothiophene (DBT) units have been synthesized in Figure 1. PTZ-DBTO2[34,38,39] was chosen because it exhibits strong TADF and AIE features. DBT with high triplet energy of 3.04 eV and good hole transporting ability[38,42] was introduced as a blue fluorescence emitter[43,44] and as a TADF host.[45,46] The blue emitting DBT units together with yellow emitting PTZ-DBTO2 units could lead to a white light emitting copolymer, while the DBT units disperse the PTZ-DBTO2 components and thus regulate the aggregation and quenching. The obtained copolymers P1–P3 display obvious TADF and AIE features and most significantly P3 shows warm-white electroluminescence.

9.2 Molecular Characterization

Polymers P1–P3 were synthesized by radical copolymerization of 2-vinyldibenzothiophene and 2(10*H*-phenothiazin-10-yl)-8-vinyldibenzothiophene-*S,S*-dioxide with the molar feed ratios of 50:50, 80:20, and 90:10, respectively.

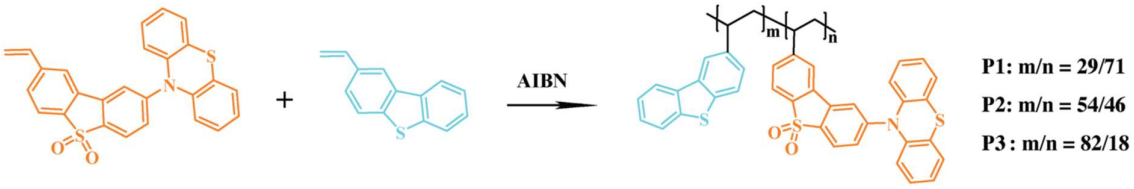

Figure 1 – Synthetic route and structure of the polymers studied in this work. PTZ-DBTO2 and DBT content for copolymers P1, P2 and P3.[1]

The actual content of the TADF unit, PTZ-DBTO2, in the copolymers is estimated from elemental analysis data as 71%, 46%, and 18% for P1–P3, respectively, indicating the slightly greater reactivity of the PTZDBTO2 monomers. The copolymers are readily soluble in chloroform, toluene, and tetrahydrofuran. The weight-average molecular weights (M_w) of P1–P3 were determined to be 11.6, 30.1, and 22.8 kDa with PDIs of 1.33, 1.67, and 1.65, respectively (Table1). The structures of the polymers were confirmed by 1H NMR spectra.

[1] Polymers were synthesised by Shouke Yan's research group.

Table 1 – Polymeric properties for P1, P2 and P3.

	Mw/PDI	λ_{max} (nm)	Eg (eV)	HOMO (eV)	LUMO (eV)	ΔE_{ST} (eV)	$\Phi_{PL\text{-}Film}$ (%) (O_2/Vacuum)	$\Phi_{PL\ Toluene}$ (%) (O_2/Dgas)
P1	11600/1.33	547	2.76	-5.08	-2.32	0.09	10.4/11.1 ± 3.6	9.9/19.8 ± 2.7
P2	30100/1.67	542	2.77	-5.10	-2.33	0.06	23.5/26.5 ± 3.1	16.1/28.3 ± 2.1
P3	22800/1.65	535	2.82	-5.08	-2.26	0.04	19.5/25.8 ± 3.2	15.9/52.9 ± 2.4

9.3 Photophysical properties

Figure 2 shows the UV–vis absorption spectra of polymers P1–P3. The absorption in neat films shows π–π* transitions of the DBT moiety at 290 nm and electronic transitions of PTZ-DBTO2 at 330 nm. In addition, relatively wide energy gaps (Eg) of 2.76, 2.77, and 2.82 eV for P1, P2, and P3, respectively, were obtained from the onset of the absorption. The homopolymer is also presented here in order to contextualize the absorption spectra of the spacer (DBT) and the pendant units (PTZ-DBTO2) (Figure 2a). With increasing content of DBT, from P1 to P3, the contribution of the spacer in the absorption spectra becomes more evident, showing a sharp transition around 290 nm (Figure 2b).

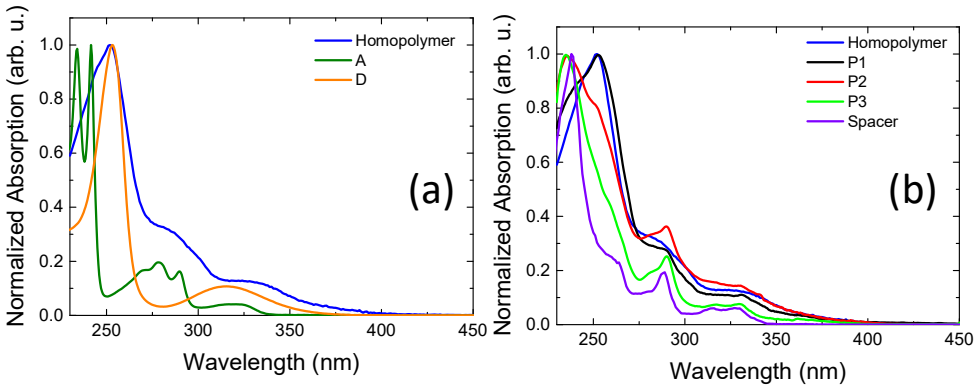

Figure 2 - Absorption spectra in DCM: a) Homopolymer (blue), Acceptor (green) and Donor (orange) units; b) Homopolymer (blue), P1 (black), P2 (red) and P3 (green) and the spacer, Dibenzothiophene (purple).

The photoluminescence (PL) spectra of P1-P3, Figure 3, in their thin films display a similar profile. The maximum of the PL spectra gradually shifts to longer wavelengths with increasing content of PTZ-DBTO2 units. This might result from changes on the film dielectric constant due to a larger PTZ-DBTO2 content, and clearly indicates that the DBT units can effectively disperse the TADF units. The emission of P3 shows a more obvious signature of DBT units between 412 and 435 nm, as expected.

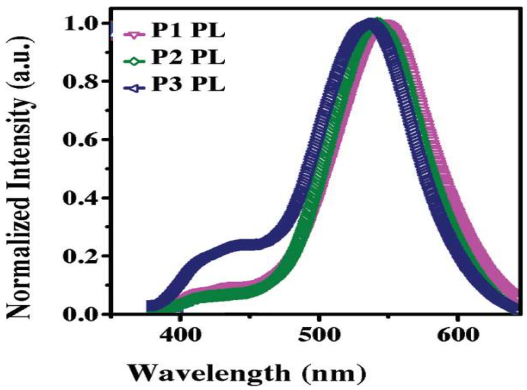

Figure 3 – Steady-state photoluminescence of P1 (purple), P2 (green) and P3 (dark blue) in pristine thin film at room temperature.

9.4 The influence of Molecular Aggregation on Emission Spectra of Copolymers P1-P3

The Φ_{PL} values of P1, P2, and P3 in solid films are 10.4%, 23.5%and 19.5%, respectively. The Φ_{PL} values (Table 1) in dilute toluene solutions are 9.9%, 16.1% and 15.9%, respectively, indicating that these polymers are AEE-active. After N_2 bubbling, the values increase to 19.8%, 28.3%, and 52.9%, respectively, which shows that triplet excitons are substantially quenched by oxygen.[14]

To further study the effects of aggregation, the PL measurements were performed in tetrahydrofuran/water (THF/water) mixtures. The very weak emission of P3 in pure THF solution increases steadily with increasing the water content and the emission peak at ca. 550 nm is sharply enhanced at 10:90 (v/v) THF/water fraction. This confirms the presence of an aggregate-enhanced emission effect in copolymer P3, see Figure 4.

It is propose that the enhancement of PL intensity in P3 is caused by the aggregation of the PTZ-DBTO2 units, which may result on shielding these chromophores from the high polar environment. The twisted conformation of PTZ-DBTO2 units[13a] will favour loose packing with weak molecular interactions, and thus rotation and vibration will occur easily in the dilute solution. In contrast, in the aggregated state, intramolecular motions are restricted, and the non-radiative pathways of the excited state are suppressed.[13b]

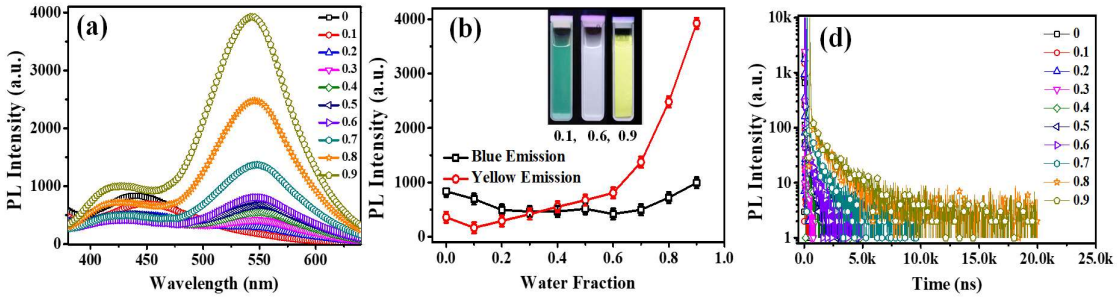

Figure 4 - a) PL spectra of P3 in THF/water mixtures with different fractions of water. (b) Plot of PL intensity versus the different water fractions for P3; the inset is fluorescent images of P3 in different THF/water mixtures under UV light irradiation. c) Transient photoluminescence decay curves at 550 nm for P3 with different THF/water ratios.

Therefore, as shown in Figure 4b, with increasing the water fraction, the emission of P3 is enhanced. Interestingly, the emission colour of P3 can also be tuned by adding water because of its dual emission, namely sky-blue from the DBT units and yellow from PTZ-DBTO2. As a result, the fluorescence of P3 varies from greenish-blue with 10% water, white with 60% water, and yellow with 90% water. This represents the first example of tuning the emission colour of a TADF polymer by only adding water. Furthermore, the AEE phenomenon of P3 was also confirmed by PLQY data in the THF/water mixture with quinine sulphate as a reference standard. The PLQY value of P3 in the THF solution is low (2.4%) and increases with the content of water to 41.8% when the content of water is 90%. The transient PL decays of P3 in aqueous THF solution, see Figure 4c, show that the excited state lifetimes are significantly enhanced with increasing water fraction. In pure THF, biexponential decays are observed for P3 with two distinct lifetimes of 9.25 ns and 35.61 ns. At ratios of 1:9 THF/water, the biexponential decay lifetimes increase to 32.56 and 1643 ns, respectively. When P3 aggregates, the nonradiative decay due to vibrations that affect the PTZ-DBTO2 units is effectively impeded, and thus the excitons are less quenched. Moreover, the lifetime of P3 in the aggregated state is longer than those of P1 and P2; similar results are observed for copolymers P1 and P2, see Figure 5. However, the small amount of DBT in these polymers makes the changes on the emission colour less pronounced.

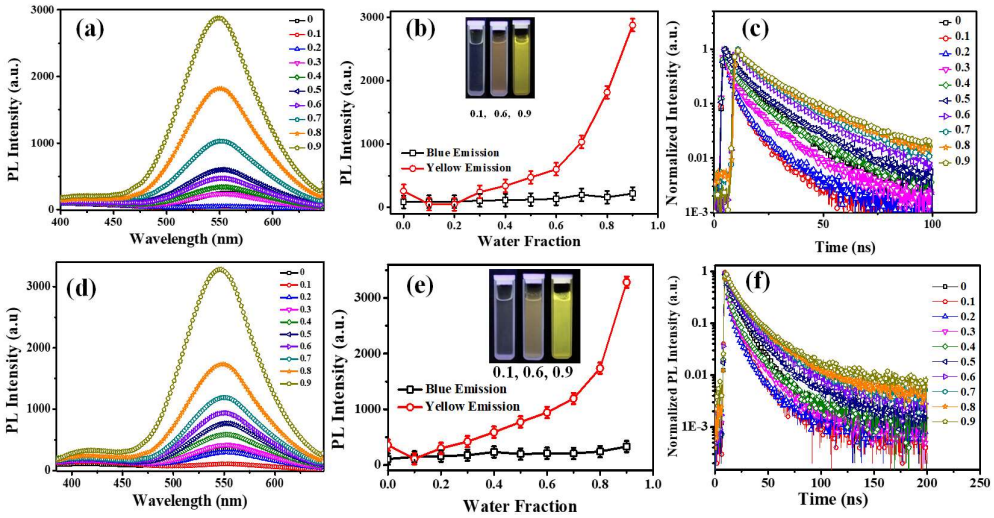

Figure 5 - Photoluminescence spectra of P1 (a) and P2 (d) in THF/water mixtures with different amounts of water; plot of PL intensity versus the different water fractions of P1 (b) and P2 (e), and fluorescence images of P1 and P2 in different THF/water mixture under UV light irradiation (inset). Transient photoluminescence decay (excited at 340 nm) curves at 550 nm for P1 (c) and P2 (f) in aqueous THF with different THF/water ratios.[2]

The emission colour of the copolymer films is also affected by aggregation and can be controlled by dispersing the copolymers in poly(methyl methacrylate) (PMMA) matrix (Figure 6). This effectively disperses the PTZ-DBTO2 and DBT chromophores in PMMA. The fluorescence of P3 for example, varies from greenish yellow with 10% PMMA to white with 90% PMMA. Comparable spectra for P1 and P2 are shown in Figure 6a and b, respectively. The crescent content of DBT from P1 to P3 exhibits an increased intensity of the blueish emission, and P3 is therefore the copolymer giving white emission.

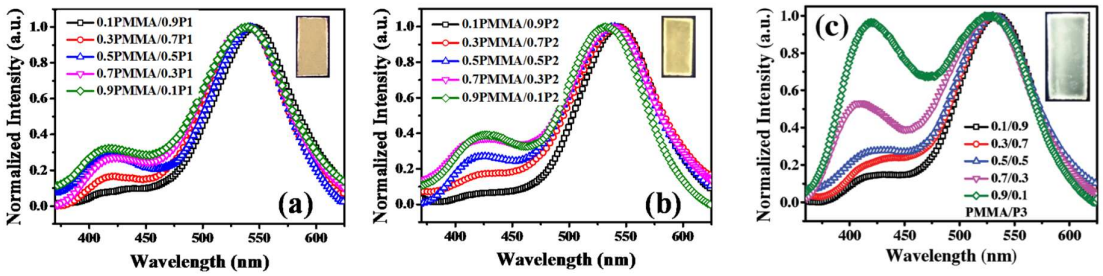

Figure 6 – Steady-state photoluminescence spectra in function of PMMA content; inset is the PL image of 0.9PMMA/0.1P under UV light irradiation: a) P1, b) P2 and c) P3.[3]

[2] Transient photoluminescence decay were collected by Shouke Yan's research group.
[3] Steady state photoluminescence in function of PMMA were collected by Shouke Yan's research group.

9.5 Time resolved measurements

The time-dependent fluorescence decays of thin films of P1-P3 at room temperature are seen in Figure 7. Prompt (PF) and delayed fluorescence (DF) components are clearly observed, with DF increasing gradually in the sequence P1 < P2 < P3.

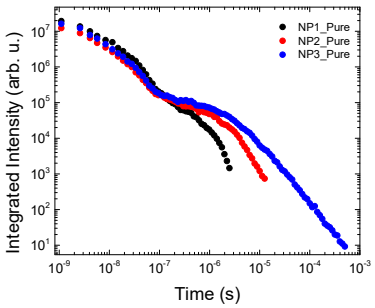

Figure 7 -Decay at room temperature of pristine thin films: P1 (black), P2 (red) and P3 (blue).

This is consistent with reduced quenching of triplet states due to vibrations and triplet–triplet annihilation, a longer triplet lifetime leads to a longer DF lifetime and stronger emission. The better confinement of PTZ-DBTO2 units in P3 is favourable for more efficient TADF emission.

Figure 8 shows the integral of the DF in P3, collected with 0.1 µs delay time, and integrated over 50 µs, as a function of excitation power. A clear linear dependence with slope 1, is obtained confirming that the DF originates from a monomolecular process rather than from triplet-triplet annihilation (for which the slope is 2).[17]

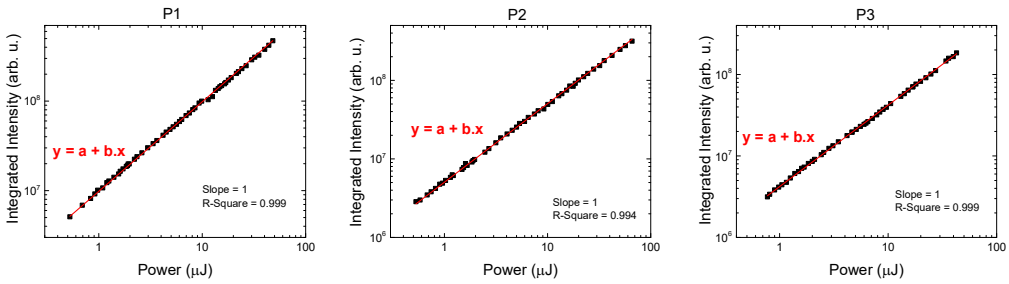

Figure 8 - Power dependence of the integrated delayed fluorescence in pristine thin films of P1, P2 and P3.

Figure 9 depicts the temperature dependence of fluorescence decay of the polymeric thin films. The PF shows almost no variation with temperature, which is consistent with negligible internal conversion. However, the DF component shows clear temperature

dependence, as expected, decreasing in intensity and increasing in lifetime at low temperatures. All these observations are consistent with the TADF mechanism.

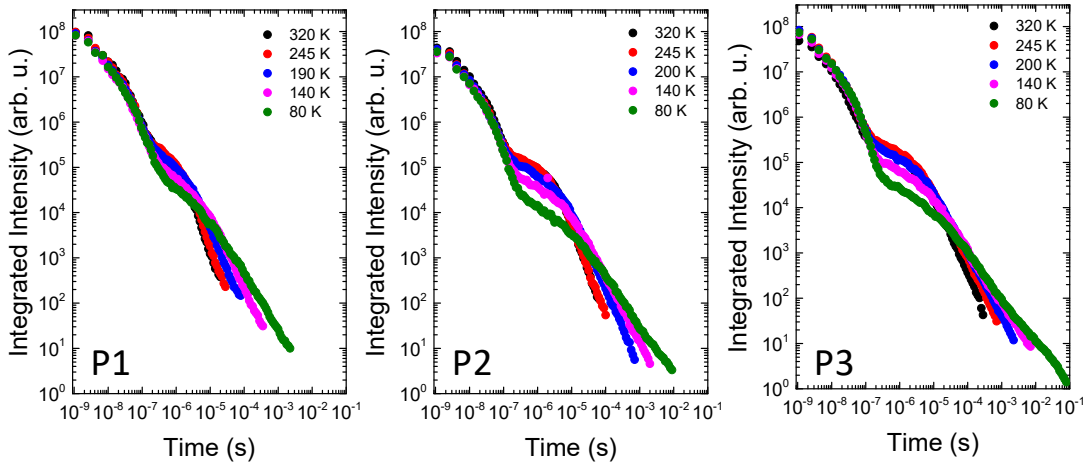

Figure 9 – Decays in function of temperature for P1, P2 and P3 in pristine thin film.

To estimate the TADF characteristic in these copolymers, the triplet energies of the three copolymers were determined according to the phosphorescent spectra as shown in Figure 10. The triplet energy, $E_{T,}$ of P1–P3 are 2.54, 2.57, and 2.60 eV, respectively, with E_T decreasing with decreasing DBT content. In P3, with the larger proportion of DBT spacers, the TADF units behave more as isolated chromophores, and the phosphorescence is at higher energy. Since the energy of the singlet state is not so affected, the singlet–triplet energy gap is smaller in P3 than in the other polymers. This facilitates reverse intersystem crossing (RISC) and leads to a higher TADF contribution in P3. The ΔE_{ST} values for P1–P3 are calculated to be 0.09, 0.06, and 0.04 eV, respectively. It is well known that a small ΔE_{ST} is necessary for efficient RISC, which is required for TADF, and the smaller the value of ΔE_{ST}, the higher the rate of RISC. Therefore, P3 is a better TADF polymer that the others.

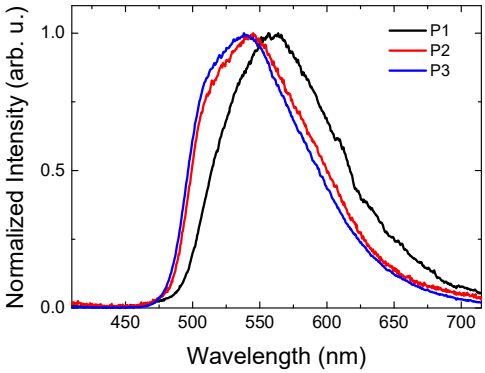

Figure 10 – Phosphorescence in pristine thin film at 80 K of P1 (black), P2 (red) and P3 (blue).

9.6 Doped Properties

For the fabrication of OLEDs using P1, P2 and P3 as emitters (see below) a tris(4-carbazol-9-yl-phenyl)amine (TCTA) / 4,4′-cyclohexylidenebis[N,N-bis(4-methylphenyl) benzenamine] (TAPC) mixture was used as the host (Figure 12). The film-forming ability, morphological stability of solution-processed films of the copolymers doped with TCTA/TAPC (65/25 wt%) were investigated by atomic force microscopy (AFM). The films were spin-coated from 10 mg.mL^{-1} toluene solution with 2000 rpm and then annealed for 30 min at 120 °C. As shown in Figure 11, the AFM images display smooth and homogeneous morphology with small root-mean square (RMS) roughness values of 0.383 nm for P1, 0.454 nm for P2 and 0.446 nm for P3. It is free of particle aggregation or phase separation, suggesting both good film-forming ability and good miscibility. Thus, the mixture of TCTA/TAPC (65/25 wt%) appears to be a suitable host for OLEDs.

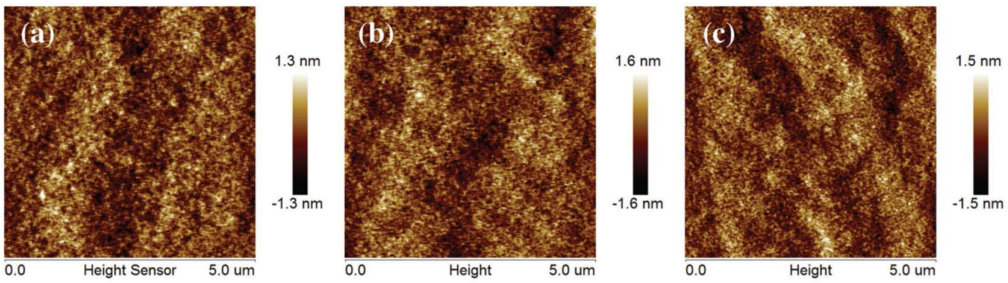

Figure 11 – AFM height image of P1 (a), P2 (b) and P3 (c) doped with 65 wt% TATC and 35 wt% TAPC. The films were spin-coated from the 10 mg.mL^{-1} toluene solution with 2000 rpm and then were annealed for 30 min at 120 °C.[4]

[4] AFM measurements were performed by Shouke Yan's research group.

Figure 12 shows the time-dependent fluorescence decays of the copolymer thin films doped with TCTA/TAPC (65/25 wt%) at room temperature. The copolymers show longer TADF lifetimes in the hosts than as pure films (Figure 7), probably due to effectively reduced triplet exciton annihilation through host dispersing. Furthermore, the contribution of delayed fluorescence (DF) to the overall emission of thin films of P1–P3/TCTA/TAPC (10/65/25 wt%) was evaluated. The DF contribution is 47% for P1, 54% for P2, and 56% for P3.

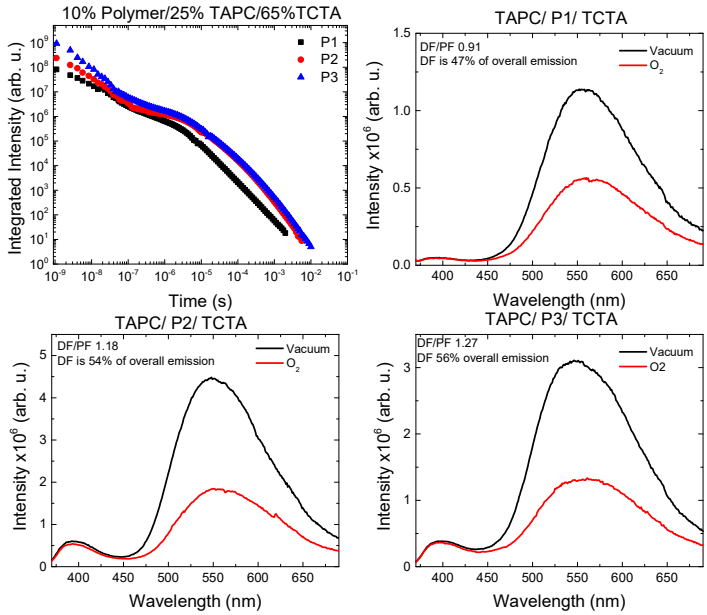

Figure 12 – Decay of P1, P2 and P3 in a mixed host TCTA/TAPC (65%:25%) and DF/PF ratio determined by the steady-state photoluminescence in vacuum and in air conditions.

For the pure polymer films, the DF contribution is 7%, 13%, and 32%, respectively (Figure 13). The DF contribution in the hosts is considerably higher than that of the pure films, indicating the hosts can effectively reduce triplet quenching due to triplet–triplet annihilation.

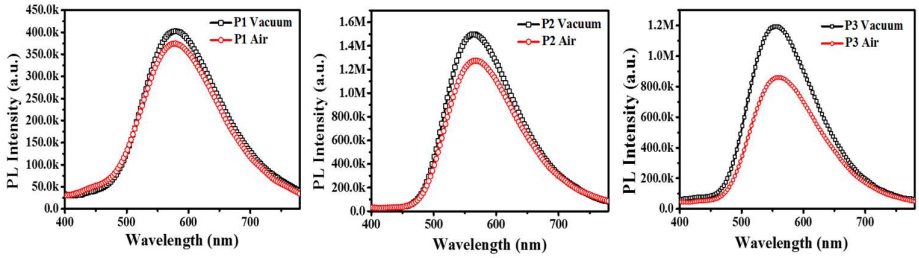

Figure 13 – Stead-state photoluminescence in vacuum and in air conditions (in black and in red, respectively) for pristine P1, P2 and P3.

PL spectra of P1, P2, and P3 doped with a different ratio of mixture of TCTA/TAPC can be seen in Figure 14. The emission colour of P1 and P2 films shows greenish yellow light with the increase of host, which is mainly derived from the strong emission of TADF units. This is consistent with their PMMA doped spectra. In contrast, fluorescence of P3 varies from greenish yellow to two-colour white with adding the host, which confirms the stronger blue emission with increasing contents attributed to DBT units. The higher ratios of TCTA/TAPC efficiently disperse the DBT units, which as a result emit stronger blue light. This is consistent with the result shown in Figure 14.

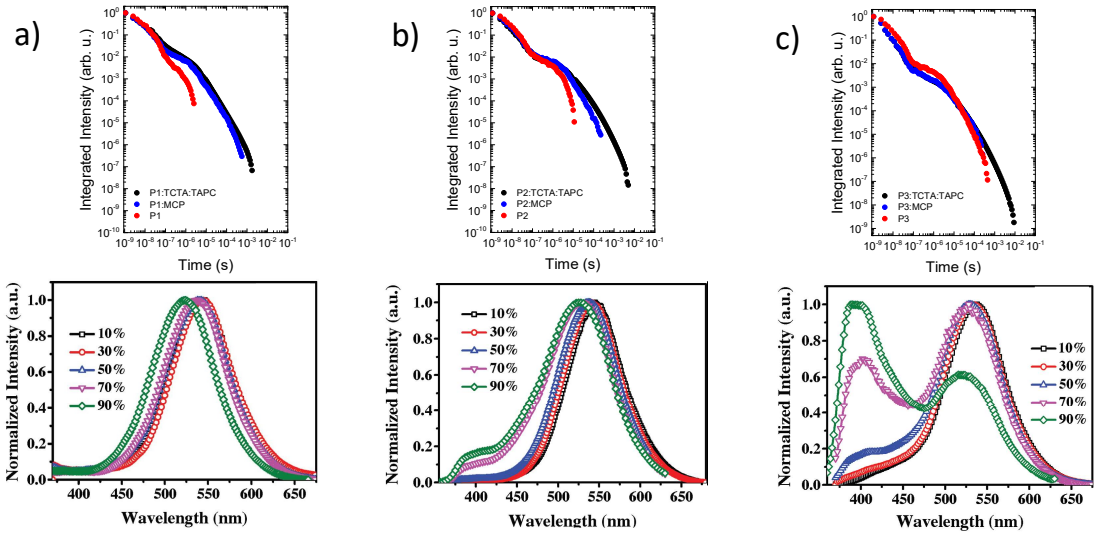

Figure 14 – Decay at room temperature for copolymers a) P1, b) P2 and c) P3 dispersed in three different hosts: 65% TCTA:25%TAPC (black), 90%MCP (blue) and pristine film (red). Bottom: Steady-state emission with different content (%) of TCTA:TAPC host.

9.7 OLED prototype fabrication and characterization[5]

As shown in Figure 15a, the OLED architecture is: ITO/PEDOT:PSS (40 nm)/polymer: TCTA: TAPC (10:65:25 wt%) (40 nm)/TmPyPB (50 nm)/LiF (0.8 nm)/Al (80 nm). A mixture of hole-transporting hosts tris(4-carbazol-9-yl-phenyl)amine (TCTA) and 4,4'-cyclohexylidenebis[*N,N*-bis(4-methylphenyl) benzenamine] (TAPC) with high triplet energies of 2.78 and 2.87 eV was used to reduce the driving voltage and improve charge balance and injection.[18] PEDOT:PSS (poly(3,4-ethylenedioxythiophene:poly(styrene sulfonate)) and 1,3,5-tris(3-pyridyl-3-phenyl)benzene (TmPyPB) served as the hole-injection layer and the electron-transport layer, respectively. TmPyPB also acts as an exciton blocking layer to prevent excitons quenching at the metal electrode interface.

[5] Devices were performed and characterized by Shouke Yan's research group.

Current density versus voltage, and luminance versus voltage curves are shown in Figure 15-b. All devices reach a maximum luminance of 1500 cd/m^2, and exhibit low turn-on voltages of 3.0-3.1 V. This may be attributed to the suitable HOMO level (-5.3 eV) which reduces the hole injection barrier from PEDOT:PSS (φ = -5.2 eV).

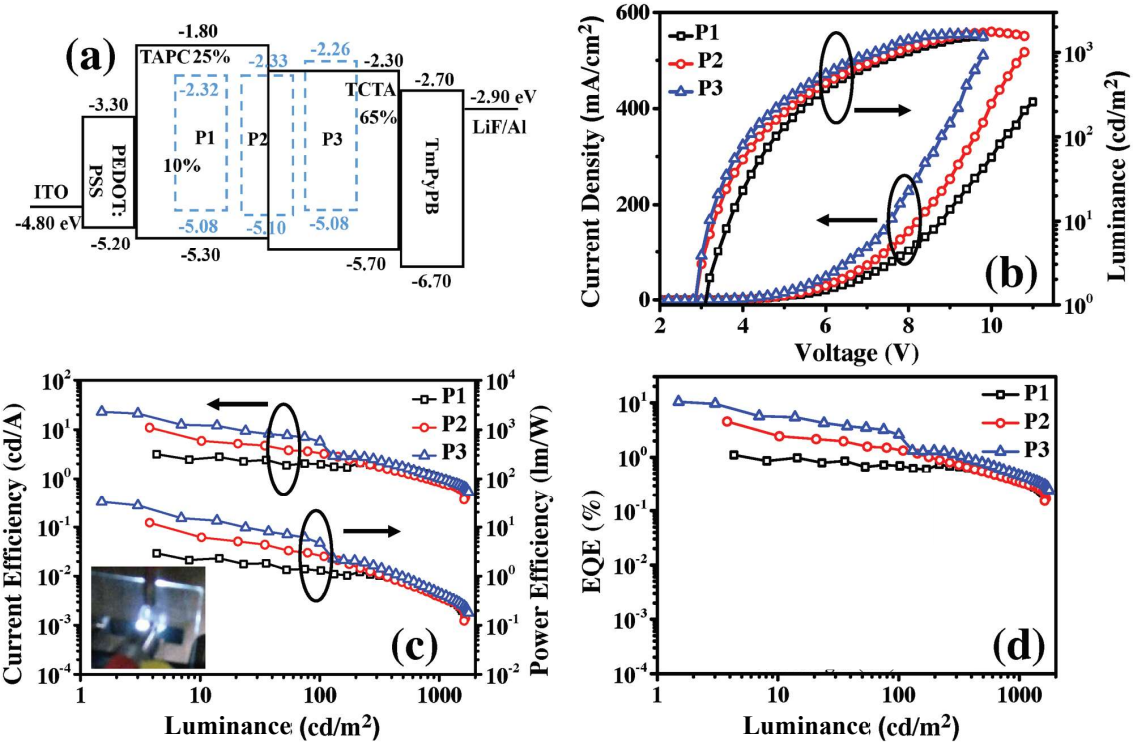

Figure 15 – a) Energy-level diagram and structure of OLED devices. b) Current density–voltage–luminance (*J–V–L*) curves. c) Current and power efficiency versus Luminance, the inset is the electroluminescence of P3. d) External quantum efficiency (EQE) versus Luminance.

Figure 15c shows the current and power efficiencies and Figure 15d the external quantum efficiencies with respect to current density. The key EL parameters are summarized in Table 2. The best EL performance is achieved with the P3 device giving CE_{max} of 11.5 cd/A, PE_{max} of 12.9 lm/W, and EQE_{max} of 4.7%, and can be attributed to the high DF contribution and long TADF lifetime in the host. Furthermore, the EQE at the practically relevant brightness of 100 and 500 cd m^{-2} are 2.6% and 0.8%, respectively.

Table 2 - Device Performance Data.

	V_{ON}[a] (V)	L_{max}[b] (cd/m)	CE_{max}[c] (cd/A)	PE_{max}[d] (lm/W)	EQE_{max} (%) [e]	CIE[f] (x/y)
P1	3.1	1552	3.1	2.3	1.1 ± 1.5	(0.31,0.43)
P2	3.1	1687	9.3	8.8	3.2 ± 0.9	(0.32,0.44)
P3	3.0	881	11.5	12.9	4.7 ± 0.8	(0.37,0.36)

[a]The voltage at 1 cd/m^2. [b]Maximum luminance. [c]Maximum current efficiency. [d]Maximum power efficiency. [e]Maximum external quantum efficiency. [f]CIE coordinates at 6 V.

P1 and P2 based OLEDs show yellow light with $CIE_{x,y}$ (0.31, 0.43) and (0.32, 0.44), which is mainly derived from the TADF units (Figure 16a and 16b). P3 devices show two-colour white light emission. Additionally, good colour stability in the EL spectra of P3 devices is observed with the CIE coordinates varying from (0.37, 0.38) at 5 V to (0.40, 0.37) at 8 V (Figure 16c). Impressively, the WOLED has a high colour rendering index (CRI) of 77 at 6 V, which is comparable with those of the reported two-colour TADF WOLEDs (38–77).[23, 49] The contribution of the blue emission component is confirmed in P2 and P3 devices but no blue component is observed in P1 devices.

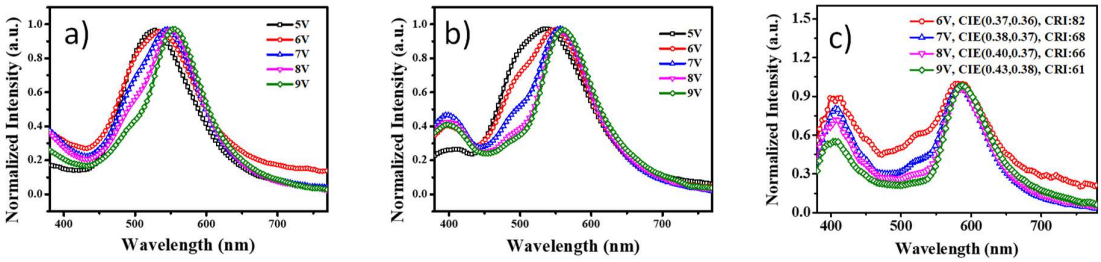

Figure 16 – Electroluminescence of P1, P2 P3 from 5 V to 9 V.

Remarkably, compared with the corresponding PL spectra of P3 in TCTA/TAPC and PMMA films, the P3 EL spectra exhibit a broad emission bands located at 416 nm from the DBT units and 535 nm from the TADF units. However, a new emission band is clearly visible at 580 nm. The possibility that the emerging 580 nm emission could be caused by exciplex excitons formed between P3 and TmPyPB was investigated. However, the PL spectrum of P3/TmPyPB (1:1) (Figure 17) shows no 580 nm emission, which indicates that an exciplex is not formed between these two materials, nor between P3 and TCTA or TAPC.[50]

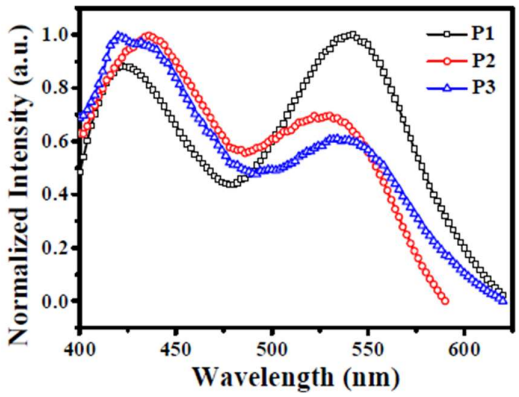

Figure 17 - PL spectra of P1, P2 and P3 doped with host and TmPyPB.

Therefore, the assignment of the 580 nm peak in the EL spectrum is due to the effect of the electric field on the randomly oriented dipole moments of the TADF units,[51] i.e., electroplex emission, or most probably due to the formation of an electromer, which cannot be observed in PL spectra. The formation of an electromer state is observed usually when trapped carriers recombine under the interaction with an electric field, and cause the emission to red-shift with respect to photoluminescence.[52,53] Therefore, the white emission of the device originates from the combination of the CT and electromer emission. According to the literature, when the HOMO (P3)–HOMO (TmPyPB) gap is smaller than LUMO (P3)–LUMO (TmPyPB) gap, the LUMO(EML) → LUMO(ETL) electron transfer rate is reduced to some extent enabling a spatially cross electron transfer from the LUMO of emissive layer (EML) to the HOMO of ETL (electron transport layer), producing electroplex emission.[54] As shown in Figure 15a, the HOMO–LUMO alignment of P3 fits this rule well. In addition, the ratio of intensity of blue-green emissions and orange-red emissions in the EL spectra increases along with the voltage increasing, which is consistent with the nature of the electric-field dependence of electroplex emission.[55,56] Moreover, the EL spectrum of non-doped devices (ITO/PEDOT:PSS/P3/TmPyPB/LiF/Al) (shown in Figure 18) shows 580 nm emission as well, which again confirms the electroplex formation between P3 and TmPyPB.

The results obtained with non-doped devices are summarized in Table 3. In spite of the reasonable value for maximum luminance when compared with the doped (TCTA/TAPC) devices, the non-doped devices show low values for the current efficiency and EQE. However, the relative long roll-off of the brightness in these devices indicates the absence of triplet-triplet annihilation even in the neat copolymer films.

Table 3 - Non-doped Device Performance Data.

	V_{on}[a] (V)	L_{max}[b] (cd/m^2)	CE_{max}[c] (cd/A)	PE_{max}[d] (lm/W)	λ_{max} (nm)	EQE_{max}[e] (%)	CIE[f] (x,y)
P1	4.4	945	1.0	0.5	600	0.6	(0.48,0.45)
P2	5.4	801	2.2	0.9	585	1.2	(0.42,0.44)
P3	4.8	1246	3.4	1.3	570	1.6	(0.39,0.42)

a: The voltage at 1 cd/m2. b: Maximum luminance. c: Maximum current efficiency. d: Maximum power efficiency. e: Maximum external quantum efficiency. f: CIE coordinates at 6 V.

In summary, the formation of the electroplex in the devices has the benefit of making P3 to be warm-white (CIExy: 0.37, 0.38) emission source instead of the cool-white (CIExy: 0.25, 0.33) that is originated from PL. According with recent literature warm-white EL is desirable for comfortable ambient lighting that does not cause eye fatigue.[57,58] Therefore, this work reports the first example of warm-white TADF polymer OLEDs.

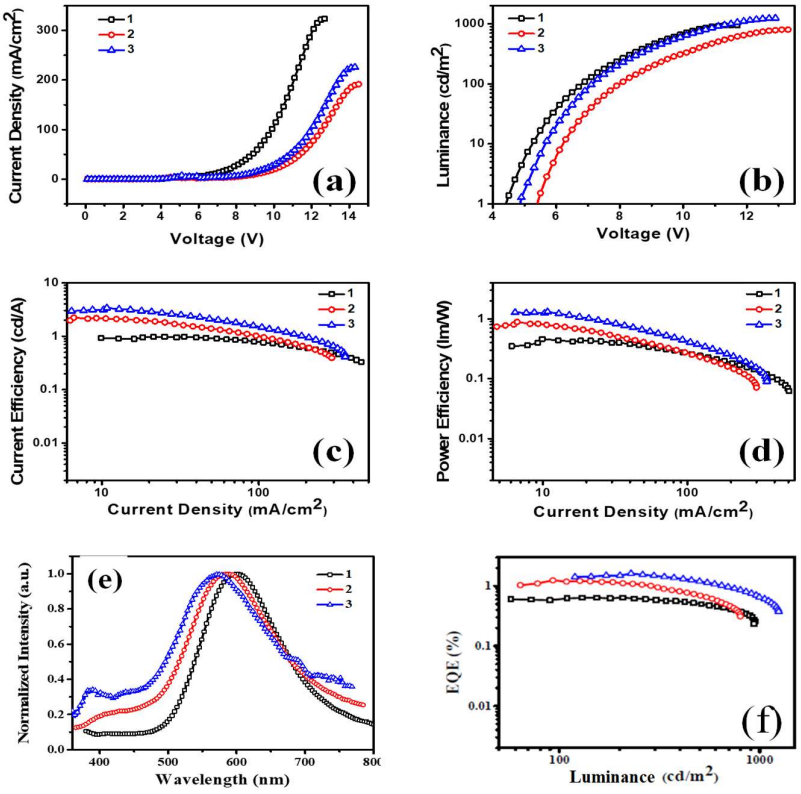

Figure 18 –Non-doped P1 (black), P2 (red) and P3 (blue) devices data: (a) Current density-voltage (*J-V*) curves; (b) Voltage-luminance curves; (c) Current efficiency; (d) Power efficiency; (e) Electroluminescent spectra of at 6 V; (f) External quantum efficiency (EQE) versus brightness.

9.8 Conclusion

In conclusion, a series of copolymers was synthesized in which 2-(10*H*-phenothiazin-10-yl)dibenzothiophene-*S,S*-dioxide units give yellow TADF and AIE, while dibenzothiophene units act as a blue fluorophore and host. The emission of P3 in THF solution can be tuned by simply increasing the water fraction, varying from sky-blue through white to yellowish-green. The copolymerization of lower bandgap TADF monomers with higher bandgap fluorophore is a promising method to tune the light wavelength and realize white light-emitting from a single polymer. OLEDs based on P1 and P2 show yellow emission, while P3 OLEDs show two-colour white emission with high CRI of 77, CE_{max} of 23.0 cd.A^{-1}, PE_{max} of 32.8 lm.W^{-1}, EQE_{max} of 10.4% with CIE coordinates of (0.37, 0.38) at 5 V. Moreover, EQE of 2.6%, CE of 5.7 cd.A^{-1}, PE of 4.7 lm.W^{-1} at 100 cd.m^{-2} are obtained. These new TADF copolymers provide guidelines to prepare higher efficiency polymeric TADF-based OLEDs and white emitters for displays and lighting. The macromolecular design is versatile allowing for a systematic variation of the steric and electronic properties of the spacer units, and their ratio in the copolymer structure: this could also be an effective strategy to tune the emission color.

9.9 Bibliography

1 Kido J, Kimura M, Nagai K, *Science* **1995**, *267*, 1332.

2 Sun Y, Giebink N. C, Kanno H, Ma B, Thompson M. E, Forrest S. R, *Nature* **2006**, *440*, 908.

3 Reineke S, Lindner F, Schwartz G, Lüssem B, Leo K, *Nature* **2009**, *459*, 234.

4 Lee S. Y, Yasuda T, Yang Y. S, Zhang Q, Adachi C, *Angew. Chem., Int. Ed.* **2014**, *126*, 6520.

5 Rao K. V, Datta K, Eswaramoorthy M, George S. J, *Adv. Mater.* **2013**, *25*, 1713.

6 Yang Q. Y, Lehn J. M, *Angew. Chem., Int. Ed.* **2014**, *53*, 4572.

7 Han M, Tian Y, Yuan Z, Zhu L, Ma B, *Angew. Chem., Int. Ed.* **2014**, *53*, 10908.

8 Shao S, Ding J, Wang L., Jing X., Wang F, *J. Am. Chem. Soc.* **2012**, *134*, 20290.

9 Poulsen D. A, Kim B. J., Ma B., Zonte C. S., Fréchet J. M. J., *Adv. Mater.* **2010**, *22*

10 Ying L, Ho C. L, Wu H, Cao Y, Wong W. W, *Adv. Mater.* **2014**, *26*, 2459.

11 Friend R, Gymer R, Holmes A, Burroughes J, Marks R, Taliani C, Bradley D, Dos Santos D, Bredas J., Lögdlund M., *Nature,* **1999**,*397*, 121.

12 Baldo M. A, O'Brien D, You Y, Shoustikov A, Sibley S, Thompson M, Forrest S, *Nature* **1998**, *395*, 151.

13 Schmidbauer S, Hohenleutner A, König B, *Adv. Mater.* **2013**, *25*, 2114.

14 Uoyama H, Goushi K., Shizu K., Nomura H, Adachi C, *Nature* **2012**, *492*, 234.

15 Zhang Q, Li B., Nomura H., Tanaka H., Adachi C., *Nat. Photonics* **2014**, *8*, 326.

16 Dias F. B, Bourdakos K. N., Jankus V., Moss K. C., Kamtekar K. T., Bhalla V., Santos J, Bryce M. R., Monkman A. P., *Adv. Mater.* **2013**,*25*, 3707.

17 Dias F. B, Santos J., Graves D. R., Data P., Nobuyasu R. S., Fox M. A., Batsanov A. S, Palmeira T, Berberan-Santos M. N., Bryce M. R., Monkman A. P., *Adv. Sci.* **2016**, *3*, 1600080.

18 Nishide J, Nakanotani H., Hiraga Y., Adachi C., *Appl. Phys. Lett.* **2014**, *104*, 233304.

19 Cho Y. J, Yook K. S., Lee J. Y., *Sci. Rep.* **2015**, *5*, 7859.

20 Kim B. S, Yook K. S., Lee J. Y., *Sci. Rep.* **2014**, *4*, 6019.

21 Zhang D, Duan L., Li Y., Zhang D., Qiu Y., *J. Mater. Chem. C* **2014**, *2*, 8191.

22 Li X. L, Xie G., Liu M., Chen D., Cai X., Peng J., Cao Y., Su S. J., *Adv. Mater.* **2016**, *28*, 4614.

23 Liu X. K, Chen W., Chandran H. T., Qing J., Chen Z., Zhang X. H., Lee C. S., *ACS Appl. Mater. Interfaces* **2016**, *8*, 26135.

24 Grimsdale C, Leok Chan K., Martin R. E., Jokisz P. G., Holmes A. B., *Chem. Rev.* **2009**, *109*, 897.

25 Xie G, Luo J., Huang M., Chen T., Wu K., Gong S., Yang C., *Adv. Mater.* **2017**, *29*,

26 Nikolaenko E, Cass M., Bourcet F., Mohamad D., Roberts M., *Adv. Mater.* **2015**, *27*

27 Lee S. Y, Yasuda T., Komiyama H., Lee J., Adachi C., *Adv. Mater.***2016**, *28*, 4019.

28 Luo J, Xie G., Gong S., Chen T., Yang C., *Chem. Commun.* **2016**, *52*, 2292.

29 Zhu Y, Zhang Y., Yao B., Wang Y., Zhang Z., Zhan H., Zhang B., Xie Z., Wang Y., Y. Cheng, *Macromolecules* **2016**, *49*, 4373.

30 Ren Z, Nobuyasu R. S., Dias F. B., Monkman A. P., Yan S., Bryce M. R., *Macromolecules* **2016**, *49*, 5452.

31 Xie Z, Chen C., Xu S., Li J., Zhang Y., Liu S., Xu J., Chi Z., *Angew. Chem. Int. Ed.* **2015**, *54*, 7181.

32 Xu S, Liu T., Mu Y., Wang Y. F., Chi Z., Lo C. C., Liu S., Zhang Y., Lien A., Xu J., *Angew. Chem., Int. Ed.* **2015**, *54*, 874.

33 Furue R, Nishimoto T., Park I. S., Lee J., Yasuda T., *Angew. Chem. Int. Ed.* **2016**

34 Gan S, Luo W., He B., Chen L., Nie H., Hu R., Qin A., Zhao Z., B. Z. Tang, *J. Mater. Chem. C* **2016**, *4*, 3705.

35 Hong Y, Lam W. J., Tang B. Z., *Chem. Soc. Rev.* **2011**, *40*, 5361.

36 Hong Y, Lam J. W., Tang B. Z., *Chem. Commun.* **2009**, 4332.

37 Mei J, Hong Y., Lam J. W., Qin A., Tang Y., Tang B. Z., *Adv. Mater.* **2014**, *26*,

38 Nobuyasu R. S, Ren Z, Griffiths G. C., Batsanov A. S., Data P., Yan S., Monkman A. P., Bryce M. R, Dias F. B., *Adv. Opt. Mater.***2016**, *4*, 597.

39 Ward J. S, Nobuyasu R. S., Batsanov A. S., Data P., Monkman A. P., Dias F. B., Bryce M. R, *Chem. Commun.* **2016**, *52*, 2612.

40 Tong H, Hong Y., Dong Y., Ren Y., Häussler M., Lam J. W., Wong K. S., Tang B. Z, *J. Phys. Chem. B* **2007**, *111*, 2000.

41 Li S, Shang Y., Zhao E., Kwok R. T., Lam J. W., Song Y., Tang B. Z., *J. Mater. Chem. C* **2015**, *3*, 3445.

42 Yook K. S, Lee J. Y., *Adv. Mater.* **2012**, *24*, 3169.

43 Yang W, Hou Q., Liu C., Niu Y., Huang J., Yang R., Cao Y., *J. Mater. Chem.* **2003**

44 Wang L, Wu Z. Y., Wong W. Y., Cheah K. W., Huang H., Chen C. H., *Org. Electron.* **2011**, *12*, 595.

45 Jeong S. H, Lee J. Y., *J. Mater. Chem.* **2011**, *21*, 14604.

46 Han C, Zhang Z., Xu H., Yue S., Li J., Yan P., Deng Z., Zhao Y., Yan P., Liu S., *J. Am. Chem. Soc.* **2012**, *134*, 19179.

47 Dias F. B, *Phil. Trans. R. Soc. A* **2015**, *373*, 20140447.

48 Fu Q, Chen J, Shi C., Ma D., *ACS Appl. Mater. Interfaces* **2012**, *4*, 6579.

49 Peng T, Yang Y., Bi H., Liu Y., Hou Z., Wang Y., *J. Mater. Chem.* **2011**, *21*, 3551.

50 Matsumoto N, Nishiyama M., Adachi C., *J. Phys. Chem. C* **2008**, *112*, 7735.

51 Al Attar H. A, Monkman A. P., *Adv. Mater.* **2016**, *28*, 8014.

52 Angioni E, Chapran M, Ivaniuk K, Kostiv N, Cherpak V, Stakhira P, Lazauskas A, Tamulevičius S, Volyniuk D, Findlay N. J, Tuttle T, Grazulevicius J. V, Skabara P. J, *J. Mater. Chem. C* **2016**, *4*, 3851.

53 Shin D. M, *J. Nanosci. Nanotechnol.* **2010**, *10*, 6794.

54 Yang C.-C, Hsu C.-J, Chou P.-T, Cheng H. C, Su Y. O, Leung M.-K, *J. Phys. Chem. B* **2010**, *114*, 756.

55 Kalinowski J, Cocchi M, Di Marco P, Stampor W, Giro G, Fattori V, *J. Phys. D: Appl. Phys.* **2000**, *33*, 2379.

56 Yang S, Zhang X, Hou Y, Deng Z, Xu X, *J. Appl. Phys.* **2007**, *101*, 096101.

57 Cui L. S, Liu Y, Liu X. Y, Jiang Z. Q, Liao L. S, *ACS Appl. Mater. Interfaces* **2015**, *7*, 11007.

58 Liu X. K, Chen Z, Qing J, Zhang W. J, Wu B, Tam H. L, Zhu F, Zhang X. H, Lee C. S, *Adv. Mater.* **2015**, *27*, 707.

59 Jaadane I., Boulenguez P., Chahory S., Carre S., Savoldelli M., Jonet L., Behar-Cohen F, Martinsons C., Torriglia A., *Free Radical Biol. Med.* **2015**, *84*, 373.

10. Thermally Activated Delayed Fluorescence in Cu(I) Complexes Originating from Restricted Molecular Vibrations

The mechanism of thermally activated delayed fluorescence (TADF) in molecules in aggregated or condensed solid states has been rarely studied and is not well understood. Nevertheless, many applications of TADF emitters are strongly affected by their luminescence properties in the aggregated state. In this study, two new isomeric tetradentate Cu(I) complexes which simultaneously show aggregation induced emission (AIE) and TADF characteristics were designed for the first time. We firstly provide direct evidence that effectively restricting the vibrations of individual molecules is a key requisite for TADF in these two Cu(I) complexes through in-depth photophysical measurements combined with kinetic methods, single crystal analysis and theoretical calculations. These findings should stimulate new molecular engineering endeavours in the design of new AIE-TADF active materials with highly emissive aggregation states.

*This work is published in: Guangfu Li, Roberto S. Nobuyasu, Baohua Zhang, Yun Geng, Bing Yao, Zhiyuan Xie, Dongxia Zhu, Guogang Shan, Weilong Che, Likai Yan, Zhongmin Su, Fernando B. Dias, and Martin R. Bryce, Thermally Activated Delayed Fluorescence in Cu(I) Complexes Originating from Restricted Molecular Vibrations, Chemistry-A European Journal, **2017**, 11761–11766*

10.1 Introduction

Recent developments of thermally activated delayed fluorescence (TADF) materials have attracted tremendous attention as they can be used as highly efficient emitter materials for organic light emitting diodes (OLEDs).[1-9] TADF is a promising solution for converting electricity into light at an internal quantum efficiency (IQE) of nearly 100%, which utilizes the up-conversion from triplet excitons to singlet states by reverse intersystem crossing (RISC).[10-13] However, a stubborn problem for TADF materials in practical applications is that most TADF emitters suffer from aggregation-caused quenching (ACQ) in the condensed phase. Therefore, effective TADF could only be realized in a doped host-guest system with careful control of their concentrations to restrict the nonradiative deactivation processes. Aggregation-induced emission (AIE) materials are, therefore, able to respond to these challenges. AIE molecules were first reported by Tang,[14] and while they show weak emission in dilute solution, upon aggregation they emit strongly, due to restriction of intramolecular rotation. Recently, Yasuda et al. reported a series of carborane derivatives that simultaneously show AIE and TADF characteristics.[15] OLEDs utilizing these o-carborane derivatives as a non-doped emission layer exhibited

maximum EQEs as high as 11%. Thus, AIE-TADF active materials are regarded as promising highly efficient luminescent materials and widely used in the numerous optoelectronic applications especially for non-doped OLEDs. However, the mechanism of TADF in aggregated molecules is still unclear and has not been studied in detail, although it is essential for many of the desired applications of these emitters. Fundamental factors that lead to enhanced emission of dyes in viscous and solid-state environments are of ongoing interest.[16-20]

Cu(I) complexes with TADF character have been used in OLEDs and some derivatives show impressive EL performance. Recently, dual-emissive Cu(I) complexes which can simultaneously show TADF and phosphorescence emission have been demonstrated by Yersin et al. and other groups.[21-24] Cu(I) complexes have the practical advantages of relatively low-cost, high abundance of copper, and no presence of rare metals, such as iridium.

10.2 Results and Discussion

The aim of the present study is to explore the coexistence of TADF and AIE in the new copper complexes **1** and **2**. We demonstrate that both complexes show almost no emission in solution, but strong luminescence and obvious TADF is observed with an extremely short delay lifetime in their aggregation state. To our knowledge, this photophysical phenomenon has not been previously reported in Cu(I) complexes, although the coexistence of both TADF and AIE in all-organic molecules has been reported in a few cases.[25-32] The relationship between AIE and TADF is still not clear. Herein, we address the pertinent question: does aggregation induce or promote TADF. Addressing this question is of fundamental importance for a better understanding of the mechanism of AIE-TADF and further designing this kind of material for use in OLEDs.

The kinetics of TADF is investigated in two Cu(I) complexes in pristine film state and in PMMA matrices. The PMMA matrices of different molecular weight, doped with complexes **1** and **2**, are used in solid-state 'dilution' experiments to probe the role of intramolecular vibrations on the observation of TADF. The similar TADF behaviour presented in both high molecular weight host (H-PMMA) and in pristine films clearly reveals that effectively restricting specific vibrations of individual emitter molecules is the origin of TADF for these Cu(I) complexes. Thus, a guideline for designing AIE-TADF active materials is presented for the first time.

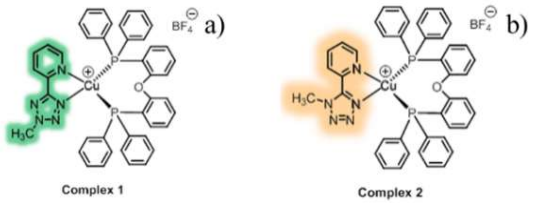

Figure 1 - Chemical structure of isomeric complexes a) **1** and b) **2**.

The chemical structures of the two new isomeric complexes **1** and **2** are shown in Figure 1a and 1b.[1] The UV/vis absorption and emission spectra of **1** and **2** in degassed solution (CH_2Cl_2) are depicted in Figure 2.

Upon photoexcitation, **1** and **2** are almost non-emissive in pure CH_2Cl_2 solution at room temperature. However, bright emission is observed in the pristine film state with a short luminescence decay time.

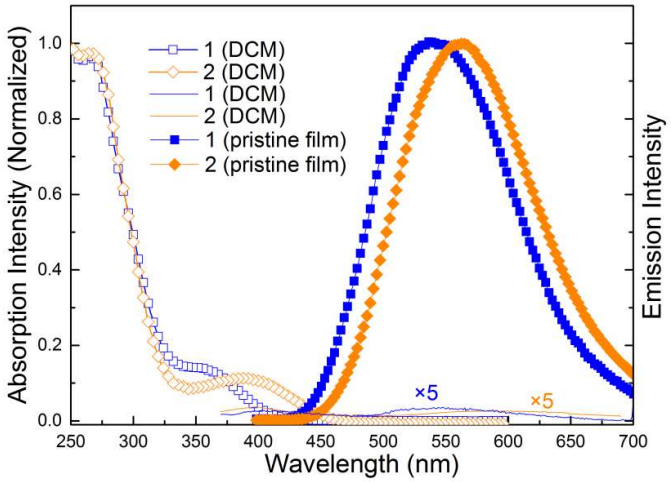

Figure 2 - UV/vis absorption and emission spectra of **1** and **2** in degassed solution (CH_2Cl_2) and pristine film at room temperature.

This short-lived luminescence is in contrast with conventional Cu(I) complexes, where luminescence is observed with relatively long decay times (phosphorescence decay times of several 100 µs up to a few ms).[33] The luminescence decays of complexes **1** and **2** in their pristine film state are even shorter than all the recently reported decay times in mono-nuclear Cu(I) complexes with TADF.[4,16-18,21] This implies that **1** and **2** may be potential outstanding TADF materials with high reverse intersystem crossing rate (k_{RISC}) by efficiently eliminating the triplet-triplet annihilation and triplet-polaron quenching in

[1] The Cu(I) complexes studied in this chapter were synthesized at *Dongxia Zhu's Research Group*.

their pristine film state.[33] The detailed photophysical data of **1** and **2** are summarized in Table 1.

Table 1 - Photophysical data for complexes **1** and **2** at room temperature.

Complex	λ_{abs}[a] (nm)	λ_{em}[b,c,d] (nm)	τ[b] (μs)	Φ_L[b,e] (%)
1	264, 358_{sh}	533, 516, 516	0.90, 5.0	15.5, 47.1%
2	269, 386_{sh}	572, 556, 556	0.95, 4.2	2.9, 9.4%

[a] Measured in CH_2Cl_2 (1.0×10^{-5} M). [b] Measured in the pristine film; error ± 5%. [c] Measured in low molecular weight (L-PMMA) film. [d] Measured in the high molecular weight (H-PMMA) film. [e] Measured in the crystalline state.

The energy levels of the complexes calculated from their electrochemical and photophysical data are listed in Table 2.

Table 2 - Energy levels and S1-T1 gaps of the complexes **1** and **2**.[2]

Complex	ΔE_g[a] (eV)	HOMO[b] (eV)	LUMO[c] (eV)	S_1[d] (eV)	T_1[e] (eV)	ΔE_{ST} (eV)
1	3.0	-5.5	-2.5	2.75	2.58	0.17
2	2.72	-5.49	-2.77	2.72	2.50	0.22

10.3 Environmental effect

To investigate the effect of molecular vibrations on the emission of **1** and **2** in their aggregation state, steady-state and time-resolved photoluminescence experiments were performed in their pristine film state, and in composite films of both complexes dispersed in PMMA hosts. Two PMMA samples, one with low molecular weight, L-PMMA (Mn = 15,000), and the other with high molecular weight, H-PMMA (Mn = 960,000), were used to fabricate thin films of **1** and **2**. Thermal gravimetric analysis (TGA) data showed that H-PMMA has a significantly higher Tg (130 °C) than L-PMMA (86 °C) consistent with H-PMMA being a stiffer material.[3]

The temperature dependence of the steady-state emission spectra of the Cu(I) complexes **1** and **2** in neat film and doped in PMMA are compared in Figure 3. This allows the roles of thermal vibrations and intermolecular interactions on the excited state dynamics in these two complexes to be determined.

[2] These results were simulated by Dongxia Zhu's Research Group.
[3] These studies were performed at Martin R. Bryce's Research Group.

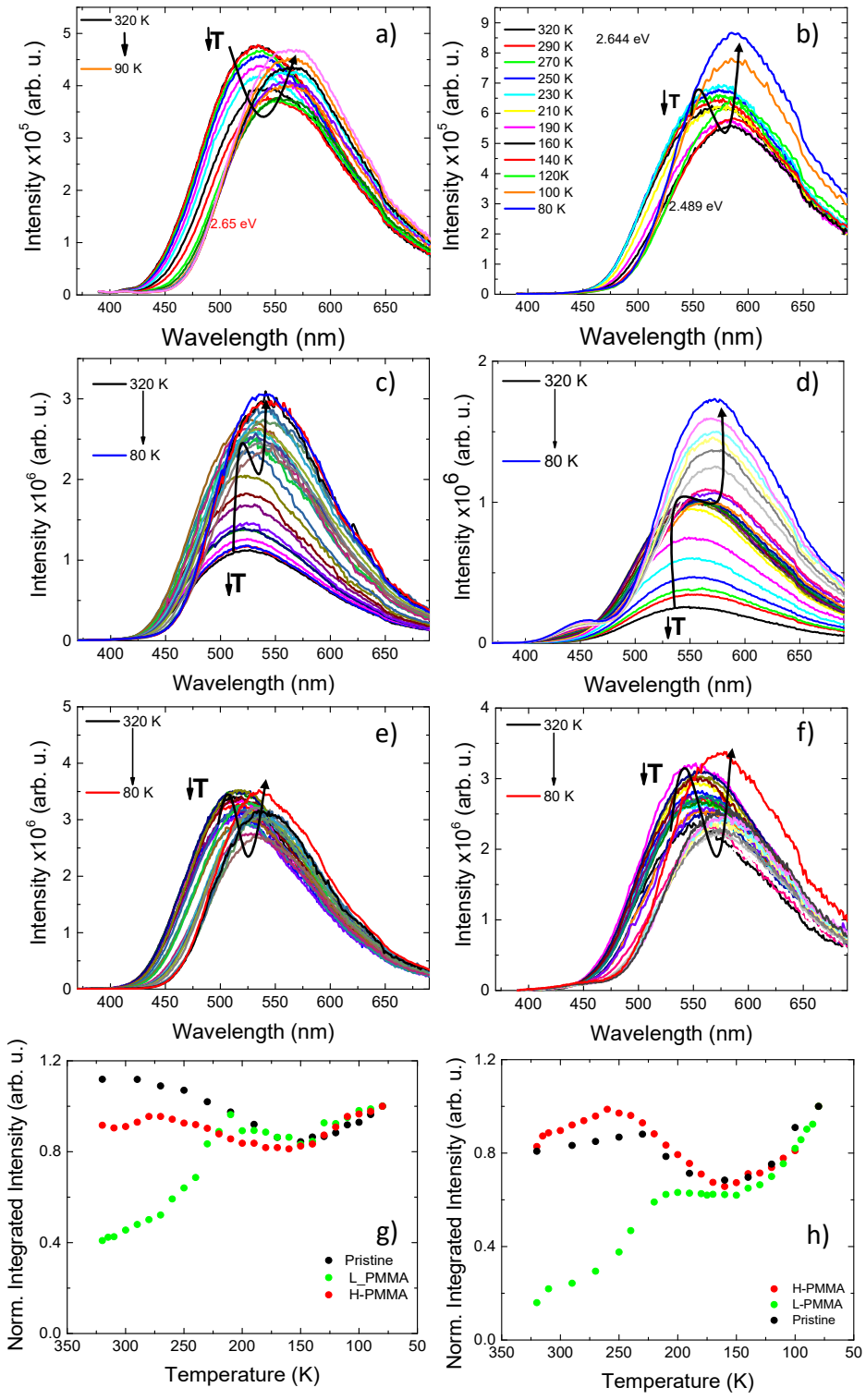

Figure 3 - The steady steady-state fluorescence from 320 to 80 K in pristine film for **1** a) and **2** b), respectively. The steady steady-state fluorescence from 320 to 80 K in L-PMMA for **1** c) and **2** d), respectively. The steady-state fluorescence from 320 to 80 K in H-PMMA for 1 e) and **2** f), respectively. Temperature dependence of the luminescence intensity as a function of temperature (T) for g) **1** and h) **2**.

The two PMMA hosts with different molecular weight appear to be able to suppress molecular vibrations to different degrees. This results in marked differences of the temperature dependence of the photoluminescence of **1** and **2**, collected in pristine films (Figures 3a and 3b) in L-PMMA (Figures 3c and 3d) and in H-PMMA (Figures 3e and f). Additionally, in Figures 3g and 3h the temperature dependence of the photoluminescence in the three samples shows clear differences in the high temperature region (above 170 K), but agree extremely well at low temperatures (below 170 K).

In the pristine film, the photoluminescence spectra of **1** and **2** show a dominant TADF mechanism between 320-170 K (Figures 3a and b). In this temperature range the emission intensity first increases and then decreases with decreasing temperature, showing a typical bell-shape that is characteristic of the equilibrium between the singlet and triplet states, mediated by the k_{RISC}, which drive the up-conversion of triplets back to the singlet manifold, and the thermal vibrations (internal conversion, IC) that quench the excited state population. Below 170 K the TADF contribution to the steady-state emission is negligible and phosphorescence dominates. In this temperature region the luminescence is dominated by phosphorescence from the lowest T1 state, and is thus controlled by the decrease in the internal conversion, and as this continues decreasing with temperature, the steady-state emission slowly increases as observed in Figure 3g. Note also the change observed in the emission spectra in Figures 3a and b. With decreasing temperature λ_{max} shifts to longer wavelengths. This is consistent with the emission being dominated by TADF at high temperatures, i.e. emission from the singlet excited state, and by phosphorescence at low temperatures, i.e. emission from the low energy triplet state. Remarkably, this behaviour is not observed for the films of **1** and **2** in L-PMMA. Here, the emission comes mainly from the triplet state and the contribution of TADF is practically non-existent. In this host the vibrational quenching dominates. The emission intensity, therefore, increases with decreasing temperature in the entire temperature range, and more markedly from 320 K to 170 K, where the effect of suppressing vibrations is more pronounced. This is presented in Figures 3c, and 3d.

In H-PMMA (Figures 3e and f), as in L-PMMA, the intermolecular interactions between **1** (or **2**) molecules are practically non-existent. This, therefore, indicates that the H-PMMA host is more able to suppress vibrations, in the same way as the intermolecular interactions between **1** (or **2**) molecules do in the pristine film. This enables the reverse intersystem crossing to become operative and to activate the TADF emission. However, in L-PMMA this is not the case, and the internal conversion dominates in the entire temperature range.

Below 170 K the temperature dependence of the photoluminescence is similar in all samples. This shows that once k_{RISC} is suppressed, and as the effect of vibrations is decreasing due to lowering the temperature, the differences in the host are not so important to the outcome of the emission. These experiments highlight the fact that the nonradiative pathways play a crucial role in the triplet harvesting mechanism in complexes **1** and **2**. Moreover, in the case of **1**, and to lesser extent in **2**, the intermolecular interactions present in the pristine films, due to the molecular packing, are able to effectively suppress vibrations which otherwise will quench TADF.

10.4 Time resolved photoluminescence

Time resolved spectroscopy was used to follow the excited state dynamics in 1 and 2. The luminescence decays of **1** and **2** at 300 K in pristine films and dispersed in L-PMMA are shown in Figure 4a and b.

Both luminescence decays of 1 at 300 K are characterized by a fast component around 5 ns and 7.9 ns in pristine film and L-PMMA, respectively. These fast components are followed by a long bi-exponential decay, with time constants of 0.9 µs and 5 µs in the pristine film, and of 9 and 30 µs in L-PMMA.

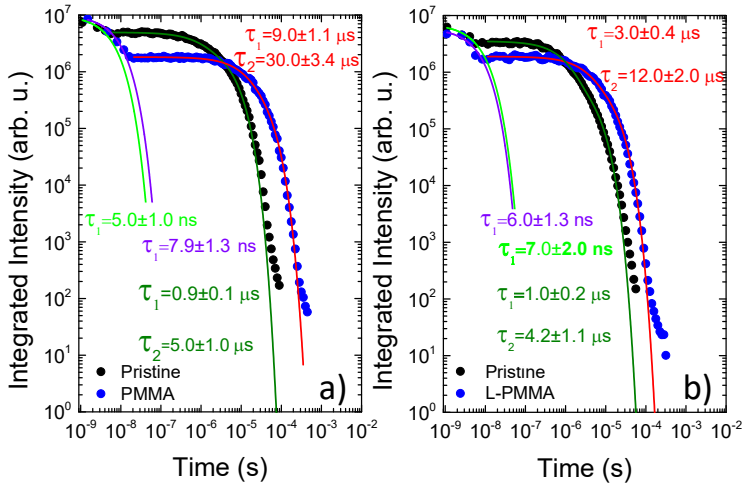

Figure 4 – The fluorescence decays collected in pristine and L-PMMA films at room temperature for **1** a) and **2** b), respectively.

The lifetime in L-PMMA is thus longer than in the pristine film. This reflects the effect of TADF in the pristine film, which at 300 K more rapidly quenches the triplet state, whereas in L-PMMA the emission occurs mainly directly from the triplet state, e.g. phosphorescence. These observations are consistent with the more intense emission in the pristine film below 1 µs, where the TADF dominates. The complex **2** shows similar behaviour (Figure 4b).

Importantly, this shows also how the presence of TADF is important to accelerate the excited state decay in Cu(I) complexes and minimize the roll-off effect in devices.

The decays obtained as a function of temperature for the pristine films, L-PMMA and H-PMMA films, and crystalline samples are entirely consistent with the relative importance of TADF (Figure 5 and Figure 6).

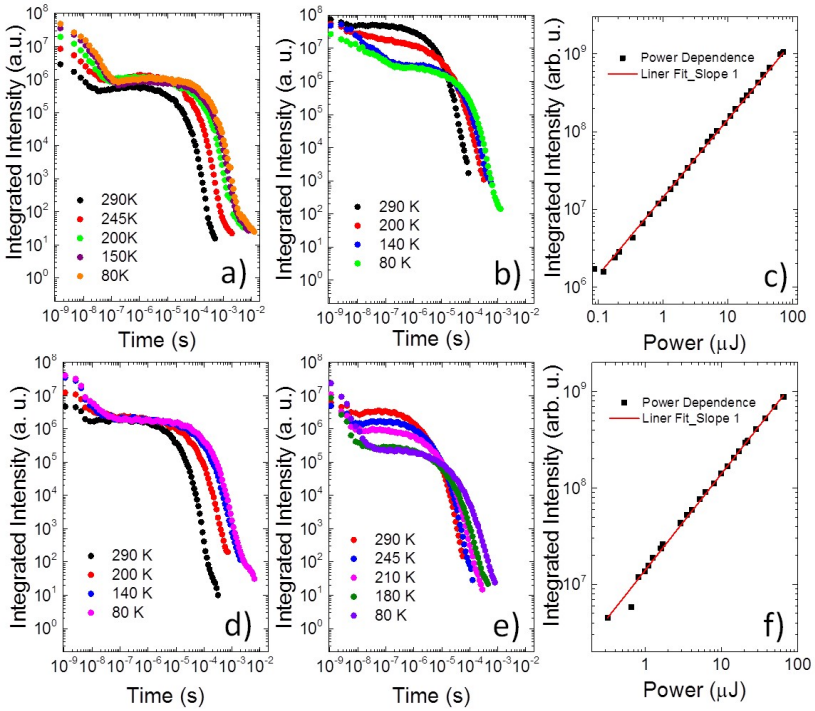

Figure 5 - Temperature dependence of emission decays in L-PMMA for **1** a) and **2** d), respectively. Temperature dependence of emission decays in pristine film for **1** b) and **2** e), respectively. Power dependence of DF emission in pristine film for **1** c) and **2** f), respectively.

In pristine films, H-PMMA and crystalline samples both complexes **1** and **2** exhibit clear temperature dependence for the delayed fluorescence which is characteristic of the TADF mechanism (Figure 5b, 5e and Figure 6). Here with decreasing temperature the emission intensity decreases and the lifetime increases, consistent with a slower depopulation of the triplet state. In contrast, in the L-PMMA host (Figure 5a and 5d) the photoluminescence decay is dominated by the non-radiative constants. This is clearly observed in the temperature dependence of the prompt fluorescence component which increases in intensity with a decrease in temperature, and the increase of the phosphorescence lifetime in both compounds, as a direct response of suppressing the non-radiative decay pathways.

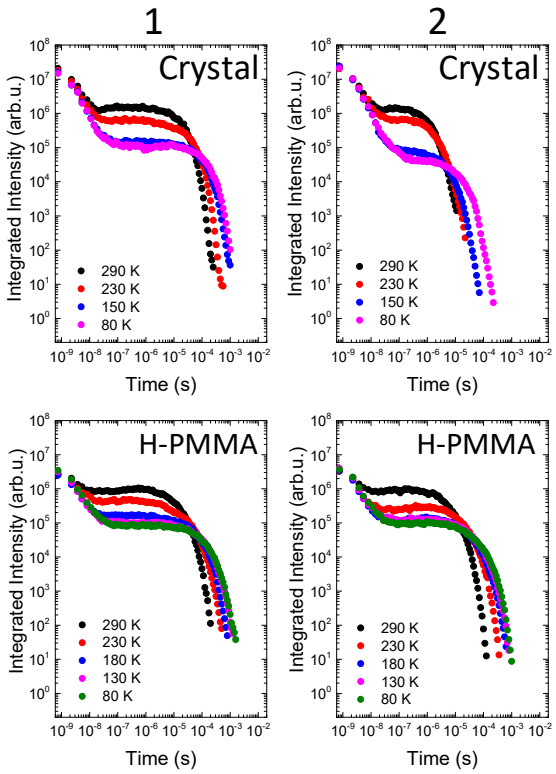

Figure 6 - Temperature dependence of emission decays of crystals and H-PMMA films of **1** and **2**.

Note that no TADF component is observed on these decays. In Figure 5c and 5f the power dependence of the delayed fluorescence is shown for both compounds to confirm the origin of the mechanism responsible for the long-lived fluorescence as TADF (slope 1) and not triplet-triplet annihilation (TTA) (slope 2).[34] These experiments were performed on pristine films, where the TADF component is stronger.

10.5 X-Ray structure[4]

The two isomeric complexes **1** and **2** differ only in the substitution pattern on the tetrazolate ring, yet this is shown to have a profound effect on the supramolecular structure and photophysical properties. It is very instructive to compare the single-crystal X-ray structures of the two isomeric complexes. Both complexes **1** and **2** exhibit highly-distorted tetragonal coordination, typical of Cu(N^N)(POP) complexes (Figure 7).[18]

[4] X-ray crystal structures were determined by Dongxia Zhu's Research Group.

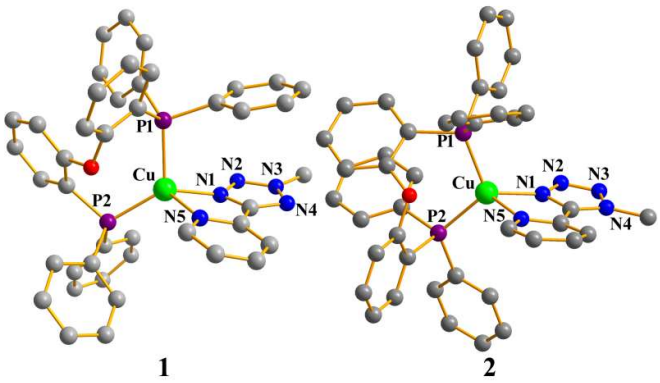

Figure 7 - ORTEP drawing of 1 and 2.

Crystals of **1** revealed multiple modes of intra- and intermolecular interactions leading to a fascinating 3D supramolecular structure (Figure 8). Important interactions are summarized in Table 3.

Table 3 - The distances of intra- or intermolecular interactions for 1 and 2.

1		**2**	
Intramolecular π···π stacking	3.6 Å	Intramolecular π···π stacking	3.5 Å
Intermolecular π···π stacking	3.5 Å	Intermolecular CH···π interaction	2.5 Å
Intermolecular head-to-tail stacking	3.7 Å	Intermolecular head-to-tail stacking	3.9 Å

Generally, the presence of strong intra- and intermolecular interactions would supply a more rigid environment and thereby effectively limit molecular distortions in the excited state, leading to bright emission through restricting the non-radiative processes.[19,35] Furthermore, due to the small ΔE(S1-T1) value obtained from photophysical experiments, and from the DFT calculations (see below), TADF is triggered in the pristine aggregation state of complex **1** which is similar to the situation in H-PMMA. It is worth noting that intermolecular aromatic stacking has been shown to offer a charge-transfer pathway and to enhance the carrier-transport ability, which is essential for excellent electroluminescent materials.[36,37]

Due to the relatively weak intermolecular interactions in **2**, compared with **1**, complex **2** showed less distortion of the tetragonal coordination in the ground state.

For the excited state, Riesgo et al. stated that the distortion of Cu complexes is directly related to their ‘‘Stokes-like’’ shift, that is, the difference in wavelength between absorption and emission spectra.[38] Indeed, the smaller Stokes-like shifts for **1** compared with **2** (Figure 2 and Table 1) indicate that excited-state distortion is suppressed more effectively in 1 which, in turn, means that for 1 the non-radiative process is suppressed. It

could, therefore, be expected that the PLQY for **1** is substantially higher than **2**. Indeed PLQYs of 47.1% and 9.4% were measured in the crystalline state for **1** and **2**, respectively (Table 1).

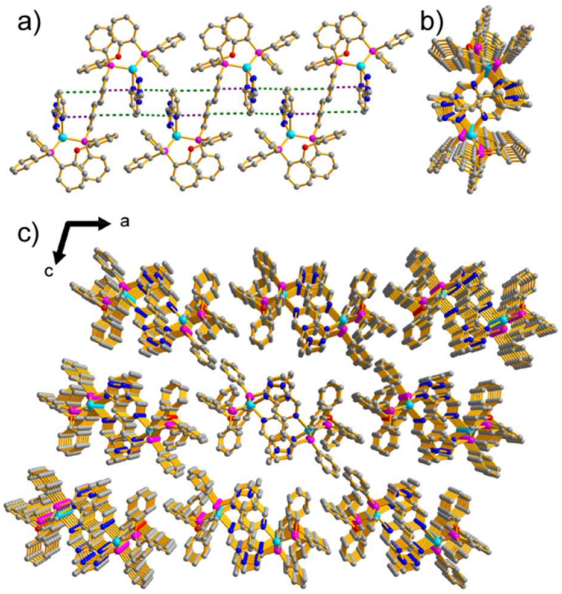

Figure 8 - a) The one-dimensional supramolecular chain structure in **1**. (Purple dashed lines represent intramolecular π···π interactions and green dashed lines represent two kinds of intermolecular π···π interactions). b) The cross-section view of the one-dimensional supramolecular chain structure unit in **1**. c) The three-dimensional supramolecular structure of **1**.

To further probe the interesting optoelectronic phenomena discussed above, we performed (Time-Dependent) Density Functional Theory ((TD)DFT) calculations on complexes **1** and **2**.[5] The electronic structures based on the optimized geometries of **1** and **2** plotted in Figure 9 clearly shows the separate electronic occupations in the highest occupied molecular orbital (HOMO) and the lowest unoccupied molecular orbital (LUMO) for each complex, facilitating a small ΔE(S1-T1) which is a characteristic of TADF materials.[39]

[5] All calculations were performed by Dongxia Zhu's Research Group.

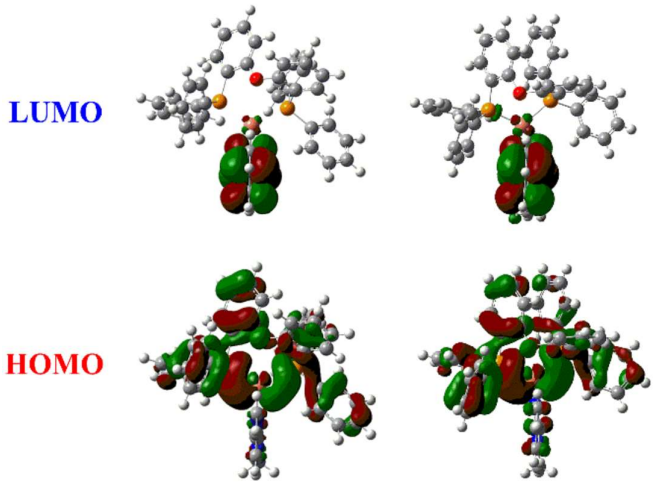

Figure 9 – The frontier molecular orbitals of **1** and **2** based on optimized ground-state geometries calculated at B3LYP/6-31G(d,p) (LAND2DZ for Cu atoms) level.[6]

Since the value of ΔE(S1-T1) is usually used to assess the ability of reverse intersystem crossing from T1 to S1,[41] it was evaluated here for every structure (IM, LPM and CM) presented in Figure 10 to explain the change of luminescence properties in the different situations mentioned above.

Table 4 - The ΔE(S1-T1) (eV) values of three models (IM, LPM and CM) for **1** and **2** obtained by B3LYP/6-31G(d,p) (LAND2DZ for Cu atoms) method. For a definition of θ see Figure 10.

	1			**2**	
IM 1		0.136	**IM 2**		0.177
LPM 1	θ = 92	0.185	**LPM 2**	θ = -6	0.271
	θ = 97	0.202		θ = -11	0.277
	θ = 102	0.224		θ = -16	0.283
	θ = 107	0.248		θ = -21	0.290
	θ = 112	0.271		θ = -26	0.297
	θ = 117	0.291		θ = -31	0.303
	θ = 122	0.307		θ = -36	0.308
	θ = 127	0.319		θ = -41	0.311
	θ = 132	0.326		θ = -46	0.314
	θ = 137	0.325		θ = -51	0.315
	θ = 142	0.316		θ = -56	0.315
CM 1		0.185	**CM 2**		0.271

[6] HOMO/LUMO simulation were performed by *Dongxia Zhu's Research Group.*

The nomenclature IM, LPM and CM defines the optimized isolated molecule, the simulated molecule in low PMMA (L-PMMA) host material, and the molecule in the crystal structure, respectively. As mentioned above, the complex in L-PMMA host material has more freedom to rotate the phenyl group than in the crystal structure. Therefore, an important dihedral angle θ, which corresponds to the nearest phenyl group to the tetrazole ring, as a representative angle, was changed and scanned for **1** and **2**.

The results collected in table 4 shows: (i) both the IM and CM structures have a smaller ΔE(S1-T1) value, further verifying that TADF may occur in isolated molecules (solution state) and in the aggregation state (crystal structure). However, there is a huge difference in optimized geometries between ground state and S_1 along with T_1 collected in the aggregation state(crystal structure). This is crucial for the quenching of TADF in the solution state.

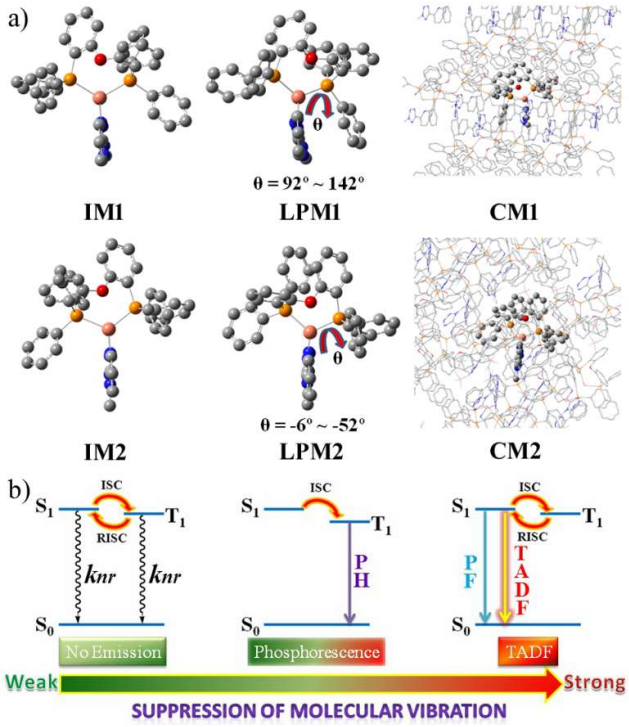

Figure 10 - a) Diagram of three models (IM, LPM and CM) for 1 and 2. The IM, LPM and CM represent the optimized isolated molecule, simulated molecule in low PMMA host material, and the molecule in the crystal structure, respectively. (Hydrogen atoms are omitted for clarity). b) The relationship between restriction of molecular vibrations and luminescent properties in two Cu(I) complexes.

(ii) With the increase of θ, ΔE(S1-T1) becomes larger for both 1 and 2, suggesting the rotation of the nearest phenyl group to the tetrazole ring raises ΔE(S1-T1) relative to the crystal structure. In which might reduce the ability for transfer from the T1 to the S1 state. Thus for 1 and 2 phosphorescent emission, rather than TADF, appears in the L-

PMMA environment in which case the molecules are free to rotate their phenyl groups. Hence, the relationship between restriction of molecular vibrations and luminescence property in two Cu(I) complexes has been summarized in Figure 10b. Moreover, a singlet-triplet gap around 0.2 eV, as predicted in the calculations, is in excellent agreement with the energy difference determined from the onset of the emission spectra in pristine films (shown in Figures 3a and 3b).

10.6 Conclusion

In summary, two new AIE-TADF active isomeric Cu(I) complexes were synthesized. Solid-state 'dilution' experiments investigated their photophysical properties at different degrees of suppression of molecular vibrations, revealing phosphorescence in low M_{Wt} PMMA (L-PMMA), but efficient TADF in high M_{Wt} PMMA (H-PMMA). The similar TADF behavior in H-PMMA and in the pristine aggregated state (neat thin films) suggests that TADF behaviour is strongly influenced by effectively restricting the vibration of individual molecules through intermolecular interactions. TD-DFT calculations are in excellent agreement with the observed photophysical properties of the complexes. Our findings may stimulate new molecular engineering endeavors in the design of new AIE-TADF active materials with highly emissive aggregation states. Moreover, the extremely short delayed lifetime in pristine film state suggests that both complexes are candidates for non-doped OLEDs.

10.7 Bibliography

1. Etherington M. K, Gibson J, Higginbotham H. F, Penfold T. J, Monkman A. P, *Nat. Commun.* **2016**, 7, 13680
2. Lee S. Y, Adachi C, Yasuda T., *Adv. Mater*. **2016**, 28, 4626-4631
3. Rajamalli P, Senthilkumar N, Gandeepan P., Huang P. Y., Huang M. J., Ren-Wu C. Z., Yang C. Y, Chiu M. J, Chu L. K, Lin H. W., Cheng C. H, *J. Am. Chem. Soc*. **2016,** 138, 628-634
4. Wang S, Yan X, Cheng Z, Zhang H, Liu Y, Wang Y, *Angew. Chem. Int. Ed*. **2015**, 54, 13068-13072
5. Wong M. Y, Zysman-Colman E., *Adv. Mater*. **2017**, 29, 1605444
6. Yang Z, Mao Z, Xie Z, Zhang Y, Liu S, Zhao J, Xu J, Chi Z,. Aldred M. P, *Chem. Soc. Rev*. **2017**, 46, 915-1016

7. Park I. S, Numata M, Adachi C, Yasuda T, *Bull. Chem. Soc. Jpn*. **2016**, 89, 375-377
8. Etherington M. K, Franchello F, Gibson J, Northey T, Santos J, Ward J. S. Higginbotham H. F, Data P, Kurowska A, Dos Santos P. L, Graves D. R, Batsanov A. S, Dias F. B, Bryce M. R, Penfold T. J, Monkman A. P, *Nat. Commun.* **2017**, 8, 14987
9. Dai D, Romanov A. S, Yang L, Richter J. M, Rivett J. P. H, Jones S, Thomas T. H, Jalebi M. A, Friend R. H, Linnolahti M, Bochmann M, Credgington D, *Science* **2017**, 356, 159-163.
10. Dias F. B, Bourdakos K. N, Jankus V, Moss K. C, Kamtekar K. T, Bhalla V, Santos J., Bryce M. R, Monkman A. P, *Adv. Mater*. **2013**, 25, 3707-3714
11. Endo A, Sato K, Yoshimura K, Kai T, Kawada A, Miyazaki H, Adachi C, Appl. *Phys. Lett*. **2011**, 98, 083302
12. Leitl M. J, Krylova V. A, Djurovich P. I, Thompson M. E, Yersin H, *J. Am. Chem. Soc*. **2014**, 136, 16032-16038
13. Uoyama H, Goushi K, Shizu K, Nomura H, Adachi C, *Nature* **2012**, 492, 234-238.
14. Luo J, Xie Z, Lam J. W. Y, Cheng L, Tang B. Z, Chen H,. Qiu C, Kwok H. S, Zhan X, Liu Y, Zhu D*, Chem. Commun*. **2001**, 1740-1741.
15. Furue R, Nishimoto T, Park I. S, Lee J, Yasuda T, *Angew. Chem. Int. Ed*. **2016**, 55
16. Qian H, Cousins M. E, Horak E. H, Wakefield A, Liptak M. D, Aprahamian I., *Nat. Chem*. **2017**, 9, 83-87.
17. Leitl M. J,. Zink D. M, Schinabeck A, Baumann T, Volz D, Yersin H, *Top. Curr. Chem.* **2016**, 374, 25-68
18. Wada A, Zhang Q, Yasuda T, Takasu I, Enomoto S, Adachi C, *Chem. Commun.* **2012**, 48, 5340-5342
19. Chen X.-L, Yu R, Zhang Q.-K, Zhou L.-J, Wu X.-Y, Zhang Q, Lu C.-Z, *Chem. Mater*. **2013**, 25, 3910-3920
20. Volz, D. Chen Y, Wallesch M, Liu R., Flechon C, Zink D. M, Friedrichs J,. Flugge H, Steininger R, Gottlicher J, Heske C, Weinhardt L, Brase S, So F, Baumann T, *Adv. Mater*. **2015**, 27, 2538-2543.
21. Chen X. L, Yu R, Wu X. Y, Liang D, Jia J. H, Lu C. Z, *Chem. Commun*. **2016,** 52, 6288-6291
22. Hofbeck T, Monkowius U, Yersin H, J. Am. *Chem. Soc*. **2015**, 137, 399-404
23. Nitsch J, Lacemon F, Lorbach A, Eichhorn A, Cisnetti F, Steffen A, *Chem. Commun.* **2016**, 52, 2932-2935

24. Zhang J, Duan C, Han C, Yang H, Wei Y, Xu H, *Adv. Mater.* **2016**, 28, 5975-5979.
25. Aizawa N, Tsou C.-J, Park I. S, Yasuda T, *Polymer J.* **2016**, 49, 197-202
26. Guo J, Li X.-L, Nie H, Luo W, Gan S, Hu S, Hu R, Qin A, Zhao Z, Su S.-J, Tang B. Z, *Adv. Funct. Mater*. **2017,** 1606458
27. Matsuoka K, Albrecht K, Yamamoto K, Fujita K, *Sci. Rep*. **2017,** 7, 41780
28. Tsujimoto H, Ha D. G., Markopoulos G., Chae H. S, Baldo M. A, Swager T. M., *J. Am. Chem. Soc*. **2017**, 139, 4894-4900
29. Gan S, Luo W, He B, Chen L, Nie H, Hu R, Qin A, Zhao Z, Tang B. Z., *J. Mater. Chem. C* **2016**, 4, 3705-3708
30. Hu J, Zhang X, Zhang D, Cao X, Jiang T, Zhang X, Tao Y, *Dyes and Pigments* **2017**, 137, 480-489
31. Xie Z, Chen C, Xu S, Li J, Zhang Y, Liu S, Xu J, Chi Z, *Angew. Chem. Int. Ed*. **2015**, 54, 7181-7184
32. Xu S, Liu T, Mu Y, Wang Y. F, Chi Z, Lo C. C, Liu S, Zhang Y, Lien A, Xu J, *Angew. Chem. Int. Ed*. **2015**, 54, 874-878.
33. Czerwieniec R, Leitl M. J, Homeier H. H. H., Yersin H, *Coord. Chem. Rev*. **2016**, 325, 2–28.
34. Dias F. B., *Phil. Trans. R. Soc. A* **2015**, 373, 0447.
35. Yersin H, Rausch A. F., Czerwieniec R., Hofbeck T., Fischer T., *Coord. Chem. Rev*. **2011**, 255, 2622-2652
36. Wang Y, Zhang W, Li Y, Yang G, *Chem. Mater*. **1999,** 11, 530-532
37. Wang K, Zhao F, Wang C, Chen S, Chen D, Zhang H, Liu Y, Ma D, Wang Y, *Adv. Funct. Mater.* **2013**, 23, 2672-2680.
38. Riesgo E. C, Hu Y.-Z, Bouvier F, Thummel R. P, *Inorg. Chem*. **2001**, 40, 3413
39. Ishimatsu R, Matsunami S., Kasahara T., Mizuno J., Edura T, Adachi C, Nakano K, Imato T, *Angew. Chem. Int. Ed*. **2014**, 53, 6993-6996
40. Tanaka H, Shizu K, Miyazaki H, Adachi C*, Chem. Commun.* **2012**, 48, 11392-11394.
41. Nakanotani H, Higuchi T, Furukawa T, Masui K, Morimoto K, Numata M, Tanaka H, Sagara Y, Yasuda T, Adachi C, *Nat. Commun.* **2014**, 5, 4016.

11 Conclusions

The research carried out in this thesis has established experimental evidence for the role of triplet excited states, localized on the electron donor (D) or electron acceptor (A) moieties of D-A and D-A-D molecules, to promote efficient TADF emission.[1–3] At the time when this work started, the reverse intersystem crossing mechanism (RISC), by which triplets are promoted to the singlet manifold, was still not entirely understood. It was however well-known that a small energy gap between singlet and triplet states is necessary to achieve efficient delayed fluorescence. Molecules with D-A or D-A-D structure create excited states of charge transfer character (CT), which show small exchange energy and give origin to a small energy gap between the singlet (^{1}CT) and the triplet (^{3}CT) states. It was, therefore, thought that an ideal TADF molecule would have the ^{1}CT and ^{3}CT states as the lowest energy states.[4,5] In this way RISC would occur with minimal losses, and maximum TADF efficiency would be obtained. The studies carried out in this thesis show this assumption is not correct, and confirmed previous theoretical studies, which proposed that the intersystem crossing mechanism occurring between singlet and triplet charge transfer states is not efficient via spin-orbit interactions.[6,7] The mixing of CT and local triplet states is required to efficient RISC to occur, and thus local triplet states have a key role in the TADF mechanism.[8] This was clearly confirmed in the work described in Chapters 5, 6 and 7, and was later used to validate the spin-vibronic model proposed by Penfold et al.[8–10] Critical points about the TADF mechanism were thus addressed in this thesis, and it is expected that the detailed models studied here will help to improve the design of novel TADF emitters. The work was also directed to investigate ways to obtain efficient TADF in polymers for application in solution processed OLEDs.[1,11,12] After studying the TADF mechanism in the single donor-acceptor molecule, the PTZ-DBTO2 TADF emitter was used as pendant group to design the TADF copolymer COPO1.[1] The photophysics of COPO1 is discussed in Chapter 8, along with another TADF copolymer, COPO2, also based on PTZ-DBT2 as the TADF unit, but using it as part of the copolymer backbone. In COPO2 an alternative way to confine the excited states in the TADF unit is attempted, using a spacer with higher triplet state energy to separate the TADF units. Both copolymers exhibit strong TADF luminescence in their pristine films. In Chapter 9 the influence of the spacer groups in COPO1 is studied. The triplet energy and the delayed fluorescence contribution increase with increasing content of a styrene spacer group. This demonstrates that the TADF properties in copolymers can be fine-tuned by dispersing the

TADF unit using spacer groups. In Chapter 10, this same strategy was again used, but this time replacing the styrene spacer by dibenzothiophene, to take advantage of the blue emission of dibenzothiophene to obtain dual luminescence, composed of a yellowish emission from the TADF unit and blueish emission from the spacer.[11] The luminescence of COPO2 appeared as white luminescence. The photophysics work in these copolymers was complemented by the fabrication of devices by solution processing methods, with the TADF copolymer materials used as the active layer. Although a small molecule had to be used as a co-host to achieve satisfactory efficiencies, this was pioneering work on solution-processed TADF OLEDs. Finally, in Chapter 11 a detailed photophysics study was performed in two Cu complexes, showing TADF and aggregated induced emission.[13] By following the contribution of TADF to the overall luminescence in the two complexes, the strong influence of active molecular vibrations and specific molecular structure to the quenching of luminescence is revealed, opening guidelines to design novel, more emissive, complexes.

11 Bibliography

1 Nobuyasu, R. S.; Ren, Z.; Griffiths, G. C.; Batsanov, A. S.; Data, P.; Yan, S.; Monkman, A. P.; Bryce, M. R.; Dias, F. B. *Adv. Opt. Mater.* **2016**, *4* (4), 597-607

2 Ward, J. S.; Nobuyasu, R. S.; Batsanov, A. S.; Data, P.; Monkman, A. P.; Dias, F. B.; Bryce, M. R. *Chem. Commun.* **2016**, *52*, 3–6.

3 Dias, Fernando B., Santos J., Graves D., Data P., Nobuyasu R. S., Fox M. A., Batsanov A. S., Palmeira T., Berberan-Santos M. N., Bryce M. N., A. P. Monkman, Adv. Sci. **2016**, 3, 1600080

4 Uoyama, H.; Goushi, K.; Shizu, K.; Nomura, H.; Adachi, C. *Nature* **2012**, *492* (7428), 234–238.

5 Nakagawa, T.; Ku, S.-Y.; Wong, K.-T.; Adachi, C. *Chem. Commun.* **2012**, *48* (77), 9580.

6 Sun, H.; Zhong, C.; Brédas, J.-L. *J. Chem. Theory Comput.* **2015**, *11* (8), 3851–3858.

7 Ogiwara, T.; Wakikawa, Y.; Ikoma, T. *J. Phys. Chem. A* **2015**, *119* (14), 3415–3418.

8 Gibson, J.; Monkman, A. P.; Penfold, T. J. T *ChemPhysChem* **2016**, No. 1, 2956–2961.

9 Etherington, M. K.; Franchello, F.; Gibson, J.; Northey, T.; Santos, J.; Ward, J. S.; Higginbotham, H. F.; Data, P.; Kurowska, A.; Lays, P.; Santos, D.; Graves, D. R.; Batsanov, A. S.; Dias, F. B.; Bryce, M. R.; Penfold, T. J.; Monkman, A. P. Fluorescence Emitters. *Nat. Commun.* **2017**, *8*, 1–11.

10 Etherington, M. K.; Gibson, J.; Higginbotham, H. F.; Penfold, T. J.; Monkman, A. P. *Nat. Commun.* **2016**, *7*, 13680.

11 Li, C.; Nobuyasu, R. S.; Wang, Y.; Dias, F. B.; Ren, Z.; Bryce, M. R.; Yan, S. *Adv. Opt. Mater.* **2017**, 1700435

12 Ren, Z.; Nobuyasu, R. S.; Dias, F. B.; Monkman, A. P.; Yan, S.; Bryce, M. R. *Macromolecules* **2016**, 49(15), 5452-5460

13 Li, G.; Nobuyasu, R. S.; Zhang, B.; Geng, Y.; Yao, B.; Xie, Z.; Zhu, D.; Shan, G.; Che, W.; Yan, L.; Su, Z.; Dias, F. B.; Bryce, M. R. *Chem. - A Eur. J.* **2017**, *23* (49), 11761–11766.